Applications of Computation in Acoustics: Ultrasound Bioeffects and Underwater Transmission Loss Uncertainty

by

Brandon Patterson

A dissertation submitted in partial fulfillment
of the requirements for the degree of
Doctor of Philosophy
(Mechanical Engineering)
University of Michigan
2017

Doctoral Committee:

Professor David R. Dowling, Co-Chair
Associate Professor Eric Johnsen, Co-Chair
Professor J. Brian Fowlkes
Professor Douglas L. Miller
Professor William Schultz

Brandon Patterson
awesome@umich.edu
ORCID iD: 0000-0002-3748-3865

© Brandon Patterson 2017
All Rights Reserved

DEDICATION

To Dad – Who taught me how to ”adult”, but not too much. Thanks.

ACKNOWLEDGMENTS

I would like to acknowledge my deepest appreciation to my advisors Eric Johnsen and David R. Dowling. To Eric, your mentorship was invaluable at learning to what it means to understand what you don't know. Through working with you, I have a much better understanding of how I work and what I need to succeed. Furthermore, your flexibility and encouragement as I chased my many outreach and side projects has made this experience all the more worthwhile. To Professor Dowling, you taught me the difference between science and engineering and helped me to figure which I enjoyed, and which I was good at. The support and structure you provided in the last half of my Ph.D. was essential and I couldn't have finished without it. I also extend my thanks to my committee members. To Brian Fowlkes and Doug Miller, thanks for many interesting conversations and great insight, and for keeping my theoretical work a bit more true to reality than it otherwise would have been. To Bill Schultz, thanks for being not only a mentor, but an open minded friend, our chats and adventures in Ghana are some of my favorite moments of my PhD.

This dissertation would not have been survived, let alone completed, if it were not for the support of my friends. I would like to thank: Marc for joining me in everything from cartoon bubbles to sake bomb dynamics; Brian

for consistently being a bad influence when I needed one; Louise for walks; TJ for edifying reasons to not work; Alex for brews at dive bars; Sam for unintentional deep conversations at 8am; Shahab for constant kindness; Phil for exquisite facial expressions; Adaleena for being herself; Mauro for being a kindred midwesterner; Suyash for taking over as the Linux guy; Siddhesh for the best questions; Negin for the best high fives; and Lisa for bringing continuous spirit to the office. Additionally, thanks to the ME staff who have made my life easier and more fun, especially Melissa and Kathie. Thanks also to my friends from Purdue and Chesterton for distant emphathy and Mario Kart. Thanks to my brother for never censoring himself, Aunt Diane for continuing to inspire me to chase crazy dreams, and to Dad for absolutely everything. To Mom, I wouldn't be here if it wasn't for you pushing me for all of those years, I love you and you are deeply missed. To Doe Doe and The Leviathan, thanks for bringing a sense of family to my home and keeping Liz sane. Lastly, to my wonderful wife, Liz "Chicken" Patterson for pushing me, caring for me, feeding me, and all of the many adventures in between.

This research was supported in part by the by the National Science Foundation (NSF) Graduate Research Fellowship under NSF Grant Number DGE 1256260, and by NSF grant 1253157, and by the National Institutes of Health under award number 4-R01-HL-116434-04, and by the Office of Naval Research through Award Number ONR STTR N14A-T016 (subcontract from Daniel H. Wagner Associates), and by a University of Michigan MCubed grant. This work used the Extreme Science and Engineering Discovery Environment (XSEDE), which is supported by National Science Foundation grant number ACI-1548562.

PREFACE

This dissertation presents work in which computation and modeling are used to make advancements in two separate and distinct areas of acoustics: ultrasound bioeffects modeling (which serves to motivated the bulk of this thesis) and acoustic transmission loss uncertainty quantification in uncertain ocean environments. While these works are united in the use of computation and broader field of acoustics, the underlying motivation and relevant background is separate. Hence this document is split into two separate and distinct parts along these lines. A summary of relevant background information, work performed, and conclusions in each area will be presented separately.

TABLE OF CONTENTS

Dedication ii
Acknowledgments ii
Preface v
List of Figures ix
List of Tables xi
List of Appendices xii
List of Abbreviations xiii
Abstract xiv

Part I: Ultrasound bioeffects **1**

CHAPTER

1 Introduction 2
1.1 A physical description of sound as it relates to this work 2
1.2 Ultrasound in medicine and biological effects 4
1.2.1 Physical mechanisms of ultrasound bioeffects and problem description 7
1.2.1.1 Cavitation of ultrasound contrast agent microbubbles . . 8
1.2.1.2 Ultrasound-induced lung hemorrhage 11
1.2.1.2.1 Proposed mechanism for Diagnostic Ultrasound (DUS)-induced lung hemorrhage: vorticity-driven strain of the alveolar walls 13
1.3 Tissue as a compressible fluid system 15
1.3.1 Dimensional analysis and assumptions for Contrast-Enhanced Ultrasound 17
1.3.2 Dimensional analysis and assumptions for an acoustically driven alveolus 19
1.3.3 Limitations 21
1.4 Thesis overview 22
2 Theoretical microbubble dynamics at capillary breaching thresholds 26
2.1 Abstract 26
2.2 Background & Introduction 27
2.3 Materials and Methods 30
2.3.1 Experimental Setup 30
2.3.2 Bubble Dynamics Model 32

2.4 Results and Discussion . . . 34
2.4.1 Bubble Response . . . 34
2.4.2 Dependence on the Pulse Amplitude . . . 36
2.4.3 Dependence on the Initial (Equilibrium) Bubble Radius . . . 38
2.4.4 Dependence on the Pulse Frequency . . . 39
2.4.5 Dependence on the Tissue Properties . . . 41
2.5 Conclusions . . . 42
3 Growth of liquid-gas interfacial perturbations driven by acoustic waves . . . 44
3.1 Abstract . . . 44
3.2 Introduction . . . 45
3.3 Fluid mechanics modeling of ultrasound-lung interaction . . . 49
3.4 Results and discussion . . . 55
3.4.1 Dynamics of the baseline case . . . 55
3.4.1.1 Density-based description of the perturbation growth . . . 55
3.4.1.2 Vorticity-based description of the perturbation growth . . . 59
3.4.2 Dependence of the perturbation growth on the wave amplitude . . . 62
3.4.2.1 General Observations . . . 62
3.4.2.2 Late time scaling of the perturbation amplitude . . . 63
3.4.2.3 Late time scaling of the interfacial length . . . 67
3.4.3 Dependence of the growth on the wave duration . . . 69
3.5 Conclusions . . . 70
4 Pulsed ultrasound-induced stresses and strains at gas-liquid interfaces . . . 73
4.1 Abstract . . . 73
4.2 Introduction . . . 74
4.3 Methods . . . 78
4.3.1 Stress and strain at the alveolar interface . . . 80
4.4 Results and Discussion . . . 82
4.4.1 Qualitative observations of the interface . . . 82
4.4.2 Interface strain, ε . . . 83
4.4.3 Viscous stress . . . 87
4.4.4 Ultrasound-induced vorticity dynamics and interface growth . . . 92
4.4.5 Limitations of the present work . . . 97
4.5 Summary, conclusions, and future work . . . 99
5 Conclusions and future work . . . 102
5.1 Summary of key contributions and findings . . . 102
5.1.1 Bubble Dynamics of Contrast Enhanced Ultrasound and Related Bioeffects . . . 102
5.1.2 Diagnostic Ultrasound-induced lung hemorrhage and acoustically driven gas-liquid interfaces . . . 104
5.2 Overall conclusions . . . 107
5.3 Recommendations for future work . . . 109
5.3.1 Extending and improving the study of bubble dynamics at capillary breaching thresholds . . . 109
5.3.2 Extending and improving the physical model of DUS lung-interaction 110
5.3.2.1 Improving the lung model . . . 111

5.3.2.2 Improving the ultrasound model 112

Part II: Underwater Acoustic Uncertainty 115

CHAPTER

6 Efficient Estimation of the Probability Density Function of Acoustic Transmission Loss in Uncertain Ocean Environments Using Area Statistics 116

6.1 Abstract 116

6.2 Introduction 117

6.3 Methods 121

6.4 Summary and Conclusions 137

Appendices 140

Bibliography 162

LIST OF FIGURES

1.1 An example diagnostic ultrasound image of a featus at 12 weeks in a sagittal scan. . . 5
1.2 Schematic of possible ultrasound bioeffects mechanisms 10
1.3 Schematic of baroclinic torque 14
1.4 Schematic of the Richtmyer-Meshkov Instability for a heavy-light interface 15

2.1 7.5 MHz experimental and numerical ultrasound waveforms at bioeffects threshold pressure 31
2.2 Bubble radius and input-pressure waveform histories for an essentially linear case (frequency: 1.5 MHz; peak negative pressure: 0.35 MPa) 35
2.3 Bubble radius and input pressure histories for a moderately nonlinear case (frequency: 3.5 MHz; peak negative pressure: 2.4 MPa) 35
2.4 Bubble radius and input pressure histories for a highly nonlinear case (frequency: 7.5 MHz; peak negative pressure: 6.0 MPa) 36
2.5 Dependence of the dimensionless maximum bubble radius on the peak negative pressure for $G = 100$ kPa. 37
2.6 Dependence of the bubble dynamics on the gas contents ($G = 100$ kPa). 38
2.7 Dependence of the dimensionless maximum bubble radius on the initial bubble size for the amplitude at which bioeffects are first observed, at a given frequency, for $G = 100$ kPa 39
2.8 Dependence of the bubble dynamics on the frequency for $G = 100$ kPa 40
2.9 Dependence of the dimensionless maximum bubble radius on the frequency. 41

3.1 Schematic view of the physical and model problems 51
3.2 Ideological progression from ultrasound pulse and shock to baseline trapezoidal wave 52
3.3 The evolution of the acoustically-driven, perturbed interface 56
3.4 Interface perturbation amplitude history $a(t)/a_0$ for the baseline $p_a = 10$ MPa, $L = 45\ell$ trapezoidal wave. 58
3.5 y-locations of the bubble and spike for the baseline $p_a = 10$ MPa trapezoidal wave case, during and shortly after the wave-interface interaction. 58
3.6 The evolution of the vorticity field 60
3.7 Cumulative vorticity along the interface for early, intermediate, and late times 61
3.8 Circulation history for the right-half domain for the baseline $p_a = 10$ MPa, $L = 45\ell$ trapezoidal wave case 62
3.9 The interface amplitude and circulation for long time and multiple wave amplitudes . . 64
3.10 Interface amplitude scaled by circulation density at t_Γ 66

3.11 The interface amplitude and circulation for long time and multiple wave amplitudes . . 68
3.12 The interface and circulation dependence on wave duration 70

4.1 A histological cross section of alveoli. 79
4.2 Ultrasound pulse waveform 80
4.3 Evolution of the interface for $p_a = 1.0$ MPa ultrasound wave 84
4.4 Evolution of the interface for $p_a = 2.5$ MPa ultrasound wave 85
4.5 Evolution of the interface for $p_a = 5.0$ MPa ultrasound wave 86
4.6 Interfacial strain dependence on pressure amplitude ($p_a = 1.0, 2.5, 5.0$ MPa) 88
4.7 Interfacial strain dependence on initial perturbation amplitude ($a_0 = 0.03\ell,\ 0.10\ell,\ 0.30\ell$) 89
4.8 Evolution of the viscous stress field for the $p_a = 5.0$ MPa wave 92
4.9 Interfacial viscous stress dependence on pressure amplitude ($p_a = 1.0, 2.5, 5.0$ MPa) . 93
4.10 Interfacial viscous stress dependence on initial perturbation amplitude amplitude ($a_0 = 0.03\ell, 0.10\ell, 0.30\ell$) 94
4.11 Vorticity and circulation histories for the $p_a = 10$ MPa ultrasound pulse. 96
4.12 Interface perturbation amplitude history for the $p_a = 10$ MPa ultrasound pulse. 97

6.1 Nominal bathymetry for the ten uncertain ocean environments used in this study . . . 123
6.2 Schematic of generic ocean environment and uncertain environmental parameters . . . 124
6.3 Example of Area Statistics Process 131
6.4 Comparison of area statistics- and Monte Carlo-generated TL PDFs 132
6.5 TL fields with area statistics test locations and indication of success vs failure at each . 136

A.1 Convergence of the interface length at long times 144
A.2 Convergence of the interface amplitude and circulation 145
A.3 Dependence of vorticity on volume fraction across the interface 147
A.4 Evolution of the pressure field for the $p_a = 10$ MPa trapezoidal wave. 149
A.5 Numerical reflection coefficient at the interface vs interface thickness parameter δ . . . 150
A.6 Perturbation amplitude and circulation histories for the -10 MPa trapezoidal wave . . . 151
A.7 Perturbation amplitude and circulation histories for the 10 MPa sinusoidal wave 152
A.8 Comparison of elastic and inertial forces for the $p_a = 10$ MPa trapezoidal wave 154

B.1 Dependence of circulation deposition on pressure amplitude and initial perturbation amplitude. 156
B.2 Interface amplitude, circulation, and strain histories are presented for all ultrasound pulse cases considered in Chapter 4 157

LIST OF TABLES

2.1 Base physical parameters representative of soft tissue used in the present study. 32

3.1 Circulation during the wave-interface interaction. 63
3.2 Interface amplitude growth time exponents, $\frac{a(t)}{\ell} \sim t^n$ 66

6.1 Summary of uncertain environmental parameters and their distributions 125
6.2 Summary of L_1 error of area statistics-generated TL PDFs, compared to Monte Carlo-generated PDFs 139

LIST OF APPENDICES

A Appendices for Chapter 3 141
A.1 Order of magnitude analysis of vorticity-generation mechanisms 141
A.2 Convergence: interface length per unit circulation, $s(t)/\Gamma(t)$ 143
A.3 Vorticity distribution 144
A.4 Numerical treatment of the initial interface 147
A.5 Perturbation growth for the -10 MPa trapezoidal wave 150
A.6 Perturbation growth for the 10 MPa sinusoidal wave 151
A.7 Comparison of elastic and inertial forces for the 10 MPa trapezoidal wave 152
B Appendices for Chapter 4 155
B.1 Circulation due to $1, 2.5$, and 5 MPa Ultrasound Pules with dependence on p_a and a_0 155
B.2 Ultrasound-induced interface growth, strain, and circulation 155
C Underwater uncertainty Monte Carlo Randomization Techniques 158
C.1 Area statistics randomizations 158

LIST OF ABBREVIATIONS

CEUS Contrast-Enhanced Ultrasound

DG Discontinuous Galerkin

DUS Diagnostic Ultrasound

ED Exposure Duration

FDA Food and Drug Administration

HIFU High-Intensity Focused Ultrasound

IC Inertial Cavitation

LH Lung hemorrhage

MI Mechanical Index

PCH Pulmonary Capillary Hemorrhage

PDF Probability Density Function

PRF Pulse Repetition Frequency

PRPA Peak Rarefaction Pressure Amplitude

RM Richtmyer-Meshkov

RMI Richtmyer-Meshkov Instability

RTI Rayleigh-Taylor Instability

STEM Science, Technology, Engineering, and Math

TL Transmission Loss

US Ultrasound

WENO Weighted Essentially non-oscillatory

ABSTRACT

This dissertation presents work in which computational modeling is used to advance two areas of interest in modern acoustics. First, we develop computational models to study the poorly understood physics underlying Contrast-Enhanced Ultrasound (CEUS) bioeffects and Diagnostic Ultrasound (DUS)-induced lung hemorrhage. A better understanding of these problems is critical to the development of science-based safety guidelines. Because inertial cavitation is thought to cause CEUS bioeffects, we model a spherical bubble in viscoelastic soft tissue, driven by experimentally-measured ultrasound waveforms (1.5 − 7.5 MHz), with known bioeffects thresholds. Bioeffects thresholds were compared with calculated cavitation metrics and experimentally determined bioeffects thresholds were found greater than accepted thresholds for inertial cavitation in water, and that the maximum dimensionless bubble radius R_{max}/R_0 correlated strongly with bioeffects thresholds as a function of frequency. Separately, we investigate DUS-induced lung hemorrhage and model an acoustic wave in soft tissue (water) traveling toward an alveolus (air) with a perturbed surface. First, a trapezoidal wave with ultrasonically relevant properties (5.0 – 12.5 MPa pressures amplitudes, 1.3 – 6.0 μs wave durations), drives the interface. We showed that acoustic waves may be capable of depositing sufficient baroclinic vorticity to drive significant interface perturbation growth, long after the wave has passed. This growth scaled with the circulation density (i.e., the circulation per unit length of the interface) and exhibited power-law behavior at late time. To approximate Ultrasound (US)-induced stresses and strains on alveoli, we subjected interfaces of varying initial perturbation amplitude to 1.5 MHz ultrasound pulses with peak amplitudes

from 1 – 5 MPa and observed interfacial viscous stress amplitudes up to approximately 60 Pa and interfacial strains up to 38%. While the viscous stresses appeared beneath capillary failure thresholds, the calculated strain was sometimes greater than expected failure thresholds for alveolar epithelium. Since this work considers only a single pulse, and the vorticity driving the deformation is expected to accumulate over multiple pulses, we conclude that vorticity-induced deformation is worthy of further investigation.

Finally, we develop *area statistics*, a computationally efficient method for estimating Probability Density Functions (PDFs) of acoustic Transmission Loss (TL) in uncertain ocean environments. Such PDFs of TL are useful for real-time Naval applications but impractically expensive to obtain via traditional computational methods. This work describes how to approximate the PDF of TL at a point of interest using TL statistics from the field surrounding the point of interest. The idea is that local TL variations due to environmental fluctuations are represented by spatial variations in TL in single baseline TL field calculation. The baseline calculation used the most probable values for uncertain parameters describing the sound speed profile, bathymetry, and geoacoustic bottom-layer properties. *Area statistics*-generated PDFs were compared with 2000-sample Monte Carlo-generated PDFs via the L_1 error, in ten ocean environments with varying properties and uncertainties, for source frequencies of 100, 200, and 300 Hz and depths of 91, 137, 183m. The *area statistics*-generated PDFs had an L_1 error < 0.5 in 91% of the 11,000+ test locations (depths from 20 m - 4.5 km, ranges from <1 km to >70 km). *Area statistics* PDFs were generated in milliseconds, required $\sim 10^{-6}$ times the computational effort required for Monte Carlo PDFs and were thus suitable for real-time applications.

In summary, this dissertation contains: 1.) research in which computational models of CEUS and ultrasound-alveolar interaction were developed and used to study the physics of relevant ultrasound-induced bioeffects, and 2.) *area statistics*, a real-time appropriate computational technique for estimating PDF of TL in uncertain ocean envi-

ronments, is developed and tested.

Part I:

Ultrasound bioeffects

CHAPTER 1

Introduction

In this chapter we establish the merit and relevance of the presented work. The problems approached here apply to a variety of active areas of study and modern applications within the fields of acoustics and fluid mechanics, though the primary focus and motivation of this work is to better understand the underlying physics of specific biological effects of Diagnostic Ultrasound (DUS). An understanding of the physical mechanisms underlying DUS bioeffects is necessary for evidence-based regulation. Accordingly, we describe the driving physical mechanisms of interest in these problems. We also discuss the specific problems we will be approaching and the framework we use to approach them. Finally, an overview of the goals and contributions of this part of the thesis are presented.

1.1 A physical description of sound as it relates to this work

Sounds are vibrations traveling through a medium. Parcels of material perturbed or displaced collide with their neighbors, which collide with their neighbors and so on. In this way, mechanical energy propagates as a wave at a finite speed, away from the initial perturbation location, through any gas, liquid, or solid medium. This is the basic mechanism by which sound moves through all matter whether it be the tissues in the human body, the water in the oceans, or the plasma in the stars.

The scientific study of sound, in all its many forms, is what we refer to as *acoustics*. Through years of study and experimentation, mankind has gained a deep understanding of the physical

behavior of sound and has learned to harness it as a tool, leading to high-impact advancements throughout Science, Technology, Engineering, and Math (STEM) in areas ranging from climate change (by monitoring the ocean's acoustic properties) to structural health monitoring and diagnostic and therapeutic medicine. Much of our basic understanding of sound has come from the theoretical study of sound passively propagating through a constant, infinite, homogeneous medium. However, in reality no such medium exists and sound is not always passive. Indeed many of the interesting physical questions and real-world applications of interest to modern acousticians are concerned with the scenarios in which sound is traveling through a complicated medium which it sometimes physically alters. In this thesis, we hope to advance the study of acoustics by studying a few of these scenarios.

The focus of this part of the thesis is on problems in which sound travels between multiple media and causes a physical change in the system as it travels. Typically, when sound traveling in one medium encounters another medium, a portion of the acoustic energy is transmitted into the new medium, while the remainder is reflected and scattered back into the medium from which the sound originated. In most cases, this results in little change in the media themselves, however, in some instances, acoustic energy can be converted into other forms of energy such as kinetic or thermal, resulting in bulk motion or heating of the media. Conversion of energy such as this is often consequence of nonlinearity in the system, which can arise from physical properties of the system such as a liquid-gas interface, or from sufficiently strong acoustic waves ($\textit{Acoustic pressure}/[\textit{density} \cdot \textit{sound speed}^2] \not\ll 1$). An example of acoustic energy becoming kinetic as a result of a nonlinearity in the physical system is a gas-vapor bubble within water or tissue driven by an acoustic wave. As a result of rising and falling acoustic pressure, the bubble may oscillate or collapse, changing the temperature and pressure, and driving the motion within the bubble and the surrounding medium. The absorption of acoustic energy into the medium as heat resulting in a temperature rise (due to localized compression) in a viscous medium is an example of an effect that can be particularly important for strong, nonlinear acoustic waves. Additionally, localized compression/rarefaction due to strong nonlinear acoustic waves can result in

an increase in localized sound speed, causing waves to sharpen into shocks, introducing further nonlinearity. In any case, the resulting thermal or physical stresses associated with the heating or movement of the media may result in physical (e.g., phase transition) or chemical (e.g., protein denaturation) changes. The ability of acoustic waves to physically alter a medium is of particular interest and relevance to the field of medical ultrasound, in which such alteration is relevant to both safety concerns in the context of diagnostic sonography and engineering concerns in the context of therapeutic Ultrasound (US).

1.2 Ultrasound in medicine and biological effects

Ultrasound (US) refers to sounds or vibrations with frequencies beyond that audible to the human ear, typically $>$ 20 kHz. The use of US in medicine dates back to the 1940s when Austrian neurologist Dr. Karl Theodore Dussik attempted to use transmission ultrasound to outline the ventricles of the brain (Dussik, 1942; Singh & Goyal, 2007). Since then the abilities and use of US have expanded greatly and the technology has proven to be a powerful tool for noninvasive therapies and safe, real-time diagnostic imaging (Dalecki, 2004). Consequently, the use of US has become ubiquitous throughout modern medicine. The bulk of the present work will focus on Diagnostic Ultrasound (DUS), which is routinely used for noninvasive imaging of a range of soft tissues including muscles, tendons, organs, glands and neonatal fetuses.

For context, we explain the basic physical processes that occur during US procedures. In practice, high-frequency, typically MHz-range, acoustic waves and pulses are created at the surface of the body using a piezoelectric US transducer. These acoustic waves, propagate via an impedance matching, acoustic coupling medium from the transducer into the tissue. Once in the tissue, a portion of the sound scatters at material interfaces within the body, or more simply, some of the sound echoes whenever it moves from one tissue to another or encounters a cavity in the body. More precisely put, a portion of the sound is reflected when it encounters a change in the acoustic impedance, defined as the product of the density and sound speed of the medium. This scattering

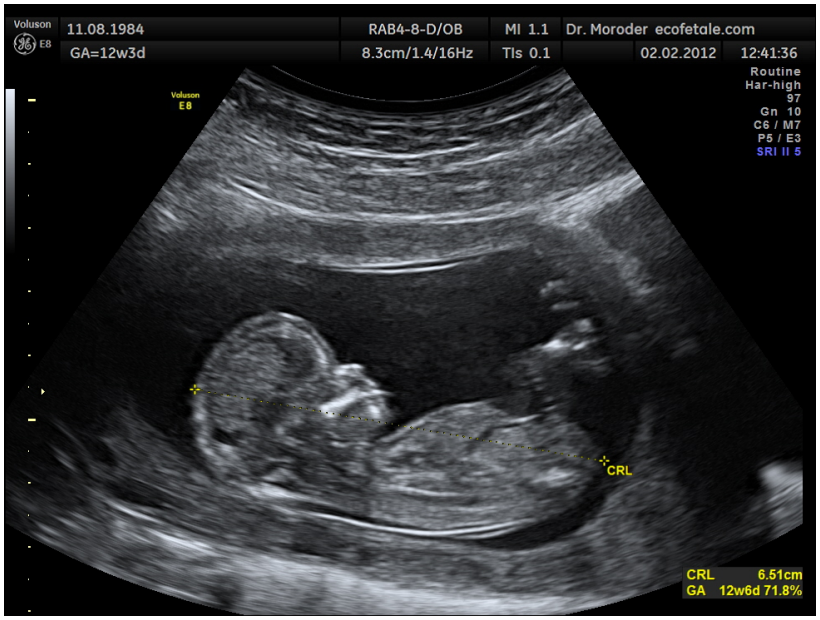

Figure 1.1: An example diagnostic ultrasound image of a featus at 12 weeks in a sagittal scan. Author Wolgang Moroder [CC BY-SA 3.0 (http://creativecommons.org/licenses/by-sa/3.0), via Wikimedia Commons]

of sound is the basic physical principle that makes ultrasound for diagnostic imaging possible. In DUS, some of the reflected sounds encounter a receiver. This receiver is typically also a piezoelectric transducer, and much like the process of generating the wave, but in reverse, the receiver is vibrated and converts the acoustic signal to a series of electrical pulses. The signal is amplified, recorded, transmitted to an ultrasound scanner or another computer where it is processed. The strength of the received signal is indicative of the impedance mismatch at the reflective surface and is indicated as brightness in an ultrasound image. The timing of the receipt of the reflected signal across the receiver is determined by the shape of the reflecting surface. By processing this information, a real-time image of the reflecting surface is generated. An example ultrasound image of a fetus is shown in Figure 1.1.

The passage of acoustic waves of diagnostically relevant amplitudes through tissue does not typically permanently alter or affect the tissues structures or processes and the use of ultrasound for imaging is typically considered safe and noninvasive. However, the passage of acoustic waves through a medium is not entirely passive under all circumstances (Nyborg, 2001). When energy

from ultrasound is converted to kinetic or thermal energy, within a tissue, it can physically alter or damage that tissue through a variety of mechanisms (O'Brien, 2007). These effects are referred to as US bioeffects and can be beneficial or detrimental depending on their exact nature. In therapeutic applications, US is used to deliberately cause desirable bioeffects that are beneficial to the patient. DUS is typically designed to minimize interaction between the acoustic field and tissue (Dalecki, 2004) (as per United States Food and Drug Administration Regulation), and bioeffects are generally undesirable side effects that are avoided if possible. Ultrasound bioeffects have motivated extensive research into the development of effective guidelines and regulations for safe US technologies and procedures.

A large portion of past research into ultrasound bioeffects has focused on determining what types of US bioeffects exist, and under what circumstances they occur. This work has shown that bioeffects may take on a variety of different forms, depending on the US parameters and type of tissue exposed (National Council on Radiation Protection and Measurements. Scientific Committee 66 on Biological Effects of Ultrasound. & National Council on Radiation Protection and Measurements., 2002). Various kinds of hemorrhage and cell death are among the most common forms of US bioeffects. In tissues containing gases such as the lung and intestines, ultrasonically induced hemorrhage has been observed. Lehmann & Herrick (1953) and Miller & Thomas (1990) observed abdominal petechial hemorrhage as a result of unfocused ultrasound in mice. And Child *et al.* (1990) found hemorrhage in mouse lungs after the animal was exposed to lithotripter pulses. Numerous other studies have been performed on the topic of US-induced lung hemorrhage and a much deeper review is given in chapters 3 and 4. Pulsed ultrasound of the heart has been shown to be capable of inducing cardiac contractions in frogs and mice (Dalecki *et al.*, 1993; MacRobbie *et al.*, 1997). Cell death has been observed in liver, kidney, and heart tissue as a result of Contrast-Enhanced Ultrasound (CEUS), which uses injections of microbubbles as additional scatterers for image contrastSkyba *et al.* (1998); Miller *et al.* (2008a).

1.2.1 Physical mechanisms of ultrasound bioeffects and problem description

Depending on the type of physical damage mechanism responsible, US bioeffects are classified into two groups, thermal and non-thermal (Dalecki, 2004). While both thermal and non-thermal bioeffects may occur simultaneously, one or the other is often dominant. The first group, thermal bioeffects, are characterized by deposition of acoustic energy into tissue as heat and are often a result of therapeutic, rather than diagnostic, ultrasound. This heating can lead to a variety of deleterious effects including the release of highly reactive free radicals, protein denaturation at the molecular level, and death at the cellular level, ultimately causing tissue damage or death. As an example, one class of therapeutic US, known as High-Intensity Focused Ultrasound (HIFU) uses strong, concentrated acoustic waves to intentionally convert acoustic energy to heat through viscous dissipation and thermal diffusion. HIFU is typically at MHz order frequencies and intensities up to 10,000 W/cm^2. HIFU is used to raise the temperature of unwanted tissues such as fat or cancer to the point of destruction via thermal necrosis (Escoffre & Bouakaz, 2016). Little else will be said about thermal bioeffects, as the bioeffects of interest here fall into the non-thermal category. Non-thermal bioeffects are attributed to a variety of physical phenomena including acoustic radiation force, radiation torque, and acoustic streaming, though the bulk of non-thermal bioeffects are commonly associated with acoustic cavitation, which is the most widely studied non-thermal mechanism (Dalecki, 2004). For certain bioeffects, such as DUS-induced lung hemorrhage, the underlying physical mechanisms are largely unknown.

The work of this thesis is primarily motivated by DUS bioeffects. DUS bioeffects tend to be a result of mechanical processes and typically take the form of hemorrhage, tissue damage or cell death. Unlike some bioeffects that occur as a result of therapeutic US, DUS bioeffects are unintentional and a represent a potential safety concern. Hence in this thesis we seek to develop a better understanding of two particular DUS bioeffects problems,

1. The first problem is motivated by CEUS and the associated cavitation-induced biological effects, which include hemorrhage and cell death in a variety of forms (e.g., cell death and/or

hemorrhage in the heart, kidney, muscle, etc...) (Miller *et al.*, 2008a). We pursue of a better understanding of the relationship between US thresholds associated with bioeffects and the physical dynamics of the system. To this end we take a novel approach, combining experimentally measured ultrasound and bioeffects thresholds with modeling and simulation. We model the problem of an ultrasound contrast agent microbubble subjected to an experimentally measured ultrasound pulse and simulate relevant bubble dynamics. Calculated cavitation dynamics are related to known bioeffects and thresholds, associated with properties of the driving waveforms.

2. The second problem we consider is that of DUS-induced lung hemorrhage. As the underlying physical mechanism that drives the hemorrhage is not clearly understood (O'Brien, 2007), we aim to gain a better conceptual understanding of the physics at play. To accomplish this, we develop a unique model of the interaction between an alveolus and an acoustic wave, traveling in soft tissue. The alveolar wall is modeled as an air-water interface, driven by trapezoidal and ultrasound pulse-like acoustic waves. We analyze the dynamics of the system to describe the interface evolution mathematically. Where possible we compare calculated stress and strain estimates of the interface with alveolar failure criteria for disruption of endothelial and epithelial tissues.

Given these bioeffects problems, we will now provide a brief overview of what is known about the physical mechanisms of CEUS cavitation bioeffects and DUS-induced lung hemorrhage. We will also include a description of a proposed mechanism for DUS-induced alveolar hemorrhage.

1.2.1.1 Cavitation of ultrasound contrast agent microbubbles

Acoustic cavitation is the phenomenon by which gas nano and microbubbles, called cavitation nuclei, are cyclically grown by low pressures and collapsed by high pressures of the field. When the bubble dynamics during collapse are dominated by the inertia of the surrounding fluid, the process is called Inertial Cavitation (IC). IC is typically violent, with the bubble rapidly collapsing to a fraction of its original size resulting in calculated internal pressures ranging from 100 to

7000 MPa and temperatures from 1000 to 20000 K (Flynn, 1982). There are several possible damage mechanisms associated with IC that may be responsible for observed US bioeffects. Due to the pressure difference between the vapor/gas mixture within the bubble at collapse and the surrounding medium, the collapsed bubble can emit a powerful shock wave that can be damaging to the bubble's surroundings. When cavitation is triggered near a rigid surface, the bubble can collapse in a radially asymmetric fashion causing a high-speed "re-entrant" jet of liquid to impinge upon the surface, effectively striking the surface with a liquid hammer. If cavitation occurs at an appropriate distance from a non-rigid surface, such as soft tissue boundaries and blood vessel walls, the jet can impinge away from the surface, potentially invaginating the surface (Brujan, 2011). The resulting stresses and strains can result in structural damage. Figure 1.2 schematically illustrates potential cavitation damage mechanisms within a blood vessel.

While IC does not typically occur during non-contrast DUS, it is of concern during CEUS, which uses contrast-agent microbubbles injected into patients' bloodstreams to act as additional, strong scatterers. The high acoustical impedance mismatch between the gas microbubbles and the surrounding soft tissues allows for high contrast imaging and can be used to ultrasonically image blood flow, which is useful for diagnosing heart valve problems, liver lesions, and more (Claudon *et al.*, 2012; Rognin *et al.*, 2008). However, the use of contrast agent microbubbles can also have potential deleterious side effects. These microbubbles can act as cavitation nuclei and the resulting cavitation has been associated with a variety of different forms of cellular death and damage. The precise ultrasonic thresholds for which cavitation and bioeffects occur have been a topic of intense study and are not completely physically described. Furthermore, the exact physical mechanisms through which cavitation causes bioeffects are also not clearly understood (Barnett *et al.*, 1994).

As a result of the potential for cavitation-related US bioeffects, the United States Food and Drug Administration called for a metric to quantify cavitation dosage and predict likely cavitation damage from ultrasound. As bioeffects are typically attributed to IC, efforts to predict cavitation damage considered the likelihood of IC based on theoretical calculations of free gas bubbles in water. In the case of acoustic cavitation, the likelihood of damage depends on the duration of

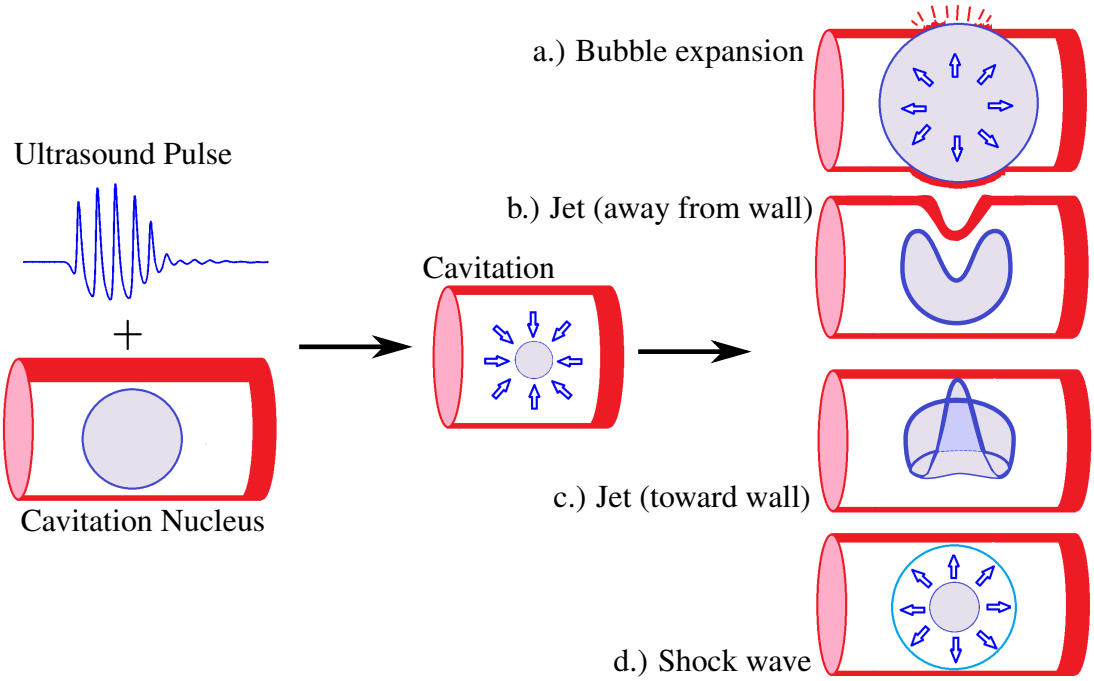

Figure 1.2: Schematic of possible cavitation-induced ultrasound bioeffects mechanisms. (Left) A microbubble within a blood vessel interacts with an ultrasound pulse. (Middle) Subsequently, the bubble undergoes cavitation. (Right) A variety of possible cavitation bubble dynamics scenarios are potential bioeffects damage mechanisms (from top to bottom): a). Bubble expansion beyond the radius of a surrounding blood vessel. b.) A cavitation jet away from the wall of a surrounding blood vessel or tissue surface causes the surface to invaginate. c.) A cavitation jet of high speed liquid strikes a vessel or tissue wall. d.) A shock wave created by the bubble collapse encounters nearby tissue.

peak negative pressure experienced by a cavitation nucleus, with longer interactions depositing more energy into the nucleus, and thus having a greater likelihood of inducing IC and bioeffects. The duration of the Peak Rarefaction Pressure Amplitude (PRPA) is inversely related to the US frequency. Holland & Apfel (1989) demonstrated that the threshold PRPA needed to trigger IC, defined based on a maximum bubble temperature ≥ 5000K, depended on the size of the cavitation nucleus. Smaller cavitation nucleii, must overcome greater surface tension effects in order to cavitate, with the Laplace pressure scaling inversely with the radius of the nucleus. Furthermore, as the initial radius of a nucleus increases, the inertia of the surrounding fluid that it must be overcome also increases (American Institute of Ultrasound in Medicine, 2000). Thus Holland & Apfel (1989) illustrated that for a given frequency there is an optimal nucleus size for triggering IC. Based on these calculations and corrections for heat dissipation in tissue the Mechanical Index (MI) was created as a measure of ultrasound-induced cavitation related bioeffects and defined as

$$\mathrm{MI} = \frac{P_{r.3}}{\sqrt{f_c}}, \tag{1.1}$$

where $P_{r.3}$ is the PRPA derated by 0.3 dB/MHz-cm (a soft tissue attenuation coefficient) and f_c is the center frequency Apfel & Holland (1991). As the MI was originally created based on theoretical thresholds for inertial cavitation in water, the derated PRPA was used to account for *in vivo* attenuation, however the effects of tissue's elastic properties are not accounted for by this metric, and because the cavitation dynamics are expected to change from tissue-to-tissue a more robust evidence-based metric would be useful. The United States Food and Drug Administration (FDA) mandates that MI≤ 1.9 for diagnostic ultrasound, though US bioeffects have been observed at MI below this in the case of DUS of mammalian lungs (O'Brien, 2007; FDA, 1997).

1.2.1.2 Ultrasound-induced lung hemorrhage

The second US bioeffects topic of interest in this thesis is DUS-induced Lung hemorrhage (LH). In the relevant literature, this is also sometimes referred to more specifically as Pulmonary Capillary

Hemorrhage (PCH). This phenomenon was first discovered in mice over twenty years ago by Child *et al.* (1990) and has since been shown to occur in a variety of other mammals including rats, pigs, rabbits, and monkeys (O'Brien & Zachary, 1997; Miller, 2012; Tarantal & Canfield, 1994). Research into this phenomenon has focused on three main areas: (1) Determining the physical mechanism of the hemorrhage; (2) Understanding how the occurrence and severity of the hemorrhage depend on the ultrasonic properties (frequency, amplitude, waveform, etc...); and (3) Understanding how the occurrence and severity of the hemorrhage depend on the characteristics of ultrasound subject (species, age, anesthesia, etc...). The work in this thesis pertains primarily to the first of these three areas.

Despite extensive previous research into DUS-induced LH, the underlying physical mechanisms are still not well understood. Furthermore, past work has shown that common US bioeffects mechanisms do not explain the observed injuries. Thermal damage mechanisms appear unlikely to be the primary source of damage as DUS-induced lung lesions do not appear similar to those induced by heat (Zachary *et al.*, 2006). Furthermore, cavitation mechanisms do not appear to be responsible, as the severity of DUS-induced LH in mice increased under raised hydrostatic pressure (O'Brien *et al.*, 2000b) and was unaffected by the introduction of US contrast agents into both rats and mice subject to lung US (Raeman *et al.*, 1997; O'Brien *et al.*, 2004). Both of these results are inconsistent with what is expected of IC-induced bioeffects. More recent work by Miller (2016a,b) investigating acoustical radiation surface pressure as a potential damage mechanism found that the pressures expected in pulsed ultrasound were likely too low to completely explain the observed hemorrhage on their own. Simon *et al.* (2012) found that atomization and fountaining occurred at tissue-air interfaces subjected to HIFU and suggested that this could potentially happen at diagnostic levels as well. Similarly, works by Tjan & Phillips (2007, 2008) model the evolution of an inviscid, free surface subjected to a Gaussian velocity potential and find that this can lead to the ejection of liquid droplets. They go on to say that DUS of the lung may similarly lead to the ejected of droplets capable of puncturing the air-filled sacs within the lung. The problem of US-lung interaction is the central motivation of chapters 3 and 4. As such, a far more in-depth

literature review is provided in these chapters.

1.2.1.2.1 Proposed mechanism for DUS-induced lung hemorrhage: vorticity-driven strain of the alveolar walls

In this thesis we propose yet another potential physical mechanism for causing DUS induced lung hemorrhage, and as such we now provide the relevant background. The physical problem underlying interactions between ultrasound waves and the various tissue and fluid layers of the body is that of a mechanical wave traveling in one medium encountering a second medium of differing physical properties. As was previously explained, this can result in acoustic energy being converted into motion or heat. In the case of the bubble, the relevant manifestation of this was cavitation. Another manifestation of this is the growth of perturbations at fluid-fluid interfaces as a result of non-uniform velocity gradients that occur at the driven interface. Another way of thinking of this is in terms of baroclinic vorticity, or localized fluid rotation, generated by the misalignment of interface density gradients and mechanical wave pressure gradients. In this dissertation we propose that (1) ultrasound-induced baroclinic vorticity may drive the growth of perturbations at liquid-gas interfaces such as those of the alveoli and (2) this perturbation growth leads to alveolar strain with possible hemorrhage. In the remaining portion of the section, we discuss in greater detail the underlying physics at play here and some of the past work that has been done to understand it.

There has been extensive past research into the physics that underlies mechanical waves interacting with and accelerating fluid-fluid interfaces. Much of this work has investigated regimes outside those of acoustic interests, including applications in fusion energy and astrophysics. Taylor (1950) predicted that, for an interface between two fluids of different densities, if the fluid was accelerated normal to the interface in the heavy-to-light direction, perturbations at the interface would grow. That is to say that a "bubble" of light fluid penetrates the heavy fluid, and a "spike" of heavy fluid penetrates the light fluid. This is known as the Rayleigh-Taylor Instability (RTI). A similar topic of past study is the Richtmyer-Meshkov Instability (RMI), which occurs when a perturbed fluid-fluid interface is instantaneously accelerated by a shock, causing the interface per-

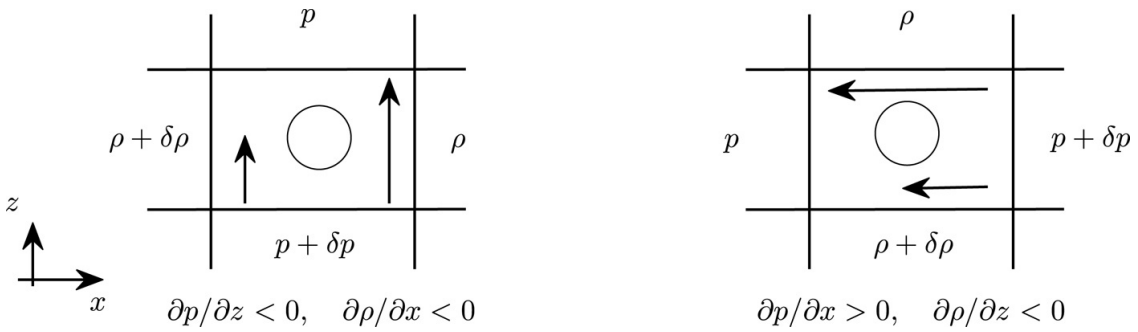

Figure 1.3: Schematic of baroclinic torque. From Heifetz & Mak (2015). A force balance upon a particle subject to perpendicular pressure and density gradients illustrates baroclinic torque on a fluid particle.

turbation to grow (Brouillette, 2002; Drake, 2006). This growth is driven by a sheet of baroclinic vorticity deposited along the interface as a result of misalignment between the pressure gradient across the shock and the density gradient across the perturbed interface. This physical mechanism, by which misaligned gradients create a torque on fluid particles generating vorticity, can be thought of in terms of a hydrostatic balance upon a particle. Pressure gradients result in acceleration of the flow that is inversely proportional to density. When these two gradients are misaligned, the result is a shearing effect or velocity differential on the fluid and vorticity is generated (Heifetz & Mak, 2015). A graphical explanations of baroclinic vorticity generation, adapted from (Heifetz & Mak, 2015) is shown in Figure 1.3. Analytically, baroclinic vorticity generation can be shown by taking the curl of the conservation of momentum equation for a fluid with variable density. It is worth noting that it is a second order, nonlinear effect and cannot be explained by traditional linear acoustics in a uniform medium.

The physics of the classical RMI are fairly well understood. The classical RMI setup consists of a planar shock impinging normally upon the peaks and troughs of a sinusoidal interface. The interface is accelerated non-uniformly such that counter-rotating vortices are generated across the interface. This drives peaks and troughs of the interface to accelerate in opposing directions, normal to the peak/trough surface. Much like in the case of the RTI, this too results in light fluid penetrating the heavy fluid and vice versa. For the case of a wave moving from a light fluid into a heavy one, the peaks and troughs of the interface accelerate away from one another, growing

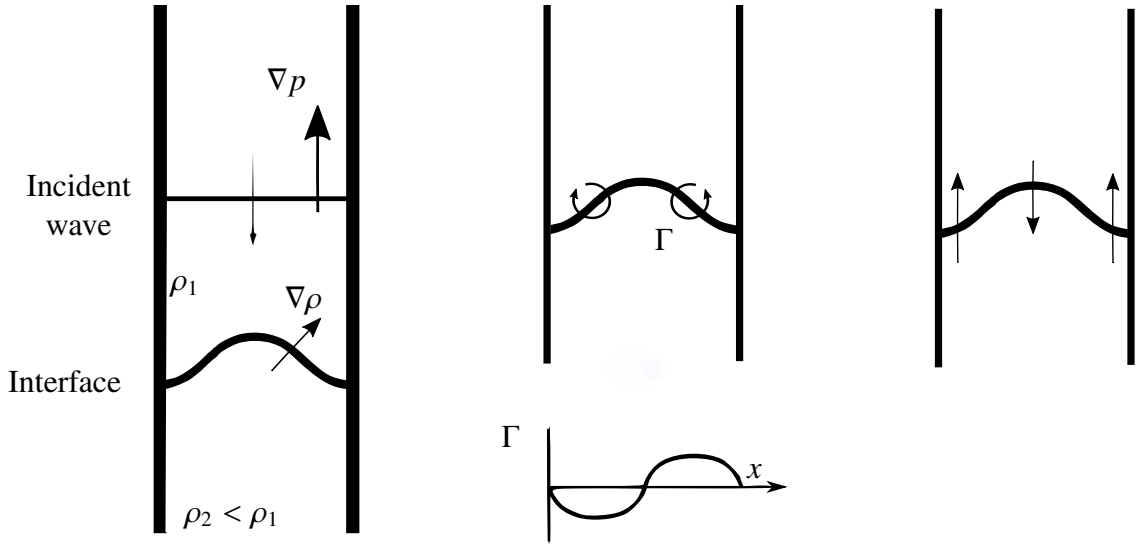

Figure 1.4: Schematic of the Richtmyer-Meshkov Instability for a heavy-light interface. Adapted from Brouillette (2002). The initial condition (left), circulation post wave-interface interaction (center), and perturbation growth (right) are shown.

the interface perturbation. For the case of a wave moving from a heavy fluid into a lighter fluid, the peaks and troughs interface initially accelerate toward one another. They then pass each other, inverting the phase of the interface perturbation, and continue moving in opposite directions, growing the perturbation amplitude. This process is illustrated in Figure 1.4, which has been adapted from Brouillette (2002). This work proposes that similar physics occur at ultrasonically driven air-tissue interfaces within the lungs. Much greater detail regarding the proposed mechanism is provided in Chapters 3 and 4.

1.3 Tissue as a compressible fluid system

To investigate CEUS and DUS-induced lung hemorrhage, throughout this dissertation we model the relevant physical problems of ultrasound in human tissue as compressible, multiphase fluid systems. In this section we attempt to justify this general approach and explain some of the applicable assumptions and implications.

The underlying governing equations upon which our models are based are the general conser-

vation equations for mass, momentum, and energy for a fluid,

$$\frac{\partial \rho}{\partial t} + \nabla \cdot (\rho \boldsymbol{u}) = 0, \tag{1.2a}$$

$$\rho \frac{D\boldsymbol{u}}{Dt} = \nabla \cdot \boldsymbol{\tau} + \rho \boldsymbol{g}, \tag{1.2b}$$

$$\frac{\partial E}{\partial t} + \nabla \cdot (E\boldsymbol{u}) = \rho (\boldsymbol{g} \cdot \boldsymbol{u}) + \nabla \cdot (\boldsymbol{u} \cdot \boldsymbol{\tau}) + \nabla \cdot \boldsymbol{q}, \tag{1.2c}$$

where ρ is density, $\boldsymbol{u}$ is the flow velocity vector, t is time, $\boldsymbol{\tau}$ is the stress tensor, $\boldsymbol{g}$ is the body force vector, $E = \rho\left(e + \frac{1}{2}[\boldsymbol{u} \cdot \boldsymbol{u}]\right)$ is the total energy defined as the sum of the kinetic energy per unit mass $\frac{1}{2}(\boldsymbol{u} \cdot \boldsymbol{u})$ and the internal energy per unit mass e, and lastly $\boldsymbol{q}$ is the heat flux vector. To model ultrasound-tissue interactions, the general conservation equations (1.2) are simplified and manipulated based on the physics appropriate to the specific problem at hand. The closure of these equations is also treated differently depending on the particular problem and model. Details on the appropriate equations of state used to relate pressure and energy, constitutive equations used to relate stress and strain, and boundary conditions are described in greater detail in sections 2.3.2 and 3.3.

To consider what physical effects are at play during diagnostic ultrasound, both contrast-enhanced and of the lung, we consider the basic physical scenario of each of these problems: an acoustic wave traveling through a multiphase medium consisting of soft tissue and gas. Soft tissues are viscoelastic materials, i.e., they exhibit solid and fluid like behaviors simultaneously under different types of forcing, i.e, viscosity, elasticity, and relaxation may all be simultaneously at play. These tissues include blood as well as lung, liver, and kidney tissue, which are relevant to the motivations of this thesis. The multiphase nature of these problems suggests that gas-liquid/gas-viscoelastic interface phenomena such as surface tension may also be of some relevance. As fluid motion is expected, inertial effects are likely to be of importance. Additionally, as ultrasonic heating is a known source of biological effects, we consider heat transfer and thermal mechanisms as well. And for completeness, since the vast majority of ultrasound procedures do not occur on the International Space Station, we consider the effects of gravity too. In the following, we introduce

dimensional analysis to assess the relative importance of each of these physical phenomena for the problems we approach in this part of the thesis.

1.3.1 Dimensional analysis and assumptions for Contrast-Enhanced Ultrasound

CEUS-related bioeffects are generally attributed to a process called IC in which a bubble or void within a fluid collapses rapidly. This can result in high temperatures, pressures, stresses, strains, and strain rates within the surrounding fluid. More details about this process and its relationship to US bioeffects are provided in Section 1.2.1.1. In this work, we consider the problem of a single US pulse interacting with a contrast agent microbubble, initially at rest within a viscoelastic soft tissue. For the sake of justification we consider a typical case here. In Chapter 2 a more in-depth analysis, specific to the work presented here, is performed. Consider an ultrasound pulse of clinically relevant frequency $f = 3$ MHz and PRPA= $p_a = 1$ MPa. The soft tissue is treated as a Voigt type viscoelastic material, as in Yang & Church (2005), and has a nominal density $\rho = 1000$ kg/m^3, an elastic modulus from $G = 5$ kPa to 1 MPa, and a dynamic viscosity $\mu = 0.015$ Pa s, and corresponding kinematic viscosity $\nu = \mu/\rho = 1.5 \times 10^{-5}$ m^2/s. Surface tension is based on that of blood, such that $S = 0.056$ N/m (Apfel & Holland, 1991). Note that the physical properties of soft tissue vary widely and are poorly characterized, particularly at the strain rates associated with cavitation. Based on the work of Patterson *et al.* (2012a) we define a characteristic velocity of $u = \sqrt{p_a/\rho} = 31.6$ m/s, which corresponds to a change in radius over a period of free oscillation. As a characteristic length scale, we use a typical bubble size such that equilibrium radius is $R_0 = 1\mu$m.

Based on this setup we perform dimensional analysis to assess the relative importance of each of the potentially relevant physical mechanisms to the problem of acoustically-driven cavitation in soft tissue:

Viscosity: To assess the relevance of viscosity we consider the Reynolds Number, which is the ratio

of inertial to viscous forces within a flow and is defined as $Re = \rho u R_0/\mu = 2.1$. A Reynolds number of order unity, suggests that inertia is on the order of viscous forces, and hence cannot be neglected.

Heat transfer and thermal effects: The Prandtl number is the ratio of momentum diffusivity to thermal diffusivity and is defined as $Pr = \nu/\alpha = 105.6$. The calculated Pr is large relative to Re and suggests that the effects of thermal diffusivity are dominated by momentum diffusivity. We infer that that minimal heat transfer occurs over the course of the collapse and as such it is neglected in our model.

Surface Tension: The Weber number is the ratio of inertial to surface tension forces in the flow and is defined as $We = \rho u^2 R_0/S = 17.9$. The calculated We is large relative to Re, but not so much as to suggest that the effects of surface tension at the bubble wall are negligible, even when the bubble is at its equilibrium radius. Additionally, we note that the effects of surface tension may have an even greater effect during collapse when the bubble radius may decrease by an order of magnitude or more. Hence surface tension is not neglected.

Elasticity: The Cauchy number is a measure of the ratio of elastic to inertial forces and is defined as $Ca = \rho u^2/G = 1 - 200$ for the range of elastic moduli considered (i.e., 5 kPa - 1 MPa). Based on this the effects of elasticity are not expected to be particularly important to the bubble dynamics for the tissues of kPa order elasticity, though this is expected to change for stiffer tissues. Additionally, we note that our work considers a Voigt type viscoelastic model, which is important as the microsecond timescales associated with cavitation can effect the relative importance of viscous and elastic forces. Accordingly, elasticity is included in the cavitation bubble model.

Gravity: The Froude number is the ratio of inertial to gravitational forces, or more generally, any applicable body forces within a flow, and is defined as $Fr = u/\sqrt{gR_0} = 10^4$, where is the gravitational constant $g = 9.81$ m/s^2. The calculated Froude number is much larger than Re and suggests

that gravitational and buoyancy effects are minimal relative to inertia and is neglected for the sake of this analysis. This is of particular importance because, for a homogeneous medium, it allows us to consider the case of a spherically symmetric collapse, which greatly simplifies the problem.

In summary, based on the dimensional analysis performed, we consider spherically symmetric bubble dynamics in a Voigt-Viscoelastic medium with surface tension. The effects of gravity and heat transfer are neglected.

1.3.2 Dimensional analysis and assumptions for an acoustically driven alveolus

In this section, we focus on the problem of an ultrasound pulse or physically similar acoustic wave impinging upon an alveolus within an adult human lung. To assess the relevant physical mechanisms here in order to layout the logic for our assumptions and approach, we present a general case relevant to the motivating problem of lung ultrasound. A more comprehensive justification and analysis, specific to the work presented can be found in chapters 3 and 4. Consider an ultrasound pulse with central frequency $f = 3$ MHz, and amplitude $p_a = 1$ MPa, which are within the expected parameter range based on past research (Miller *et al.*, 2015). We use the mean diameter of a typical adult human alveolus as a characteristic length scale length scale $\ell_A = 200\mu$m (Ochs *et al.*, 2004). The alveolus is treated as air at 37° such that the sound speed is $c_A = 353$ m/s, the density is $\rho_A = 1.14$ kg/m^3, the kinematic viscosity is $\nu_A = 16.6 \times 10^{-6}$ m^2/s, and no elasticity is present in the alveolar interior. The surrounding soft-tissue is treated as water-like, but with elasticity such that the sound speed is $c_T = 1500$ m/s, the density is $\rho_T = 1000$ kg/m^3, the kinematic viscosity is $\nu_T = 0.7 \times 10^{-6}$ m^2/s and the elastic modulus of the alveolar wall is $G = 5$ kPa (Cavalcante, 2005). We use a characteristic velocity $u_T = \sqrt{p_a/\rho_T} = 31.6$ m/s, a convenient scale based on the wave and tissue properties. Based on the physical problem described here we use dimensional analysis to access the relative importance of potentially relevant physical mechanisms:

Viscosity: In consideration of effects of viscosity, we calculate the Reynold's Number $Re = u_T \ell / \nu_T = 9035$, which suggests that the inertial forces dominate the viscous forces. Additionally, in consideration of late time effects, we calculate the approximate viscous boundary layer thickness at t_{final}, the time at the end of the simulated period such that $l_{viscous} = \sqrt{\nu_{water} t_{final}} \approx 20\ \mu$m. Furthermore, typical acoustic viscous boundary layer thicknesses for MHz frequency ultrasound are $\lesssim 1\ \mu$m. As $l_{viscous}/\ell \ll 1$, the viscous boundary layer is expected to remain far less than either a typical alveolar diameter or the length scales associated with relevant geometrical structures of the perturbed interface at the end of our baseline simulations (described in Chapters 3 and 4). Hence we exclude the effects of viscosity in our calculations.

Heat transfer and thermal effects: We use similar arguments to those used for viscous effects in consideration of thermal effects. The thermal length scale is defined as $l_{thermal} = \sqrt{\kappa / \pi f \rho C_p}$, where the C_p is the specific heat and κ is the thermal conductivity. In air $C_{pA} = 1005$ J/Kg K and $\kappa_A = 0.027$ W/m K and in tissue (based on water) $C_{pT} = 1005$ J/Kg K and $\kappa_T = 0.49$ W/m K. Hence $l_{thermal,A} = 0.3\mu$m and $l_{thermal,T} = 1.5\ \mu$m. For both fluids, on either side of the interface, $l_{thermal}/\ell \ll 1$ such that the thermal boundary layer is small relative to the characteristic length of the flow. Hence we neglect heat transfer in our approach to this problem moving forward.

Surface Tension: The role of surface tension in the alveoli is critical to healthy respiratory function. Alveoli secrete pulmonary surfactant, which lowers the surface tension at the alveolar surface, helping prevent airway collapse and easing the re-inflation of alveoli during breathing. As a result of this surfactant, alveolar surface tension is far below that of water and has been reported as $S_A = 9$ mN/m (Schürch *et al.*, 1976). Hence we define our Weber Number as $We = \rho_T u_T^2 \ell / S_A = 22222$. This suggests that forces due to surface tension are small relative to the acoustic pressure at the interface. Based on this, we neglect surface tension in our analysis as well.

Elasticity: To assess the expected importance of elasticity to the system we define a Cauchy num-

ber $Ca = \rho_T u_a^2/G$ which becomes the ratio of the acoustic pressure to the elasticity $Ca = p_a/G = 200$. This suggests that elastic effects are dominated by the acoustic pressure during the wave-interface interaction within the tissue. Within the alveolar air space, there is no elasticity and the Cauchy number is infinite. Based on this, we neglect elasticity in our model. Additional calculations considering the relevance of this assumption at later times, after the passage of the wave are provided in Appendix A.7.

Gravity: The importance of gravity is assessed based on a Froude number calculation $Fr = u_T/\sqrt{g\ell} = 714$. This suggests that gravitational forces are small relative to inertia, and can be neglected. Another reasonable justification for neglecting gravity is that the orientation of the model problem in space is arbitrary and as a 2D model we treat the flow as existing in a plane that is orthogonal to gravitational forces and thus not affected by gravity.

In summary, based on the dimensional analysis performed, we consider an acoustically-driven, perturbed, water-air interface. The effects of viscosity, elasticity, surface tension, gravity, and heat transfer are neglected.

1.3.3 Limitations

Before proceeding we would like to acknowledge that the simplifications and assumptions made in the previous sections, while justified in the specified regimes, do deviate from the true physical systems in many situations. The purpose of these simplifications is to make the relevant problems tractable with the available resources (computational, intellectual, financial, temporal, etc...). In both CEUS and in ultrasound-alveoli interactions, the presented dimensional analysis is based on tissue properties such as viscosity and elasticity and behavior that are poorly characterized in both nature and quantity. Additionally, the analysis performed here is for reference cases within the relevant range, and certain dependencies, such as the frequency dependence of sound speed in bulk lung tissue, are not captured here. Furthermore, actual tissues are often characterized by a wide

range of physical length scales ranging from submicron to meter and are heterogeneous at both micro and macroscopic scales. Despite these limitations, the models developed remain valid in the specified regimes by presented dimensional analysis. As such, for cavitation in locally homogeneous Voigt viscoelastic soft tissues with kPa order elasticity and otherwise water-like physical properties (e.g., viscosity, surface tension, density, sound speed) we expect the computed dynamics to be representative of what one would expect in the real world. Similarly for gas-liquid and gas-tissue interfaces with kPa order elasticity and otherwise water-like physical properties, driven by ultrasound waves with diagnostically relevant parameters of the order of those stated, we expect that over the timescales of interest ($\sim 100\mu$s) the dynamics are appropriately represented. The purpose of this work is to gain insight into the approximate physics applicable to these problems only within the valid regimes for which the models were designed.

1.4 Thesis overview

This part of the thesis presents work studying the physics of two problems relevant to ultrasound bioeffects: 1) Cavitation of ultrasound contrast agents microbubbles in human tissue, and 2) DUS-induced hemorrhage of the lung. For each problem, the objectives of this thesis are to

1. Develop a computational model to simulate the problem.

2. Perform simulations to gain new insights into the relevant physics of CEUS and diagnostic lung ultrasound.

3. Use the results of the simulations to develop and test new hypothesis and when possible make conclusions about the physics and its relevance to the US bioeffects.

Upon pursuit of the above objectives, the novel contributions made throughout this thesis are summarized as follows:

- A novel approach to investigating CEUS related bioeffects is taken, combining simulations of bubble dynamics in a soft tissue-like viscoelastic medium, with experimentally measured

ultrasound waveforms and known bioeffects thresholds.

- Calculated cavitation dynamics are related to known bioeffects thresholds associated with the experimentally measured US inputs.
- Further evidence is offered to suggest that existing IC thresholds may not be well suited for viscoelastic media.
- A novel model of an ultrasound-driven alveolus is developed.
- It is demonstrated that acoustic waves interacting with perturbed liquid-gas interfaces may generate sufficient baroclinic vorticity to drive appreciable interface deformation. These deformations are a result of nonlinear processes and cannot be described by purely linear acoustics.
- Vorticity-driven perturbation growth of gas-liquid interfaces perturbations is shown to exhibit power-law behavior and scale with interfacial circulation density.
- It is shown that because the morphology of the interface is changing during the wave-interface interaction, vorticity deposition depends on the transient form of the wave, and consequently so does the long-term growth (or lack thereof) of the interface perturbation.
- Approximate stresses and strains associated ultrasound-driven gas-liquid interfaces are calculated. These quantities are compared with established alveolar failure criteria to conclude that, while ultrasound-induced viscous stress in the lung is unlikely to cause hemorrhage, there is a potential for vorticity-driven alveolar wall strain that may be related to hemorrhage.

A more detailed chapter-by-chapter summary of the work and conclusions of this thesis is provided below.

In Chapter 2, we simulate the cavitation bubble dynamics of contrast agent microbubbles in soft tissue (Patterson *et al.*, 2012a). Experimentally measured US waves with known bioeffects occurrence and thresholds are used (Miller *et al.*, 2008b). A parametric study is performed, relating

ultrasound and tissue parameters to calculated cavitation bubble dynamics. The soft tissue is modeled as a Voigt viscoelastic medium based on the work of Yang & Church (2005). The calculated cavitation dynamics and theoretical inertial cavitation thresholds (Flynn, 1982; Apfel, 1982) are compared with bioeffects thresholds associated with each US pulse, as defined by the observation of kidney hemorrhage in rats exposed to CEUS by Miller *et al.* (2008b). While the results were generally dependent on US, gas, and tissue properties, it was found that the theoretical inertial cavitation thresholds were lower than observed bioeffects thresholds. It is shown that these thresholds correlate strongly to calculated metrics of cavitation, such as dimensionless maximum radius $R_{max}/R_{equilibrium}$ and that this correlation is lost when simply looking at the dimensional maximum bubble size R_{max}, which is not a cavitation metric.

In Chapter 3, we develop a model of an ultrasonically-driven alveolus as a compressible, multiphase fluid system. This model is used to study the fundamental problem of an acoustically-driven perturbed liquid-air interface. We demonstrate that under the assumptions presented in Section 1.3.2, trapezoidal acoustic waves of sufficient pressure amplitude are capable of generating enough baroclinic vorticity to appreciably deform the interface. The dependence of this deformation on the amplitude and temporal characteristics of the wave is studied. It is demonstrated that the deformation rate scales with the amount of circulation per unit length of the interface. It is also shown that the amount of circulation deposited by the wave is heavily dependent on the deformation that occurs during the wave-interface interaction, and therefore depends on the transient properties of the wave.

In Chapter 4, the work of the previous chapter is extended to increase its relevance to clinical DUS. The previously developed model of an ultrasound-driven alveolus is modified and used to simulate a perturbed liquid-gas driven by an ultrasound pulse with diagnostically relevant parameters. We calculate approximate stresses and strains at the interface and compare to accepted alveolar failure criteria. It is shown that viscous stresses are small compared to expected failure thresholds. However, it is also shown that strains at gas-liquid interfaces such as those of the lungs, driven by acoustically-generated vorticity, may be sufficient to drive hemorrhage for sufficiently

strong ultrasound pulses. This work concludes that while vorticity may be a possible mechanism for driving DUS-introduced lung hemorrhage, additional work needs to be completed to account for multiple pulses as well as physical effects of elasticity and viscosity in order fully understand the role of vorticity in this problem.

In the final chapter 5 of Part I of this dissertation, we summarize the main conclusions takeaways and accomplishments of this work. I also make recommendations for future work to overcome the limitations of the presented research and extend this work to address relevant problems within the field.

CHAPTER 2

Theoretical microbubble dynamics at capillary breaching thresholds

In this chapter, we present work in which experimentally-measured US pulses are used to simulate US contrast agent microbubble dynamics. The pulses were previously used in experiments to determine capillary breaching thresholds in rat kidneys (Miller *et al.*, 2008b). We compare the calculated bubble dynamics to the experimentally-determined bioeffects thresholds to investigate the use of theoretical IC thresholds as a predictor for bioeffects. This work was published in the Journal of the Acoustical Society of America (Patterson *et al.*, 2012a,b).

2.1 Abstract

To predict bioeffects in contrast-enhanced diagnostic and therapeutic ultrasound procedures, the dynamics of cavitation microbubbles in viscoelastic media must be determined. For this theoretical study, measured 1.5-7.5 MHz pulse pressure waveforms, which were used in experimental determinations of capillary breaching thresholds for contrast-enhanced diagnostic ultrasound in rat kidney, were used to calculate cavitation nucleated from contrast agent microbubbles. A numerical model for cavitation in tissue was developed based on the Keller-Miksis equation (a compressible extension of the Rayleigh-Plesset equation for spherical bubble dynamics), with a Kelvin-Voigt constitutive relation. From this model, the bubble dynamics corresponding to the experimentally obtained capillary breaching thresholds were determined. Values of the maximum radius and tem-

perature corresponding to previously determined bioeffect thresholds were computed for a range of ultrasound pulses and bubble sizes for comparison to inertial cavitation threshold criteria. The results were dependent on frequency, the gas contents, and the tissue elastic properties. The bioeffects thresholds were above previously determined inertial cavitation thresholds, even for the tissue models, suggesting the possibility of a more complex dosimetry for capillary injury in tissue.

2.2 Background & Introduction

Cavitation-bubble collapse has been a topic of interest in physical acoustics for nearly a century and has been the object of many experimental and theoretical studies, which have outlined the complexity of the phenomenon (Leighton, 1997). This field made a landmark contribution to non-ionizing radiation biology in medicine in the 1980s when the possibility of inertial cavitation, with potential induction of bioeffects, from diagnostic ultrasound pulses was predicted theoretically (Flynn, 1982; Apfel, 1982). This possibility was included in considerations for the regulation of the ultrasound output of diagnostic machines. Apfel & Holland (1991) performed detailed calculations of the response of different nuclei sizes in the form of free air microbubbles and found that the optimum size decreased with increasing frequency, f. In addition, the rarefactional pressure amplitude threshold, p, for inertial cavitation was determined for the optimum nuclei, using the criterion of a >5,000 K gas temperature at collapse. For nuclei in blood, the ratio of $p^{1.67}/f$ was found to have a constant value of 0.13 at the threshold, using units of MPa and MHz. This finding was used to create a Mechanical Index (MI) for regulatory purposes and for display on the screens of diagnostic ultrasound machines. The MI was set equal to the peak rarefactional pressure amplitude (PRPA) adjusted for attenuation and divided by the square root of frequency. The regulatory guideline limit for diagnostic ultrasound was considered according to the Medical Device Amendment Act of 1976 and the maximum value existing at that time. This guideline limit was eventually set from measurements on a single diagnostic ultrasound probe to be 1.9 (Nyborg, 2001). It is noteworthy that the critical value corresponding to the Apfel & Holland (1991) result

would be $p/f^{0.6} = 0.29$, which is much less than the MI limit. This discrepancy does not appear to be of concern for normal diagnostic ultrasound from both experimental (Carstensen *et al.*, 2000) and theoretical (Church, 2002) considerations.

To improve diagnostic information in ultrasound examinations, ultrasound contrast agents (UCAs) were invented. The contrast agents consist of a suspension of stabilized gas-filled microbubbles, which provide strong echoes from blood and improve contrast in sonography (Averkiou *et al.*, 2003; Raisinghani *et al.*, 2004). Soon after contrast-enhanced diagnostic ultrasound was developed, microscale bioeffects were reported (Miller *et al.*, 2008a). The typical bioeffect seen in mesentery, muscle, heart, and kidney was capillary rupture, which appeared to be caused by cavitation nucleation in blood from the circulating contrast microbubbles. Recently, hemorrhage of glomerular capillaries was studied in rat kidney to determine PRPA thresholds and the frequency dependence of the thresholds (Miller *et al.*, 2008b). Presumably, the thresholds correspond to the action of the optimum cavitation nuclei, and this approach therefore provides a means to directly compare cavitation theory with the bioeffects experiments. Over the 1.5-7.5 MHz frequency range tested, the thresholds were proportional to the frequency, such that p/f was approximately constant at 0.49 MPa/MHz for actual diagnostic ultrasound and 0.62 MPa/MHz for diagnostic ultrasound simulated by a laboratory pulsed-ultrasound system. These thresholds fell below the MI=1.9 level, especially for the lower frequencies, but above the inertial cavitation thresholds of Apfel & Holland (1991), and the frequency dependence was different. Evidently, the bioeffects thresholds depend on cavitation dynamics not specifically tied to the inertial cavitation threshold of free air bubbles in blood determined by Apfel & Holland (1991). The fundamental reason for these results remains uncertain, which revives the non-ionizing radiation biology problem of ultrasonic cavitation in medical ultrasound.

The theoretical model of Apfel & Holland (1991) applies to air microbubbles in a Newtonian liquid. However, contrast agents in the blood stream do not necessarily exhibit such properties. It is well-known that human tissue behaves in a viscoelastic fashion (Frizzell, 1976; Madsen *et al.*, 1983). The bubble dynamics greatly depend on not only the viscoelastic properties (Allen & Roy,

2000a; Yang & Church, 2005) for a given model, but also on the type of model (Johnsen & Hua, 2012) and on nonlinearity (Allen & Roy, 2000b). Furthermore, the gas contained in contrast agents is not air; for example, perfluoropropane (PFP, C_3F_8) in Definity (Perflutren Lipid Microsphere, Lantheus Medical Imaging, N Billerica MA), which may affect the collapse temperature. The stabilizing skin or shell may not be an important factor for the capillary rupture bioeffect because the nucleation process appears to liberate a free gas microbubble. The thresholds for this cavitational bioeffect are above the destabilization threshold of the optimal microbubbles, which therefore may be modeled as free microbubbles (Sboros *et al.*, 2002; Marmottant *et al.*, 2005). Basically, at low PRPAs the stabilization is lost, which releases a free microbubble, thus nucleating cavitation, followed by dissolution at the conclusion of the pulse (Porter *et al.*, 2006). In the case of diagnostic ultrasound, the microbubble is subjected to a series of pulses that start low, build to a peak and finally decline. Thus, when the peak pulse arrives to cause the injury, the microbubbles likely are already destabilized.

The detailed mechanism by which cavitation causes bioeffects is unknown, although several have been proposed, such as shock emission upon collapse, growth beyond a given size, high temperatures generating free radicals, re-entrant jets in non-spherical collapse (Zeqiri, 2003). In order for such phenomena to occur, it is expected that inertial cavitation occurs. From this observation, prior studies have used the threshold for inertial cavitation as a surrogate for bioeffects (Yang & Church, 2005). This inertial cavitation threshold was developed theoretically for bubble dynamics in water (Flynn, 1975a). In this work, we show that the bioeffects threshold is different from previously developed inertial cavitation thresholds. The difference between the inertial cavitation threshold calculated for air microbubbles in blood and the capillary rupture thresholds is likely due to an incomplete model. That is, the homogenous model results may correlate better with the bioeffects results if tissue elasticity, gas contents, pulse parameters, and possibly other factors are considered.

In the current work, a different approach combining experiments and numerical modeling to studying bioeffects is followed. *In vivo* experiments were performed to determine the pulse ampli-

tude and frequency under which bioeffects occur (Miller *et al.*, 2008b). Given these experimental pulses, bubble dynamics are modeled numerically over the entire waveform duration, which is not taken into account by Apfel & Holland (1991), to determine how the bubble response correlates with the observation of bioeffects. A detailed description of the methodology is presented. The experimental setup and numerical model are first discussed in Section 2.3. The results from the combined experimental and numerical procedure are presented in Section 2.4. The ability of established inertial cavitation thresholds, and general cavitation parameters, to predict bioeffects is discussed. The article ends with a summary of the results and considerations for future work on this topic.

2.3 Materials and Methods

2.3.1 Experimental Setup

In the previous study of glomerular capillary hemorrhage in rats by Miller *et al.* (2008b), bioeffect thresholds were determined for ultrasound exposure with diagnostic ultrasound machines and with a laboratory system set up to simulate diagnostic scanning. The ultrasonic waveforms (pressure vs. time) used for the driving pressure in this study were based on the laboratory system bioeffect thresholds at 1.50, 2.25, 3.50, 5.00 and 7.50 MHz (with corresponding bioeffects thresholds of 0.98, 1.31, 2.38, 2.82 and 6.00), which allowed more flexibility in producing the desired pulse waveforms than the diagnostic ultrasound machine.

The experiment was designed to simulate worst-case-scenario clinical conditions for CEUS. Anesthetized rats were held in place in a 75 L bath of 37° C degassed water, and exposed to ultrasound while receiving a constant 10 μl/kg/min infusion of UCA. The ultrasound probe was placed such that its focal zone was at the cortex of the right kidney. The ultrasound system consisted of a transducer, power amplifier (A-500, Electronic Navigation Industries, Rochester NY), function generator (model 3314A function generator, Hewlett Packard Co., Palo Alto CA). Five damped single element transducers (Panametrics, Olympus NDT Inc. Waltham, MA) with 1.9 cm diam-

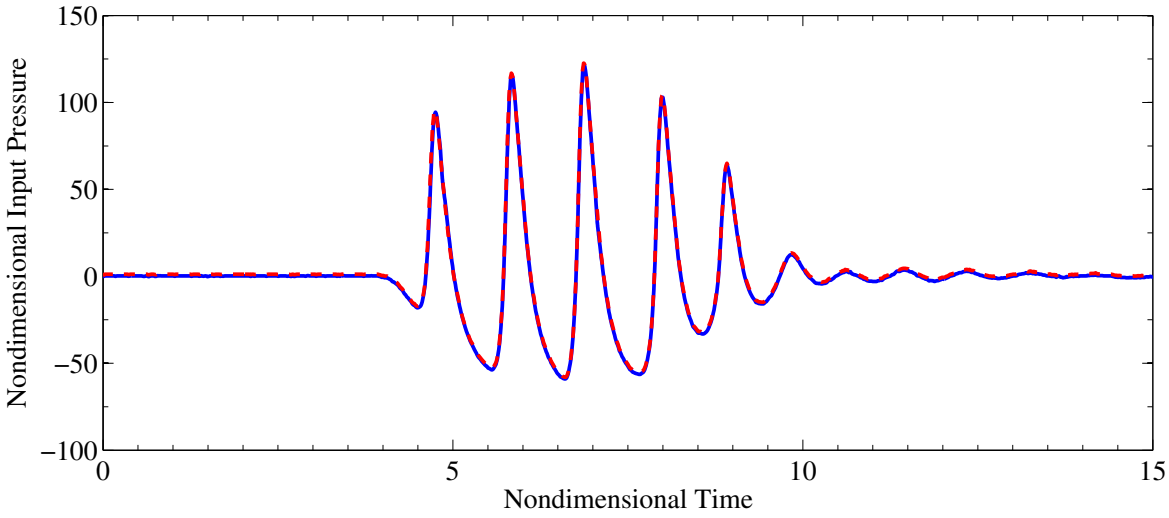

Figure 2.1: 7.5 MHz experimental and numerical ultrasound waveforms at bioeffects threshold pressure. Experimental and numerical (filtered) pressure waveforms for the 7.5 MHz pulse at the threshold (Peak negative pressure: 6.0 MPa, 543 ns duration, MI_{eq}=PRPA/$f^{1/2}$=2.2). Solid: experimental; dashed: numerical.

eter and 3.8 cm focus were used at their resonant ultrasonic frequencies in a warmed water tank. The function generator was set using the n-cycle mode with $n = 3$ to produce a simple pulse train with pulse durations and PRPAs the same as used for the *in vivo* exposures. The waveforms were measured with a calibrated PVDF bilaminar film hydrophone with 0.4 mm spot size (model 805, Sonora Medical Systems, Longmont CO) and were adjusted to equal the threshold at each frequency and to several 3 dB increments above and below the threshold. The purpose of the progressive steps was to help identify any specific cavity behavior, which recurred at each frequency as the threshold was crossed. The hydrophone measured the alternating pressure including the PRPA, to which the constant atmospheric pressure must be added to obtain the total pressure. The highest PRPA available for the higher frequencies was limited by the transducers. The experimental waveforms are imported into Matlab, and smoothened using a moving-average low-pass filter. This procedure results in waveforms, such as that shown in Figure 2.1 for the threshold at 7.5 MHz, in which the high-frequency experimental noise is removed. The smoothened waveforms are then input into the bubble dynamics code as the driving pressure.

Parameter	Dimensional value		Dimensionless number
Viscosity	$\mu = 0.015$ (Pa s)	$\mapsto$	$Re = \rho u R_o/\mu = 2/3$
Elasticity	$G = 10^5$ (Pa)	$\mapsto$	$Ca = \rho u^2/G = 1.0$
Surface tension	$S = 0.056$ (N/m)	$\mapsto$	$We = \rho u^2 R_o/S = 2$
Sound speed	$c = 1570$ (m/s)	$\mapsto$	$C = c/u = 157$

Table 2.1: Base physical parameters representative of soft tissue used in the present study.

2.3.2 Bubble Dynamics Model

The bubble dynamics are modeled under the assumption that a single spherical gas bubble is subjected to a far-field pressure change (ultrasound pulse) in an infinite medium of uniform properties. Given that bioeffects are observed in some of the experiments and that it is likely that inertial cavitation occurs, it is expected that compressibility of the surrounding medium matters. Furthermore, tissue is expected to behave in a viscoelastic fashion. To account for all of these elements, the Keller-Miksis equation (Keller, 1980), a compressible extension of the Rayleigh-Plesset equation, is considered, and the constitutive relation between the stresses and strains follows a Kelvin-Voigt viscoelastic model, as in Yang & Church (2005). Thus the nondimensional equations governing the bubble dynamics are:

$$\left(1-\frac{\dot{R}}{C}\right)R\ddot{R}+\frac{3}{2}\left(1-\frac{\dot{R}}{3C}\right)\dot{R}^2=\left(1+\frac{\dot{R}}{C}\right)\left[p_B-1-p_a-\frac{R}{C}\frac{dp_a}{dt}\right]+\frac{R}{C}\dot{p}_B, \tag{2.1}$$

where $R(t)$ is the bubble radius, C is the dimensionless sound speed, p_a is the time-varying component of the far-field pressure and the dot represents material (time) derivatives. The bubble pressure p_B is given by

$$p_B=\left(1+\frac{2}{We}\right)\frac{1}{R^{3\gamma}}-\frac{2}{WeR}+\tau_R, \tag{2.2}$$

where We is the Weber number (dimensionless surface tension), γ is the specific heats ratio for the gas, and τ_R is the shear stress in the rr-direction evaluated at $r = R$.

As in Yang & Church (2005), the Kelvin-Voigt model is used as the constitutive relation be-

tween the stresses and strains:

$$\tau_R = -\frac{4}{3Ca}\left(1 - \frac{1}{R^3}\right) - \frac{4}{Re}\frac{\dot{R}}{R}, \tag{2.3}$$

where Re is the Reynolds number (dimensionless viscosity), and Ca is the Cauchy number (dimensionless elasticity). The dimensionless numbers are defined in Table 2.1. The resulting system of equations is solved for the bubble radius using a fifth-order accurate Cash-Karp Runge-Kutta method with adaptive time-step control. In the problem under consideration, the pressure pulse is smooth and its wavelength is on the order of 1 mm. Since the bubbles are initially in the micron range and do not grow beyond a few initial radii, the present Rayleigh-Plesset-type approach is justified.

The base values for tissue properties, listed in Table 2.1, are taken from the literature (Apfel & Holland, 1991; Yang & Church, 2005). In the present work variables are nondimensionalized using a tissue density of $\rho = 1000$ kg/m^3, a characteristic speed given by $u = \sqrt{p_{atm}/\rho}$ where p_{atm} is atmospheric pressure, and a characteristic equilibrium radius of $R_0 = 1$ μm. The resulting time scale is thus close to the Rayleigh collapse time. A range of equilibrium radii within 0.1-2.0 μm, a typical size distribution for UCAs, is considered. Thus, changing the equilibrium radius modifies the nondimensional parameters. The specific heat is taken as $\gamma = 1.13$ for perfluoropropane. Reported values of tissue elasticity fall in the 1-100 kPa range (Arda *et al.*, 2011). However, it is known that the elasticity may increase up to the MPa range at high strains (Krouskop *et al.*, 1998). Here, a nominal elasticity of $G = 100$ kPa is considered as the base case.

Since the thresholds for cavitational bioeffects are above the destabilization threshold, the microbubbles are modeled as free bubbles (Sboros *et al.*, 2002; Marmottant *et al.*, 2005), *i.e.,* UCA stabilizing films and shells are neglected. Additionally, the detailed effect of the physical constraint imposed by blood vessel walls is considered by including it in the bulk elasticity of the tissue. Though non-spherical perturbations may occur due to the local heterogeneity of tissue and thus lead to a significant change in the bubble dynamics, non-spherical collapse is expected to

produce lower temperatures and pressures (Johnsen & Colonius, 2009). In this sense, the spherically symmetric model represents a worst-case scenario useful in determining safe, conservative parameters for CEUS procedures.

2.4 Results and Discussion

2.4.1 Bubble Response

Typical bubble responses are first shown to provide a qualitative understanding of the physics. Figures 2.2, 2.3 and 2.4 show the history of the dimensionless bubble radius produced by a given pressure waveform for a range of essentially linear to nonlinear cases, and different elasticities (5 kPa, 100 kPa and 1 MPa). In the linear case, the bubble oscillations are in phase with the pressure waveform. Increasing the elasticity leads to larger oscillation amplitudes, though the changes are small. At intermediate frequency and amplitude, the oscillations become larger and more nonlinear for larger elasticities. This observation, although seemingly counterintuitive, is consistent with the results of Johnsen & Hua (2012), who showed analytically that the damping of the oscillations is smaller in this range of elasticities. In the fully nonlinear case (large pulse amplitude and frequency), the oscillation amplitude becomes yet larger, thus yielding a larger maximum radius and very small minimum radius. For all elasticities, the initial behavior is similar up to the second maximum radius. Thereafter, the stiffer case (G=1 MPa) departs and collapses violently, while the other cases rebound. The maximum radius is achieved at approximately the same time in all cases, after the peak positive pressure. In all the simulations, the oscillations damp out rapidly after the passage of the pulse.

In the results of the following sections, the maximum dimensionless radius, R_{max}, and dimensional bubble temperature at collapse, T_{max}, obtained using the ideal gas law, are determined by recording their largest value over the simulation. These quantities are compared to the inertial cavitation thresholds used by Apfel & Holland (1991) and Yang & Church (2005): $R_{max} = 2$ and $T_{max} = 5000$ K. The dependence of the bubble dynamics on the pulse amplitude, initial bubble size

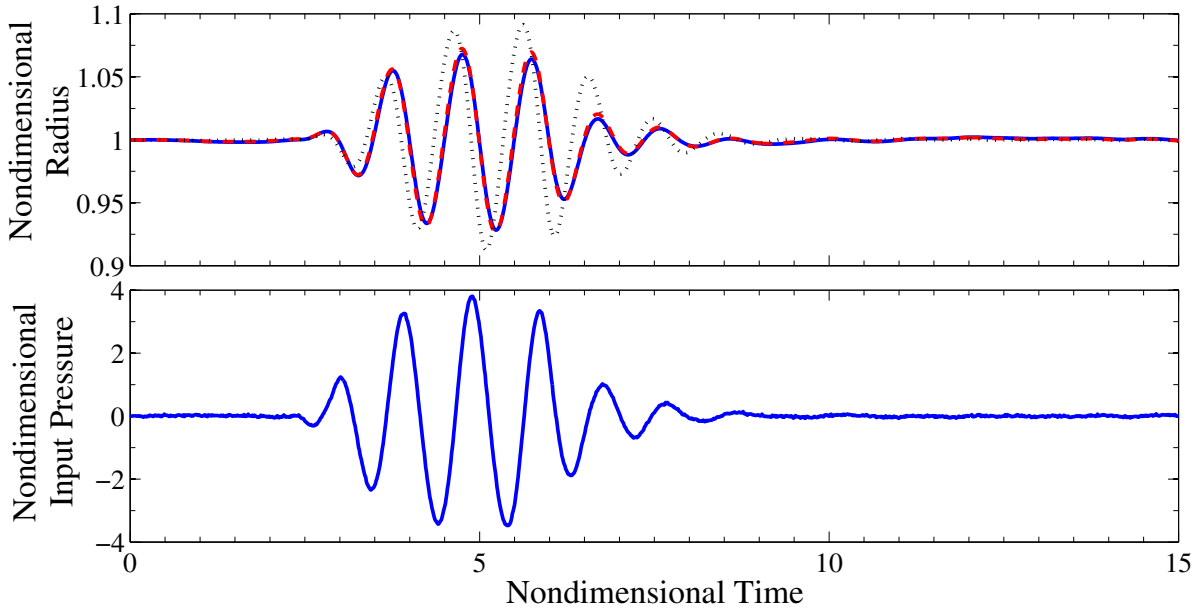

Figure 2.2: Bubble radius (top) and input-pressure waveform (bottom) histories for an essentially linear case (frequency: 1.5 MHz; peak negative pressure: 0.35 MPa). No bioeffects are observed here. $R_0 = 1$ μm; solid: $G = 5$ kPa; dashed: $G = 100$ kPa; dotted: $G = 1$ MPa.

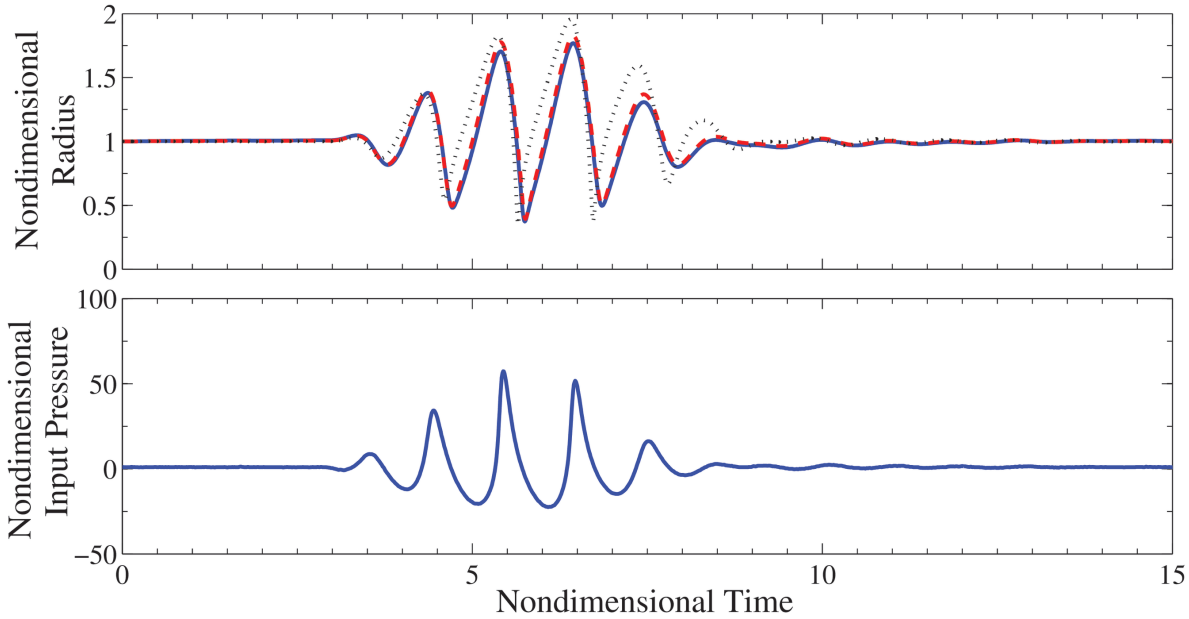

Figure 2.3: Bubble radius (top) and input-pressure waveform (bottom) histories for a moderately nonlinear case (frequency: 3.5 MHz; peak negative pressure: 2.4 MPa). Bioeffects are observed here. $R_0 = 1$ μm; solid: $G = 5$ kPa; dashed: $G = 100$ kPa; dotted: $G = 1$ MPa.

(*i.e.*, UCA size distribution), pulse frequency, and tissue properties are considered individually.

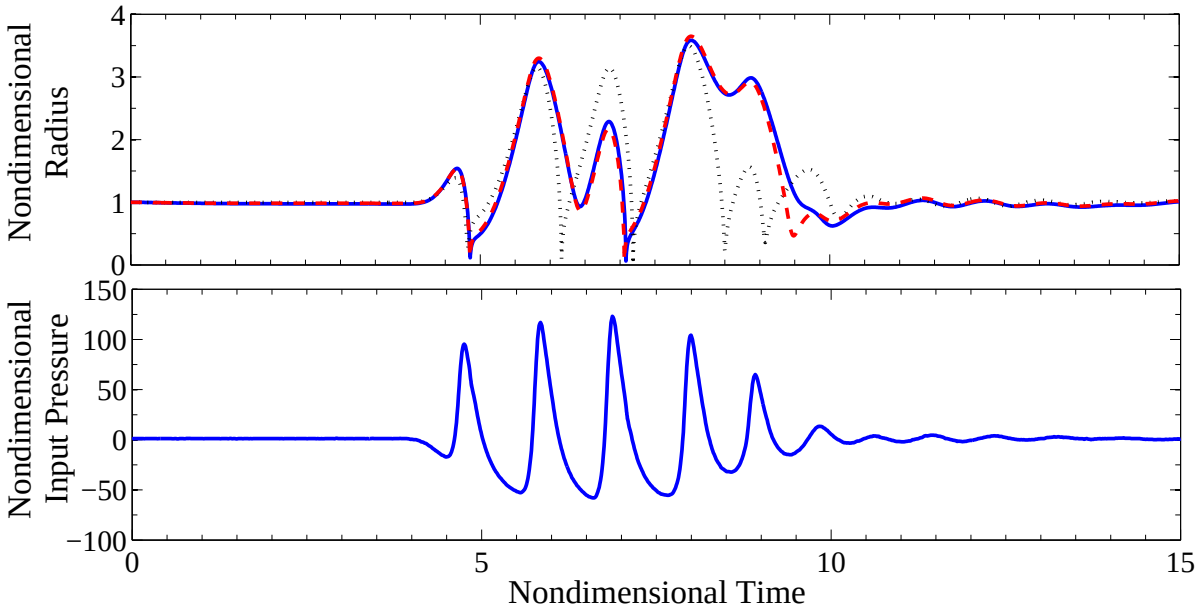

Figure 2.4: Bubble radius (top) and input-pressure waveform (bottom) histories for a highly nonlinear case (frequency: 7.5 MHz; peak negative pressure: 6.0 MPa). Bioeffects are observed here. R_0 = 1 μm; solid: G = 5 kPa; dashed: G = 100 kPa; dotted: G = 1 MPa.

2.4.2 Dependence on the Pulse Amplitude

Given the strong dependence of the MI on the rarefactional pressure amplitude, the influence of the pulse amplitude on the bubble dynamics is first evaluated. Figure 2.5 shows the dimensionless maximum radius as a function of rarefactional pressure amplitude. Initial bubble radii ranging between 0.1–2.0 μm are shown, as well as different frequencies. The open symbols denote cases where bioeffects did not occur, while the filled symbols denote the occurrence of bioeffects.

The results show that the bubble dynamics, through the maximum radius, scale with the pulse amplitude. Although the results do not collapse fully onto a line, a general trend is discernible. At low amplitude, the increase in the maximum radius is approximately linear; beyond some amplitude, the bubble undergoes nonlinear oscillations, thus explaining the different dependence and larger spread. These results are consistent with the plots shown in Figures 2.2-2.4. Over a broad range of amplitudes, the occurrence of bioeffects has little correlation with pulse amplitude alone: at a given amplitude, bioeffects may be observed or not, depending on the bubble size and pulse frequency. Only at very large pressure amplitudes (PRPA > 4.20 MPa) are bioeffects systemati-

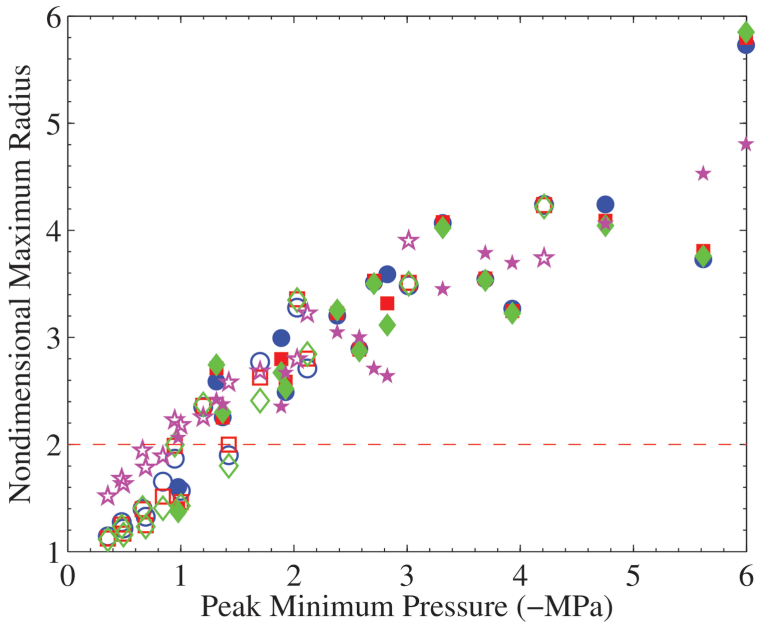

Figure 2.5: Dependence of the dimensionless maximum bubble radius on the peak negative pressure for G = 100 kPa. Empty symbols: no bioeffects; filled symbols: bioeffects. Pentagrams: 0.1 μm; circles: 0.5 μm; squares: 1 μm; diamonds: 2 μm; frequency: 1.5 - 7.5 MHz. The R_{max} = 2 inertial cavitation threshold (red, dashed line).

cally observed regardless of the bubble size and pulse frequency. This behavior is not surprising, since at these amplitudes the bubble response is expected to be highly nonlinear. Conversely, at low amplitudes (PRPA < 0.97 MPa), the oscillations are linear and no bioeffects are observed, regardless of bubble size and pulse frequency. In this latter case, most bubbles whose R_{max}/R_0 is below two do not exhibit bioeffects; however, this behavior depends on the value of elasticity, as shown in Section 2.4.5. Although not shown here for conciseness, similar results are obtained for peak positive pressure.

Similarly, the criterion T_{max} > 5000 K is not achieved with perfluoropropane. As shown in Figure 2.6, the observed temperatures for PFP are far below this value, though the results for air approach it. This result is expected since the criterion was determined for air, which has a larger specific heats ratio (γ_{air} = 1.4) than PFP (γ = 1.13). The specific heats ratio appears in the internal gas pressure term in Equation 2.2; its effect on the bubble dynamics is minor if the minimum radius is not very small, as in Figure 2.6. Still, since the adiabatic relationships for an ideal gas are used,

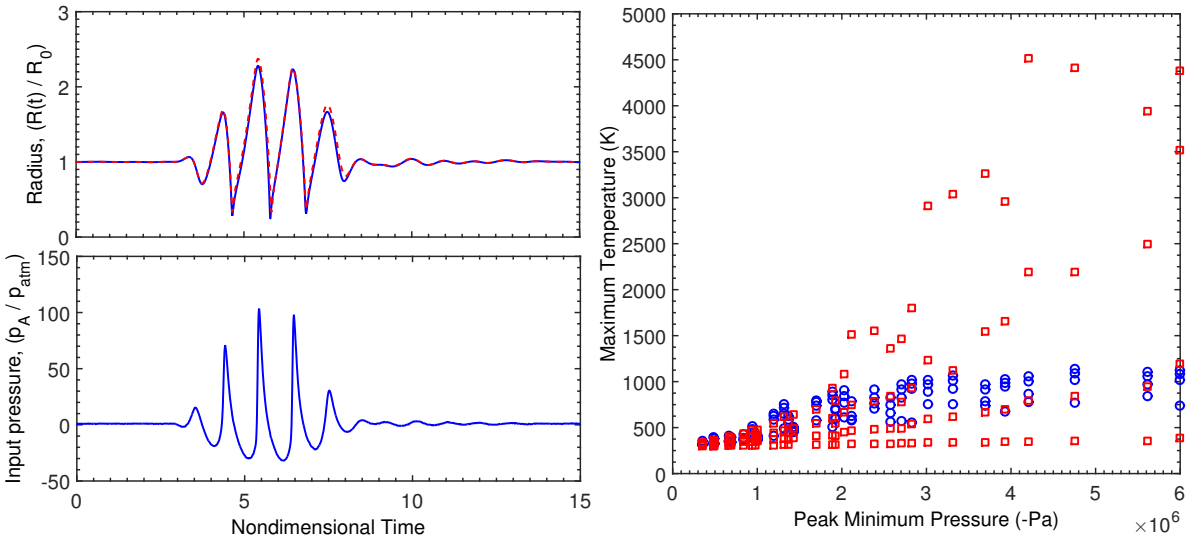

(a) (b)

Figure 2.6: Dependence of the bubble dynamics on the gas contents (G = 100 kPa). (a) History of the bubble radius for PFP (solid) and air (dashed). R_0 = 1 μm; frequency: 3.5 MHz; peak negative pressure: 3.3 MPa. (b) Maximum temperature for PFP (circles) and air (squares). R_0 = 0.1 – 2 μm; frequency: 1.5 - 7.5 MHz.

the temperature is significantly affected by the different specific heats ratio. Hence, even though the bubble dynamics are not strongly affected by the specific heats ratio, the maximum temperature is.

2.4.3 Dependence on the Initial (Equilibrium) Bubble Radius

In the experiment, the size distribution of the UCAs is not known exactly. It is desirable to know whether the observed bioeffects are caused by all bubbles responding to the ultrasound, or whether a specific size is more likely to be responsible at the bioeffects threshold. To answer this question, for each experimental frequency, bubbles of different radii ranging from 0.1–2 μm are subjected to the pressure waveform corresponding to the bioeffects threshold amplitude. It should be noted that varying the equilibrium radius changes the non-dimensional parameters. Figure 2.7 shows the maximum dimensionless radius, for both water (zero elasticity) and tissue (finite elasticity, G = 100 kPa), for the amplitude at which bioeffects are first observed at a given frequency.

Excluding the smallest size, the bubble response in tissue is monotone and changes little for a

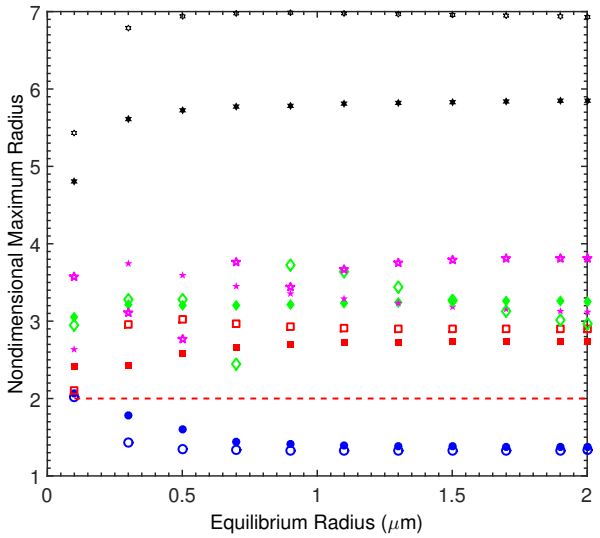

Figure 2.7: Dependence of the dimensionless maximum bubble radius on the initial bubble size for the amplitude at which bioeffects are first observed, at a given frequency, for $G = 100$ kPa. Empty symbols: water; filled symbols: tissue. Circles: 1.50 MHz; squares: 2.25 MHz; diamonds: 3.50 MHz; pentagrams: 5.00 MHz; hexagrams: 7.50 MHz. The $R_{max} = 2$ inertial cavitation threshold (red, dashed line).

given frequency; there is no initial size that consistently leads to a dramatic response. The somewhat erratic behavior of the small bubbles may imply that such sizes are not exclusively present in UCA concentrations. On the other hand, the behavior is more irregular for water, particularly at small radii: for a given frequency, there is an optimal size that exhibits the largest response; these variations are much larger than for tissue.

2.4.4 Dependence on the Pulse Frequency

The dependence of the bubble response on the pulse frequency is considered in this section. Figure 2.8 shows the maximum dimensionless and dimensional radius for all initial bubble sizes and amplitudes vs. frequency. The square symbols denote cases in which bioeffects were observed in the experiments, while the circular symbols represent no bioeffects. The initial bubble sizes are not discriminated here for simplicity.

With the exception of a few outliers, a clear separation between cases for which bioeffects did and did not occur is observed; in other words, the bioeffects threshold has a strong dependence on

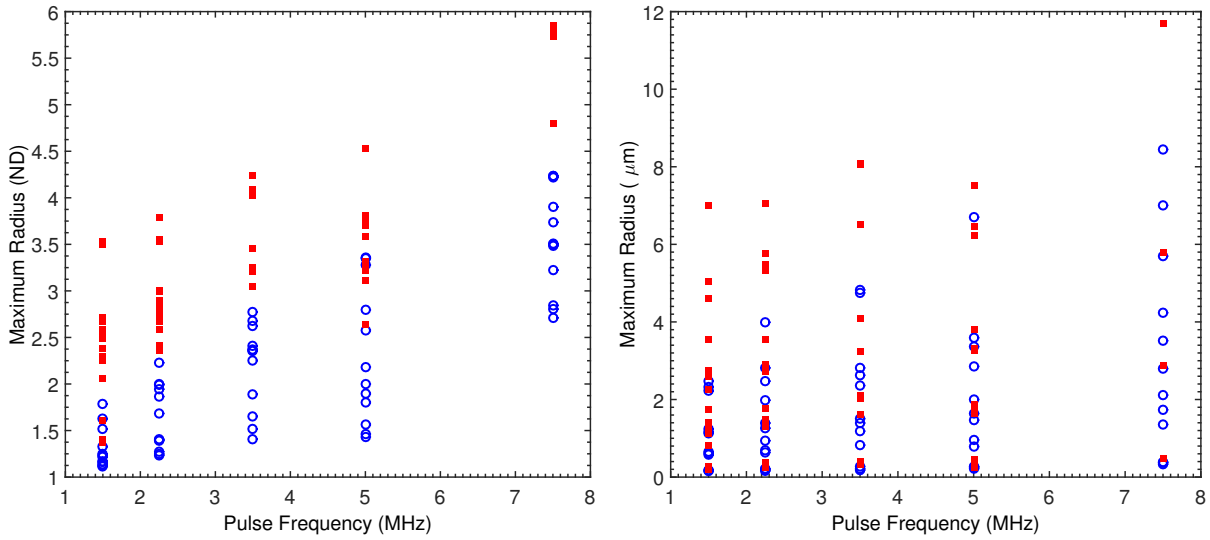

(a) R_{max}/R_0 (b) R_{max}

Figure 2.8: Dependence of the bubble dynamics on the frequency for $G = 100$ kPa. $R_0 = 0.1 - 2$ μm; empty circles: no bioeffects; squares: bioeffects. (a) Dimensionless maximum bubble radius. (b) Dimensional maximum bubble radius.

the frequency. The trend appears to be approximately linear with frequency. Large growth may be achieved with no evident bioeffects, especially at high frequencies. The quantity R_{max} is a measure of cavitation collapse, since it is related to the available energy of the bubble. Thus, the present results indicate that cavitation collapse is expected to play an important role regarding bioeffects, although the precise mechanism cannot be inferred. Again, the existing criteria for inertial cavitation thresholds are frequency-independent and do not correlate well with the bioeffects threshold, which clearly shows a strong dependence on frequency.

Another hypothesis is that bubble growth may be responsible for capillary breaching. However, the plot of the dimensional maximum radius vs. frequency does not show systematic bioeffects beyond a certain size, *e.g.*, some capillary diameter. Thus, growth is not the sole mechanism by which bioeffects occur. However, the data remains inconclusive, due to the inability to identify the cases in which cavitation collapse is the dominant effect.

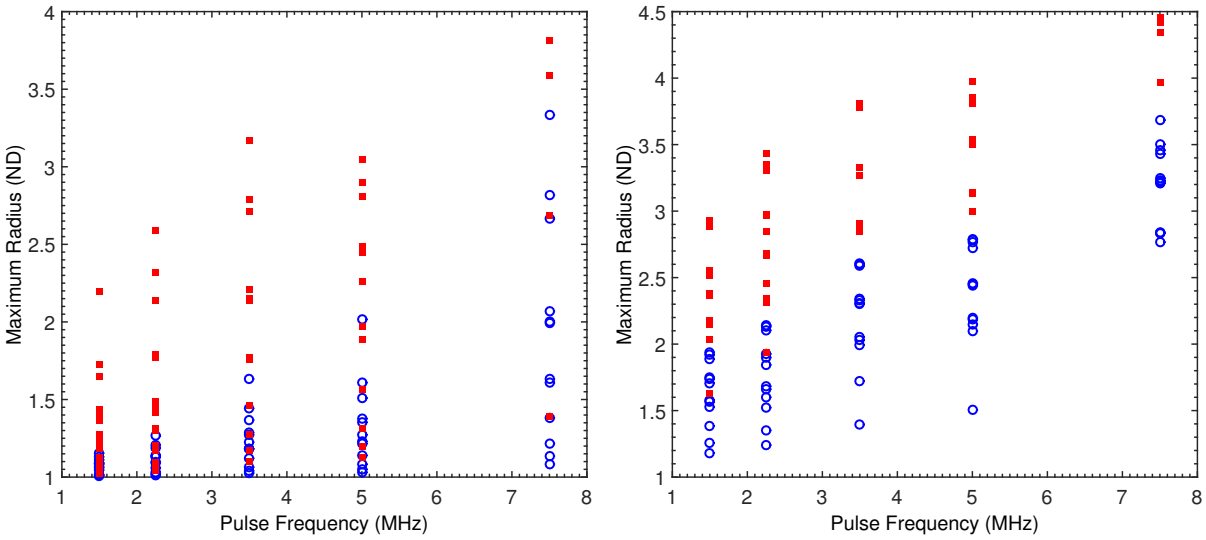

(a) $G = 5$ kPa. (b) $G = 1$ MPa.

Figure 2.9: Dependence of the dimensionless maximum bubble radius on the frequency. $R_0 = 0.1 - 2$ μm; empty circles: no bioeffects; squares: bioeffects. (a) $G = 5$ kPa. (b) $G = 1$ MPa.

2.4.5 Dependence on the Tissue Properties

As suggested in Figures 2.2-2.4, the bubble dynamics are sensitive to the tissue properties, specifically the elasticity. However, different types of tissue may have very different properties. Many of the measurements of tissue elasticity are made *in vitro*, and depend strongly on tissue preparation, storage, and degradation as well as method of measurement. Consequently, it is possible that these measurements do not accurately represent the current behavior. To explore the effect of the elasticity on the results and the correlation to bioeffects, Figure 2.9 shows the maximum dimensionless radius for all initial bubble sizes and amplitudes vs. frequency for $G = 5$ kPa and $G = 1$ MPa. Although seemingly high, the latter elasticity is chosen to match the work of Yang & Church (2005).

The bubble dynamics and correlation to bioeffects significantly change when reducing the elasticity. For a value of 5 kPa, the discrimination is no longer clear. The bubble dynamics are closer to the behavior in water, such that different sizes may have dramatically different responses to the same waveform, as explained previously. On the other hand, the stiffer medium ($G = 1$ MPa) shows an even sharper demarcation, which again appears to be approximately linear. Given the

sensitivity of the results on the elasticity, it is clear that more precise *in vivo* data is required for elasticities of tissues at the relevant strain rates.

Although not shown here, the type of viscoelastic model significantly affects the bubble dynamics (Johnsen & Hua, 2012; Patterson *et al.*, 2012a). For instance, a standard linear solid model, which includes stress relaxation in addition to elasticity, leads to very different maximum radii and oscillation properties (frequency and damping). For large relaxation times, elasticity variations become negligible.

2.5 Conclusions

In the present work, a numerical model is used to investigate experimentally observed bioeffects as a result of contrast-enhanced ultrasound. This work is unique in its combination of experimental results and numerical modeling. For the experimentally generated input pressure waveforms, it is known which of these triggered bioeffects, and from the numerical model we obtained calculated values for the dimensionless maximum radius and dimensional maximum temperature for each of these cases. By comparing the results of this study to previously established inertial cavitation thresholds used by Apfel & Holland (1991) and Yang & Church (2005), $T_{max} = 5000$ K and $R_{max} = 2$, it would appear that the inertial cavitation threshold does not play a role in determining the bioeffects threshold. However, it is unlikely that the inertial cavitation threshold is irrelevant. Instead, it is far more probable that these thresholds are not defined appropriately for cavitation in a viscoelastic medium, such as soft tissue. This work suggests the need for further experimental and numerical studies of cavitation in viscoelastic media.

The present work shows a strong correlation between cavitation dynamics and bioeffects when considering the pulse frequency. From the plot of maximum dimensionless radius vs. frequency, there is a clear separation between when bioeffects do and do not occur, and based on these results it appears that the frequency of the input pressure waveforms is of key importance to the definition of a bioeffect threshold, and likely the inertial cavitation threshold as well.

The present work shows that the elasticity of tissue significantly affects the bubble dynamics. This finding is perhaps not completely unexpected given that bubble dynamics are known to strongly depend on viscoelastic properties and model. The present study shows the need for more accurate measurements of material properties and for determining appropriate constitutive models for soft tissue, particularly at high strain rates. Finally, although the present work suggests that inertial cavitation collapse plays an important role with respect to bioeffects, it does not shed light on the exact mechanism, *e.g.*, shock emission upon collapse, growth beyond a given size, high temperatures generating free radicals, re-entrant jets in non-spherical collapse, etc. In future work we plan on investigating this injury mechanism by conducting direct simulations of the full equations of motion for bubble dynamics in a viscoelastic medium.

CHAPTER 3

Growth of liquid-gas interfacial perturbations driven by acoustic waves

In this chapter we develop a numerical model of Ultrasound (US)-alveolar interaction as an acoustically-driven, perturbed liquid-gas interface. Using the resulting computational framework we study the evolution of the interface for acoustic waves within the Diagnostic Ultrasound (DUS) regime and beyond. Using dimensional analysis, we describe the interface perturbation growth in terms of the vorticity dynamics. Finally, we consider the results and conclusions within the context of DUS of the lung. This work is in preparation to be submitted for publication (Patterson & Johnsen, (In preparation)).

3.1 Abstract

Diagnostic ultrasound has been shown to cause lung hemorrhage in a variety of mammals, though the underlying damage mechanisms are still unclear. Motivated by this problem, we use numerical simulations to investigate the interaction of an ultrasound wave with the alveolar tissue-air interface. A planar, positive, trapezoidal waveform propagates in tissue (modelled as water) and impinges upon an alveolus of the lung (modelled as air); to represent the alveolar surface roughness, the interface consists of a small-amplitude, single-mode perturbation. Because of the sharp density gradient at the interface, we hypothesize that ultrasound waves, despite their relatively low amplitude, deposit sufficient baroclinic vorticity to drive perturbation growth. Our simulations

show that the interface perturbation amplitude grows to many times larger than the original value, *well after the wave has passed*. We demonstrate that conventional (linear) acoustics cannot account for such deformations; instead, the perturbation growth is driven by nonlinear effects—the baroclinic vorticity deposited along the interface, due to the misalignment of the pressure gradient (across the wave) and the density gradient (across the perturbed liquid-gas interface). Based on dimensional analysis and scaling, we observe that the perturbation amplitude and length of the interface scale with the circulation density and grow according to power-law behavior in time. If the time-interval between the pressure increase and decrease is sufficient, both deposit vorticity of the same sign, thus enhancing the perturbation growth; conversely, if the interval is too short, the vorticity deposited by the pressure increase is canceled by the decrease. A further consequence is that one may be able to control the growth of such perturbed interfaces by modulating the incoming wave.

3.2 Introduction

DUS is one of the safest forms of medical imaging and has become ubiquitous in clinical practice. DUS-induced lung hemorrhage is the only known bioeffect of non-contrast, pulsed US, as bleeding has been shown to occur in mammals including mice, rats, rabbits, pigs, and monkeys (Child *et al.*, 1990; O'Brien *et al.*, 2006a; Tarantal & Canfield, 1994; Miller, 2012). Furthermore, this problem has been shown to occur for a wide range of frequencies from 1.5 to 12 MHz, for Mechanical indices well below the accepted safe limit for diagnostic ultrasound, MI = 1.9 (O'Brien, 2007). Although this problem does not appear to be of medical safety concern for humans under typical conditions, there is a need to better understand the physical mechanisms of DUS-induced lung hemorrhage, which cannot currently be explained by well-established US bioeffects mechanisms. Typically, US bioeffects are generally classified as thermal or non-thermal, with the bulk of non-thermal bioeffects being a result of acoustically driven inertial cavitation. Except for one study reporting cavitation activity (Holland *et al.*, 1996), the bulk of the research suggests that

inertial cavitation is not the cause of DUS-induced lung hemorrhage: Raeman *et al.* (1996) and O'Brien *et al.* (2004) found that bleeding is not worsened by the use of ultrasound contrast agents, and O'Brien *et al.* (2000b) observed that the severity of the hemorrhage increases when the hydrostatic pressure is raised. Beyond lung hemorrhage, a number of studies have explored nonlinear mechanisms as a potential cause for bioeffects. Filonenko & Khokhlova (2001) developed numerical models to study the effects of acoustic nonlinearity on wave propagation and heating in soft tissue. Khokhlova *et al.* (2006) numerically solved a KZK-type equation simulating High-Intensity Focused Ultrasound (HIFU) fields in a tissue phantom with the purpose of studying the impact of nonlinear propagation, cavitation and boiling on lesion formation. Based on potential flow simulations of an inviscid free surface subjected to a Gaussian velocity potential, Tjan & Phillips (2007) suggested another damage mechanism for DUS-induced lung hemorrhage, namely that under the right circumstances, droplets capable of puncturing the air-filled sacs within the lung may be ejected by the focused US. Simon *et al.* (2012) experimentally demonstrated atomization of water and soft tissue at air interfaces exposed to 2 MHz HIFU, though at amplitudes higher than diagnostic. Despite these efforts, the precise damage mechanism underlying DUS-induced lung hemorrhage is still unknown.

In parallel, the dynamics of accelerated interfaces separating fluids of different densities have been the subject of intensive studies in fluid mechanics. When exposed to accelerations whose sign is opposite that of the density gradient, interfacial perturbations grow exponentially as a manifestation of the Rayleigh-Taylor (RT) instability (Taylor, 1950). Bubbles of light fluids "rise" into the heavy fluid while spikes of heavy fluid "fall" into the light fluid. Although the original analysis pertained to perturbation growth at early times under constant acceleration, extensions to nonlinear growth and time varying accelerations have been performed. In the limit of instantaneous acceleration (e.g., as produced by a shock wave), perturbations initially grow linearly in time, as predicted by Richtmyer-Meshkov (RM) analysis (Richtmyer, 1960; Meshkov, 1969), regardless of the sign of the density gradient. To characterize the growth at later times, Hecht *et al.* (1994) developed a potential flow model for both RT and RM flows with Atwood Number $A = \frac{\rho_{heavy}-\rho_{light}}{\rho_{heavy}+\rho_{light}} = 1$, which

describes bubble growth in both linear and nonlinear regimes. Srebro *et al.* (2003) presented a buoyancy-drag model to describe the perturbation growth for time-dependent Atwood number and acceleration profile. In both RT and RM flows, perturbation growth can be explained by vorticity generated baroclinically, i.e., due to the misalignment of the density and pressure gradients:

$$\left.\frac{d\omega}{dt}\right|_{baroclinic} = \frac{\nabla\rho \times \nabla p}{\rho^2}, \tag{3.1}$$

where ω is the vorticity, ρ density and p pressure. The majority of RT research has examined interfacial perturbation growth under constant acceleration fields; RM research is primarily concerned with shock-accelerated interfaces, where the post-shock pressure is kept raised (Brouillette, 2002). There has been limited study of interfaces undergoing transient acceleration. Mikaelian (1996) simulated shock passage through multiple gas layers with sinusoidally perturbed interfaces to show that subsequent reshock by reflected waves caused the flow to evolve into a complex nested mushroom morphology. Mikaelian (2009) developed a model for hydrodynamic instabilities driven by time-dependent accelerations, which agreed well with full simulations. Henry de Frahan *et al.* (2015b) demonstrated that subsequent interactions between reflected and transmitted shocks and rarefactions with interfaces in layered media could be used to decrease and possibly control the long term growth of a shock-accelerated interface. Much of the past research in both RT and RM flows has focused largely on gas-gas interfaces. Haas & Sturtevant (1987) experimentally shocked helium and R22-filled bubbles in air. They showed that transmitted waves overtake one another and merge downstream as a result of nonlinear gas dynamics. Numerical simulations of shock-bubble interactions have verified the timescales and physical features observed in these experiments. These simulations, in conjunction with nonlinear theory, have shown that baroclinic vorticity is generated by the wave-interface interaction, and dominates the late-time dynamics of the system (Picone & Boris, 1988; Quirk & Karni, 1996).

We submit that an ultrasound wave propagating in tissue and impinging upon the lung may give rise to perturbation growth along the interface, much like that observed in RT and RM flows.

Despite being smooth by contrast to shocks, ultrasound waves in tissue have pressure amplitudes on the order of megapascals over millimeters; although the strength of the waves is relatively small given the large density and sound speed, the pressure gradients are not negligible. Furthermore, the density jumps by several orders of magnitude over a few microns across the tissue-air interface. These observations motivate our hypothesis, namely that baroclinic vorticity generated by the misalignment of the pressure gradient across the ultrasound wave and the density gradient across the tissue-lung interface causes interfacial perturbations to grow, even after the passage of the wave. We note that misalignment of the acoustic pressure gradient and interface density gradient also occurs for the case of non-normal wave incidence, even for a perfectly flat interface. As the alveolar structure is highly anisotropic, non-normal wave impingement is bound to occur during real DUS wave-alveolar interactions. Such a phenomenon cannot be described by linear acoustics. Ultimately, if the growth is sufficient over the relevant time scales, capillary rupture may follow. However, the fluid mechanics of this process are expected to be different from classical RT and RM theory: by contrast to conventional RT analysis, the acceleration imparted by the pressure wave is time-varying and transient; as opposed to the classical RM process, the transient wave deposits vorticity over a finite duration. Thus, the transient nature of the problem (e.g., interface deformation during wave interaction) is expected to be important. Our objective is to predict the growth of perturbations along water-air interfaces subjected to time-varying pressure waves using numerical simulations, under conditions relevant to diagnostic ultrasound. To probe the basic mechanics, the tissue-lung interface is modeled as a water-air interface, and the ultrasound waveform is idealized to a trapezoidal wave. The article is organized as follows. We first describe the problem under consideration and our methods. We then investigate the perturbation growth and vorticity dynamics for a baseline case. As we seek to understand the late-time growth, we then examine how the wave properties (amplitude and length) affect the dynamics. Finally, we summarize the main conclusions and suggest the next steps to be taken.

3.3 Fluid mechanics modeling of ultrasound-lung interaction

Consider a diagnostic ultrasound (DUS) pulse traveling into the lung. Since past studies have observed lung hemorrhage with frequencies ranging from 1.5 to12 MHz and pressure amplitudes from 1.0 to 12.3 MPa (Penney *et al.*, 1993; Child *et al.*, 1990; O'Brien *et al.*, 2000a; Miller *et al.*, 2015), we consider pulses in the MHz and MPa ranges. The wave traverses several layers of soft tissue and fluid making up the thoracic wall ($\sim$ 2 cm thick) and pulmonary pleura ($\sim$ 1 mm thick), whose acoustic properties (density and sound speed) are close to that of water (McLean *et al.*, 2011). The size of the focal region is on the order of the ultrasonic wavelength λ, approximately 1 mm for a 1.5 MHz wave in tissue. After passing through the pleurae, the wave encounters a network of openly connected, air-filled saccules with distinctly irregular surfaces—the alveoli, whose typical size in adult humans is $\ell \approx 200\ \mu$m (Ochs *et al.*, 2004). The lung is a complex organ, as exemplified by the range of length scales and physical properties (multiphase, viscoelastic, surface tension, high gas volume fraction Bayliss & Robertson, 1939; Suki *et al.*, 1994). However, dimensional arguments suggest that at sufficiently early times inertial effects dominate in the interaction of an ultrasound wave with the lung; viscous, surface tension and elastic effects are negligible. By the end of the simulations considered here, the viscous boundary layer thickness is approximately $\sqrt{\nu_{water} t_{final}} \approx 20\ \mu$m, far less than both a typical alveolar diameter and the 400 μm amplitudes achieved at that time in our baseline case. The Weber number corresponding to the lung surface tension ($\sim$ 9 mN/m, Schürch *et al.*, 1976) and a pressure amplitude of 1 MPa is $We = p_a \ell / \sigma_{lung} = O\left(10^4\right) \gg 1$. For an elastic modulus $K = 5$ kPa (Cavalcante, 2005), the acoustic Cauchy number is $Ca = p_a / K = O\left(10^2\right) \gg 1$. To reinforce the relative unimportance of elasticity within the considered problem, we compare the estimated inertial as elastic forces at the interface for our baseline case in Appendix A.7.

Our interest lies in the interaction between an incident ultrasound cycle and the first alveolar tissue-air interface it encounters, as illustrated in Figure 3.1. Given the complexity of the full problem, we simplify it to a tractable one on the basis of the above observations. Since viscous, surface

tension and elastic effects are negligible, the dominant mechanics are the wave propagation, its interaction with the tissue-lung interface and subsequent interfacial deformations. Thus, we model the thoracic wall and pleura as water, and the lung as air; both substances are compressible, with appropriate density and sound speed. To simplify the representation of the alveolar surface roughness, the interface is initially represented by a single-mode sinusoidal perturbation of amplitude a_0,

$$y_{interface}(x, t = 0) = a_0 \sin\left(\frac{2\pi x}{\ell} - \frac{\pi}{2}\right), \tag{3.2}$$

where a_0 is taken to be 0.03ℓ in this work. We define the time-dependent interfacial perturbation amplitude $a(t)$ as half the peak-to-trough distance in the $y-$direction. $\lambda \gg \ell$, and as such the incoming wave is planar the scale of an alveolus. More complex, corrugated interfaces can be described by combining such sinusoidal perturbations of varying amplitudes and wavelengths. Despite the three-dimensional geometry of the real problem, the essential physics are well approximated by this two-dimensional description.

Although our motivation is rooted in DUS-induced lung hemorrhage, a typical DUS pulse bears challenges when investigating the fundamental mechanics of acoustically driven perturbed liquid-air interfaces. For instance, the waveforms are often noisy, continuously vary and come in as pulses consisting of several cycles of variable amplitude. For simplicity, we construct an idealized waveform comprising the key elements of DUS pulses expected to drive the mechanics, as illustrated in Figure 3.2. The trapezoidal waveform is shown first, in red, as an envelope around a diagnostic pulse to show the relative amplitudes and length scales, and then by itself, describing the precise initial pressure condition as a function of distance from the interface in the $+y$-direction. By contrast to shock waves, which instantaneously and impulsively accelerate the interface and maintain a state of high pressure after their passage, an ultrasound wave continuously interacts with the interface over the finite duration of its passage; the pressure returns to its initially unperturbed ambient value thereafter. Direct application of Richtmyer-Meshkov analysis to relate the continu-

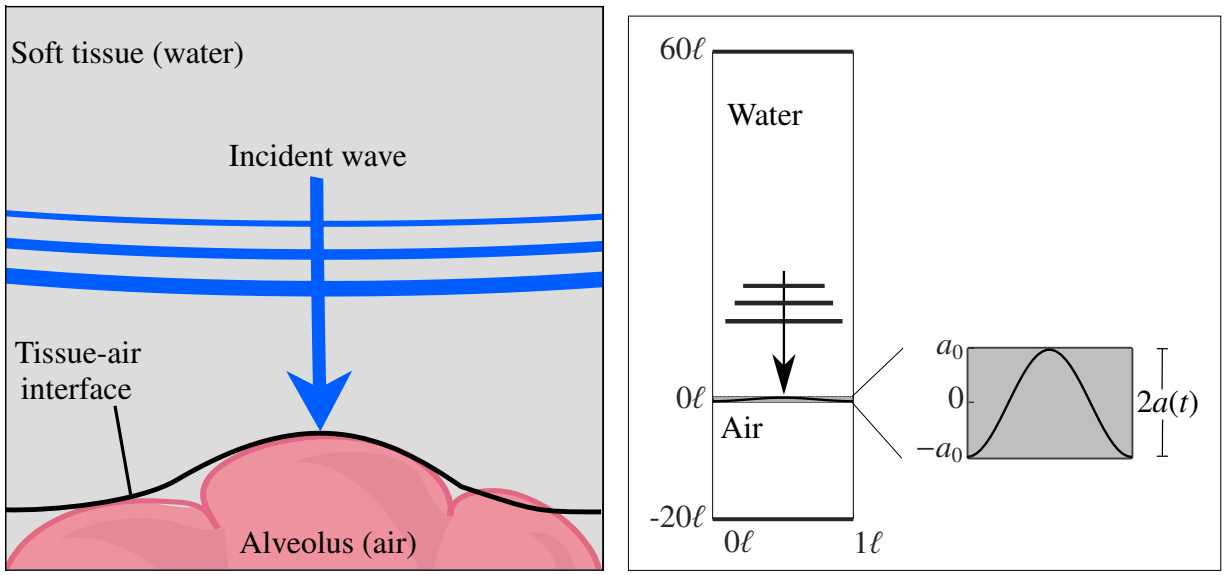

Figure 3.1: Schematic view of the physical and model problems. Left: Schematic description of the physical problem of interest (ultrasound pulse in tissue impinging upon the first alveolus it encounters). Right: Computational set-up of the model problem (acoustic wave in water impinging upon a sinusoidally perturbed air interface of initial amplitude a_0).

ously varying pressure profile to baroclinic vorticity deposition is thus not straightforward. For this reason, we consider a single, positive trapezoidal wave of amplitude and length relevant to DUS, consisting of a linear pressure increase followed by a constant elevated pressure, itself followed by a linear pressure decrease back to ambient. Noting that its intensity is approximately trapezoidal, the complex, multi-cycle DUS pulse is simplified to a waveform to which Richtmyer-Meshkov-inspired analysis can be applied: though finite duration, the pressure gradients are constant and the time intervals over which vorticity is deposited (pressure increase/decrease) are clearly defined. Despite this specific choice for the waveform, we explain in Section 3.5 how these results are generalizable to arbitrary waveforms with positive and negative pressure contributions. Results for an ultrasound pulse waveform, a negative trapezoidal waveform, and a sinusoidal waveform are provided in Chapter 4, Appendices A.5, and A.6, respectively.

The amplitude and length of the wave are chosen to be relevant to DUS. The pressure increases from atmospheric by amplitude $p_a = 5.0$ to 12.5 MPa over a distance $\Delta L_a = 1$ mm for an alveolus of diameter 200 μm. The wave is symmetric in time such that the pressure decreases over the same

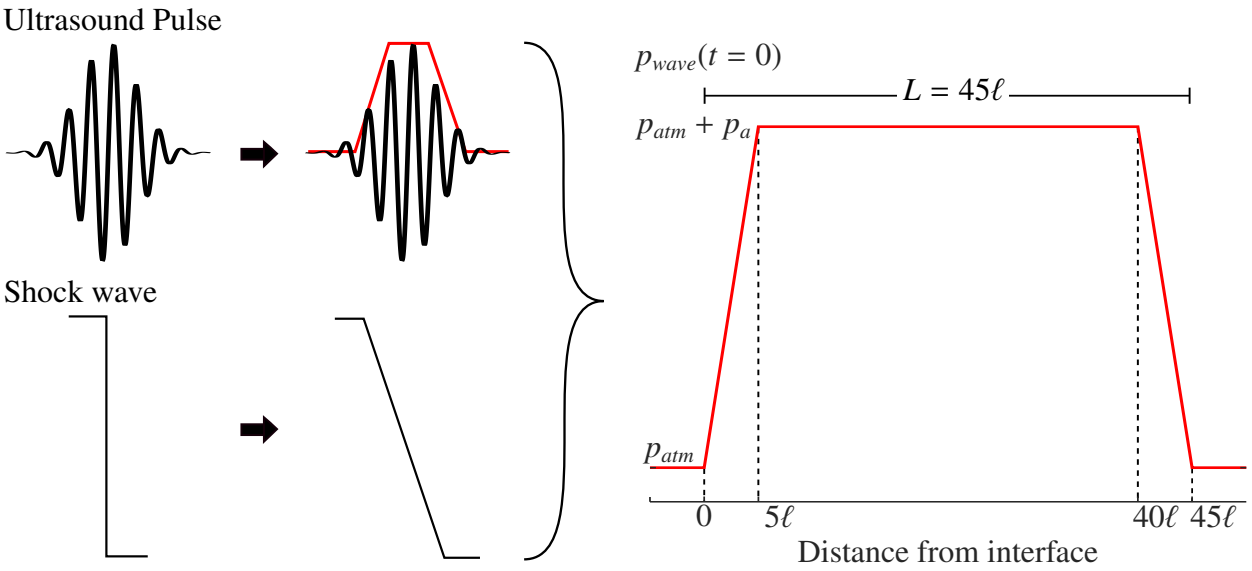

Figure 3.2: Ideological progression from ultrasound pulse and shock to baseline trapezoidal wave. This wave can be analyzed with Richtmyer-Meshkov-inspired analysis.

ΔL_a. To keep the pulse duration consistent with DUS, we choose as a baseline a total pulse length of $L = 45\ell$ corresponding to 9 mm in soft tissue or a 5.5 μs pulse duration, in the range relevant to previous research (Child *et al.*, 1990; O'Brien *et al.*, 2006b). Thus, the length of the constant elevated pressure is 35ℓ. Thus, the initial pressure waveform is prescribed as

$$p(y_f, t=0) = p_{atm} + p_a \begin{cases} 0, & y_f \le 0, \quad \text{or} \quad y_f \ge 45\ell, \\ \frac{y_f}{5\ell}, & 0 \le y_f \le 5\ell, \\ 1, & 5\ell \le y_f \le 40\ell, \\ 1 - \frac{y_f - 40\ell}{5\ell}, & 40\ell \le y_f \le 45\ell, \end{cases} \tag{3.3}$$

where $y_f = y - (a_0 + 0.3\ell)$ is the y-location, relative to the initial location of the wave leading end. At these amplitudes and frequencies, linear acoustics describes ultrasound propagation in homogeneous tissue, such that the initial $x-$ and $y-$velocity components are set to $u = 0$ and $v = -\Delta p_a/(\rho c)$, respectively, and initial density is $\rho_{water} + \Delta p_a/c^2$ (Anderson, 1990), where $\Delta p_a = p(y, 0) - p_{atm}$ is the acoustic perturbation pressure.

Once the ultrasound reaches the interface, the pressure differential (due to the geometrical

perturbation) over a short distance applies a torque on fluid particles along the sharp, perturbed interface, thus generating rotation (or baroclinic vorticity). Since this effect is nonlinear, and thus cannot be described by linear acoustics, we solve the Euler equations, written here in two dimensions (x, y):

$$\frac{\partial \rho}{\partial t} + \frac{\partial}{\partial x}(\rho u) + \frac{\partial}{\partial y}(\rho v) = 0, \tag{3.4a}$$

$$\frac{\partial}{\partial t}(\rho u) + \frac{\partial}{\partial x}\left(\rho u^2 + p\right) + \frac{\partial}{\partial y}(\rho u v) = 0, \tag{3.4b}$$

$$\frac{\partial}{\partial t}(\rho v) + \frac{\partial}{\partial x}(\rho u v) + \frac{\partial}{\partial y}\left(\rho v^2 + p\right) = 0, \tag{3.4c}$$

$$\frac{\partial E}{\partial t} + \frac{\partial}{\partial x}(u[E + p]) + \frac{\partial}{\partial y}(v[E + p]) = 0, \tag{3.4d}$$

where t is time, ρ density, p pressure, u and v are still the $x-$ and $y-$velocity components and E the total energy. A stiffened equation of state relates the pressure to the internal energy,

$$E = \frac{\rho\left(u^2 + v^2\right)}{2} + \frac{p + nB}{n - 1}, \tag{3.5}$$

where B is an empirically determined measure of liquid stiffness that allows water to be treated as an ideal gas under high pressure. For perfect gases, such as in our treatment of air, n is the specific heats ratio and $B = 0$.

The interface evolution is captured using a $\gamma-$based (Shyue, 1998), such that

$$\frac{\partial}{\partial t}\left(\frac{1}{n-1}\right) + u\frac{\partial}{\partial x}\left(\frac{1}{n-1}\right) + v\frac{\partial}{\partial y}\left(\frac{1}{n-1}\right) = 0, \tag{3.6a}$$

$$\frac{\partial}{\partial t}\left(\frac{nB}{n-1}\right) + u\frac{\partial}{\partial x}\left(\frac{nB}{n-1}\right) + v\frac{\partial}{\partial y}\left(\frac{nB}{n-1}\right) = 0. \tag{3.6b}$$

We initially prescribe a small, finite-thickness parameter δ to the interface (Latini *et al.*, 2007),

such that the initial volume fraction field is

$$\alpha_0 = \begin{cases} 1 & \text{(water)}, \\ \exp\left(\log\left(10^{-16}\right)|d|^8\right) & \text{(mixture)}, \\ 0 & \text{(air)}, \end{cases} \qquad d = \frac{\delta + y_{interface}(x) - y}{2\delta}, \tag{3.7}$$

where $\delta = 0.08\ell$. While our choice of this parameter is based purely on previous research, we demonstrate in Appendix A.4 that, within a reasonable range of values, our results are largely independent of δ.

The dimensional fluid properties used for air are determined at 300 K and 1 atm such that $\rho_{air} = 1.18$ kg/m^3 and $c_{air} = 347.2$ m/s. For water, $\rho_{water} = 996$ kg/m^3 and $c_{water} = 1648.7$ m/s. The parameters in the stiffened equation of state are $n_{air} = 1.4$, $B_{air} = 0$, $n_{water} = 5.5$, and $B_{water} \approx 492$ MPa (Marsh & Los Alamos Data Center for Dynamic Material Properties (U.S.), 1980; Holian, 1984; Cocchi *et al.*, 1996). The density and sound speed of water, as well as the alveolar diameter, equal here to the interface perturbation wavelength, are used for non-dimensionalization.

The equations are solved on a domain ranging in the $xy-$plane from $0 \leq x \leq 1\ell$ (periodic in x) and $-20\ell \leq y \leq 60\ell$ (outflow boundary conditions in y). The $y-$length of the domain is chosen such that the entire initial wave and subsequently deforming interface fit in the domain. We use a third-order accurate Discontinuous Galerkin (DG) scheme ($p = 1$) in space with the Roe solver and a fourth-order accurate, adaptive Runge-Kutta method to march forward in time (Henry de Frahan *et al.*, 2015a). To isolate the effects of a single pulse, the longest time span reasonable to observe the evolution of the system is the time between consecutive pulses, which for a typical pulse repetition frequency of 1 kHz is 1000 μs (O'Brien *et al.*, 2000a). Here, due to computational limitations, we consider up to a final time $t_{final}/(\ell/c) = 4748$ or approximately 576 μs of dimensional time. The grid resolution is 100 points per ℓ in x and y, except for the top and bottom-most 10ℓ segments of the domain, where the grid is stretched geometrically to minimize artificial reflections. Given the exceedingly long time duration, we used the highest possible grid

resolution based on our computing resources and time constraints. Though the solution cannot be fully converged in a pointwise sense with the Euler equations (Samtaney & Pullin, 1996), the results show grid dependence of certain integral quantities. Nevertheless, the conclusions made on the basis of our results are still valid. Convergence of various quantities for our baseline case is examined in Appendix A.2.

In this study, we determine the dependence of the time-evolution of the interfacial perturbation amplitude on the wave amplitude p_a and length L of the wave. To remain clinically relevant, we consider wave amplitudes between $p_a = 5.0$ and 12.5 MPa and lengths between $L = 10\ell$ and 45ℓ. For our baseline case, $p_a = 10$ MPa and $L = 45\ell$. As our results indicate, this baseline is convenient because the pulse amplitude is sufficiently strong to evolve the dynamics to late time within a computationally feasible time, yet not so strong as to drive the system to behave qualitatively differently than weaker waves within the diagnostic ultrasound regime.

3.4 Results and discussion

3.4.1 Dynamics of the baseline case

3.4.1.1 Density-based description of the perturbation growth

To exemplify the growth of a perturbation along a water-air interface driven by the trapezoidal wave of interest, Figure 3.3 shows the time evolution of the density field for the baseline case. The wave propagates from water (top) to air (bottom). Frame 1 shows the interface shortly after it first encounters the wave at $t/(\ell/c) = 4.75$, near the end of the compression. Upon interaction with the interface, nearly all of the acoustic energy is reflected back into the water as a rarefaction due to the significantly lower acoustic impedance of air. The transmitted wave in air is weakly focused or defocused, depending on the convex or concave nature of the curved interface. Between frames 1 and 2, the mean interface location moves in the negative y-direction by 0.31 (corresponding to the mean acoustic velocity multiplied by the time between the pressure rise and decrease), as it

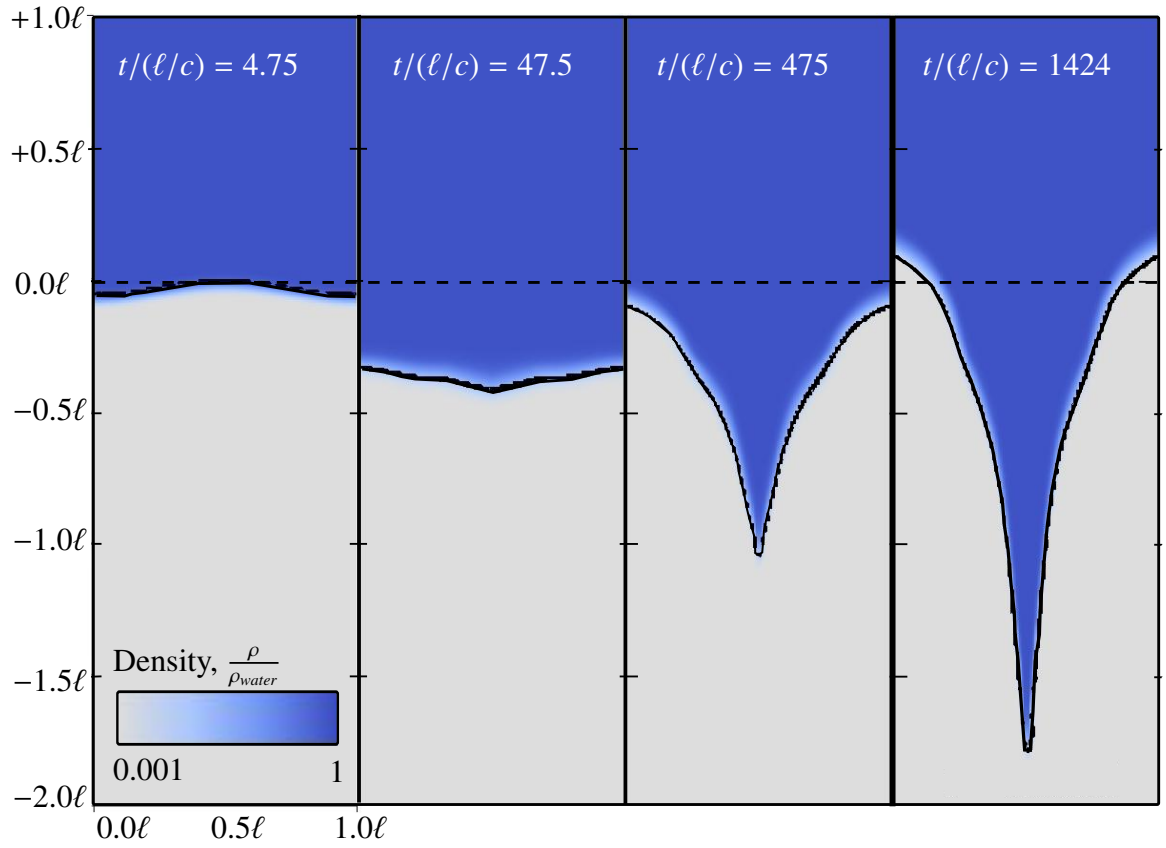

Figure 3.3: The evolution of the acoustically-driven, perturbed interface. Density contours at $t/(\ell/c) = 4.75$, 47.5, 475, and 1424 for the baseline $p_a = 10$ MPa, $L = 45\ell$ trapezoidal wave. Black line: $\alpha = 0.5$ volume fraction isoline; black dashed line: initial mean interface location.

is advected by the velocity corresponding to the elevated pressure. Between these two frames, the perturbation phase reverses sign as evidenced by the initial perturbation peak at $x/\ell = 0.5$ becoming a valley. From frame 2 on, bubbles of air are observed to rise into the water along the sides at $x/\ell = 0,\ 1$, while a liquid spike penetrates the air in the middle at $x/\ell = 0.5$. This bubble and spike evolution continues well after the incident wave has passed. The cumulative effect is that the interface perturbation grows from an initially smooth sinusoid to a pointed spike at late times.

We turn to a more quantitative description of the time-evolution of the perturbation in Figures 3.4 (amplitude) and 3.5 (bubble and spike locations). The bubble and spike locations are defined as the highest and lowest y-coordinate, respectively, of the constant $\alpha = 0.5$ volume fraction isoline, and are meaningful really only after phase reversal; the interface amplitude is calculated by taking the difference between the bubble and spike locations. As the volume fraction is not equal to the

mass fraction, this isoline does not always align with the apparent interface in the figure. We note that this area of mixed fluid around the interface where the volume fraction is between 0 and 1 is a product of the numerical treatment and is not necessarily a property of the physical system.

The early time behavior is characterized by several distinct events. Following the impingement of the leading end of the wave at non-dimensionalized time $t/(\ell/c) = t_1 = 0.3$, the interfacial pressure rises until $t_2 = 5.3$, at which point the pressure has reached its maximum amplitude. As the initial perturbation peak moves in the negative y-direction, the interface amplitude decreases to nearly zero (flat interface) at $t_p = 24$, the instant when the phase reverses. The amplitude increases thereafter as the initial peak (now the spike) continues its progress in the negative y-direction. The interfacial pressure remains constant until $t_3 = 40.3$, at which point the leading end of the rarefaction reaches the interface. The pressure decreases until $t_4 = 46.1$, at which point the full wave has left the interface and the pressure is atmospheric again, as it was originally. The perturbation amplitude continues to grow well after the wave has passed, reaching many times its initial value. At these late times, the growth appears to be smooth, continuous and monotonic in time. This large growth may have significant implications in the context of potential ultrasound-generated damage to the lung as the alveolar surface elongates, thus potentially giving rise to capillary rupture.

Slightly before t_4, the slope of the bubble and spike locations changes significantly, at a time we define as $t/(\ell/c) = t_\Gamma = 44.6$. We remark that between t_2 and t_3 the bubble and spike velocities consist of the superposition of the wave velocity corresponding to the elevated pressure and the velocity induced by the baroclinic vorticity, to be discussed in greater detail in the next section. Once the magnitude of the former is sufficiently small (toward the end of the passage of the wave), the latter becomes dominant. At this time, the net bubble velocity becomes positive and rises. This time t_Γ, defined as the minimum in the bubble location after phase reversal, plays an important role in our analysis from Section 3.4.2.

The most important contribution of linear acoustics is the interface translation (downward on the contour plots) during the interaction with the wave; the overall interfacial perturbation evolution

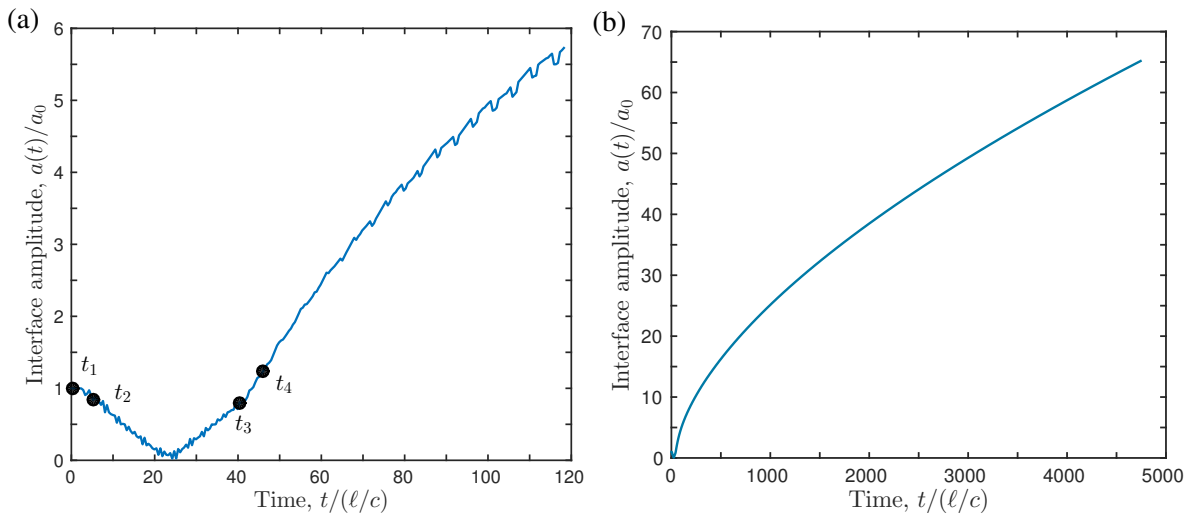

Figure 3.4: Interface perturbation amplitude history $a(t)/a_0$ for the baseline $p_a = 10$ MPa, $L = 45\ell$ trapezoidal wave. $t/(\ell/c) \leq 120$ (a) and $t/(\ell/c) \leq 5000$ (b). In (a), times at which different stages of the incoming trapezoidal pressure wave first encounter the interface are indicated as t_1 (the compression), t_2 (the constant elevated pressure, p_a), t_3 (the rarefaction), and t_4 (the return to ambient pressure).

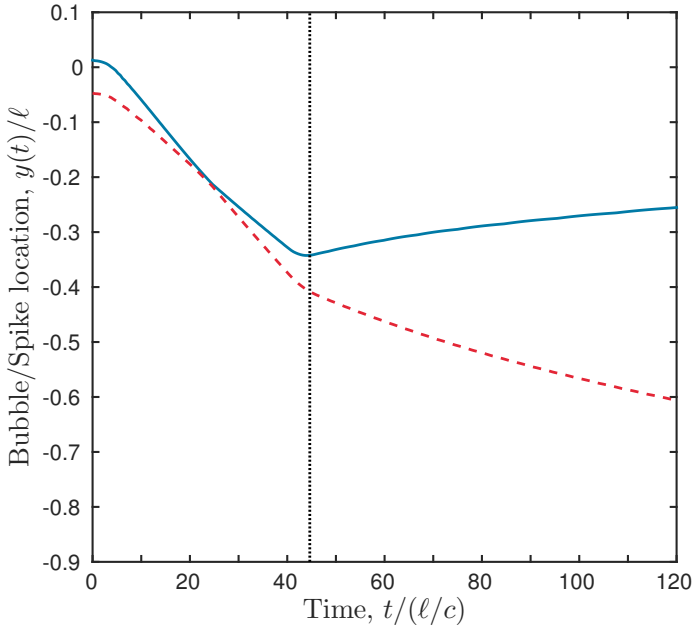

Figure 3.5: y-locations of the bubble and spike for the baseline $p_a = 10$ MPa trapezoidal wave case, during and shortly after the wave-interface interaction. By definition, the bubble is the top (solid, blue) curve and the spike is bottom (red, dashed) curve. t_Γ, as defined by the minimum bubble location, is the vertical (black, dotted) line.

cannot be explained solely by this principle. The combined effects of the compression and the deformations occurring between the time the wave travels from the perturbation peak to trough would yield a perturbation amplitude change of approximately $0.01a_0$. Linear acoustics would further imply that the perturbation should no longer evolve after the wave passage. It follows that nonlinear mechanisms must drive the perturbation growth.

3.4.1.2 Vorticity-based description of the perturbation growth

The results presented in the previous section demonstrate that the perturbation amplitude grows well after the incident wave has traversed the interface, driven by a mechanism that cannot be explained by conventional linear acoustics. During interaction with the interface, the pressure differential (due to the geometrical perturbation) over a short distance applies a torque on fluid particles along the interface, thus generating rotation (baroclinic vorticity). Such effects would be of higher-order and thus negligible for acoustic waves encountering small density variations; in the present problem, however, the pressure and density change by significant amounts over short distances, thus giving rise to substantial gradients dominating otherwise first-order (acoustic) effects. For these reasons, we examine the perturbation growth in terms of vorticity, $\boldsymbol{\omega} = \nabla \times \boldsymbol{u}$, whose evolution in two dimensions is given by

$$\frac{\partial \boldsymbol{\omega}}{\partial t} + (\boldsymbol{u} \cdot \nabla)\,\boldsymbol{\omega} = -\boldsymbol{\omega}\,(\nabla \cdot \boldsymbol{u}) + \frac{\nabla\rho \times \nabla p}{\rho^2}. \tag{3.8}$$

The high impedance mismatch and relatively low dilatation at the wave amplitudes of interest make the first term on the right-hand side (dilatation) essentially negligible compared to the last term (baroclinic), which is large given the nearly discontinuous density gradient and the significant pressure variations over relatively short lengths; Appendix A.1 quantitatively supports this claim. Figure 3.6 depicts vorticity contours at $t/(\ell/c) = 4.75, 47.5, 475$, and 1424, for the baseline case. At time zero, there is no vorticity in the domain. Frame 1 shows that near the end of the compression-interface interaction a vortex sheet exists along the interface, with negative vorticity between $x/\ell \in$

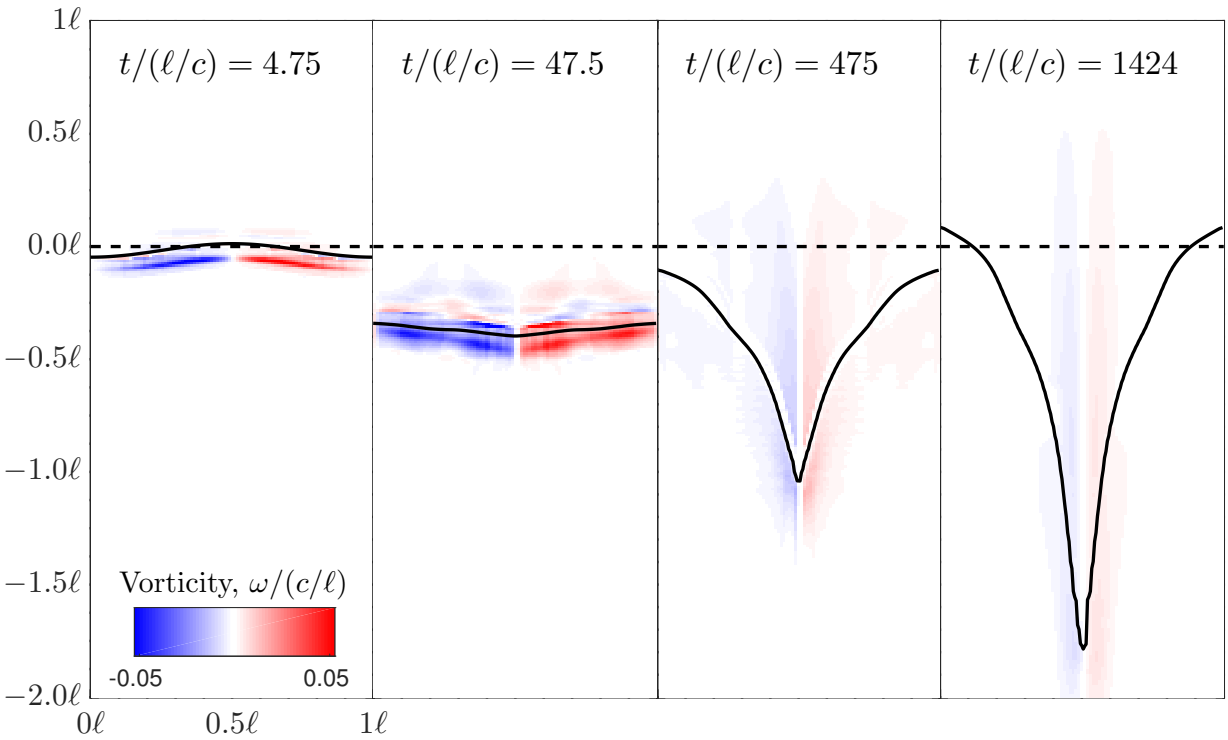

Figure 3.6: The evolution of the vorticity field. Vorticity contours at $t/(\ell/c) = 4.75, 47.5, 475$ and 1424 for the baseline $p_a = 10$ MPa, $L = 45\ell$ trapezoidal wave case. Black solid line: $\alpha = 0.5$ volume fraction isoline; black dashed line: initial mean interface location.

$[0.0, 0.5]$ and positive vorticity between $x/\ell \in [0.5, 1.0]$. The vorticity appears to be primarily in the air as the interface location (black line) is taken to be the $\alpha = 0.5$ volume fraction isoline. By frame 2, the initially deposited vorticity has driven the perturbation peak downward such that the phase is now reversed during the passage of the rarefaction. As a consequence of this phase reversal, most of the vorticity deposited by the rarefaction has the same sign as the distribution generated by the compression, despite the corrugation of the interface. If the interface had remained undeformed, the vorticity deposited by the rarefaction would have been opposite sign and thus act to reduce that due to the compression. Instead, the enhanced vorticity gives rise to a clockwise (left-half domain) and counter-clockwise (right-half domain) vortex pair driving the spike to form at $x/\ell = 0.5$. Over time, the vorticity contours become fainter, but appear to spread over a larger region.

During the interface evolution, the vorticity redistributes itself along the interface. To quantify this behavior, we plot in Figure 3.7 the cumulative vorticity (in y) along the interface, $\int_{-\infty}^{+\infty} \tilde{\omega}(x, y)dy$, where $\tilde{\omega} = \omega$ for $0 < \alpha < 1$ and is otherwise zero (in pure water or air). Initially, the vorticity

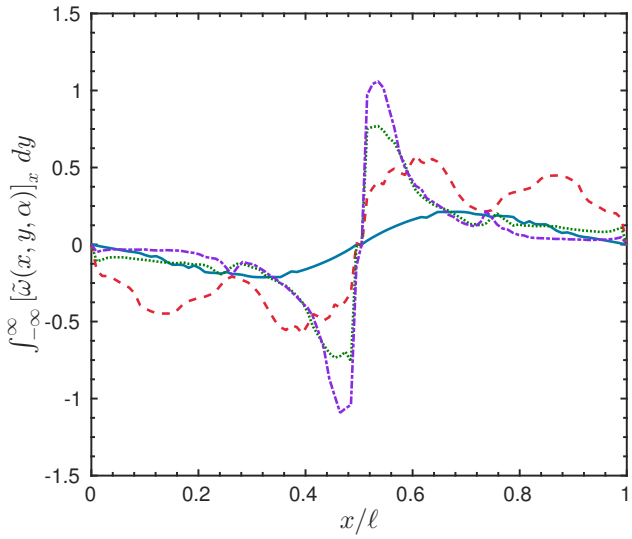

Figure 3.7: Cumulative vorticity along the interface for early, intermediate, and late times. Cumulative vorticity (in y) along the interface, $\int_{-\infty}^{+\infty} \tilde{\omega}(x,y)dy$, where $\tilde{\omega} = \omega$ for $0 < \alpha < 1$ and is otherwise zero (in pure water or air), at $t/(\ell/c) = 4.75$ (blue, solid), 47.5 (red, dashed), 475 (green, dotted), and 1424 (purple, dashed-dotted).

is smooth and nearly sinusoidal, as expected (Samtaney & Zabusky, 1994). During the phase reversal process, the vorticity peaks move toward $x/\ell = 0.5$. Given the geometry at the time when the rarefaction arrives, a second peak in the vorticity distribution is observed near $x/\ell = 0.0, 1.0$ at $t/(\ell/c) = 47.5$. Though apparently fainter in the contour plots, the vorticity is clearly concentrated near the spike, driving the heavy fluid into the light one.

For a more quantitative global measure of vorticity, we consider the circulation produced in the right-half domain (the left is equal and opposite by symmetry) for the baseline case in Figure 3.8. The same times at which different stages of the incoming trapezoidal pressure wave first encounter the interface are indicated on this figure. From t_1 to t_2 (during the interaction of the compression with the interface), positive vorticity (circulation) is deposited given the direction of the density and pressure gradients. This circulation increase is linear since the pressure and density gradients are constant over the interaction interval. Other than small changes due to transverse wave reflections, the circulation remains essentially constant until t_3, at which point the leading edge of the rarefaction encounters the interface. Since the phase has reversed at t_p, the deposited vorticity is of the same sign (i.e., positive) as that deposited by the compression, such that the circulation

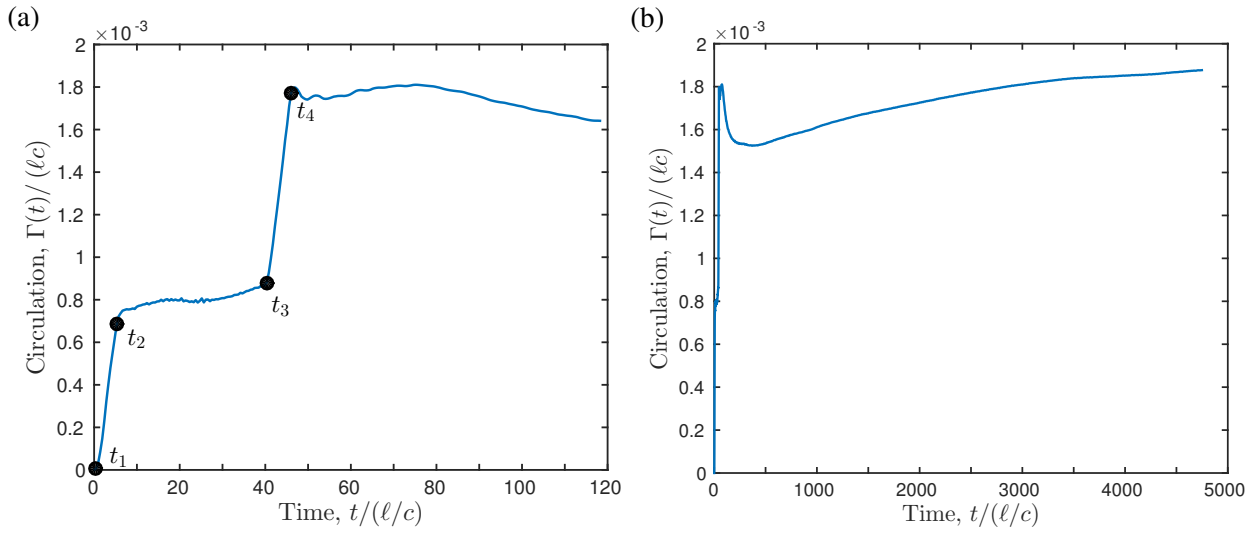

Figure 3.8: Circulation history for the right-half domain for the baseline $p_a = 10$ MPa, $L = 45\ell$ trapezoidal wave case. $t/(\ell/c) \leq 120$ (a) and $t/(\ell/c) \leq 5000$ (b). In (a), times at which different stages of the incoming trapezoidal pressure wave first encounter the interface are indicated as t_1: the compression; t_2: the constant elevated pressure p_a; t_3: the rarefaction; t_4: the return to ambient pressure.

approximately doubles by the time the trailing end of the rarefaction arrives at t_4. Thereafter, any changes in vorticity after this point, are no longer due to the primary incoming wave. The decrease in circulation observed after the wave passage is due to the intersection of the transverse reflections of the rarefaction (now compressions) near the bubble, while the late-time increase is attributed to the acceleration of the heavy fluid into the light one as the spike penetrates the air, which is a form of secondary baroclinic vorticity generation (Peng *et al.*, 2003).

3.4.2 Dependence of the perturbation growth on the wave amplitude

3.4.2.1 General Observations

Since the perturbation growth is driven by residual baroclinic vorticity deposited by the interaction of the ultrasound wave with the interface, it follows that the growth rate increases if more vorticity is deposited. Thus, holding all other parameters fixed, we anticipate the perturbation amplitude growth rate to increase with increasing wave amplitude given that the baroclinic term is

Table 3.1: Circulation during the wave-interface interaction.

	$\Gamma(t_i)/(\ell c) \times 10^3$			
p_a (MPa)	t_1	t_2	t_3	t_4
5.0	0	3.3	3.8	2.9
7.5	0	5.0	6.0	8.7
10.0	0	6.8	8.8	18.0
12.5	0	8.5	11.9	30.5

proportional to the pressure difference. This behavior is confirmed by Figure 3.9, which shows the amplitude and circulation histories for wave amplitudes ranging from 5.0 to 12.5 MPa; to help analyze the results, Table 3.1 lists the circulation at times t_{1-4}. As expected, after the initial transient, the late-time growth rate increases with increasing pressure amplitude. The circulation at the different t_i follow a consistent behavior, as the values increase with increasing pressure amplitude. At t_2, we observe that the circulation deposited by the compression increases at a nearly constant rate with pressure amplitude, consistent with the fact that the time rate of change of the circulation is proportional to the baroclinic term, itself proportional to the pressure difference. From t_2 to t_3 and t_3 to t_4, the rise in circulation generally increases with increasing amplitude, except for the 5 MPa wave between t_3 to t_4. In this latter case, there is a decrease in circulation, due to the fact that phase inversion has not occurred by the time the rarefaction encounters the interface. After t_4, we observe that both the decrease and late-time rise in circulation depend on the pressure amplitude; greater amplitudes lead to greater changes. In the 12.5 MPa case, the circulation appears to decrease at very late times ($t \geq 4000$). This behavior is caused by round-off level errors accumulating over the course of this long simulation, thus breaking the left-right symmetry of the simulation (Movahed & Johnsen, 2013).

3.4.2.2 Late time scaling of the perturbation amplitude

The smooth and monotonous behavior of the perturbation amplitude growth suggests that a more general scaling describing its dependence on the pressure amplitude may exist. Clearly, the perturbation growth is related to the circulation Γ. As the perturbation grows, the vorticity redistributes

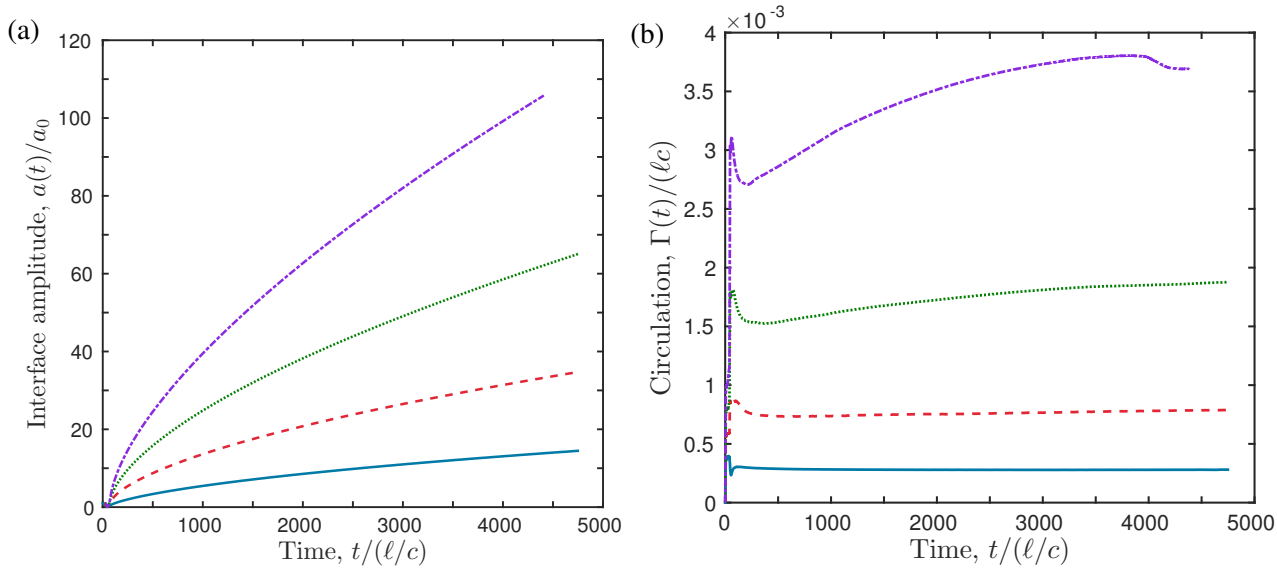

Figure 3.9: The interface amplitude and circulation for long time and multiple wave amplitudes. Histories of the interface perturbation amplitude (a) and circulation (b) for trapezoidal wave cases with $L = 45\ell$, $p_a = 5.0$ (blue, solid), 7.5 (red, dashed), 10.0 (green, dotted), and 12.5 (purple, dashed-dotted) MPa, for $t/(\ell/c) \leq 5000$.

itself along the interface, such that dependence on the interface length s and the initial wavelength ℓ are expected. Finally, given that the waves traverse the interface over a finite duration, dependence on the sound speed c is expected. Thus, the dependence of the amplitude on these variables can be formulated as a dimensional analysis problem:

$$a(t) = f(\Gamma, s, \ell, c; t) \quad \Rightarrow \quad \frac{a(t)}{\ell} = G\left(\frac{\Gamma}{\ell c}, \frac{s}{\ell}; \frac{t}{\ell/c}\right), \tag{3.9}$$

where ℓ and c are used for non-dimensionalization. We note that there is likely an Atwood number dependence, but since the density fields do not significantly change we ignore this parameter here. Well after the wave passage (e.g., for $t \gtrsim 500$), the circulation no longer changes significantly (except perhaps in the $p_a = 12.5$ MPa case, where the circulation changes up to approximately 30%), as there is no dominant mechanism to affect it. However, as the interface deforms and elongates (i.e., $s(t)$ increases), the vorticity gets redistributed along the interface. The circulation density Γ/s is thus a relevant quantity describing the vortex dynamics (Pozrikidis, 2000). As observed in

Section 3.4.1.2, the baroclinic vorticity is the dominant contributor to the interface perturbation growth after t_Γ. Thus, we expect the perturbation amplitude to depend on the circulation density at this time, which we define $\Gamma(t_\Gamma)/s(t_\Gamma) = \Gamma_0/s_0$. It therefore follows that

$$\frac{a(t)}{\ell} = F\left(\frac{\Gamma_0}{s_0 c}, \frac{tc}{\ell}\right). \tag{3.10}$$

Finally, we hypothesize that the perturbation growth scales linearly with the circulation density, such that

$$\frac{a(t)}{\ell} = \frac{\Gamma_0}{s_0 c}\mathcal{F}\left(\frac{tc}{\ell}\right). \tag{3.11}$$

To verify this hypothesis, we plot the perturbation amplitude $a(t)$ scaled by the circulation density at t_Γ in Figure 3.10. To facilitate the comparison, the time origin has been shifted by t_p such that the instant the phase inversion occurs has been synchronized for all cases. Two observations stand out. First, the scaled growths collapse onto what appears to be a single curve. Second, this curve appears to asymptote to a constant slope exhibiting a power-law behavior, i.e., $\mathcal{F} = (tc/\ell)^n$. To compute n, we write

$$\ln\left[(a(t-t_p)/\left(\frac{\Gamma_0}{s_0}\frac{\ell}{c}\right)\right] = b + n\ln\left[(t-t_p)/(\ell/c)\right], \tag{3.12}$$

where t_p is still the time of phase reversal and b is the $y-$intercept of the best fit line, which depends on the value of $a(t-t_p)/\left(\frac{\Gamma_0}{s_0}\frac{\ell}{c}\right)$ when the interface growth becomes asymptotic. Using data from $(t - tp) \geq 2000$, we perform a linear regression analysis to determine the best fit values for n in a least squares sense. We find that $n \approx 3/5$, as illustrated in Table 3.2. Though difficult to distinguish in Figure 3.10, the $p_a = 12.5$ exhibits a slightly higher time exponent, with n closer to $2/3$; this discrepancy may be due to the fact that circulation, even at late times, still grows in a non-negligible fashion in this case. We note however that this amplitude falls beyond those typically used in clinical diagnostic ultrasound. We should also point out that grid independence is

Table 3.2: Interface amplitude growth time exponents, $\frac{a(t)}{\ell} \sim t^n$

p_a (MPa)	$n(t \geq 2000)$
5.0	0.61
7.5	0.59
10.0	0.61
12.5	0.66

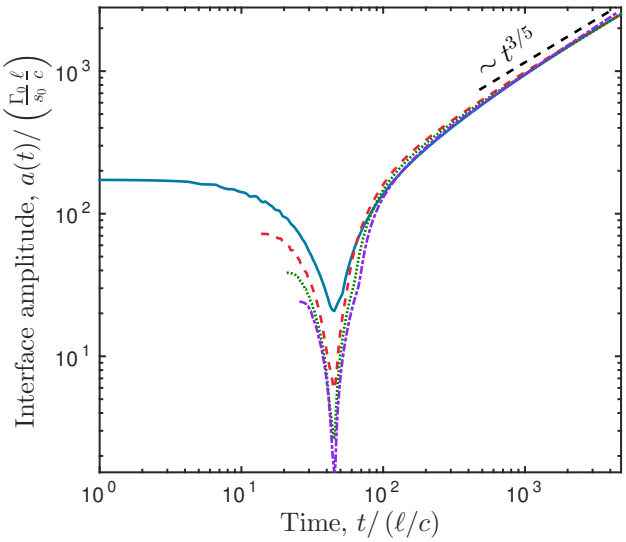

Figure 3.10: Interface amplitude scaled by circulation density at t_Γ. For the trapezoidal wave cases with $L = 45\ell$, $p_a = 5$ (blue, solid), 7.5 (red, dashed), 10 (green, dotted), and 12.5 (purple, dashed-dotted) MPa. Time is synchronized based on phase inversion. Black dashed line: power-law growth as $t^{3/5}$.

not achieved on the current grid, such that the actual value of the exponent may change slightly as finer grids are used; on the other hand, the collapse of the data does not appear to depend on the grid spacing. As we are only considering the small perturbation case here $a_0/\ell \ll 1$, the dependence on the initial perturbation amplitude a_0 is not considered here. Because the angle of misalignment between the density and pressure gradients is small, vorticity changes should scale linearly with small changes in this angle that arise from varying a_0, such that the above analysis should hold (see Appendix A.1). As larger changes in a_0 would effect the morphology of the interface throughout its interaction with the wave, the effects of a_0 are not immediately obvious.

3.4.2.3 Late time scaling of the interfacial length

The tenfold to hundredfold perturbation amplitude growth is accompanied by a corresponding increase in interfacial length s. This quantity is important for the dynamics of the vortex sheet produced along the interface by the ultrasound passage (Pozrikidis, 2000); vortex sheet dynamics have in fact been explored in the context of the Rayleigh-Taylor instability (Tryggvason, 1988). In such analysis, the quantity of interest is the circulation density Γ/s. We expect this quantity to depend on the wave amplitude p_a, the initial wavelength ℓ, the density and sound speed of the liquid, ρ and c, respectively. Following a dimensional analysis process similar to that in the previous section, we find that the inverse of the circulation density (in other words: the interfacial length scaled by instantaneous circulation) bears the following dependence on the relevant dimensionless parameters:

$$\frac{s(t)}{\Gamma(t)}c = \psi\left(\frac{p_a}{\rho c^2}, \frac{tc}{\ell}\right). \tag{3.13}$$

Given that the growth is baroclinic, we hypothesize that the circulation scales linearly with pressure amplitude, such that

$$\frac{s(t)}{\Gamma(t)/c} = \frac{\rho c^2}{p_a} f\left(\frac{tc}{\ell}\right). \tag{3.14}$$

To determine the time dependence of the interfacial length, we plot in Figure 3.11 the time histories of the interfacial length and scaled interfacial length. Again, time is synchronized based on phase inversion. As for the amplitude, the growth rate of the length increases with pressure amplitude. Furthermore, with the exception of the $p_a = 5$ MPa case, our simple scaling collapses the interfacial length onto a single curve after a sufficiently long time ($t \gtrsim 500$). The collapsed curve exhibits a power-law dependence on time $f = (tc/\ell)^m$, where $m \approx 1/2$ for $p_a = 7.5$, 10 and 12.5 MPa. This scaling confirms that the interfacial deformations are governed by the dynamics of the vortex sheet produced by the ultrasound interaction. The result from the $p_a = 5$ MPa case does not follow the

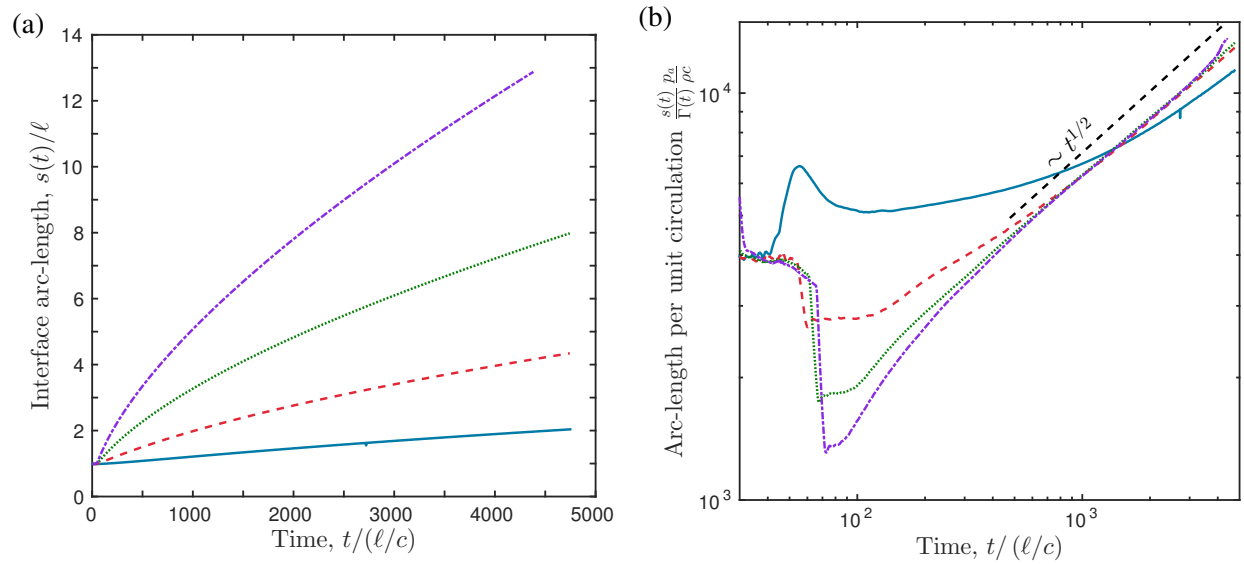

Figure 3.11: Histories of the interfacial length (a) and scaled interfacial length (b). For the trapezoidal wave cases with $L = 45\ell$, $p_a = 5$ (blue, solid), 7.5 (red, dashed), 10 (green, dotted), and 12.5 (purple, dashed-dotted) MPa. Time is synchronized based on phase inversion. Black dashed line: power law growth as $t^{1/2}$.

same behavior for two main reasons. First, the rarefaction encounters the interface during phase inversion, at which point the interface is essentially flat. Thus, the vorticity contribution is negligible; nevertheless, the rarefaction accelerates the interface and increases its length, thus decreasing the circulation density. As a result, the geometry at t_p is different from that observed in the other cases. Second, s/Γ has yet to achieve its asymptotic behavior. However, running the simulation to asymptotic behavior would be prohibitively expensive from a computational standpoint.

We highlight the different dependence of the perturbation amplitude and interfacial length on circulation. The growth of the former is dictated by the geometry and the amount of circulation at the end of the interaction. Thus, the instantaneous circulation at that time is sufficient to describe the growth. On the other hand, the interfacial length depends on the details of the vortex sheet dynamics. Thus, the interfacial length is sensitive to the instantaneous circulation and in fact local vorticity.

3.4.3 Dependence of the growth on the wave duration

The results from the previous sections indicate that the interface morphology during the interaction of the rarefaction, at the end of the trapezoidal wave, with the interface plays a key role in the dynamics. If the interface has undergone phase inversion by the time the rarefaction has arrived, vorticity of the same sign as that due to the compression is deposited, thus enhancing the growth. On the other hand, if the rarefaction arrives before the phase has inverted, vorticity of the opposite sign is deposited and counteracts the vorticity initially deposited by the compression. In the limit where the rarefaction immediately follows the compression, zero net vorticity would be deposited *only if the interface has not deformed*, thus leading to no growth. The amount of baroclinic vorticity deposited by the rarefaction depends on the interface morphology at the time of interaction, described by the sine of the angle between density and pressure gradients, such that the effect of the rarefaction on the interface perturbation growth depends heavily on the time-dependent features of the wave. To examine this behavior, we hold the pressure amplitude constant at $p_a = 10$ MPa and vary the time (or length L) between the compression and rarefaction. The corresponding amplitude and circulation histories are shown in Figure 3.12. For the two longest waves, $L = 35\ell$ and 45ℓ, the rarefaction encounters the interface well after phase inversion. In these cases, the rarefaction deposits additional vorticity of the same sign as that due to the compression (e.g., positive vorticity in the right side of the domain) and enhances growth. For the $L = 30\ell$ case, the rarefaction impinges upon the interface shortly after the interface phase-reversal, when the interface is nearly flat. As a result, the pressure and density gradients are nearly aligned and little additional circulation is generated. Thus the growth is driven purely by the circulation deposited by the compression. For shorter waves ($L \leq 25\ell$), the rarefaction encounters the interface before the perturbation reverses phase, thus reducing the circulation. Among cases for which the interface inverts phase before encountering the rarefaction, the larger the instantaneous perturbation amplitude at the time of the rarefaction, the greater the circulation generated, since the average angle between the density and pressure gradients is greater. The same is true when comparing cases for which the interface inverts

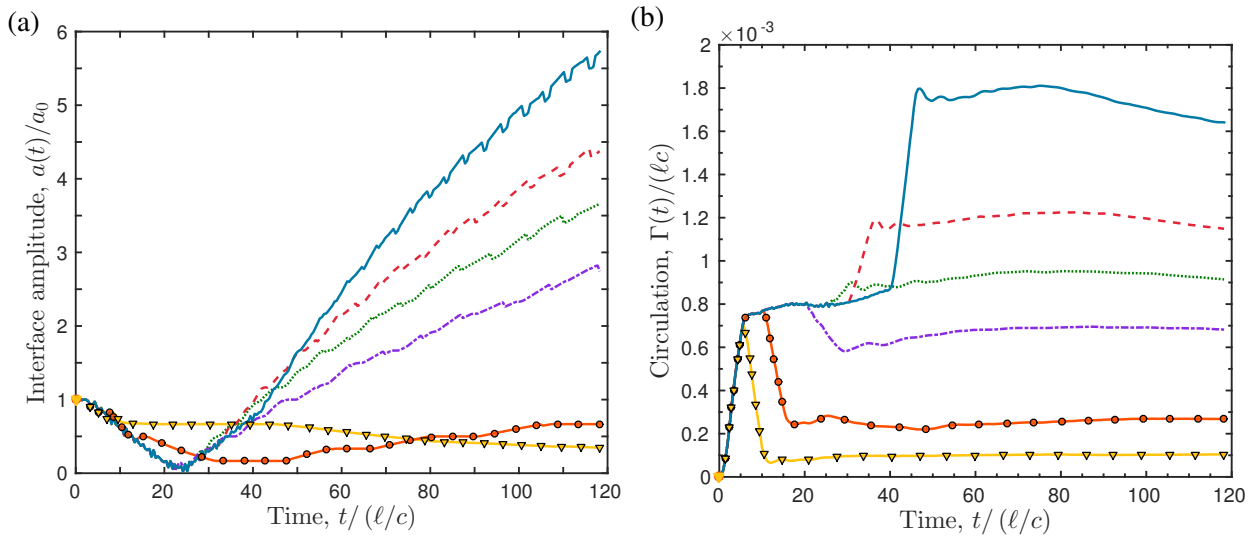

Figure 3.12: The interface and circulation dependence on wave duration. Interface amplitude (a) and circulation (b) histories for the $p_a = 10$ MPa trapezoidal wave case with $L = 45\ell$ (blue, solid), 35ℓ (red, dashed), 30ℓ (green, dotted), 20ℓ (purple, dashed-dotted), 15ℓ (orange, with circles), 10ℓ (yellow, with triangles).

its phase before encountering the rarefaction.

These results suggest that by appropriately modulating the incoming wave the perturbation growth can be controlled. This observation is particularly important for waves for which the pressure returns to its ambient value after the wave passage, which is the case for acoustic waves in general by contrast to the conventional shock-accelerated (Richtmyer-Meshkov (RM) instability) problem.

3.5 Conclusions

We investigated the interaction of an acoustic wave propagating in a liquid and impinging upon a perturbed liquid-gas interface, as a model for wave-interface interaction with alveoli, in consideration of lung hemorrhage. Despite selecting a simplified, yet relevant waveform (trapezoidal, symmetric in time, returns to ambient conditions after pressure rise) to facilitate the analysis, the results are generalizable to more complex, continuous ultrasound waveforms. For waveform parameters relevant to the application, we observed that acoustic waves in water lead to interface

perturbation phase inversion, followed by perturbation growth to amplitudes many times larger than the initial value well after the wave passage. We further characterized the dependence of the perturbation growth on the wave amplitude and length.

We demonstrated that the mechanism driving the perturbation growth is the torque generated by the misalignment of the pressure and density differentials during the wave interaction, manifested by the production of baroclinic vorticity along the interface. This effect, usually higher-order in acoustics, is dominant in our problem due to the substantial pressure difference over a short length (megapascals over millimeters), and the nearly discontinuous density profile. Although the symmetric nature of the wave may suggest that vorticity deposited by the compression should be exactly canceled by that produced by the rarefaction, such an argument overlooks the transient nature of the process, namely the fact that the baroclinic torque drives the interface to deform during the passage of the compression, during the time when the pressure amplitude is kept high, and during the passage of the rarefaction. As a result, the alignment between the pressure and density gradients is different during the passage of the rarefaction, compared to that produced by the compression. This result can be generalized to state that, except for very special cases, waves interacting with an interface over a finite duration and producing interface deformation generate net baroclinic vorticity, whether the wave is symmetric in time or not.

An immediate consequence of the problem of interest is the observation of two perturbation growth regimes, depending on whether phase inversion has occurred by the time when the rarefaction reaches the interface. If the phase has inverted, vorticity of the same sign as that deposited by the compression is produced, thus leading to enhanced growth; conversely, if phase has not yet inverted, vorticity of the sign opposite that deposited by the compression is produced, thus leading to reduced growth. Varying the amplitude and length of the wave can push the dynamics from one regime to the other. We also note that at sufficiently high amplitudes the late time perturbation growth obeys a power-law scaling. By considering the evolution of the interfacial length and the vorticity redistribution along the interface, we found that this result is consistent with a vortex-sheet-based description of the interface dynamics. Finally, the dependence of the results on the

wave length suggests that perturbation growth may be controlled by modulating the waveform.

This work is a step toward a fundamental understanding of the effects of acoustically generated vorticity along liquid-gas interfaces. The results suggest that significant strains may be imposed upon the interface. To directly relate these findings to ultrasound-induced lung hemorrhage, however, a more comprehensive description of the tissue-lung rheology (viscoelastic properties) and geometry is required, along with the use of application-specific waveforms.

CHAPTER 4

Pulsed ultrasound-induced stresses and strains at gas-liquid interfaces

In Chapter 3 we introduced the problem of Diagnostic Ultrasound (DUS)-induced lung hemorrhage, however, the focus was on the fundamental physical problem of an acoustically driven gas-liquid interface, such as those of the alveoli. In this chapter, we aim to extend that work to increase its relevance to DUS of the lung. Here, we hypothesize that real DUS waves may be capable of generating sufficient baroclinic vorticity at alveolar interfaces in the lung to drive deformation and hemorrhage. To investigate this hypothesis we again model the alveolus as a perturbed water-air interface and examine the dynamics when driven by ultrasound pulses with clinically relevant parameters. We compare the interface evolution to that expected of a vorticity driven interface based on the work of Chapter 3. Furthermore, we infer the viscous stress and calculate the approximate strain at the interface and compare computed values to expected alveolar damage thresholds, based on previous published research.

4.1 Abstract

DUS-induced lung hemorrhage in mammals is the only known biological effect of non-contrast diagnostic ultrasound. Despite years of study, the underlying physical mechanism remains unknown. In this work we model the interaction between an ultrasound pulse and an alveolus as an acoustic wave in water propagating toward a water-air interface. To capture the alveolar surface rough-

ness the interface contains a single-mode sinusoidal perturbation, representing the alveolar surface roughness, of variable initial amplitudes equal to 3, 10, and 30% of the perturbation wavelength, which represents the alveolar diameter. By solving the Euler equations of fluid motion we study the evolution of the interface for 1.5 MHz ultrasound with peak amplitudes of 1.0, 2.5, and 5.0 MPa. The interface is observed to continue deforming long after the passage of the wave. Interfacial strains of up to 38% after 288 μs. Viscous stresses are estimated and maximum amplitudes are found to be on the order of 10 Pa. For a 10 MPa pulse, interface perturbation amplitudes are shown to grow approximately as $t^{3/5}$, which is expected of vorticity-driven growth based on the work of Chapter 3.

4.2 Introduction

Lung Ultrasound (US) has become a common tool for imaging and diagnostics in critical and point-of-care situations and its use is growing (Lichtenstein, 2009). Currently, Pulmonary Capillary Hemorrhage (PCH) is the only biological effect known to occur in mammals as a result of non-contrast diagnostic ultrasound. It has been shown to occur under clinically acceptable parameters with Mechanical Index (MI)$\leq$ 1.9 (FDA, 1997) and peak pressures as low as 1.0 MPa (Dalecki *et al.*, 1997). The physical mechanism underlying this damage is still not well understood. While the occurrence of hemorrhage as a result of diagnostic lung US has not been directly studied in human lungs for obvious ethical reasons, an understanding of the underlying cause is important for the development of evidence-based safety guidelines and regulations.

US-induced Lung hemorrhage (LH) is not a new problem. It was first discovered in mice over twenty years ago (Child *et al.*, 1990). And since then, there has been considerable work to progress our understanding. Much of this previous research has primarily aimed at three specific ends: (1) investigating the physical damage mechanism causing the hemorrhage; (2) determining the dependence of damage characteristics and bioeffects thresholds on the US properties; and (3) determining the dependence of damage characteristics and thresholds on the characteristics of

the US subject. This study aims to contribute to the first of these areas: we aim to estimate the potential stresses and strains imparted by a single ultrasound pulse on a perturbed liquid-gas interface, similar to that of a single alveolus. To do this we will extend the computational fluids model of an US-driven alveolus developed in Chapter 3 to include US pulse-like waveforms and interface geometries with larger perturbation amplitudes than previously considered, which are more representative of physical alveoli.

In Chapters 1 and 3, a portion of the body of past research into the physical mechanisms of DUS was reviewed, so only a brief summary is provided here. US-induced pulmonary hemorrhage is characterized by alveoli filling with blood as well as plasma proteins and erythrocytes (Miller, 2016a; Penney *et al.*, 1993). Alveolar edema or frank hemorrhage has also been shown to occur as a result of mechanical stress failure of the alveolar membrane induced by over pressure (West *et al.*, 1991). The cause of DUS-induced hemorrhage in the lungs appears mechanical in nature and thermal mechanisms appear unlikely to cause the observed damage (Zachary *et al.*, 2006; Dalecki, 2004). Cavitation, acoustic radiation force, resonance, and acoustic fountaining or atomization have all been studied as possible mechanical damage mechanisms for DUS-induced LH (Holland *et al.*, 1996; Miller, 2016a; Jabaraj & Jaafar, 2012, 2013; Jabaraj & S., 2013; Tjan & Phillips, 2007; Simon *et al.*, 2012). Experimental results suggest that the most common mechanical ultrasound bioeffect mechanism, cavitation, is unlikely, and for reasons detailed in the previous chapters, none of the remaining mechanisms completely explains the damage (O'Brien *et al.*, 2000b; Raeman *et al.*, 1996; Miller, 2016a).

Research investigating the dependence of US-induced LH on the characteristics of the US subject has considered species, age, physiological development, and pulmonary state of the US subject. Within mammals, the occurrence of DUS-induced LH has been observed to be largely species-indiscriminate and has been found to occur in mice, pigs, rats, rabbits, and monkeys (Baggs *et al.*, 1996; Child *et al.*, 1990; Dalecki *et al.*, 1997; Frizzell *et al.*, 1994, 2003; Harrison *et al.*, 1995; Holland *et al.*, 1996; Kramer *et al.*, 2001; O'Brien & Zachary, 1997; O'Brien *et al.*, 2001a, 2003a, 2005, 2000b, 2001c; Penney *et al.*, 1993; Raeman *et al.*, 1993, 1996; Taran-

tal & Canfield, 1994; Zachary & O'Brien, 1995; Zachary *et al.*, 2001a,b). Dalecki *et al.* (1997) subjected neonatal, juvenile, and adult mice to pulsed ultrasound of the lung and observed that while hemorrhage thresholds were similar in all mice, the degree of hemorrhage was much greater in the adult mice than in the younger subjects. Similarly, O'Brien *et al.* (2003a), studied the age dependence of hemorrhage in pigs, and found that older pigs had a significantly lower hemorrhage thresholds than juvenile and middle-aged pigs. In an unexpected result, the study also found that if one lung was exposed to US and the pig was then rolled over and the second lung exposed, the hemorrhage threshold in the second lung was substantially lower than in the first. To study the dependence of hemorrhage on the impedance boundary condition at the lungs pleural surface, O'Brien *et al.* (2002) subjected rats with variable degrees of lung inflation to 3.1 MHz pulsed US with Peak Rarefaction Pressure Amplitude (PRPA) = 8.6, 16 MPa. It was found that deflated lungs, which had less impedance mismatch with their surroundings, were more easily damaged than partially deflated lungs, which were more easily damaged than inflated lungs. While no direct experimentation has been performed on humans, for obvious ethical reasons, Meltzer *et al.* (1998) found that transesophageal echocardiography with similar US parameters to those causing lung hemorrhage in animal studies (3.1 MHz, PRPA= 2.4 MPa) did not lead to visible hemorrhage on the surface of the lung. While DUS-induced LH has not been shown to occur in humans, its occurrence in a wide variety of mammals under diagnostically relevant conditions suggests a need for further investigation.

The body of research investigating the dependence of lung hemorrhage on US properties is extensive and has investigated the dependence of hemorrhage occurrence and severity on a wide variety US parameters. Zachary & O'Brien (1995) used continuous-wave and pulsed-wave US in mice, rabbits, and pigs, and found that continuous- and pulsed-wave-induced lesions appear macroscopically similar, but differed microscopically. Hemorrhage induced by continuous wave US consisted primarily of plasma and contained some cells, whereas pulsed-wave induced hemorrhage was composed mostly of cells and contained little plasma. Raeman *et al.* (1996) subjected mice to 2.3 MHz pulsed US with peak pressures up to 3 MPa and varying exposure time and

found that while threshold amplitudes appeared insensitive to exposure time, suprathreshold damage increased with increasing exposure. In a review of previous work, Miller (2016a) indicated that previously observed differences in bioeffects thresholds between studies may be attributable to exposure duration differences. O'Brien *et al.* (2001b) investigated the effects of US beamwidth and found that for rats subjected to 2.8 and 5.6 MHz ultrasound, incidence, surface area, and volume of hemorrhage increased with increasing beamwidth. It was noted that lung hemorrhage is perhaps the only known beamwidth-dependent mechanical bioeffect of US. O'Brien *et al.* (2003b) found evidence that increasing US pulse duration decreases the PRPAs threshold associated with a 5% likelihood of lung hemorrhage in rats subjected to 2.8 MHz ultrasound with peak amplitudes ranging from 4-9 MPa. Given that the dependencies of bioeffects on waveform amplitude and frequency are not fully understood, we consider the dependence of the alveolar wall dynamics on acoustic wave amplitude.

Separately, the structure, mechanical behavior, and failure properties of alveoli have been studied extensively and are of particular interest to the present work. The alveoli can be thought of as a network of openly connected, air-filled saccules with distinctly irregular surfaces. Past research suggests that alveolar size is species dependent (Faffe *et al.*, 2002). While alveoli are not perfect spheres, their mean diameters range from tens to hundreds of microns, with reported values of 45 μm in mice and 200 μm in adult humans (Knust *et al.*, 2008; Ochs *et al.*, 2004). The septa separating adjacent alveoli are nearly planar structures that contain several tissue layers and are coated with a thin layer of liquid surfactant (Gil *et al.*, 1979; Reifenrath, 1975; Perlman & Wu, 2014). Within the alveolar septa surrounding the alveoli, are the pulmonary capillaries, a sheet-like web which is almost completely unsupported by surrounding tissue (West *et al.*, 1991). Separating the blood from the air is a multi-layer wall of tissues, 0.2 - 0.3μm thick, referred to as the blood-gas or blood-air barrier (West, 2000). West *et al.* (1991) raised the pulmonary capillary pressure of anesthetized rabbits and observed consistent stress failure of the capillary and alveolar epithelium for transmural at or above 40 mmHg (5.3 kPa). It was observed that failure corresponded to approximately 25 mN/m wall tension in the capillaries, and noted that "this tension is small, comparable

with the tension in the alveolar wall associated with elastic recoil." The capillary wall stress at failure was calculated to be approximately 8 kPa. Alveolar wall strain has also been studied and linear, alveolar strain due to normal tidal breathing is reported to range from 0 – 5% for humans (Roan & Waters, 2011). Belete *et al.* (2010) found that when subjected to cyclical linear stretch at 0.5 Hz for 30 minutes, rat alveolar epithelial cells experiencing linear strains of 8% or greater were frequently damaged, whereas those experiencing strains of 3 – 6% were often undamaged.

This work is the first to use a fully nonlinear, Euler-based computational fluids approach to study the dynamics of an alveolus driven by a single ultrasound pulse. Extending the alveolar model of Chapter 3, we perform numerical experiments to simulate the dynamics of gas-liquid interfaces driven by ultrasound pulse waveforms within the clinically relevant range. Using simple models, we approximate the linear interfacial strain and infer viscous stress at the interface, which we compare to alveolar failure criteria from relevant literature. Additionally, we compare the interface evolution to that expected of a vorticity-driven growth of interfacial perturbation, based on our past work (Patterson & Johnsen, (In preparation), 2017).

4.3 Methods

Much of the basic problem setup and computational framework detailed in Chapter 3 are reused here. In this section we briefly summarize the model and then focus specifically on three specific areas where changes have been to better suit our focus on DUS-induced LH: (1) problem geometry, (2) incoming waveform, (3) calculation of stress and strain.

v

In the previous chapter, we simulated trapezoidal acoustic waves impinging upon a nearly planar interface with a sinusoidal perturbation. The width of the domain represents a single alveolar diameter, $\ell = 200\mu$m in adult humans (Ochs *et al.*, 2004), which is also the wavelength of the perturbation. The initial perturbation amplitude used $a_0 = 0.03\ell$, implies a nearly flat alveolar surface, which is not always the case, as can be seen in the histological cross section of alveoli

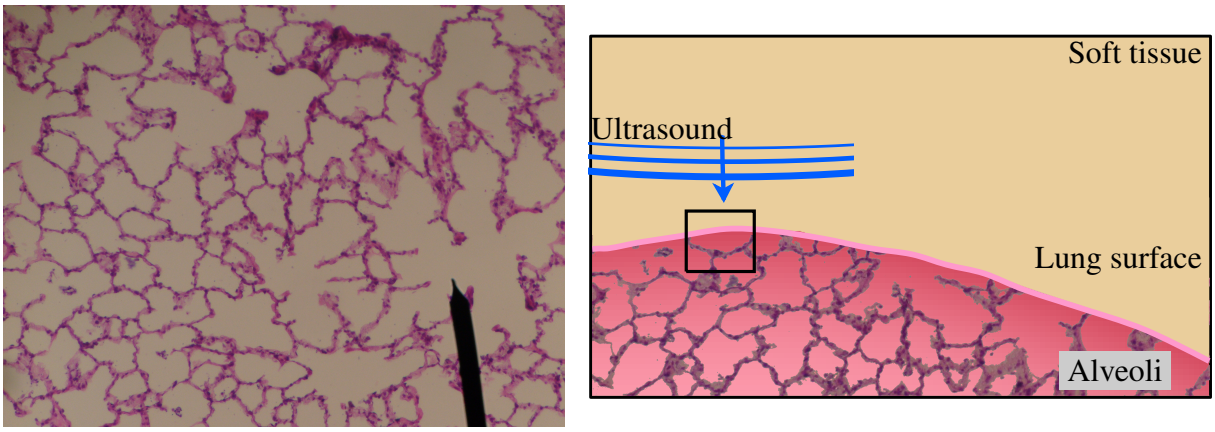

Figure 4.1: A histological cross section of alveoli (Left). A schematic of ultrasound impinging upon the lung surface and alveoli, from the surrounding soft tissue (Right). A black box surrounds an alveolar surface, which schematically illustrates the physical problem upon which the initial condition is created.[Alveolar cross section adapted from work by Jpogi [CC BY-SA 4.0 (http://creativecommons.org/licenses/by-sa/4.0), via Wikimedia Commons]

shown in Figure 4.1. To account for the variety of geometries in alveolar tissue, many of which are not particularly flat. A typical surface radius of curvature for a human alveolus has been reported as 109 μm (Mercer *et al.*, 1994). We will now consider perturbation amplitudes of $a_0 = 0.03\ell, 0.10\ell$ and $a_0 = 0.30\ell$. We acknowledge that this does not capture the true range of cross-sectional alveolar geometries. However, this simplified geometry, necessitated by computational constraints, will allow for the generalization of the conclusions of this work broadly to relevant geometries. The diagnostic ultrasound pulse waveform, as illustrated in the time domain in Figure 4.2 is modeled as a sinusoidal carrier wave of amplitude p_a and frequency f modulated by a Gaussian Envelope, and as such that the initial pressure condition can be described as,

$$p(y_f, t = 0) = p_a \sin\left(2\pi f \frac{y_f - L}{c}\right) \exp\left(-\frac{\left(\left[y_f - L/2\right] c\right)^2}{FWHM/\left(2\sqrt{2\ln(2)}\right)}\right), \tag{4.1}$$

where $y_f = y - 11a_0$ is the y-location, relative to the initial location of the wave leading end. The carrier wavelength $\lambda = c_{water}/f$ and the full width of the Gaussian envelope at half of the maximum amplitude, or $FWHM$, are designed to scale appropriately with respect to the alveolar length scale $\ell = 200\,\mu$m. Here, we choose design parameters of $f \approx 1.25c/2\pi\ell$ and $FWHM = 15\ell$

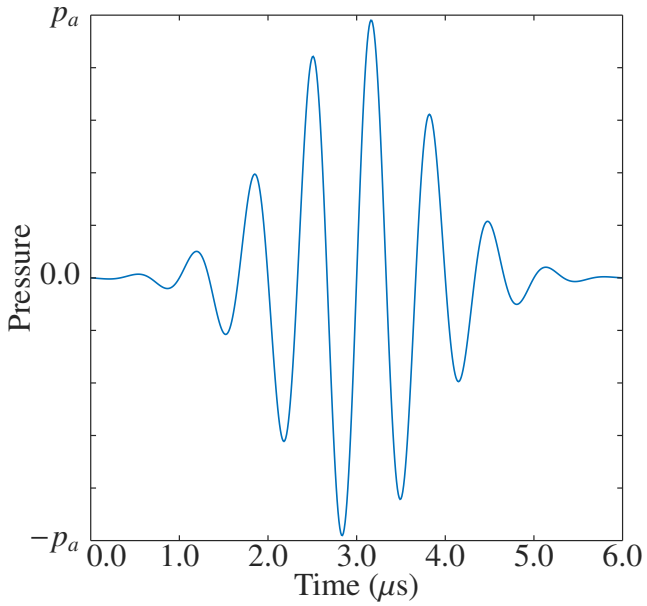

Figure 4.2: Ultrasound pulse waveform

such that the corresponding center frequency is approximately $f = 1.5$ MHz and $FWHM = 3$ mm. Accordingly, the pulse length $L = 45\ell$ is defined such that the pulse duration is approximately 6 μs. In implementation L is the length of the computational domain, over which the wave is defined to exist (i.e., pressure is set to ambient outside the wave region, effectively truncating the ends of the Gaussian envelope). This waveform is an analytical approximation of a true DUS pulse, which allows us to manipulate the parameters of interest.

4.3.1 Stress and strain at the alveolar interface

As previously mentioned, among the tissue layers surrounding the alveoli are the pulmonary capillaries, a sheet-like, blood-filled web, almost completely unsupported by surrounding tissue (West *et al.*, 1991). It is the hemorrhage of these capillaries that interests us, and thus, to interpret the results of the numerical experiments in the context of DUS-induced lung hemorrhage, we will calculate the linear strain and infer the viscous stress at the liquid-gas interface, which represents the alveolar septa, where these capillaries lie. We aim to compare the calculated stresses and strains to relevant injury criteria. We note that from the available strain and strain rate data, it would be possible to infer a total viscoelastic stress at the interface if a constitutive model were known.

However, constitutive models appropriate to this work do not appear available at this time and the development of such models would require experiments far beyond the scope of this work.

Calculation of the viscous stress

Viscous stresses resist motion of the flow, however since the Euler equations, which are inherently inviscid, are solved, we aim to infer the viscous stress resulting from the interfacial motion and deformation. We do this because, while the justifications in Chapter 3 suggest that flow dynamics can be reasonably approximated by neglecting viscosity an understanding of the approximate viscous stress associated with DUS is necessary to understand the results in the context of alveolar injury. To do this we infer the viscosity at each point in space and time as $\mu(x, y, t)$ based on the physical properties of air and water, and the volume fraction of water $\alpha(x, y, t)$ given that $\mu = \alpha\mu_{water} + (1-\alpha)\mu_{air}$. The shear stress in a two-dimensional, Newtonian flow is calculated using the computed viscosity field and the velocity gradients as

$$\tau_{xy}(x, y, t) = \mu\left(\frac{\partial u}{\partial y} + \frac{\partial v}{\partial x}\right), \tag{4.2}$$

where u and v represent the x- and y-components of the velocity. The maximum viscous stress amplitude is extracted from the field at each point in time from our simulations.

Calculation of the interface strain

The linear interfacial strain is calculated as

$$\varepsilon = \frac{s(t) - s_0}{s_0} \tag{4.3}$$

where $s(t)$ is the arc length of the interface, which is initially $s_0 = s(0)$. While some of the large deformations we observe in our results may actually be out of the realm of finite strain, we choose this metric, which is consistent with previous alveolar strain calculations in the literature. For example, Roan & Waters (2011) used the relative change in alveolar diameters, which is analogous

to relative change in the interface arc length here.

4.4 Results and Discussion

To accomplish the aims of this study, two sets of numerical experiments are performed. The first set of experiments is designed to determine the stresses and strains on a perturbed liquid-gas interface, driven by clinically relevant ultrasound pulses. Simulations of interactions between sinusoidally perturbed water-air interfaces and diagnostic ultrasound pulses are performed for wave amplitudes of $p_a = 1.0$, 2.5, and 5.0 MPa and initial perturbation amplitudes of $a_0 = 0.03\ell$, 0.10ℓ and 0.30ℓ. The second set of experiments is designed to test the hypothesis that US pulses are capable of generating sufficient baroclinic vorticity at an air-water interface to drive appreciable interface deformation. For this second set of experiments, which is described in greater detail in Section 4.4.4, we perform simulations of an US pulse-driven gas-liquid interface, with parameters similar to those of the baseline trapezoidal wave in Chapter 3 ($p_a = 10$ MPa, $a_0 = 0.03\ell$, $L = 45\ell$) and compare interface growth dynamics driven by a US pulse to those driven by the trapezoidal wave of Chapter 3.

4.4.1 Qualitative observations of the interface

To illustrate the evolution of the interface, Figures 4.3, 4.4, and 4.5 show density contours for pulse amplitudes of 1.0, 2.5, and 5.0 MPa, respectively, at dimensionless times $t/(\ell/c) = 4.75, 47.5, 475$, and 2374. While these dimensionless quantities are used for comparison of this work to that of Chapter 3, for the sake of physicality, we will report times and stresses in this section as dimensional quantities. As such, for an $\ell = 200$ μm alveolar diameter, these dimensionless times approximately corresponds to dimensional times of $0.6, 6.0, 60$, and 290 μs. In each case, subfigures (a), (b), and (c) correspond to initial perturbation amplitudes of $a_0 = 0.03\ell, 0.10\ell$, and 0.30ℓ respectively; $t = 0.6$ μs occurs just after the wave first encounters the interface and by $t = 6.0$ μs the wave has completely passed. For the $p_a = 1.0$ MPa pulse, the interface remains largely un-

moved and undeformed by the interaction with the wave, even at late times (illustrated in Figure 4.3). For the $p_a = 2.5$ MPa pulse, little deformation is observed for $a_0 = 0.03\ell$, however at higher initial amplitudes ($a_0 = 0.10\ell$ and 0.30ℓ), the interface is clearly deformed at late times and a cusp is observed to form along the interface at $x/\ell = 0.5$ (illustrated in Figure 4.4). For the $p_a = 5.0$ MPa pulse, obvious deformation is observed for all considered values of a_0 (illustrated in Figure 4.5). For $a_0 = 0.10\ell$ and 0.30ℓ, a spike of heavy fluid with a cusp at $x = 0.5$ is again observed to form at late times. For all incoming waves, the degree of deformation appears to increase with increasing initial perturbation amplitude a_0 and wave amplitude p_a. The observed sharp features, which evolved from an initially smooth interface perturbation, could potentially lead to stress concentration, which in alveoli, may lead to hemorrhage.

4.4.2 Interface strain, ε

In consideration of possible strain-related damage of the alveolar wall we examine the linear interface strain $\varepsilon(t)$, as defined in Equation (4.3), and its dependence on wave amplitude p_a and perturbation amplitude a_0. Figure 4.6 shows strain histories $\varepsilon(t)$ for variable $p_a = 1.0$ (blue), 2.5 (red), and 5.0 (green) MPa and constant initial perturbation amplitude $a_0 = 0.03\ell$ (a), 0.10ℓ (b), and 0.30ℓ (c), while Figure 4.7 shows these data re-plotted for variable $a_0 = 0.03\ell$ (blue), 0.10ℓ (red), and 0.30ℓ (green) and constant wave amplitudes $p_a = 1.0$ (a), 2.5 (b), and 5.0 (c) MPa. For all pressure amplitudes p_a and initial perturbation amplitudes a_0, negative strain is observed during and immediately following the wave-interface interaction, indicating a net reduction in interfacial length. This reduction is observed to correspond to the flattening of the interface perturbation during and after the interaction with the acoustic pulse. For the $p_a = 1.0$ MPa wave with all a_0 and the 2.5 MPa wave with $a_0 = 0.03\ell$ and 0.10ℓ, this reduction in interface length is observed to slowly continue at a decreasing rate throughout the duration of the simulation. For the $p_a = 2.5$ MPa wave with $a_0 = 0.30\ell$ and the $p_a = 5.0$ MPa wave with all a_0, a stretching or increase in interfacial length follows the length reduction. Based on Figures 4.4 and 4.5, the increased interfacial length corresponds to the growth of the liquid spike into the gas. It is observed that this deformation and

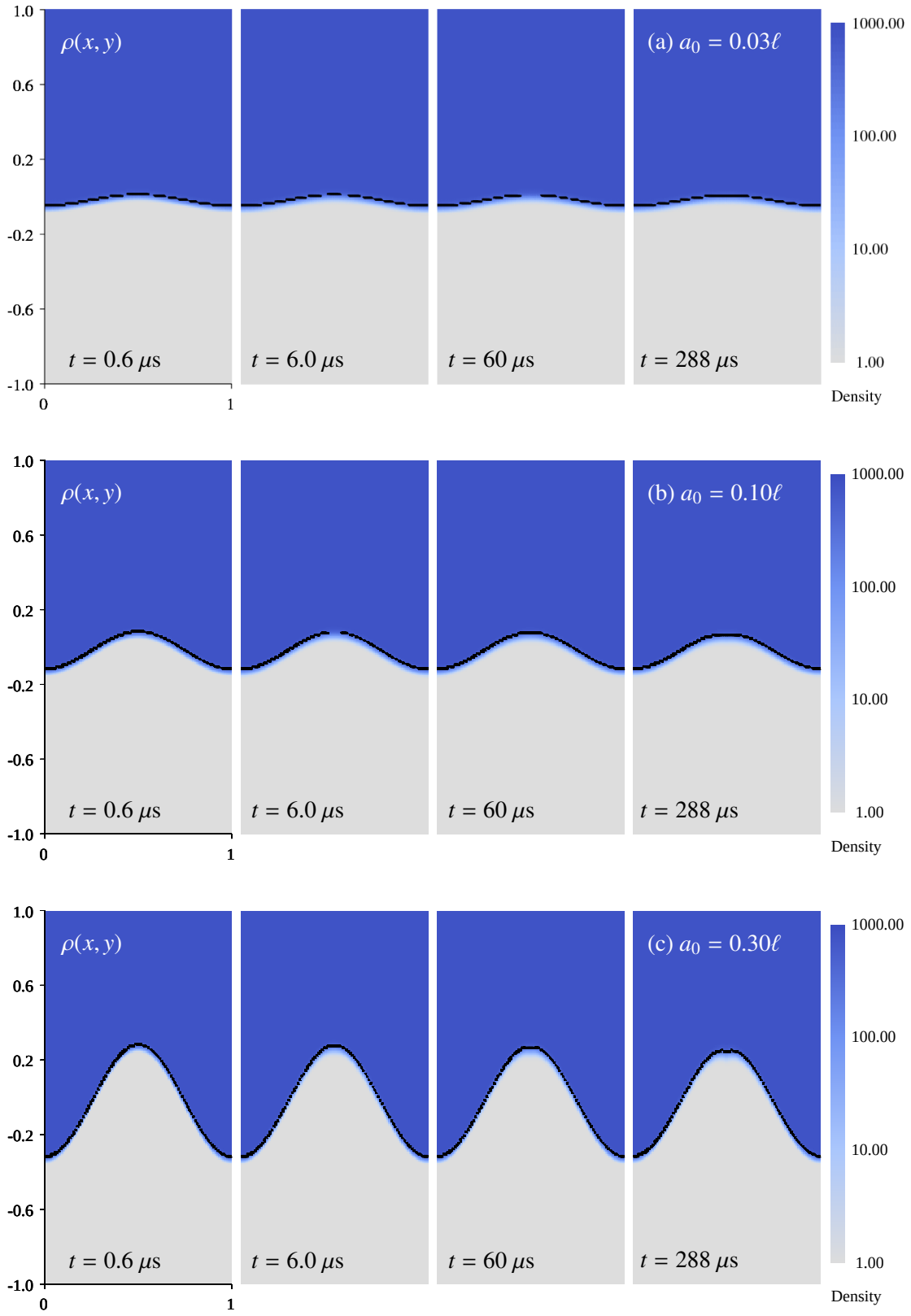

Figure 4.3: Evolution of the interface for $p_a = 1.0$ MPa ultrasound wave. Density contours at $t = 0.6, 6.0, 60$, and 288 μs for initial perturbation amplitudes (a) $a_0 = 0.03\ell$, (b) $a_0 = 0.10\ell$, and (c) $a_0 = 0.30\ell$.

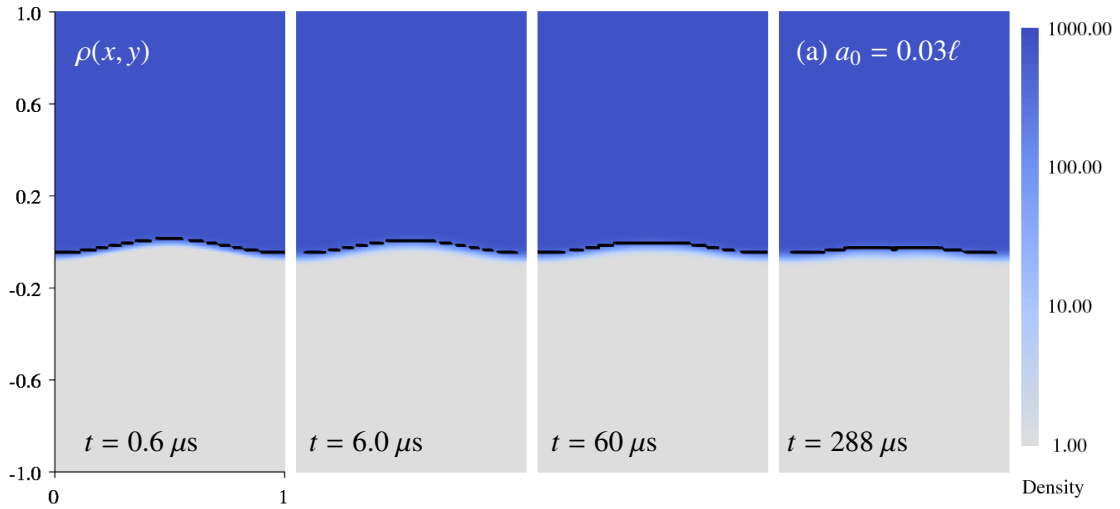

(a) $a_0 = 0.03\ell$

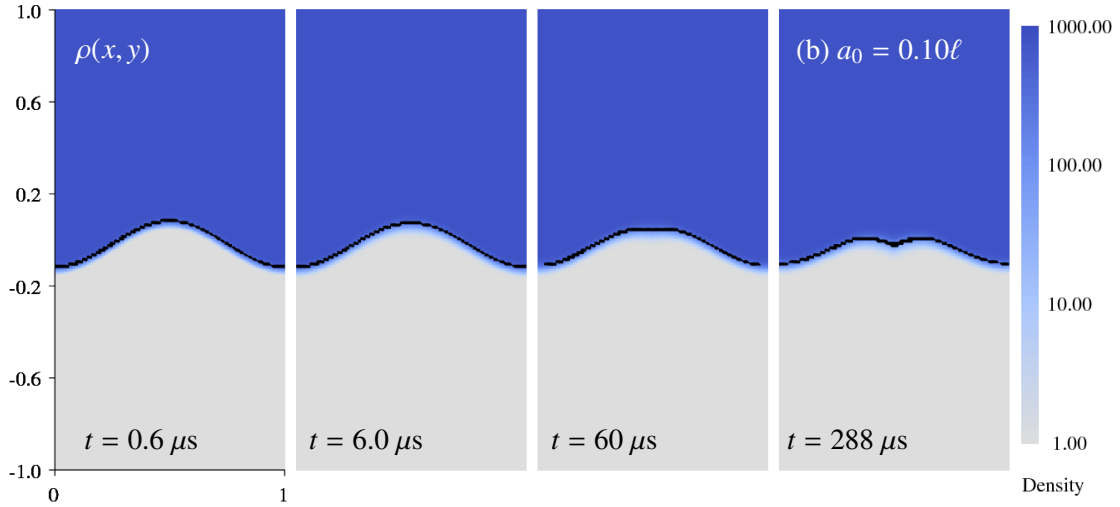

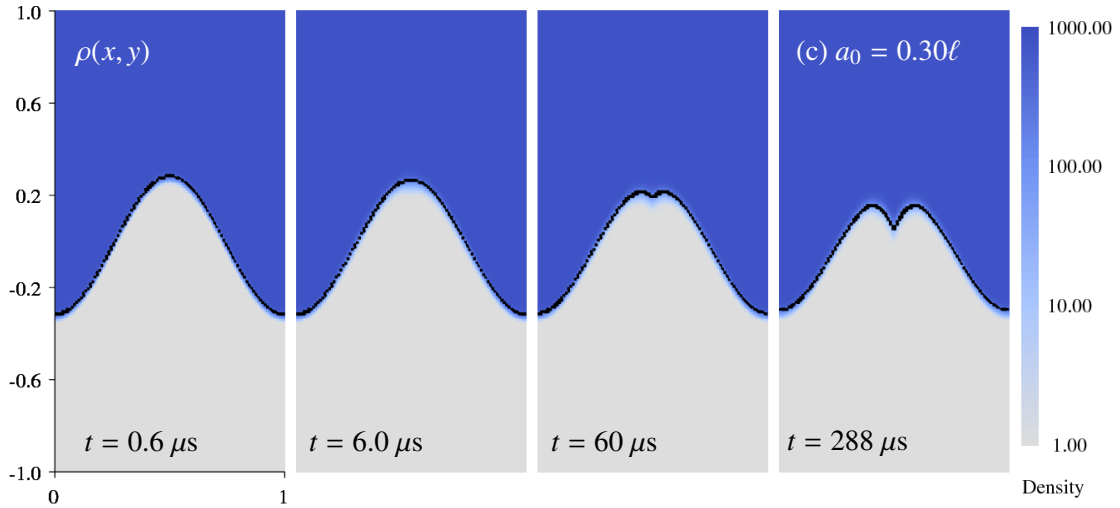

Figure 4.4: Evolution of the interface for $p_a = 2.5$ MPa ultrasound wave. Density contours at $t = 0.6, 6.0, 60$, and 288 μs for initial perturbation amplitudes (a) $a_0 = 0.03\ell$, (b) $a_0 = 0.10\ell$, and (c) $a_0 = 0.30\ell$.

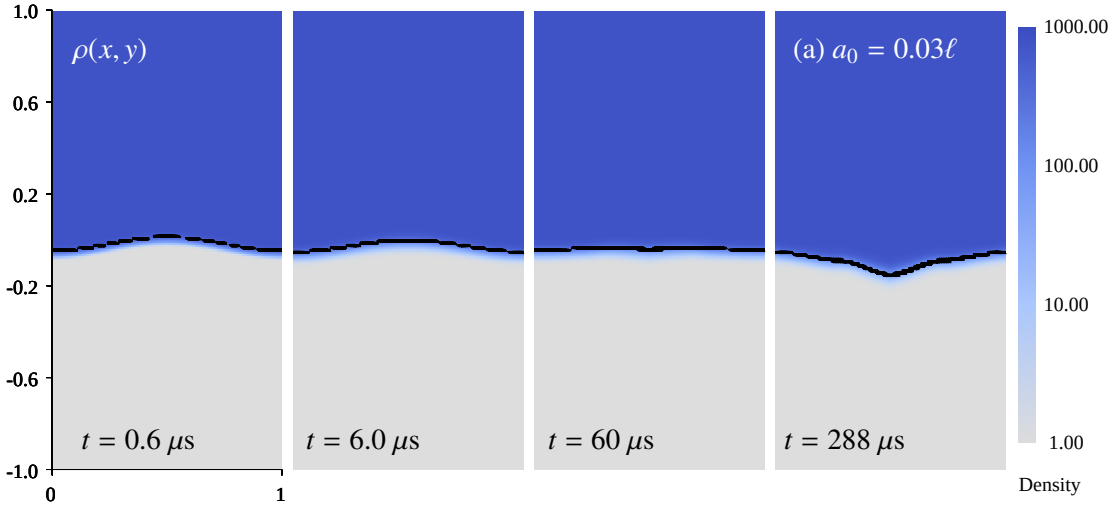

(a) $a_0 = 0.03\ell$

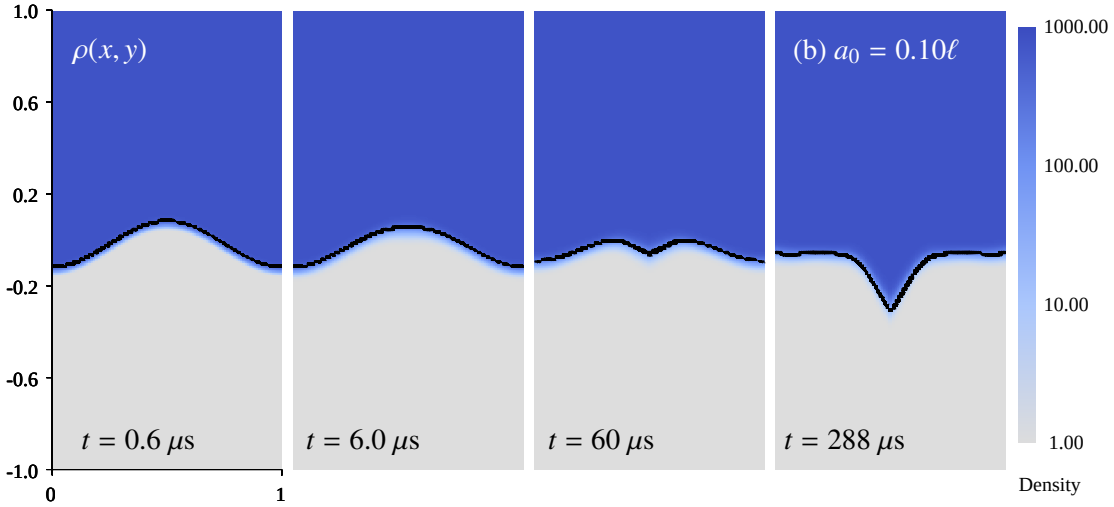

(b) $a_0 = 0.10\ell$

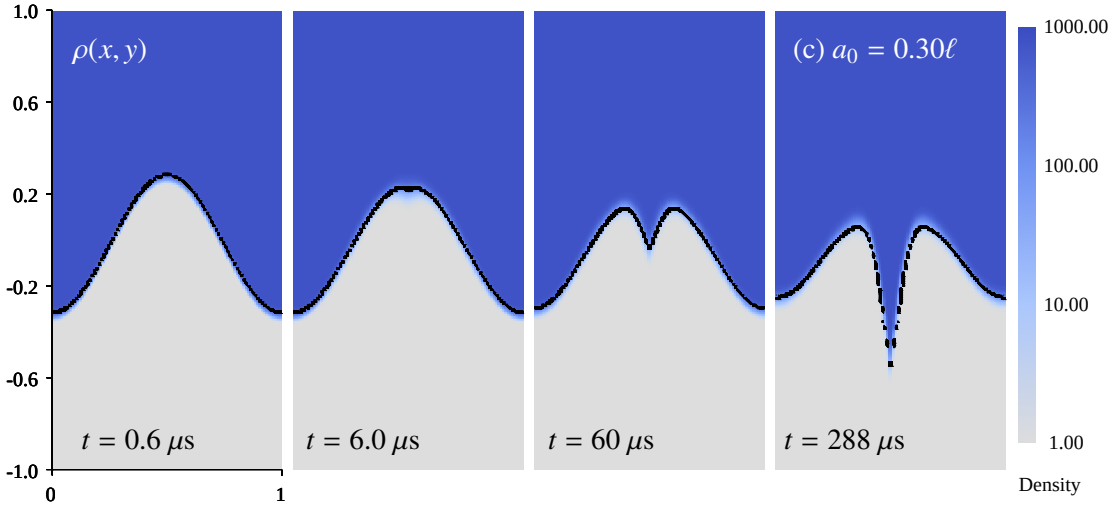

(c) $a_0 = 0.30\ell$

Figure 4.5: Evolution of the interface for $p_a = 5.0$ MPa ultrasound wave. Density contours at $t = 0.6, 6.0, 60$, and 288 μs for initial perturbation amplitudes (a) $a_0 = 0.03\ell$, (b) $a_0 = 0.10\ell$, and (c) $a_0 = 0.30\ell$.

strain increase takes place long after the passage of the wave, when the acoustic pressure is negligible ($t/(\ell/c) \gtrsim 47.5$). As explained in Chapter 3, the deformation cannot be explained by linear acoustics, which predicts negligible deformation after the passage of the wave.

The interface strains increase with increasing p_a and a_0, which is consistent with baroclinic vorticity-driven growth because these quantities determine the wave pressure gradient and its degree of misalignment with interface density gradient. The minimal strain case is observed for the smallest considered initial perturbation and wave amplitudes ($a_0 = 0.03\ell$, $p_a = 1.0$ MPa), for which a maximum strain amplitude of $\varepsilon = 0.001$ was observed at the final computed time $t = 288$ μs. Conversely, the maximum strain case occurs for the largest considered initial perturbation and wave amplitudes ($a_0 = 0.30\ell$, $p_a = 5.0$ MPa), for which, a maximum strain amplitude of $\varepsilon = 0.38$ was observed at the final computed time $t = 288$ μs. We highlight that for the $p_a = 5.0$ MPa case, these are not small strains and linear strain theory is not likely to apply, even if failure of the interface has not yet occurred. We consider the strain results relative to the $\varepsilon = 0.08$ strain failure criteria (Belete *et al.*, 2010). Over the simulated duration, this threshold was exceeded only for the $p_a = 5.0$ MPa wave with $a_0 \geq 0.10\ell$ and 0.30ℓ, in which cases the strain exceeded $\varepsilon = 0.08$ at approximately $t = 100$ and 220 μs respectively.

4.4.3 Viscous stress

In further consideration of possible alveolar damage mechanisms, we compute the inferred viscous shear stress field, based on the motion of the inviscid flow, and the extract the maximum along the interface. To illustrate the viscous stress around the interface, color contours of the viscous stress fields are provided for the $p_a = 5.0$ MPa wave in Figure 4.8 at $t = 2.9$ μs, approximately when the acoustic pulse and viscous stress are at their maximum amplitudes. Subfigures (a), (b), and (c) again correspond to initial perturbation amplitudes of $a_0 = 0.03\ell, 0.10\ell$, and 0.30ℓ, respectively. Black lines indicate isocontours of the volume fraction of water $\alpha = 0.5$. Since the viscous shear stress is governed by the velocity gradients in the fluid, which scale linearly with the acoustic pressure gradients (See Equation A.1), it is unsurprising that the greatest viscous shear stress am-

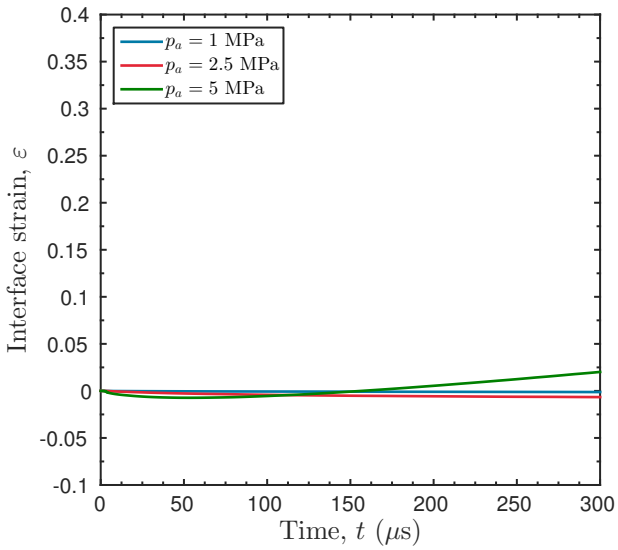

(a) $a_0 = 0.03\ell$

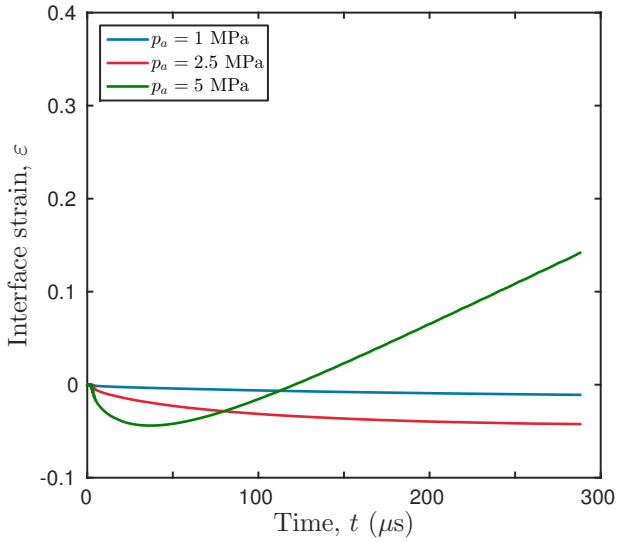

(b) $a_0 = 0.10\ell$

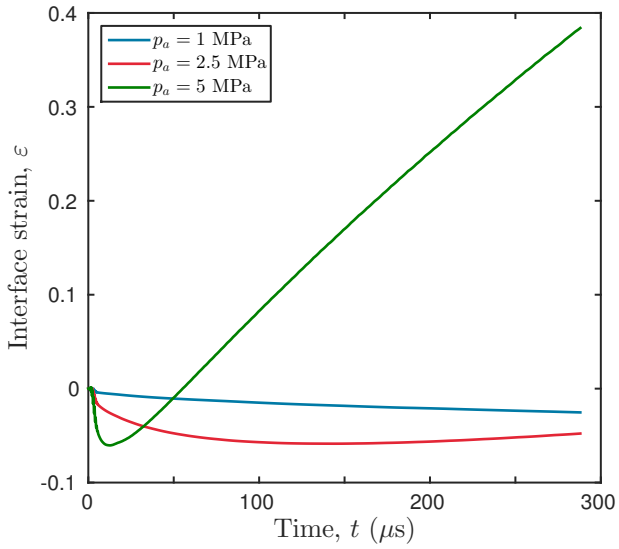

(c) $a_0 = 0.30\ell$

Figure 4.6: Interfacial strain dependence on pressure amplitude ($p_a = 1.0, 2.5, 5.0$ MPa). Each plot shows ε for a different initial condition: $a_0 = 0.03\ell$ (a), 0.10ℓ (b), and 0.30ℓ (c).

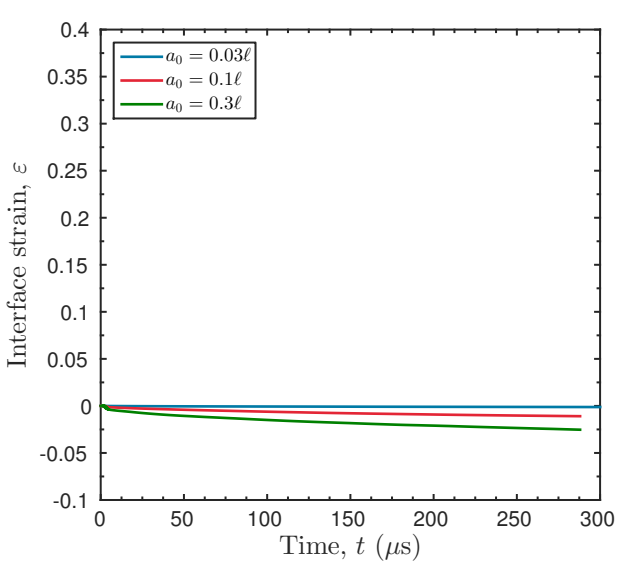

(a) p_a = 1.0 MPa

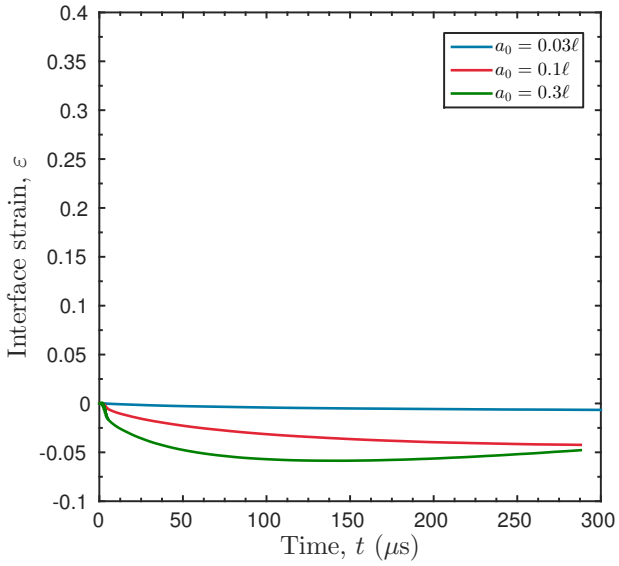

(b) p_a = 2.5 MPa

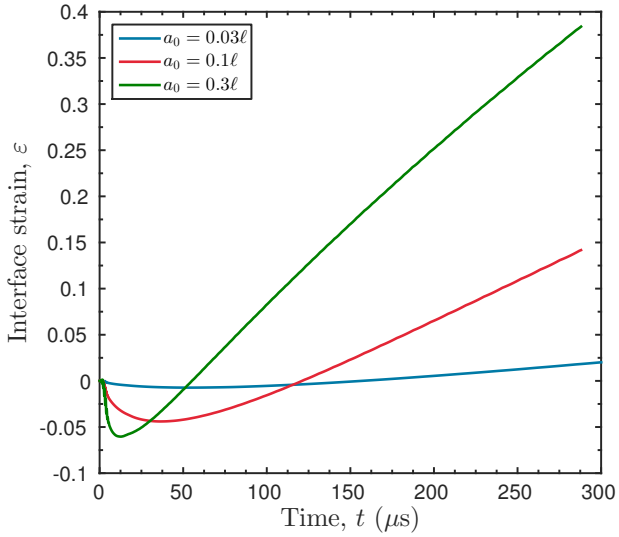

(c) p_a = 5.0 MPa

Figure 4.7: Interfacial strain dependence on initial perturbation amplitude ($a_0 = 0.03\ell,\ 0.10\ell,\ 0.30\ell$). Each plot shows ε for a different pulse amplitude: p_a = 1.0 MPa (a), 2.5 MPa (b), and 5.0 MPa (c).

plitudes occur during the wave-interface interaction, and in particular close to the time when the maximum pressure amplitude encounters the interface. The maximum viscous stress is observed to occur in the lighter region of the interface, in which the fluid is mostly air and the velocity gradients are greatest. At this point in time, the fluid around the interface has had little time to move as a result of the wave and consequently the interface remains largely undeformed.

We extract the maximum viscous stress amplitudes from field $\left|\tau_{xy}\right|_{max}$, which were found to lie consistently along the interface for all cases. To illustrate the dependence of $\left|\tau_{xy}\right|_{max}$ on the pulse amplitude p_a and initial perturbation amplitude a_0, Figure 4.9 shows $\left|\tau_{xy}\right|_{max}$ histories for variable p_a = 1.0 (blue), 2.5 (red), and 5 (green) MPa and constant initial perturbation amplitude $a_0 = 0.03\ell$ (a), 0.10ℓ (b), and 0.30ℓ (c), and Figure 4.10 shows this data re-plotted for variable $a_0 = 0.03\ell$ (blue), 0.10ℓ (red), and 0.30ℓ (green) and constant wave amplitudes p_a = 1.0 (a), 2.5 (b), and 5.0 (c) MPa. We highlight the fact that, because we are intentionally only interested in the maximum interfacial stress amplitude, the location along the interface at which $\left|\tau_{xy}\right|_{max}$ occurs changes in time, which is not captured in the figures. For all waves and initial perturbation conditions, $\left|\tau_{xy}\right|_{max}$ oscillates with the wave during the wave interaction, around a mean value which appears to rise and fall with the acoustic intensity. We note that there is a component of these oscillations that coincide with the fluctuations in the US pulse. These fluctuations occurs at approximately twice the pulse frequency because we are considering the absolute value of the viscous stress, which we expect to scale with the magnitude of the velocity gradients and therefore the pulse amplitude (see the acoustic relationships described in Chapter 3).

It is clear from both Figure 4.9 and 4.10 that, on average, increasing the wave amplitude increases the viscous stress amplitude at the interface as expected (neglecting chronologically local oscillations). Regarding the dependence of $\left|\tau_{xy}\right|_{max}$ on a_0, we make two observations. First, as a_0 increases, the chronologically local mean value of $\left|\tau_{xy}\right|_{max}$ also increases, though this is slightly less obvious from the figures due to the varying degree of oscillation between the curves. Second, based on differences between Figures 4.9(a), (b), and (c), as a_0 increases, the oscillation behavior changes. The overall magnitude of the osccillations in $\left|\tau_{xy}\right|_{max}$, relative to the chronologically local

mean, decreases. This is because as a_0 increases, a greater portion of the reflected wave propagates in the transverse direction. These transverse waves introduce additional oscillations in the shear stress field, which are small when compared to those generated directly by the incoming wave. These oscillations are identified according to their timing and are most clearly explained with an example. Consider $\left|\tau_{xy}\right|_{max}$ for the $p_a = 5$ MPa, $a_0 = 0.3\ell$ case, as shown in Figure 4.7(c). The larger stress peaks occur approximately regularly during the wave interaction every 0.3 μs, and correspond to the interactions of the peaks and troughs of the wave with the interface, as shown in Figure 4.2. Shortly after each of these larger peaks there is a slight drop in the peak stress. The time separating the peak and drop is approximately $\ell/c \approx 0.12$ μs, indicating these fluctuations are a consequence of the transversely reflected wave, which has the opposite sign of the incoming wave. We note that axial reflections are small and do not return to the interface until after the passage of the initial wave. After the passage of the wave, the maximum shear stress drops to nearly zero in all cases.

In consideration of DUS-induced alveolar hemorrhage, we note that for the parameters considered here the maximum viscous stress amplitudes observed at the interface occur during the interaction with the wave and ranged from 2 to 61 Pa. Even the greatest observed stress is two orders of magnitude smaller the 8 kPa minimal stress failure threshold observed by West *et al.* (1991) for disruption of alveolar epithelium. These stresses occur during the wave-interface interaction, and quickly fall off thereafter, in much less time than a typical period between pulses ($\sim$ 1 ms). This suggests that viscous stresses are not likely to quickly accumulate between pulses. A possible, exception to this could occur if the velocity field were to change significantly, perhaps as a result of accumulated vorticity from subsequent US pulses. The computational cost of testing this possibility numerically is not feasible under the current framework, and as such is beyond the scope of this work.

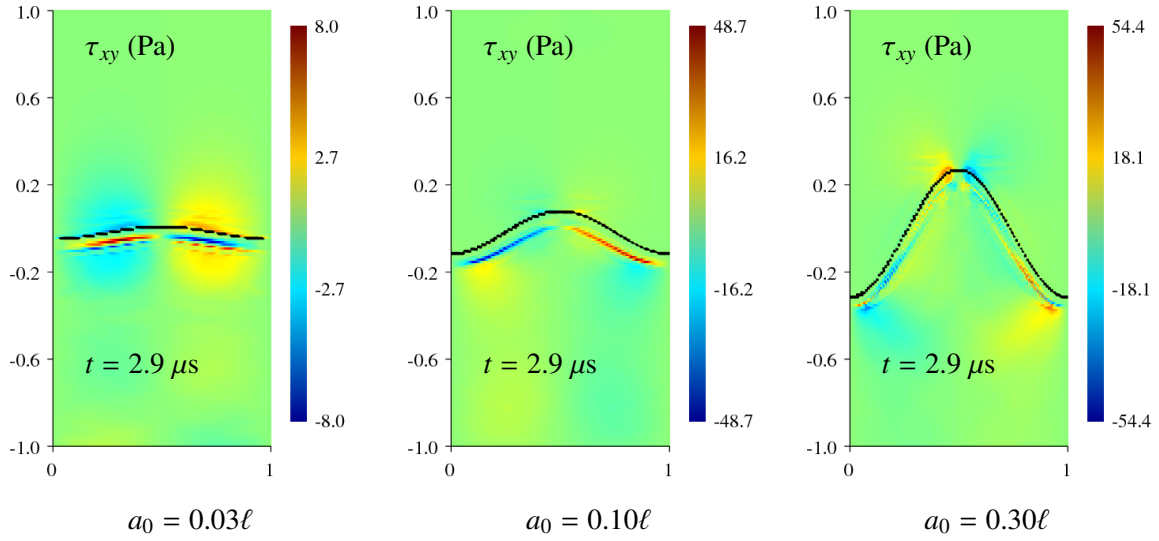

Figure 4.8: Evolution of the viscous stress field for the $p_a = 5.0$ MPa wave. Contour plots of the Newtonian viscous stress τ_{xy} in Pascals are shown for each initial perturbation amplitude, at $t = 5$, near the point when the maximum stress occurs. In Figures (a), (b), and (c) $a_0 = 0.03\ell$, 0.10ℓ, and 0.30ℓ respectively.

4.4.4 Ultrasound-induced vorticity dynamics and interface growth

Having examined the stresses and strains associated with liquid-gas interfaces driven by US pulse waves, within the regime relevant to clinical DUS, we now hypothesize that the observed deformation is driven by baroclinic vorticity deposited at the liquid-gas interface by the US pulse. As there is still a highly nonlinear density gradient across the interface, misaligned with strong ultrasonic pressure gradients, the potential for meaningful baroclinic vorticity deposition, and consequently persistent of the system, exists. As we demonstrated that this was possible for a trapezoidal acoustic wave in Chapter 3, we consider a second set of experiments, designed to test if this holds true for the ultrasound pulse. We will compare the interface and vorticity dynamics of an ultrasound driven pulse, with those of the trapezoidal pulse of the Chapter 3. The 1.0 to 5.0 MPa pulses used earlier in this chapter drive the system too slowly for the interface growth to reach its late-time behavior within a computationally feasible period. Additionally, we aim to compare to our previous results and as such we choose our acoustic pulse parameters and initial interface perturbation amplitude to match that of our baseline trapezoidal wave case Chapter 3: $a_0 = 0.03\ell$; $p_a = 10$

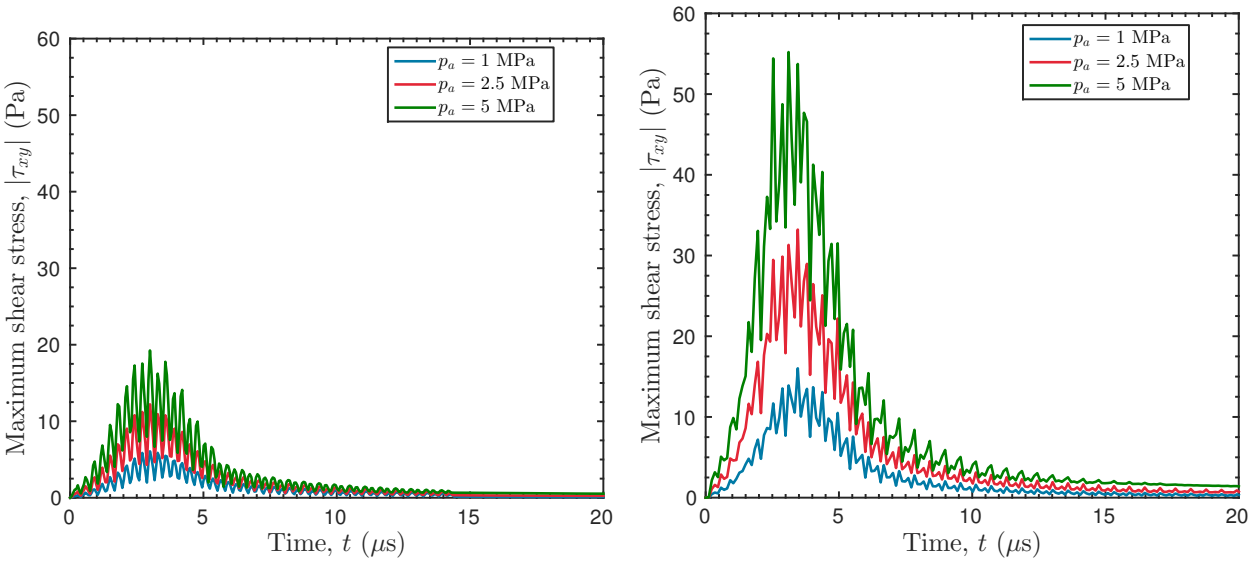

(a) $a_0 = 0.03\ell$ (b) $a_0 = 0.10\ell$

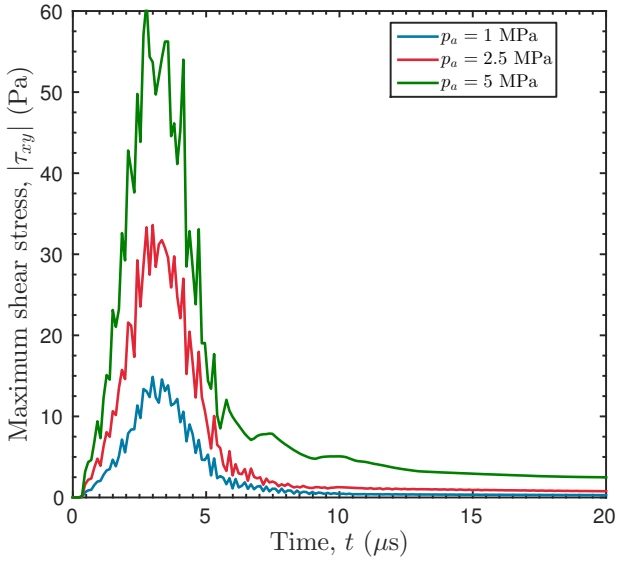

(c) $a_0 = 0.30\ell$

Figure 4.9: Interfacial viscous stress dependence on on pressure amplitude ($p_a = 1.0, 2.5, 5.0$ MPa). Each plot shows $\left|\tau_{xy}\right|_{max}$ for a different initial condition: $a_0 = 0.03\ell$ (a), 0.10ℓ (b), and 0.30ℓ (c).

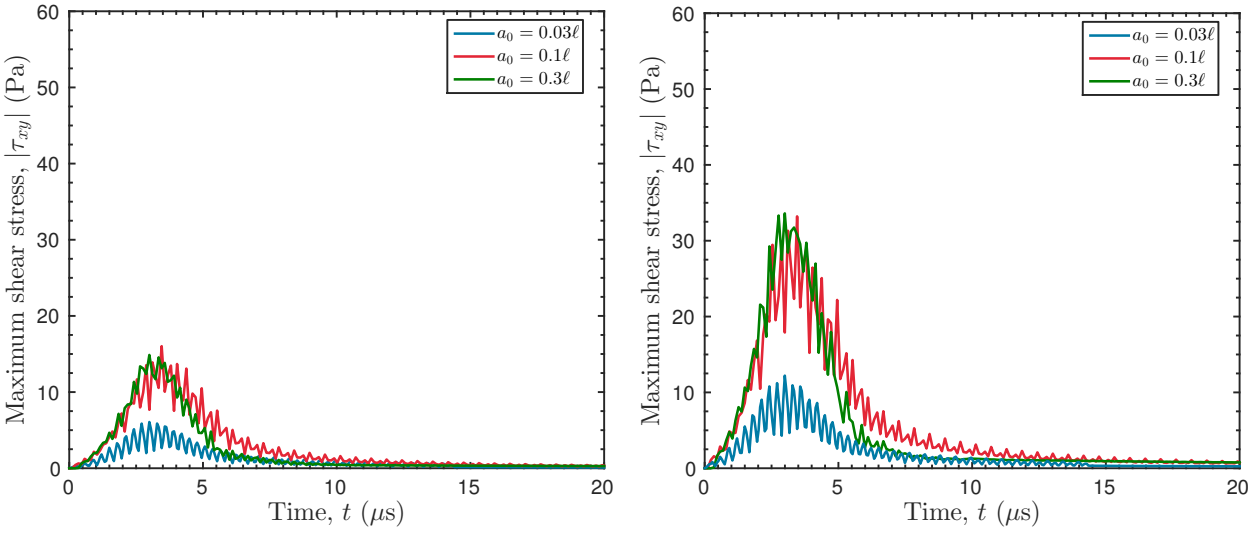

(a) p_a = 1.0 MPa (b) p_a = 2.5 MPa

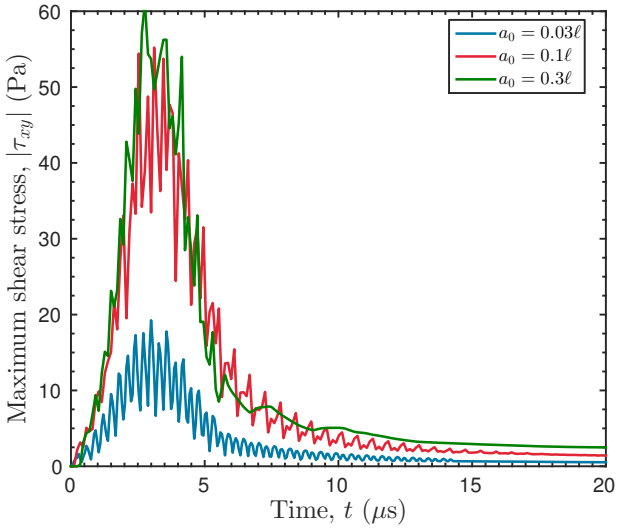

(c) p_a = 5.0 MPa

Figure 4.10: Interfacial viscous stress dependence on initial perturbation amplitude amplitude ($a_0 = 0.03\ell, 0.10\ell, 0.30\ell$). Each plot shows $\left|\tau_{xy}\right|_{max}$ for a different pulse amplitude: p_a = 1.0(a), 2.5(b), and 5.0(c) MPa.

MPa; $L = 45\ell$. To further facilitate comparison of this experiment to those of the previous chapter, all results presented here will be non-dimensionalized by ℓ and c_{water} unless otherwise indicated.

To illustrate the vorticity during and after the passage of the wave, Figure 4.11(a) shows vorticity contours for the $p_a = 10$ MPa pulse wave case, at $t/(\ell/c) = 4.75$ and 90 (or $t = 0.6$ and 12 μs). It can be clearly seen that vorticity is deposited along the interface by the ultrasound wave, and remains after its passing. In consideration of a quantitative, cumulative measure of vorticity deposited by the ultrasound wave we integrate the vorticity at over the right-half domain for each point in time to obtain the circulation, $\Gamma(t)$. Figure 4.11(b) plots the right-half domain circulation history during the wave interaction and shortly thereafter. The end of the interaction between the incident wave and the interface is indicated as a black, dashed vertical line $t/(\ell/c) = 47.5$. It can be seen that the wave deposits circulation, which remains approximately constant after its passage. The circulation left at the end of the wave is approximately 3×10^{-4}, which is roughly 1/5 that left by the $p_a = 10$ MPa trapezoidal wave in Chapter 3. We note that unlike the trapezoidal wave, which consists entirely of positive pressure, the US pulse consists of cyclic positive and negative pressure, such that each subsequent cycle is expected to deposit vorticity of sign opposite that of the previous cycle, since a phase inversion of the interface perturbation was not observed during the wave-interface interaction. Hence it is perhaps unsurprising that less circulation is deposited by the ultrasound pulse than by the trapezoidal wave of equivalent maximum amplitude. As in the previous chapter, the circulation in the left-half domain is equal and opposite, such that the total circulation is zero. Similar circulation histories for the $p_a = 1.0, 2.5$, and 5.0 MPa waves, used in the earlier stress and strain calculations, are provided in Appendix B.1, and reveal that similar to the $p_a = 10$ MPa case, circulation remains after the passage of the wave. Appendix B.1 also explores the dependence of that circulation on a_0 and p_a for the case of the ultrasound pulse.

To compare the late time growth of the perturbation amplitude driven by the ultrasound wave, with that driven by the trapezoidal wave, Figure 4.12 displays the perturbation amplitude history $a(t)/a_0$ on a log-log scale. For $t/(\ell/c) \leq 4000$ we calculate the interface perturbation amplitude growth exponent t^n, as was done in Chapter 3 and find that $n = 0.57$. This result is consistent with

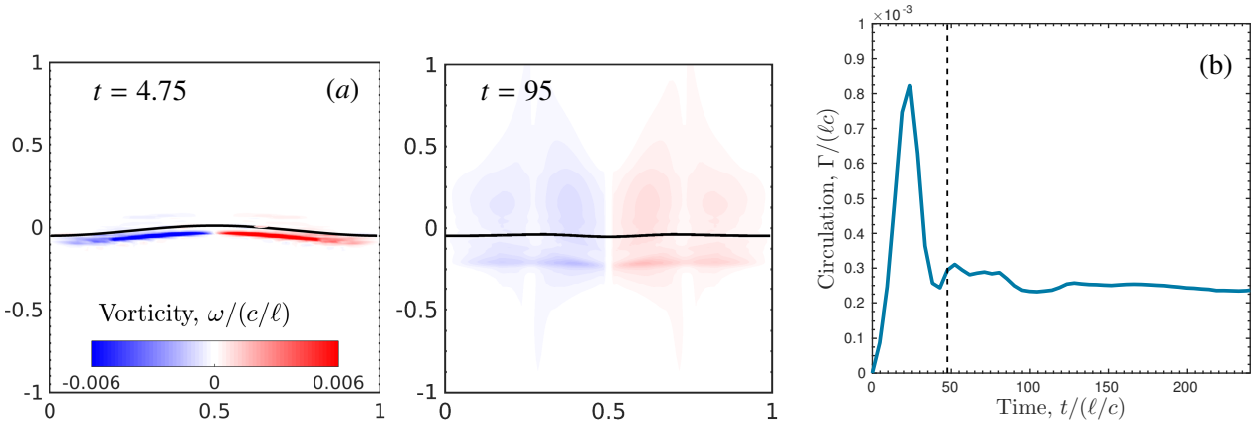

Figure 4.11: Vorticity and circulation histories for the $p_a = 10$ MPa ultrasound pulse. (a) Vorticity contours during the wave interaction, at $t/(\ell/c) = 4.75$ and after its passage at $t/(\ell/c) = 90$. (b) The dimensionless circulation history. The passage of the wave at $t/(\ell/c) = 47.5$ is indicated as a black, dashed vertical line.

the $t^{3/5}$ power-law growth obtained for a trapezoidal wave in Chapter 3.

After the passage of the US pulse, there are no obvious mechanisms, beside baroclinic vorticity, to drive the continued deformation of the interface. As such, it is worth discussing what precisely contributes to the circulation remaining after the passage of the wave. Throughout the wave-interface interaction, the interface itself deforms such that while US pressure gradient is continuously misaligned with portions of the interface density gradient, though the degree of that misalignment changes in time along the entire interface. While this deformation appears to be nominally small (note the barely observable difference between frames 1 and 2 for each subfigure within Figures 4.3, 4.4, 4.5), it is finite, calculable, and critical to the vorticity dynamics. Because the pressure returns to ambient after the passage of the wave, it must be true that the integral of the acoustic pressure gradient over all time is zero, just as it was for the trapezoidal wave. Thus the only way that baroclinic vorticity can remain after the passage of the wave is through changes in the density gradient during the interaction. As the interface deforms the direction these small changes in the direction and local magnitude of the density gradient result in a net deposition of circulation that remains to deform the interface after the passage of the wave. This has particular relevance to ultrasound which relies on many subsequent pulses, potentially resulting in the

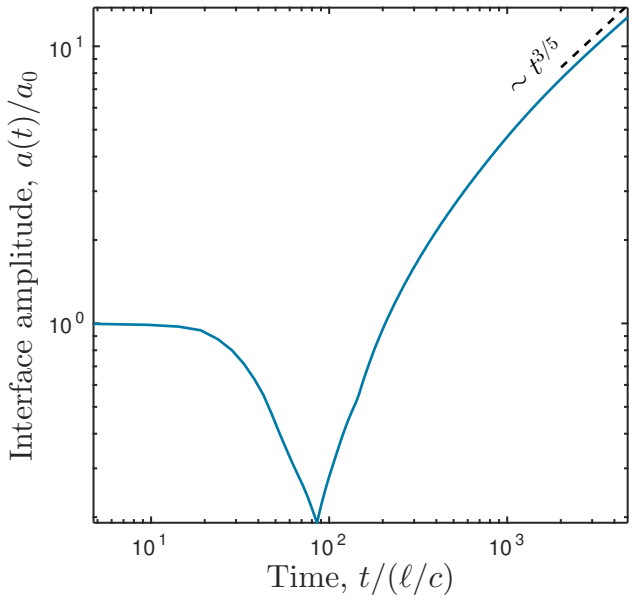

Figure 4.12: Interface perturbation amplitude history for the $p_a = 10$ MPa ultrasound pulse. $a(t)/a_0$ is plotted vs time on a log-log scale. $t^{3/5}$ growth is indicated by the dashed black line.

accumulation of vorticity over time.

4.4.5 Limitations of the present work

The model of an ultrasound-driven alveolus used in this work is exactly that, a model. This work aims only to offer insight into the physics and potential physical damage mechanisms of DUS-induced lung hemorrhage. Our approximation of the physical system is perhaps not a particularly, naturally intuitive one. Moreover the vorticity mechanisms that we suggest are driving the system are not intuitive for a viscoelastic solid. The concept of vorticity, even in a viscoelastic solid (e.g., soft tissue), can be thought of rather simply at a fixed instant in terms of a velocity magnitude (not direction) difference between opposite sides of a particle of continuum, such that the instantaneous tendency of the particle is to rotate. Our conceptual arguments for overcoming this arise out of our understanding of this as a continuum of viscoelastic solids, which may act as a solid or liquid depending on the physical regime of interest. The model is based on highly fundamental laws of mechanics (conservation of mass, momentum, energy) and neglected physical effects are justified in the relevant regime based on dimensional analysis. Additionally, the problem geometry and

setup are chosen based on the relevant application. While the author recognizes that treatment of an alveolar septum as a perturbed water-air interface intuitively seems a bit too simple, all of the dimensional and order of magnitude arguments suggest that specifically for the timescales considered here, the simulated dynamics are reasonable. Though there are several limitations to this study that would not allow the simulated physics to capture the physics of diagnostic ultrasound-alveolar interactions over longer time spans. Here we specifically consider limitations that arise from our constitutive model of the lung tissue and the model problem geometry. Based on our physical understanding, it is not unreasonable to speculate about how each of these limitations is likely to effect the simulated physics.

In this study, we treat the alveolar septa and capillaries therein as a liquid-gas interface, and within our physical model we neglect certain physical features characteristic of soft tissue, including viscoelasticity and the mechanical failure. Rather than repeat the dimensional analysis arguments used to initially justify the model in Chapters 1 and 3 we will consider how each of these could affect the physical system. Viscosity and elasticity both have potential importance at late times. In the context of the present work, viscosity may act to serve as a mechanism to dissipate vorticity, thus reducing strain on the interface. However, the characteristic timescale over which we expect the vorticity to dissipate over a relevant area $\sim \ell^2/\nu_{air}$ is multiple milliseconds, and is thus unlikely to greatly effect the dynamics over the considered period. Elasticity is likely to provide a restoring force to resist the deformation of the interface, however this is likely to be small relative to the fluid inertia, which we show quantitatively in Appendix A.7. Additionally, this model is no longer valid after the alveolar septum fails, which may occur in some of our simulations based on the considered failure criteria. As the strains observed are large, before the elastic force is likely to overcome the fluid inertia, the elastic restorative force may not be particularly useful at mitigating vorticity-induced strain. Many of these specific limitations are in part a result of limitations of the existing body of knowledge concerning the mechanical properties and failure behavior of alveolar tissue under stresses and strains, which is poorly characterized within the timescales and physical regimes relevant here. We highlight the fact that the available stress and

strain failure criteria available for alveoli are based on much slower processes than occur during DUS, making for an imperfect comparison at best. Additionally, the stress 8 kPa stress failure criterion of West *et al.* (1991) is for wall stress, which is not the same as shear, but was the best available metric at the time of this writing.

In consideration of the limitations of our model geometry, we will start from the fact that this work aims only to study interactions between a single ultrasound pulse and a single alveolus. As such we consider the effect of a treating the alveolar septum as a slightly perturbed sinusoidal interface between fluids. In comparison to the histological slide of alveoli shown in Figure 4.1, the geometry considered here is smoother and flatter than true alveolar boundaries. As such, there is the potential for greater shear stress concentrations and baroclinic vorticity generation with subsequent strain in the real physical system. Additionally, the 2D representation of the problem as a single alveolus neglects any physical support the system may receive from its surroundings. And while it has been suggested that pulmonary capillaries are largely unsupported by surrounding tissues (West *et al.*, 1991), without quantification of that support, it is possible that it would help to reduce vorticity-driven motion of the interface, particularly at the edges. However, the deformation and strain observed here is largely driven by vorticity local to the interface perturbation, such that it would likely not be greatly effected by such support. Lastly, we acknowledge that this model cannot capture 3D fluid effects (e.g., turbulence, vortex-stretching, etc...) that are expected to be negligible over the timescales considered based on the Reynolds number and order of magnitude analysis of the individual terms of the vorticity equation (see Appendix A.1).

4.5 Summary, conclusions, and future work

In summary, US pulse waves were simulated propagating from water into sinusoidally perturbed water-air interfaces to model a single US-pulse impinging upon an alveolus from surrounding soft tissue. We assume a typical adult mean alveolar diameter of $\ell = 200$ μm (Ochs *et al.*, 2004) as a characteristic length scale, such that the maximum simulation time was approximately 288 μs.

To estimate viscous stresses and interfacial linear strains relevant to DUS-induced alveolar hemorrhage, 1.5 MHz ultrasound pulse waves with amplitudes of $p_a = 1.0, 2.5$, and 5.0 MPa were used. Initial interface perturbation amplitudes of $a_0 = 0.03\ell, 0.10\ell$, and 0.30ℓ were considered. For each case, the wave-interface interaction generated vorticity along the interface and resulted in long-term deformation of the interface, which continued well after the passage of the wave. Relevant calculations of the density fields, inferred viscous stress fields, and linear interfacial strain within the simulated period are reported. The computed peak interface strain amplitudes $|\varepsilon|$ ranged from 0.01 to 0.38. During the computed period, only for the 5.0 MPa wave did strains exceed the $|\varepsilon| = 0.08$ damage threshold, reported by Belete *et al.* (2010). The peak passive viscous stress estimates at the interface were on the order of tens of Pascals, which is far below the 8 kPa stress failure criterion reported by West *et al.* (1991). A second experiment was performed to determine that baroclinic vorticity is the driver of the observed deformation. For this experiment, a $p_a = 10$ MPa pulse was propagated toward a perturbed water-air interface of amplitude $a_0 = 0.03\ell$ and the vorticity and interface dynamics were compared to those of the trapezoidal waves in Chapter 3. It was found that ultrasound pulses deposited circulation of similar distribution and order of magnitude to those previously observed for the trapezoidal waves. The perturbation was found to grow approximately as $t^{3/5}$, as was expected for baroclinic vorticity-driven growth, based on our previous work.

This work is a first step toward investigating the possibility of baroclinic vorticity-induced strain as potential mechanism for ultrasound-induced alveolar hemorrhage. This work is novel in its modeling using the nonlinear equations of fluid motion to study the dynamics of an alveolus interacting with a single DUS pulse. Furthermore, this work is unique in its comparison of alveolar stress and strain estimates with previously determined failure criteria. While the calculated stresses and strains observed based on the interaction between an air water interface and a single ultrasound pulse may be representative of some of the physics associated with DUS-alveolar interactions, we cannot confidently say that baroclinic vorticity is the likely cause of DUS-induced hemorrhage in the lung. As true DUS typically involves many subsequent pulses, further investigations will need

to account for this. However, based on the work reported here, we draw the following conclusions:

1. **Newtonian, viscous stress alone is unlikely to be sufficient to cause DUS-induced hemorrhage of the alveolar wall**. While many approximations and simplifications were made throughout the course of this work, the work presented estimates *worst case* viscous shear stresses. Here, the velocity gradients are higher than would be expected in the true physical system because neglected viscous and elastic effects would resist interfacial motion in the true physical system. In spite of this, the calculated shear stresses are multiple orders of magnitude less than expected alveolar stress failure thresholds.

2. **DUS pulses within clinically relevant regimes have the potential to deposit baroclinic vorticity within gas-liquid interfaces in the lungs, which is capable of driving deformation.** This work clearly demonstrates that diagnostically relevant ultrasound pulses are capable of creating lasting baroclinic vorticity at liquid-gas interfaces which are dynamically similar to alveolar tissue-gas interfaces. For the 10 MPa case, the interface perturbation exhibits $\sim t^{3/5}$ power-law growth at late times, as was previously shown to occur for interfaces driven by trapezoidal acoustic waves. For weaker waves, running the simulations to sufficiently late time to observe this behavior was too computationally costly to be done. This indicates that ultrasonically driven vorticity is a viable mechanism for driving the observed growth. The observed interfacial strains created by pulses as weak $p_a = 5.0$ MPa were more than sufficient to cause damage based on previously observed alveolar failure criteria. Furthermore, based on dimensional arguments, dissipation of the observed vorticity is expected to occur over multiple milliseconds, which is greater than the typical time between subsequent DUS pulses. Hence US may be capable of accumulating vorticity in the lungs over several subsequent pulses and thus driving greater deformation. This will depend on the morphology of the interface during the arrival of each pulse, which is likely to vary widely depending on the initial conditions and ultrasound parameters, as the minimum strain cases showed practically no deformation over a third of a typical pulse interval, and the large strain cases are likely to cause alveolar failure before subsequent pulses arrive.

CHAPTER 5

Conclusions and future work

Two problems within the area of diagnostic ultrasound bioeffects motivate the work of this thesis presented up to this point. For the first problem, we study the dynamics of ultrasonically driven microbubbles as it relates to Contrast-Enhanced Ultrasound (CEUS)-induced bioeffects. For the second problem, we study the physics of acoustic wave interactions with gas-liquid interfaces, as it relates Diagnostic Ultrasound (DUS)-induced lung hemorrhage. The two primary objectives of this work are:

1. To develop computational models of the aforementioned Ultrasound (US) bioeffects problems.

2. To perform numerical experiments using these computational models to gain insight into the physics and fluid mechanics underlying DUS bioeffects in the context of CEUS and DUS of the lung.

5.1 Summary of key contributions and findings

5.1.1 Bubble Dynamics of Contrast Enhanced Ultrasound and Related Bioeffects

To accomplish the first objective in the context of CEUS and related cavitation bioeffects, we developed **a model of a contrast agent microbubble subjected to a DUS pulse within a com-**

pressible, viscoelastic soft tissue (Patterson *et al.*, 2012a), based on the works of Keller (1980); Yang & Church (2005). As such, the bubble is modeled as a spherically symmetric ideal gas body. The surrounding tissue is modeled as a compressible, Voigt viscoelastic material with properties relevant to soft tissues based on the literature. The ultrasound wave is modeled as a uniform change in the pressure immediately surrounding the bubble. In a novel contribution to the field, experimentally measured ultrasound waveforms, with known bioeffects thresholds (Miller *et al.*, 2008b) were used to drive the bubble.

To accomplish the second objective, **we performed simulations of bubble dynamics for bubbles driven by several experimentally measured US pulses in soft tissue with variable material parameters including viscosity and elasticity**. Ultrasound waves with frequencies ranging from 1.5 to 7.5 MHz and PRPA ranging from less than 1 to greater than 6 MPa were used. For each frequency, the threshold Peak Rarefaction Pressure Amplitude (PRPA) associated with the onset of bioeffects (specifically, glomerular kidney hemorrhage in rats) was known (Miller *et al.*, 2008b). Metrics associated with the simulated cavitation and bubble dynamics were related to the ultrasound parameters and bioeffects thresholds and the following four conclusions were drawn:

- Calculated cavitation metrics in a theoretical viscoelastic media correlate with experimentally observed bioeffects. Simulation results for the maximum dimensionless bubble radius R_{max}/R_0, a measure of the violence of a cavitation event, were classified based on whether or not the waveform was known to cause kidney hemorrhage in rats subject to CEUS in a previous study (Miller *et al.*, 2008b). From a plot of R_{max}/R_0 (a common cavitation metric) vs US frequency, it is clear that for a given frequency there are distinct regimes in which bioeffects do and do not occur. Explicitly, it was observed that above a certain threshold values of R_{max}/R_0 and PRPA, bioeffects always occurred, below a different set of threshold values they did not occur. These bioeffects thresholds increased with increasing frequency, and it is likely that the inertial cavitation thresholds increased in a similar fashion.

- Cavitation dynamics and bioeffects thresholds depend on elasticity, though the relationship is not trivial. Within the simulations, tissue elasticity ranged from 5 to 1000 kPa. It was

found that increasing the elasticity could either enhance or diminish the strength of the simulated bubble response, based on standard cavitation metrics. For kilopascal order values of elasticity, the bubble dynamics mimicked those expected for an identical experiment in water. The effect of elasticity was found to depend on the waveform of the driving US pulse. With the bubble response showing a greater deviation from that expected in water, for higher amplitude and increasingly nonlinear wave.

- While never intended to accurately represent cavitation in tissue, previously established thresholds for inertial cavitation in water, $T_{max} = 5000$ K and $R_{max}/R_0 = 2$ (Apfel & Holland, 1991; Flynn, 1975b), are not equivalent to bioeffects thresholds. Based on the results of this study, these thresholds do not correspond to cases in which bioeffects were observed. Moreover, observed bioeffects thresholds for R_{max}/R_0 were shown to have strong frequency dependence. It seems unlikely that bioeffects thresholds are independent of cavitation thresholds, but rather that these thresholds need to be adjusted for ultrasonically driven cavitation in a viscoelastic media.

- Here, we perform a parameter sweep of several uncertain values, such as elasticity and bubble size demonstrate that deviations of these parameters, within a range of reasonable values, can lead to significantly different results in the simulated dynamics. However, better characterization of tissue and bubble properties is needed. Existing values and viscoelastic constitutive models for the mechanical properties and behavior of tissue are incomplete. There is particularly little information available for stresses and strains that occur on the length and time scales relevant to cavitation and ultrasound.

5.1.2 Diagnostic Ultrasound-induced lung hemorrhage and acoustically driven gas-liquid interfaces

To accomplish the first objective, **a novel model of an ultrasound pulse-driven alveolus was developed.** An ultrasonically driven alveolus is modeled as a 2D compressible fluid system. The

alveolus is modeled as air and the surrounding tissue as water, with a sinusoidally perturbed interface between the two. The ultrasound wave is treated as an acoustic wave existing initially in water, which is then allowed to propagate toward the interface. As such the overall computational model system consists of a rectangular domain containing an acoustic wave in water propagating toward a perturbed air interface. Using dimensional analysis, it is shown that this model is appropriate for studying the dynamics that occur during the ultrasound-alveolar interaction, and for at least a brief period thereafter. This work is unique, as the developed model appears to be the first model of diagnostic-ultrasound alveolar interaction to consider the nonlinear conservation equations for mass, momentum, and energy. As a consequence of this, the developed model is able to capture nonlinear phenomena that cannot be explained by linear acoustics, but which we show are important to the system dynamics.

In pursuit of the second objective, the model described above was used in a two-part study: **First, numerical experiments of perturbed gas-liquid interfaces driven by trapezoidal acoustic waves were performed and studied to describe the fundamental fluid dynamics of an acoustically driven gas-liquid interface.** Acoustic parameters such as the peak pressure amplitude and wave duration (length) are varied and their effect on the system dynamics, particularly with regards to vorticity and interface perturbation growth, is studied. Using dimensional analysis we develop mathematical relationships to describe the response of the interface to the trapezoidal acoustic wave. **Second, we simulate alveoli-like perturbed liquid gas-interfaces, driven by ultrasound pulse waveforms.** Peak acoustic pressure amplitude and initial perturbation amplitude (which corresponds to geometry) are varied to study the dynamics for a range of parameters relevant to diagnostic lung ultrasound. Computed interfacial stresses and strains are compared with alveolar failure criteria. The following five conclusions are drawn with regard to acoustically driven gas-liquid interfaces and DUS-induced lung hemorrhage.

- Acoustically generated baroclinic vorticity may be capable of appreciably deforming perturbed liquid-gas interfaces. For the cases studied here, this was due to the substantial acoustic pressure difference over a short length (megapascals over millimeters), and the nearly

discontinuous density profile of the interface. Although the rise from and return to ambient pressures associated with acoustic waves suggests that net vorticity deposited should be zero, such an argument overlooks the transient nature of the process, namely the fact that the baroclinic torque may drive the interface throughout the wave-interface interaction, such that the density gradient is non-constant.

- Initially smooth interface perturbations, driven by residual baroclinic vorticity may experience asymptotic power-law growth. The rate of this growth depends on the circulation density at the point in time when the direction of the bubble and spike (interfacial peaks and troughs) velocity can no longer be explained by linear acoustics, necessitating a description of the dynamics which captures the effects of vorticity.

- Changes in the acoustic waveform that have little effect on the interface dynamics during the wave-interface interaction, may have a significant long-term effect on the evolution of the interface through the residual vorticity deposited at the interface.

- US pulses with diagnostically relevant parameters may be capable of inducing significant deformation of gas-liquid interfaces through the generation of baroclinic vorticity at interface perturbations. Gas-liquid interfaces driven by 1.5 MHz DUS pulses with PRPAs ranging from 1 to 5 MPa were found to deform long after the passage of the wave. For the 5 MPa waves, observed interfacial strains were reached as high as 38%, far greater than 8% expected strain failure thresholds for alveolar walls Belete *et al.* (2010). This deformation occurred over a period of fewer than 300 μs, which is less the time period between pulses for a typical DUS pulse repetition frequency of 1 kHz. Furthermore, based on dimensional arguments, it was found that the baroclinic vorticity driving the deformation is likely to persist over multiple milliseconds ($\ell^2/\nu = O\,(\text{ms})$), suggesting that the use of many subsequent pulses, as is the case for clinical DUS, may result in an accumulation of vorticity, and thus greater interfacial strain.

- Newtonian viscous stresses alone are not likely to be responsible for DUS-induced lung

hemorrhage. The largest estimated viscous stresses observed were on the order of tens of pascals and were multiple orders of magnitude beneath expected stress failure thresholds.

5.2 Overall conclusions

Beyond the specific problems of interest studied in this thesis, we consider the bigger picture of using computational modeling and numerical experiments to study US bioeffects problems. With regard to this theme, the following two conclusions are drawn based on the cumulative efforts presented in this thesis:

- Computational modeling can play a unique and useful role in investigating the physics that underlies ultrasound bioeffects. The purpose of computational studies such as those presented here is to gain insight which can be useful for supplementing, explaining, and guiding experiments. When used as a supplement to experimental techniques computational models can provide estimates of difficult to measure physical quantities that may play an important role in the occurrence of the biological effects such as elevated temperature and pressure in a collapsing bubble, as Chapter 2. Additionally computational models can be useful when trying to answer questions that cannot be readily treated through modern experimental methods. For instance DUS-induced lung hemorrhage cannot be directly observed in real time through modern medical imaging techniques due to the structural complexity of the lung and surrounding tissues and the small spatial and time scales associated with the hemorrhage. Partly as a consequence of this, the mechanism driving the hemorrhage is still unknown. However, potential physical damage mechanisms can be discovered and studied through computational modeling. This is the case in Chapters 3 and 4, in which acoustically-generated baroclinic vorticity induced strain is shown to occur at alveoli-like gas-liquid interfaces. This possible damage mechanism has not been previously considered. And while this mechanism cannot be confirmed numerically, it highlights the importance of nonlinearity in the problem, an aspect of the physics that is often ignored and worthy of

further study.

- Based on the cumulative results of this part of the dissertation, we conclude that for computational modeling of ultrasound bioeffects to be optimally useful for research purposes, there is a necessity for more accurate physical characterizations of tissue than are currently available. And secondarily, for these models to ever be clinically useful for predicting individual occurrence of bioeffects, they will likely need to be adapted on a case-by-case basis. The models developed and used in this thesis are justified for their stated regimes based accepted data available at the time of their creation. However, it is widely known that soft tissues are complex media which exhibit a wide variety of physical properties that are not well characterized in all regimes. Physical properties such as elasticity, viscosity, and stress-strain relationships can vary widely depending on variable physical state of tissue (e.g., stress, strain, strain rate, temperature, degree of hydration, etc...). Reported values for these properties vary widely in the literature and are frequently unavailable entirely for the regimes of interest to many ultrasound bioeffects problems. For example, repeatedly experimentally validated viscoelastic models for soft tissues subject to strain rates of the order of those associated with inertial cavitation are rather hard to come by in this author's experience. In spite of this scarcity of information, the dynamics of the US bioeffects problems can be highly dependent on these poorly characterized parameters, as in the case of the elasticity-dependent cavitation bubble dynamics of Chapter 2. Furthermore, there are certain aspects of these problems that can vary widely from person to person, and as such for computational models to be of clinical use for predicting or estimating ultrasound bioeffects they will likely need to be adapted for these variations. For instance, in our consideration of diagnostic lung ultrasound in Chapters 3 and 4, we neglect the attenuation of the wave that would realistically occur before it enters the lungs. This attenuation depends on the thickness of the thoracic wall and as can be readily observed in any populated area, human geometries vary significantly between individuals. As such, two different people subject to identical DUS pulses for diagnostic lung imaging may experience very different degrees of biological effects. If the models developed

here are to be used in the future, it will be important to adapt them for the specific problem of interest based on the best available data at the time.

5.3 Recommendations for future work

In this section, we offer suggestions for which some of the works of this thesis may be improved upon or expanded. With the end goals of increasing the relevance of this dissertation work to the motivating problems and applications and better understanding the underlying physics, the suggested strategies for advancing the works of this thesis can be generally summarized into a broad three-part strategy. First, advance the computational model by adding physical phenomena neglected here for fundamental study and problem tractability, but which may be of relevance to the motivating problem or application. Second, where possible, use experimental data as part of the initial problem setup, such as experimentally measured acoustic waves or physical geometries. Third, perform simulations which attempt to computationally replicate experimental studies or portions thereof and compare results. For example, parametric studies with variable ultrasound parameters could examine trends and dependencies which have already been observed experimentally, such as the difference in thresholds pressures with varying exposure duration. Where sensible, use the resulting information gained from the numerical experiments to look for new insight into the cause of the observed trends. In the remainder of this section there is a short piece with more specific recommendations for future work related to the study of CEUS bioeffects as in Chapter 2 and a more extensive piece focusing on extending the work of Chapters 3 and 4.

5.3.1 Extending and improving the study of bubble dynamics at capillary breaching thresholds

As the work of Chapter 2 was published several years before the writing of this thesis, it is perhaps unsurprising that the author's labmates and colleagues have already extended areas of that work significantly. Specifically, bubble dynamics models that account for heat and mass flux and incor-

porate more robust viscoelastic constitutive models have been developed (Gaudron *et al.*, 2015; Warnez & Johnsen, 2015; Barajas & Johnsen, 2017). By combining these advanced bubble models with the experimentally measured US pulses and bioeffects thresholds featured in Chapter 2, it may be possible to obtain a better understanding of the relationship between the cavitation dynamics and observed bioeffects thresholds. Specifically one could look for qualitative changes in the bubble dynamics behavior that happens at or around the PRPA thresholds associated with the onset of hemorrhage. Though our work considers contrast agent microbubbles after their shells have ruptured, one could extend this work by also incorporating the effects of the protein and lipid coatings that surround CEUS microbubbles, as was done by Marmottant *et al.* (2005). While these suggestions extend the work by advancing the spherically symmetric bubble model, none of the proposed recommendations thus far captures 3D effects which may also be of importance. Along these lines, one could use the basic problem setup, driving pressure waves, and initial conditions from Chapter 2 to design direct numerical simulation experiments, solving appropriate forms of the equations for conservation of mass, momentum, and energy with a relevant constitutive relationship and equation of state for closure.

5.3.2 Extending and improving the physical model of DUS lung-interaction

One of the directions upon which one could build upon the work of Chapters 3 and 4 is to increase the relevance to actual physical lung ultrasound. In the design of our model, the consider an idealized problem setup with a well defined interface and waveform. This is well suited for the type of fundamental studies that are performed in this dissertation, because various parameters carefully controlled and the dependence of the dynamics on each can be isolated. Additionally, results from the simplified model are more generalizable than those obtained from a more realistic setup which would inherently require more specified, unique geometries and waveforms. However, there is value in aiming to increase the relevance of the model to the physical problem and there are a variety of areas upon which our model could be made more realistic and relevance to the motivating problem, by adjust the model system's physics and geometry. Here we discuss a few of

the limitations of the present work in this regard and offer suggestions for ways to overcome these limitations and extend and improve the current work.

5.3.2.1 Improving the lung model

- **Inclusion of presently neglected physical mechanisms**

  In the introduction to the present work we present conservation equations 1.2 for mass momentum and energy and then perform dimensional analysis to justify neglecting various physical effects during the time and spacial scales of interest to the studies performed here, and in Appendix A.7 we go one step further modeling the elastic and inertial forces at the interface to show that elasticity is of relatively little importance for the problems we consider. However, we note within this work that two of these effects, viscosity and elasticity, are likely to be more important if considering longer time scales, over which viscosity will dissipate energy and elastic forces will increase with increasing strain. These effects may be considered by adding the appropriate terms to the equations of motion that are solved here. While the ideal constitutive equation to relate the stress and strain is not well known for ultrasonic regimes, there has been work in this area that could be integrated into the existing framework and built upon. Lanir (1983) developed a viscoelastic constitutive model relating the alveolar membrane and its liquid interface to the bulk tissue properties and later Kowe *et al.* (1986) and Denny & Schroter (2000) built upon this, developing alveolar finite element models. As these effects are completely excluded in the present work, any reasonable extension in this direction is likely to help generate solutions that are closer to the physical reality, particularly over the longer timescales associated with typical diagnostic imaging exposure durations.

- **Use of realistic alveolar geometries** In the present work, the morphology of the alveolar wall is approximated as a smooth sinusoidal perturbation between fluids. However, as was illustrated in Figure 4.1, the true morphology is far more complicated. This relevance of this work to mammalian DUS could greatly be improved by building a problem geometry

based on a histological cross-section of alveolar tissue, which can be obtained at micron-resolution using microfocal X-ray (Litzlbauer, 2006). These images could then be used to define an initial volume fraction field based on the brightness of each pixel. This could be further extended to 3D by using the methods described by Parameswaran *et al.* (2009). While the numerical methods used in this work are too computationally expensive to be practical for geometries such as this over the timescales of interest, experiments such as this would be useful for investigating the mechanism by which hemorrhage propagates into successive layers of alveoli.

5.3.2.2 Improving the ultrasound model

- **Experimentally measured US pulse waveforms**

  The ultrasound pulse used in the work presented in Chapter 4 was a simplified waveform consisting of a sinusoidal wave modulated by a Gaussian envelope. Consequently, certain potentially important features of experimental ultrasound waveforms, such as nonlinearity and the resulting high pressure gradients, are not captured. By using experimentally measured waveforms to drive the problem, the effects of these features can be studied. This would also aid in the comparison of numerical and experimental results, which will be discussed in more detail at the end of this section.

- **Simulations over clinically relevant timescales, with multiple pulses**

  Research suggests that the total number of pulses (Pulse Repetition Frequency (PRF) $\times$ Exposure Duration (ED)) used in DUS of the lung has a significant effect on US-induced hemorrhage (O'Brien *et al.*, 2005, 2001c). And the results of Section 3.4.3 suggest that circulation deposition and therefore interfacial strain and perturbation growth may be controllable using multiple carefully designed pulses. However, the current computational model of an ultrasound-driven alveolus is too computationally expensive to simulate multiple US pulses at a realistic PRF (e.g, $\sim$ 1 KHz). This problem is in large part a consequence of the highly variable length and timescales that exist in DUS of the lung. First, we consider the

difference in length scales between the alveolus ($O\left(10^{-4}\right)$ m) and the physical length of the acoustic wave ($O\left(10^{-3}\right)$ m). Because the acoustic wave begins in the domain, the domain must be sufficiently large enough to capture it entirely and allow it to leave without significant boundary effects. However, to also capture the dynamics of the interface, it is necessary to use sufficiently high resolution, particularly within portion of the domain containing the interface, which often changes considerably over the course of a simulation. Second, we consider the difference in timescales between the wave-interface interaction ($\sim \mu$s) and the amount of time between pulses, over which the interface is expected to continually evolve (~ms). Such that even using an adaptive timestep obeying the Courant-Friedrichs-Lewy condition (CFL = $\frac{\boldsymbol{u}_{max}\Delta t}{\Delta x} \leq 0.5$), the problem must run for many timesteps (typically $\sim 10^5$ for a 300μ s simulation) due to the high spacial resolution. Thus we have a large domain, at high resolution, running for many timesteps, and hence a computationally expensive problem, which in practice takes weeks to months of real-time to simulate.

To decrease the computational cost of the simulation in a way that simultaneously allows for the use of multiple ultrasound pulses we suggest implementing time-dependent boundary conditions to prescribe the incoming acoustic wave and prevent reflections. This could be done using the methods described by Thompson (1987, 1990). The dynamic creation of the acoustic waves at the boundary, such that they do not need to be prescribed in the initial domain, would allow the computational domain to be shortened by the length of the wave at the very least. Furthermore, because these boundaries can be designed to be strongly non-reflective, the need for the stretched grid at the top and bottom of the domain is removed. As such, the overall domain size may be decreased by as much as tenfold in the vertical direction, greatly reducing the computational costs. Additionally, a time-dependent boundary formulation would allow for the creation of waves at late times, such that multiple pulses could be simulated.

The implementation of the suggested time-dependent boundary conditions Discontinuous Galerkin (DG) spatial schemes is technically difficult. While it is possible to adapt these

techniques (Toulopoulos & Ekaterinaris, 2011), it is recommended that if this course of research is undergone, one might consider other numerical techniques suitable for these problems, such as Weighted Essentially non-oscillatory (WENO) methods. While these methods lack certain advantages of DG (e.g., compact stencil), they offer benefits such as being more readily developed for the solution of the Navier-Stokes equations, if one wished to add viscosity to the problem, as suggested above.

- **Comparison of computational and experimental results**

  In order to test the hypotheses proposed within this thesis, there is a need for fundamental liquid-gas interface experiments with waveforms relevant to DUS. Once an theoretical explanation of the fluid mechanics of these interface problems (as is offered in this thesis) is experimentally validated, simulations closer to reality should be performed. While the studies and simulations performed as part of this dissertation work do not occur over the typical timescales associated with DUS-induced lung hemorrhage, by implementing the previous suggestions we can begin to simulate something much closer to the typical experimental setups used to study this problem. As was done for CEUS in Chapter 2, simulated dynamics can be compared to experimental results. To further study the feasibility of the proposed physical mechanism underlying DUS-induced lung hemorrhage: baroclinic vorticity driven strain of the alveolar wall, one could begin to more rigorously study the dependence of the vortex dynamics and associated strain on ultrasonic parameters for which the hemorrhage dependence is already well understood. The dependence of lung hemorrhage on a variety of ultrasonic parameters (e.g., pulse repetition frequency, pulse duration, effective dose, pulse frequency, exposure duration) been studied extensively. The dependence of baroclinic vorticity-induced strain on these parameters has not been rigorously investigated. One could go a long way toward supporting or ruling out the proposed damage mechanism by comparing the relationships between these parameters and hemorrhage to relationships between these parameters and simulated vorticity dynamics and strain.

Part II:

Underwater Acoustic Uncertainty

CHAPTER 6

Efficient Estimation of the Probability Density Function of Acoustic Transmission Loss in Uncertain Ocean Environments Using Area Statistics

In this chapter we develop *area statistics* a computational technique for estimating the Probability Density Function (PDF) of Transmission Loss (TL) in ocean environments with uncertain environmental parameters, using a single TL field calculation. PDFs are generated using *area statistics* are compared with PDFs generated from accepted Monte Carlo methods via the L_1 error for many environments and locations. It is found that *area statistics*-generated PDFs are engineering-level accurate ($L_1 < 0.5$) in 91% of cases and require less than one-millionth the computational effort of the Monte Carlo-generated PDFs on average. As the *area statistics*-generated PDFs can be generated in milliseconds on a typical desktop computer, the technique is useful for real-time applications. This work is in preparation to be submitted for publication (Patterson & Dowling, (In preparation)).

6.1 Abstract

Calculations of acoustic transmission loss (TL) in the ocean are useful in naval and ocean monitoring applications. These TL calculations are often uncertain because they are based on uncertain environmental parameters, but standard methods for determining TL uncertainty are computation-

ally expensive and inappropriate for real-time applications. The present work describes how TL statistics in a range-depth area surrounding a point of interest within a single TL field calculation can efficiently estimate the probability density function (PDF) of TL that results from ocean environmental uncertainty. The underlying idea is that at a range-depth (r, z) location within an uncertain ocean sound channel, variations in the TL value resulting from varying environmental uncertainties can be represented by spatial variations in TL found near the point of interest in a baseline TL calculation. Here, such area statistics-estimated PDFs of TL are compared to PDFs of TL obtained from 2000-sample Monte Carlo calculations at source frequencies of 100, 200 and 300 Hz and source depths of 91, 137, and 183 m (300, 450, 600 ft), in ten uncertain ocean environments, at test location depths ranging approximately from 20 m to 4.5 km and source-receiver ranges from a less than 1 km to more than 170 km. These comparisons show that the estimated PDFs of TL have an L_1 error < 0.5 when compared to Monte Carlo PDFs, and are thus considered engineering-level accurate in 91% of tested locations. Additionally, the PDFs were produced with tens of thousands to millions of times less computational effort than the Monte Carlo calculations.

6.2 Introduction

Sensing in the ocean is primarily managed through the broadcast and/or reception of acoustic waves. Computational acoustic field models are commonly used to assess the extent of radiated sound fields, and to extract information from recorded signals via signal processing routines. Unfortunately, the ocean environmental parameters necessary for fully exploiting the capabilities of modern acoustic field models are seldom (if ever) known with sufficient precision to prevent uncertainty in ocean parameters from influencing the predicted acoustic fields. Yet, understanding and quantifying the uncertainty associated with a given field calculation is important for determining its utility. The focus of this work is on the development of a computationally efficient procedure for estimating the uncertainty of acoustic Transmission Loss (TL) computations that arises as a result of an uncertain environment.

In underwater acoustics, the uncertainty in acoustic field predictions arises from limited knowledge of the physical and geometric properties of the ocean environment of interest. Consequently, acoustic field predictions are typically made using imperfect estimates of environmental parameters, and as a result, the predicted fields themselves are also uncertain. For a harmonic acoustic field produced by a point source, the most fundamental attribute at any point in space is the field's amplitude and this is commonly reported as TL, a field quantity that has been part of sonar engineering for many decades (Urick, 1962). Knowledge of the uncertainty in TL predictions has utility in practical naval applications (Abbot & Dyer, 2002; Pace & Jensen, 2002) and ocean measurement system design (Munk, 1994). Unfortunately, there is no known general relationship between environmental uncertainty and TL field uncertainty, and the most common techniques for calculating TL uncertainty, Monte Carlo and direct sampling methods, are too computationally expensive for implementation in real-time applications. The purpose of this paper is to introduce and describe an approximation procedure, herein named *area statistics*, as an approximate but computationally efficient alternative to Monte Carlo and direct sampling methods (or other means) for producing the probability density function of TL at a point of interest within an uncertain ocean environment.

The topic of acoustic uncertainty in ocean environments has seen considerable interest in the last decade or so (Livingston *et al.*, 2006). The physical uncertainty of an ocean environment has been shown to have considerable impact on naval applications ranging from sonar performance prediction to tactical decision aids and threat assessment. Accordingly, there has been much work within the field of underwater acoustics toward two goals: (1) understanding and quantifying environmental and acoustic field uncertainties, and (2) determining how these uncertainties affect relevant applications (Abbot & Dyer, 2002; Emerson *et al.*, 2014; Sha & Nolte, 2005; Stone & Osborn, 2004). The technique described here primarily addresses the first goal through computationally efficient predictions of TL field uncertainty based on typical ocean environment uncertainties.

There have been multiple studies aimed at accurately describing environmental uncertainties. This is a challenging task given the complexity and variability of the ocean water column and seabed properties, especially in shallow waters (Livingston *et al.*, 2006). Uncertainties associated

with archived bathymetry data sets obtained without the use of modern multi-beam technology have been reported (Calder, 2006), and historical data have been used to describe seasonal sound speed uncertainties on the continental shelf and slope in the Middle Atlantic Bight (Linder *et al.*, 2006).

Here we propose the area statistics procedure for estimating acoustic TL field uncertainties that arise as a result of the uncertain environment. The starting point for the area statistics technique is a single baseline TL field calculation that provides TL for a unity-strength point source (at range = 0) as function of range and depth within the ocean along a chosen azimuthal direction. For this baseline calculation, all uncertain environmental parameters are set to their most probable values. The probability density function (PDF) of TL is used here to quantify the uncertainty of baseline TL values since it contains all the relevant TL statistics for ocean applications (Gerstoft *et al.*, 2006). The mean and standard deviation of TL, which may be reflective of the macro- and micro-states of the ocean, respectively (Abbot *et al.*, 2006), are readily calculated from the PDF of TL. The techniques currently available for predicting the PDF of TL require differing levels of computational effort. These are described in the following paragraphs from highest to lowest computational cost, as assessed by the number of additional TL field calculations beyond the baseline calculation necessary to implement the technique.

Monte Carlo and direct sampling methods are well-accepted techniques for obtaining PDFs of TL, but their computational effort increases exponentially as the number (M) of uncertain environmental parameters increases. For both techniques, a potentially large set of TL calculations is undertaken that sample the M-dimensional space of uncertain environmental parameters in a random (Monte Carlo) or structured (direct sampling) manner. The PDF of TL at any location in physical space is then constructed from the computed TL values found at that location in each of the many field TL calculations. Monte Carlo calculations have been used to obtain the probability distribution of TL subject to geoacoustic inversion uncertainty (Gerstoft *et al.*, 2006), and to explore acoustic sensitivity to environmental parameters and assess the utility of a stochastic description of environmental variables (Heaney & Cox, 2006). More recently, Monte Carlo and

direct sampling calculations have been used to generate reference PDFs of acoustic field amplitude to assess the accuracy of approximate PDF construction techniques (James & Dowling, 2008, 2011). Monte Carlo calculations based on 2000 TL field calculations are used for this purpose in the work reported here.

The mathematically rich technique of polynomial chaos expansions (PCE) has also been used to assess acoustic uncertainty (Finette, 2005, 2006, 2009). Here the uncertain acoustic field is represented as a series of Q basis functions with each function having its own range-, depth-, and frequency-dependent coefficient. The coefficients are determined from the solution of a set of Q coupled partial differential equations. The technique produces converged uncertainty assessments as Q increases, with Q being a proxy for the number of field calculations when there is a single uncertain environmental parameter ($M = 1$). However, when there are more uncertain parameters ($M \geq 2$), a different PCE solution technique is needed and the approximate correspondence between Q and the number of field calculations is lost. For comparison, the area statistics technique described herein is simpler to implement than PCE and it does not require the solution of any additional partial differential equations beyond the baseline TL field calculation.

There are also approximate methods for predicting acoustic uncertainty that do not involve the computational expense of Monte Carlo simulation or mathematical complexity of PCE. A technique for estimating TL confidence bounds for environments in which acoustic propagation can be described by a sum of propagating modes has been previously described (Zingarelli, 2008). The technique can be applied when there are multiple uncertain parameters and it is computationally efficient, as it only requires the baseline field calculation. However, it inherently relies on range, depth, or frequency averaging, and does not provide the full PDF of TL. Another approximate method for predicting the PDF of acoustic field amplitude for multiple uncertain environmental parameters is based on determining spatial shifts between acoustic field calculations completed with a difference in one uncertain parameter (James & Dowling, 2008). However, this field-shifting technique requires one additional field calculation for each uncertain parameter.

The area statistics technique described here provides estimates of the PDF of TL, and only

requires the baseline TL field calculation. The technique is a quantitative implementation of the idea that the uncertainty in the TL value of harmonic wave transmissions at a range-depth (r, z) location in an uncertain ocean sound channel is represented in the TL values found near the point of interest within a baseline TL calculation at that frequency. The usefulness of the area statistics technique lies in its simplicity and low computational cost. It can be used in any environment for which TL field calculations can be completed, and unlike Monte Carlo and direct sampling methods, it is consistently fast enough for implementation in real-time sonar applications. As implemented here, it incorporates $M = 6$ uncertain physical parameters, represented by many more random variables. When compared to Monte Carlo results based on 2000 TL field calculations, area statistics-generated PDFs of TL had an L_1 error [defined by Equation (6.7)] below] less than 0.5 , and were hence labeled engineering-level accurate, in 91 % of tested locations.

The remainder of this paper is divided into three sections. The next section describes the ten uncertain ocean environments used in this study, the area statistics technique, and the procedures followed for generating the Monte Carlo results. The third section presents quantitative comparisons between area statistics and Monte Carlo results in the ten ocean environments for three different source depths and three different frequencies at field point depths from 20 m to 4.5 km, and ranges from less than 1 km to more than 174 km. The final section summarizes this effort and states the conclusions drawn from it.

6.3 Methods

This section describes the main components of this investigation: the uncertain ocean environments and their characterization, the algorithm steps followed for the area statistics technique, the implementation details for the Monte Carlo calculations, and the quantitative means for assessing the accuracy of the PDFs of TL produced from area statistics. Sample results are provided to illustrate each component.

Ten ocean environments with uncertain bathymetry, sound speed profiles (SSPs), and seabed

properties were considered in this study. The environments, labeled 1 through 10 and ordered according to their maximum depth from shallowest to deepest, are shown in cross-section in Figure 6.1. For all environments, bathymetry data were taken from privately available databases. The 10 environments are located in the Pacific, Atlantic, and Indian Oceans. Nine of the environments were chosen to include a wide variety of bathymetric features. The location of a tenth environment was chosen randomly to ensure objectivity. We note that Environment 3 consists of the first 15 km of Environment 4, in order to test the algorithm at higher resolution near the source. Additionally, Environment 7 is the horizontal mirror of Environment 8 in order to evaluate area statistics-generated PDFs of TL in equivalent upslope and downslope environments.

Six uncertain physical parameters were considered within each environment: bathymetry (depth) fluctuation $\Delta D\,(r)$, seabed density ρ_b, seabed sound speed c_b, seabed attenuation α_b, and water column sound speed fluctuations $\Delta c\,(z)$, which is the sum of two constituent pieces: fluctuations from seasonal variability $\Delta c_\Omega\,(z)$ and fluctuations from variations in the temperature and salinity $\Delta c_\Gamma\,(z)$. These are labeled and depicted in Figure 6.2. For each Monte Carlo sample calculation n, of $N = 2000$ total calculations, each uncertain parameter required one or more random samples drawn from appropriate Gaussian Distributions. In a typical simulation, between 89 and 741 random samples were drawn: 1 for each seabed property ρ_b, c_b, α_b, 1 for SSP fluctuations $\Delta c_\Gamma\,(z)$ arising from temperature and salinity variations, 1 – 3 for SSP fluctuations $\Delta c_\Omega\,(z)$ arising from seasonal variation, and 82-734 for bathymetry fluctuations $\Delta D\,(r)$ (i.e., one per range point in the bathymetry profile). The most probable value μ and Gaussian standard deviation σ of each random variable distribution is provided in Table 6.1. The most probable values, standard deviations, and parametric ranges in Table 6.1 were intended to mimic the actual uncertainties associated with readily available information about ocean environmental parameters. Note that for each environment, source frequency, source depth combination, the situation where all random parameters take on their most likely values are referred to as the *baseline* case. Detailed specifications of how these were used to complete the Monte Carlo calculations are provided below.

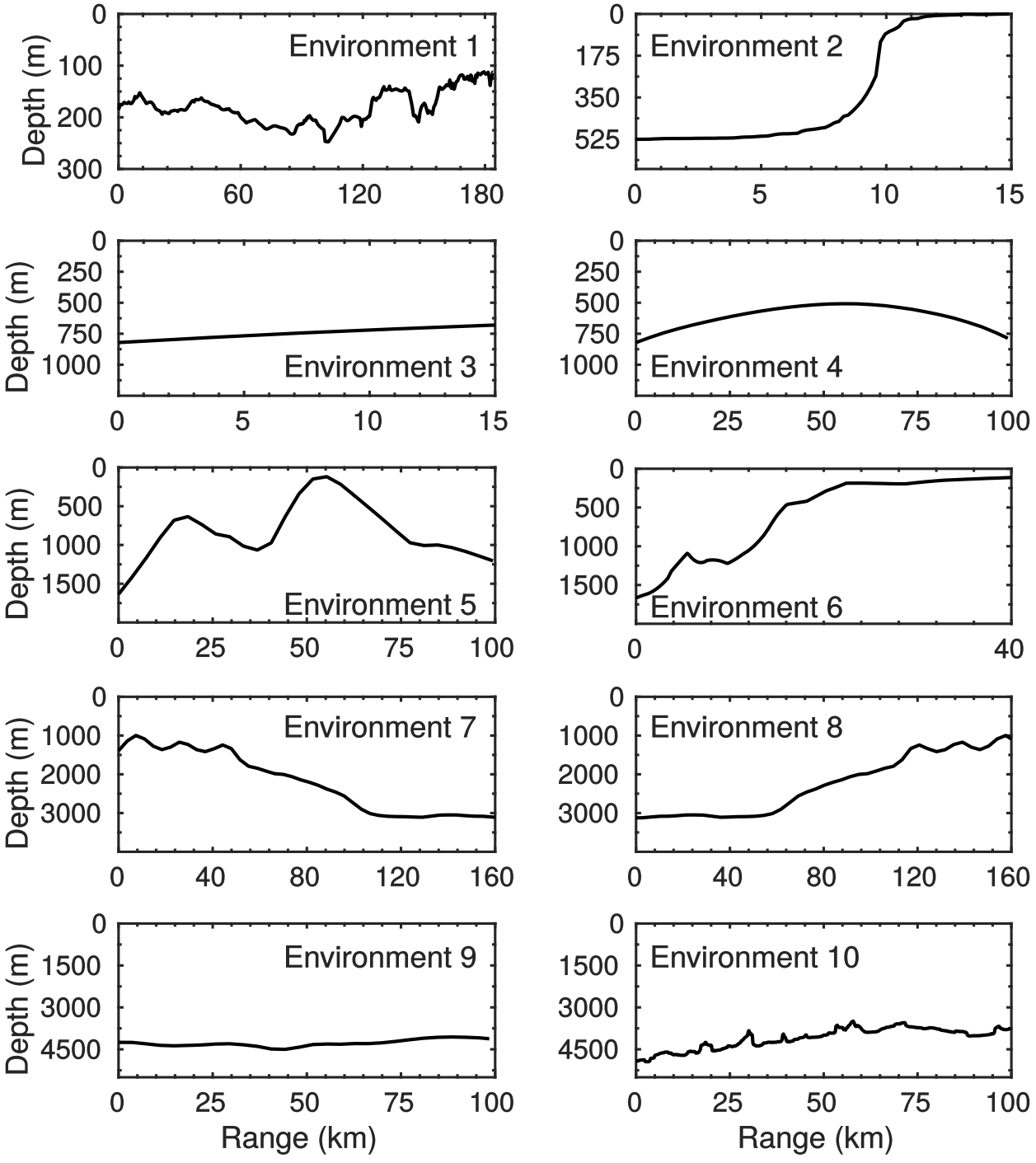

Figure 6.1: Nominal bathymetry for the ten uncertain ocean environments used in this study. Environments are ordered according to increasing maximum depth from shallowest (1) to deepest (10).

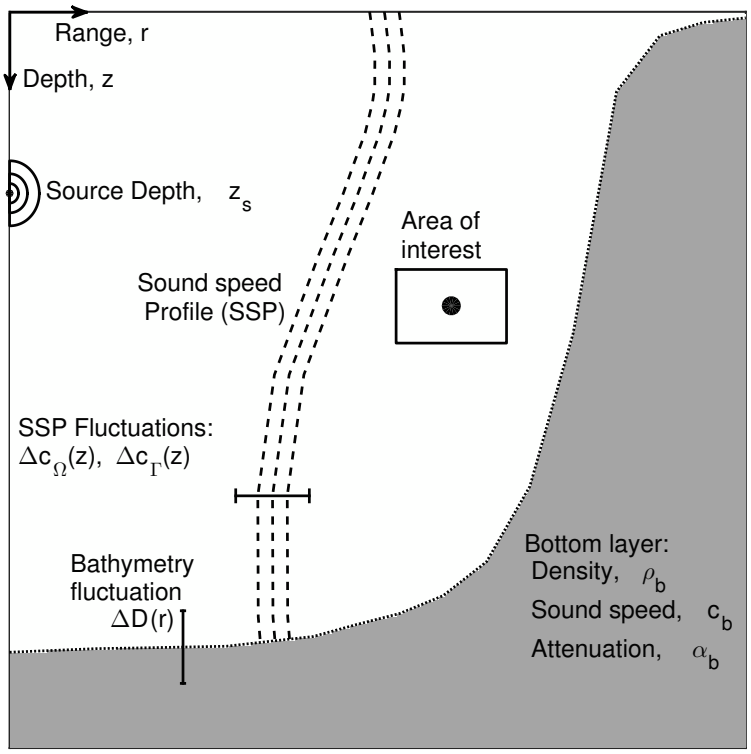

Figure 6.2: Schematic of generic ocean environment and uncertain environmental parameters: bathymetry fluctuation $\Delta D(r)$; sound speed profile fluctuations due to seasonal variation $\Delta c_\Omega(z)$ and due to temperature and salinity fluctuations $\Delta c_\Gamma(z)$; and seabed properties (density ρ_b , sound speed c_b , attenuation coefficient α_b). The distributions of relevant random variables are provided in Table I. With the exception of bathymetry, all uncertain parameters are assumed to be range independent. The source depth was z_s = 91, 137, 183 m (300, 450, 600 ft). The point of interest for recovering the PDF of TL is indicated by a black dot. The rectangle surrounding this dot nominally indicates the range-depth area utilized by the area statistics technique.

Uncertain environmental parameters and distributions			
Uncertain parameter	**Mean, μ**	**Std. Dev., σ**	**Range**
Bottom layer density, ρ_b (kg/m^3)	1971	304	1060, 2883
Bottom layer sound speed, c_b (m/s)	1982	541	1500, 3000
Bottom layer attenuation, α_b (dB/λ)	0.47	0.34	0.1, 1.0
Bathymetry fluctuation weight, $\xi(r)$	0	1	N/A
Water column SSP temperature and salinity fluctuation standard deviation weights, γ	0	1	N/A
Water column SSP seasonal fluctuation eigenfunction weights, ω_i	0	1	N/A

Table 6.1: Summary of the uncertain environmental parameters and their distributions. The mean values were chosen for the baseline TL field calculation, upon which area statistics was performed. For the Monte Carlo samples, random variables were sampled for each uncertain parameter from Gaussian distributions with the mean and standard distributions shown here.

In this investigation, for each Monte Carlo sample calculation the seabed was treated as a single layer with random range-independent properties (ρ_b, c_b, and α_b). The seabed property values were sampled from a Gaussian distribution based on the mean and standard deviation of the tabulated bottom layer properties found in Jensen *et al.* (2011) for clay, silt, sand, gravel, moraine, chalk, and limestone. The distributions of ρ_b, and α_b were truncated at $\mu \pm 3\sigma$. And, the distribution of c_b was truncated by the properties of clay on the low end and limestone on the high end to ensure that the value of c_b remained physically realistic.

The bathymetry profile for each Monte Carlo sample calculation $D_n(r;\xi_n)$ was the sum the most probable bathymetry profile $D_\mu(r)$, based on available databases and a random fluctuation $\Delta D_n(r)$. Fluctuations in the ocean depth were a function of range r , and were determined through a stochastic process represented by $\xi_n(r)$, such that

$$\Delta D_n(r) = \epsilon D_\mu(r) \frac{\left|\nabla D_\mu(r)\right|}{max\left(\left|\nabla D_\mu(r)\right|\right)} \xi_n(r)\,. \tag{6.1}$$

Based on the work of Lermusiaux et al., (2010), the random fluctuation ΔD_n depends upon the

most probable local depth, the local slope normalized by the maximum slope of the most probable bathymetry profile, and a global parameter $\epsilon = 3\%$, which represents relative deviation from the most probable depth. $\xi_n(r)$ is composed of random weights sampled from a Gaussian distribution with 0 mean and unit variance at each range point in the bathymetry profile. For each Monte Carlo realization in the various ocean environments $\xi_n(r)$ was obtained from 82 to 734 random samples (i.e., one per range point in the bathymetry profile).

Because $\xi_n(r)$ is randomly assigned at each range point and has an equal likelihood of being positive or negative, the resulting bathymetric profiles were made artificially and unrealistically rough. This enhanced roughness was found to lead to enhanced acoustic attenuation that increases with increasing range. To remedy this problem, the mean bathymetry profile and the random portion were smoothed with a sliding boxcar average having a 5-range-point span to produce an nth bathymetry profile:

$$D_n(r;\xi_n(r)) = D_\mu(r) + \Delta D_n(r;\xi_n(r)) \tag{6.2}$$

The description of the SSP, $c(z)$, and the chosen treatment of its randomization has many steps and requires a bit more attention than the other pieces. Information regarding the SSPs within the environments of interest was obtained from privately available ocean databases. The Chen-Millero-Lee equation (Chen & Millero, 1977; Millero & Li, 1994) was used to compute the SSP from temperature, pressure, and salinity. Here, fluctuations in the SSP were treated as a function of depth z , and were attributed to two separate sources: uncertainty in database-provided salinity and temperature profiles and seasonal variation, each determined through stochastic processes γ and ω , respectively. As such, for each n^{th} Monte Carlo sample calculation we write the SSP as

$$c_n(z;\omega_{i,n},\gamma_n) = c_\mu(z) + \Delta c_{\Gamma,n}(z;\gamma_n) + \Delta c_{\Omega,n}(z;\omega_{i,n})\,. \tag{6.3}$$

Here, $c_\mu(z)$ is the most probable SSP at $r = 0$ based on available databases, obtained by taking the month-averaged sound speed at each depth z over 12 months; $\Delta c_{\Gamma,n}(z;\gamma_n)$ is the contribution

to SSP uncertainty due to uncertainty in the temperature $T(z)$ and salinity $S(z)$ of the database-provided SSPs, respectively and depends on a single random weight γ_n for each Monte Carlo sample calculation; and$\Delta c_{\Omega,n}(z;\omega_{i,n})$ is the contribution to the SSP uncertainty due to seasonal variation, which for each n^{th} Monte Carlo sample calculation is a sum of empirical orthogonal eigenfunctions. Each i^{th} eigenfunction was weighted by an independent random weight $\omega_{i,n}$. The random weights γ_n and $\omega_{i,n}$ are sampled from Gaussian distributions with 0 mean and unit variance.

For each Monte Carlo sample calculation $\Delta c_{\Gamma_n}(z;\gamma_n)$ was calculated by using the database-provided temperature $T(z)$ and salinity $S(z)$ profiles and standard deviations $\sigma_T(z)$ and salinity $\sigma_S(z)$. Fluctuations in the temperature and salinity were treated as uncorrelated. Fluctuations in the SSP due to uncertainty in the salinity and temperature were calculated as the product of the standard deviation in $c(z)$ due to fluctuations in $T(z)$ and $S(z)$ and a random weight γ_n , sampled from a Gaussian distribution with zero-mean and unit variance such that

$$\Delta c_{\Gamma,n}(z) = \gamma_n \sqrt{\left(\frac{\partial c}{\partial T}\right)^2 \sigma_T^2(z) + \left(\frac{\partial c}{\partial S}\right)^2 \sigma_S^2(z)}. \tag{6.4}$$

For each Monte Carlo sample calculation a SSP fluctuation $\Delta c_{\Omega,n}(z;\omega_{i,n})$ due to seasonal variation of the SSP was included too. This fluctuation was calculated as a sum of empirical orthogonal functions determined from 12 monthly SSPs. This technique has been previously used to quantifiably describe sound speed fluctuations (Kundu *et al.*, 1975; LeBlanc & M., 1980; Yang & Y., 1999). Each i^{th} eigenfunction was composed of an eigenvalue η_i and an eigenvector $\boldsymbol{v}_i$ and was weighted by an independent random weight $\omega_{i,n}$. The relevant contribution to each of the random SSPs is constructed using a sum over P randomly weighted orthogonal eigenfunctions, where P is the minimum number of eigenfunctions necessary to capture 95% of the variance in the monthly SSPs. As such, P is the minimum integer which satisfies

$$0.95 \leq \frac{\sum_{j=1}^{P} \eta_j}{\sum_{j=1}^{\infty} \eta_j}, \tag{6.5}$$

where η_j is the j^{th} eigenvalue in descending order by magnitude (i.e., η_1 is the largest eigenvalue).

In practice, it was found that P was typically 1 or 2. Hence, for the n^{th} Monte Carlo sample calculation, the SSP fluctuation due to seasonal variation is

$$\Delta c_{\Omega,\ n}\left(z;\omega_{j,n}\right) = \sum_{j}^{P} \omega_{j,n}\sqrt{\eta_j}\boldsymbol{v}_j\left(z\right) \tag{6.6}$$

Thus 2000 Monte Carlo TL field sample calculations were performed using the Range-Dependent Acoustic Model (RAM)(Collins, 1994),each with randomly determined bathymetry, SSP, and seabed properties according to the previously described methods.

The area statistics procedure is based on the assumption that the uncertainty in the TL value at any range-depth (r, z) location in an uncertain ocean sound channel can be represented by spatial variations in TL found near that location in the baseline TL calculation. The area statistics procedure for developing an estimate of PDF(TL) merely requires the baseline TL calculation at the frequency of the sound source, the (r, z) location of interest within the calculated TL field, and an algorithm or recipe for choosing and combining TL values. Given the simple assumption upon which the area statistics technique is based, the primary development effort involved empirically determining how to sample the TL field near the point of interest to achieve acceptable results for the six uncertain environmental parameters.

For the area statistics technique, the baseline TL field calculation may come from any acoustic propagation model. For this investigation, computed TL fields were obtained using RAM.In each case, TL field calculations were performed along an outward radial from a unity-strength harmonic monopole sound source with frequency f_s = 100, 200, or 300 Hz, and depth z_s = 91, 137, or 183 m (300, 450, or 600 ft). The source frequency and a nominal sound speed c_s = 1500 m/s were used to calculate the nominal wavelength, $\frac{c_s}{f_s} = \lambda_s$, where needed.

Using the baseline TL field calculation, a simple algorithm or recipe with four steps was used to produce area statistics results for any range-depth (r ,z) location of interest. First, all the TL values within a range-depth rectangle centered on (r ,z) were collected and weighted uniformly. Second, these TL values were sorted into a histogram. Third, a boxcar average with a span of 5

bins was performed on the histogram to smooth it. Fourth, the smoothed histogram was normalized to form an estimate of the PDF of TL. For this study, the baseline sample-rectangle's range and depth dimensions were $30\lambda_s$ and $13\lambda_s$, respectively, and a nominal histogram bin width of 1 dB was used. These baseline sample-rectangle dimensions were chosen to produce suitable results for the environmental uncertainties defined in Table 6.1. Though, if sufficient resolution of the TL field was provided, the results were often insensitive to factor of two changes in the sample rectangles dimensions. Different sample rectangle dimensions, different TL sample weighting, and other adjustments to the area statistics algorithm may be necessary for alternative treatments of the uncertainties.

The version of RAM used was designed to output TL fields at a fixed number of range-depth points, independent of the size of the environment or calculation field resolution. Thus, for large environments it was necessary to modify the size of the sample rectangle to ensure that a sufficient number of TL sample points were obtained. As such, if fewer than nine columns of TL were obtained in the original box width, the box width was doubled until this condition was met. The minimum number of acceptable columns, nine, was chosen empirically, though fewer columns appeared to function adequately in most cases. Although results are not shown here, it was also found that by increasing the output resolution of the TL field, one can avoid increasing the box size. Such an increase in computational resolution was not taken to ensure that the method was capable of working robustly with the default version of RAM,as it cannot be expected that others implementing area statistics will be inclined to change the PE-solver source code. Of the 4020 test locations in all 10 environments, the area statistics sample area width was increased in roughly 3500 cases, with a little over half of all sample boxes taking on a width of $120\lambda_s$, but with none wider than $240\lambda_s$. In addition, TL samples were not collected from any portion of the sample area lying above the ocean surface or below the ocean floor. When necessary, the bathymetry was linearly interpolated to calculate the water column depth at the range associated with each column of the computational output TL grid.

Figure 6.3 illustrates the area statistics procedure at the range-depth location of (r = 6703 m,

z = 240 m) in Environment 2 for a 200 Hz sound source. In Figure 6.3(a), the TL sample area is indicated by the white box near the center of the TL field plot. The TL sample area is shown in an expanded view in Figure 6.3(b) and is comprised of 1872 individual TL samples. The area statistics-estimated PDF of TL developed from the TL samples in Figure 6.3(b) is shown in Figure 6.3(c).

To assess the accuracy of the estimated PDFs of TL, they were compared with Monte Carlo-generated PDFs of TL that were created from the 2000 separately computed TL values at the location of interest. These 2000 TL samples were sorted into a histogram with 1 dB nominal width bins, and the histogram was normalized to create a PDF of TL. Here the number of Monte Carlo samples (2000) was high enough so that the Monte Carlo-generated PDFs of TL were comparably converged when compared to their counterpart area statistics-estimated PDFs of TL (typically 100 to 1500 samples).

Quantitative comparisons of the area statistics-estimated PDFs of TL (subscript 'AS') and the Monte Carlo PDFs of TL (subscript 'MC') were made with the L_1 error-norm:

$$L_1 = \int_{-\infty}^{+\infty} |PDF_{MC}(TL) - PDF_{AS}(TL)| \, d(TL), \tag{6.7}$$

which can be thought of as the integrated absolute value of the difference between the two PDFs, or perhaps more intuitively as the non-overlapping area of the two PDFs. For PDF comparisons, L_1 is a convenient metric of accuracy because it is a single dimensionless quantity that inherently accounts for differences in the mean, width, and shape of two PDFs. The L_1 error-norm is bounded between 0 and 2, with L_1 = 0corresponding to a perfect match between the two PDFs and L_1 = 2 corresponding to total mismatch (no overlap) of the two of the PDFs. In this study, $L_1 < 0.50$, which corresponds to $\geq$ 75% area overlap, was chosen as the criterion for which an area statistics-generated PDF was deemed engineering-level accurate. This criterion typically corresponded to a difference of < 3 dB mean error (a measure of PDF location) and < 3 dB standard deviation error (a measure of PDF width) at 90% and 97% of test locations, respectively.

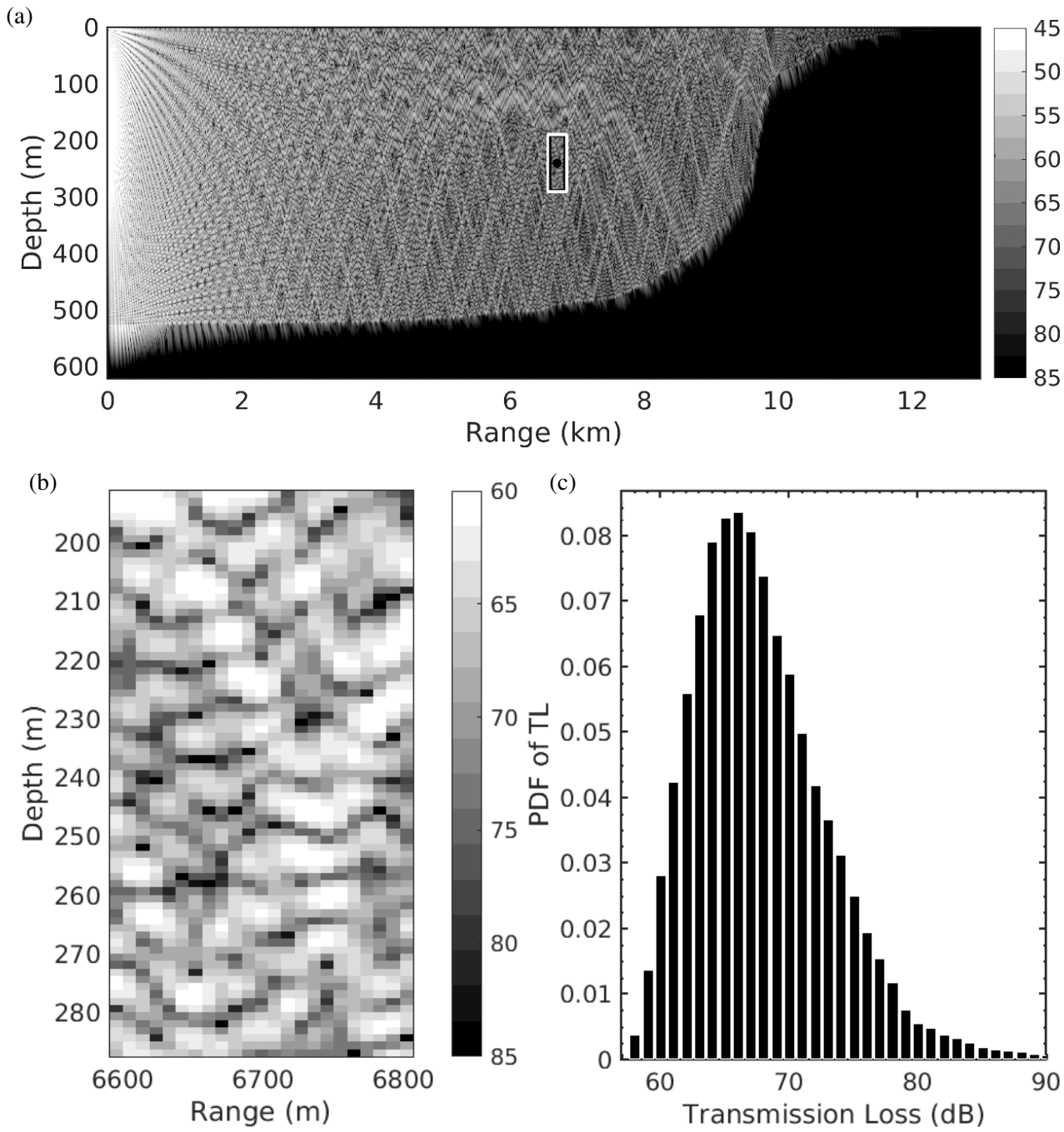

Figure 6.3: Example of Area Statistics Process. (a) Example TL field for a 200 Hz source, in Environment 2, with a $30\lambda_s \times 13\lambda_s$ (range x depth) area statistics sample area centered at range-depth location (r = 6703 m z = 240 m). (b) Expanded area statistics TL sample rectangle from the TL field shown in (a). (c) PDF of TL generated from the TL values collected in the sample area shown in (b).

The L_1 error-norm is illustrated in Figure 6.4 for engineering-level accurate, i.e. $L_1 < 0.5$, in Figure 6.4(a) and inaccurate, i.e. $L_1 \geq 0.5$, in Figure 6.4(b), estimates for the PDF of TL. In both panels, the jagged shaded area is the L_1 error. The result shown in Figure 6.4(a) comes from the range-depth location (r = 6703 m, z = 240 m) in Environment 2, and the mean and standard deviation of the area statistics PDF (solid curve) are respectively 0.3 dB greater than and 0.3 dB less than those of the Monte Carlo PDF (dashed curve). The result shown in Figure 6.4(b) comes from the range-depth location (r = 4472 m, z = 144 m) in Environment 2, and the mean and standard deviation of the area statistics PDF (solid curve) are 2.2 dB less than and 1.0 dB greater than, respectively, than those of the Monte Carlo PDF (dashed curve).

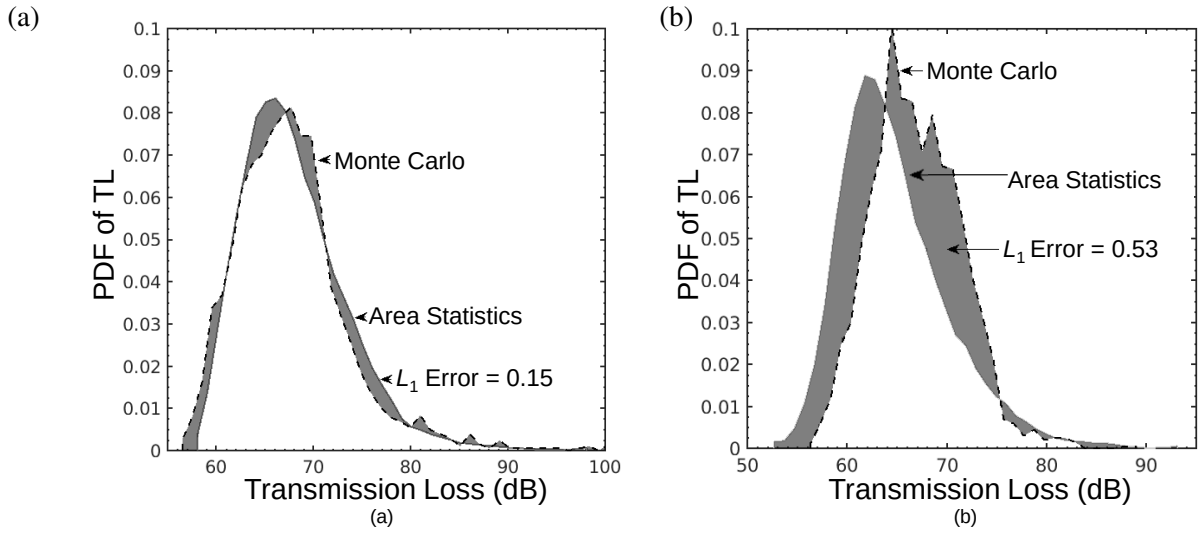

Figure 6.4: Comparison of area statistics- (solid curve) and Monte Carlo (dashed curve) generated TL PDFs. In Environment 2 at range-depth locations (a) r = 6703 m, z = 240 m, and (b) r = 4472 m, z = 144 m. In both panels, the L_1 error is the shaded area. In (a), L_1 = 0.15 while in (b), L_1 = 0.53. With the Monte Carlo PDF assumed to be correct, the mean and standard deviation errors of the area statistics PDFs in (a) are 0.3 dB and 0.3 dB, respectively. In (b), these errors are 2.2 dB and 1.0 dB, respectively. The area statistics-estimated PDF of TL in (a) is considered engineering-level accurate while that in (b) is not.

Results and Comparisons

For an overall accuracy assessment of the area statistics method, the L_1 error from Equation (6.7) was computed on a coarse rectangular grid in each of the ten uncertain ocean environments for sources with frequencies of 100, 200, and 300 Hz and depths of 91, 137, and 183 m (300, 450, 600 ft). The single exception to this is Environment 1, where the 183 m source depth was beneath the ocean floor and therefore was not considered. Hereafter, each Environment-source frequency-source depth combination is referred to as a test "case" and within each, the locations at which the L_1 error is computed are referred to as a test "locations". The results are shown in Figure 6.5 as a grid of test locations overlaid on the baseline TL field for a 200 Hz source at 137m depth, in each environment. Test locations were nominally chosen to occur at fractional intervals of one-twentieth the maximum range and one-eleventh of the maximum water column depth. However, the exact position of each location was adjusted to align with the computational grid spacing, and test points below the ocean floor were not considered. In each panel of Figure 6.5, a white circle indicates a test location where the area statistics-estimated PDF of TL was found to be engineering-level accurate ($L_1 < 0.5$), whereas a black triangle indicates a test location where engineering-level accuracy of the area statistics-estimated PDF of TL was not achieved ($L_1 \geq 0.5$). Additionally, test locations where the minimum area statistics sample TL value was greater than 100 dB were also not considered, and are not included in the results here. Ultimately, area statistics PDFs were compared with Monte Carlo PDFs for 87 test cases and 11,436 test locations in total.

In the ten environments considered, area statistics produced PDFs of TL with L_1 errors less than 0.5 at 86, 92, and 94 % or more of test locations for source frequencies of 100, 200, and 300 Hz, respectively. A quantitative summary of these results is provided in Table 6.2. Area statistics performed consistently well, within Environments 1 and 3-10. In these environments, engineering-level accuracy was achieved for 94% of tests and the mean L_1 error was just 0.25. In Environment 2, area Statistics achieved engineering level-accuracy in only 56% of cases, and the mean L_1 error was 0.51.

We hypothesize that the poor performance of area statistics in Environment 2 resulted from the combined effects of the short range of the environment (12 km) and the relatively little uncertainty associated with the SSP from both seasonal variation and temperature and salinity fluctuations. In practice, little variability in the SSP leads to narrower and taller Monte Carlo-generated PDFs of TL near the source that are not well captured by area statistics. And while small variations in the SSP create small variations in the TL field near the source, they produce greater variations in the TL field once propagated further down range. For example, in Environment 10, where the SSP variability is also low, area statistics achieved engineering-level accuracy in only 64% of test locations within the first 12 km of range, but performed much better further down range. To further test this hypothesis, a separate set of Monte Carlo sample runs was performed for Environment 2, in which the eigenvalues used to capture the seasonal SSP variation, η_j, were artificially increased by tenfold. The resulting percentage of engineering-level accurate test locations across all frequencies increased from the original 54% to 78% for the 137 m source depth. Hence we infer that for area statistics to succeed near the source, there must be sufficient sound speed variability.

To ensure that the number of Monte Carlo samples (2000) was high enough that the Monte Carlo-generated PDFs of TL were comparably converged when compared to their counterpart area statistics-estimated PDFs of TL (typically 100 to 1500 samples). A sensitivity analysis that involved decreasing the number of Monte Carlo samples to 1500 for each test location resulted in little appreciable change. Specifically, when compared to the 2000 sample results, 59 of the 87 cases experienced no change in the overall percentage of engineering level accurate (L_1 <0.5) test locations. In 27 of the remaining 28 cases the change was $\leq$ 2%, with the one outlier changing by 4%. In total, less than 0.6% of the 11436 test locations changed whether or not they were engineering level accurate and the L_1 errors when comparing the area statistics PDF to the 1500 and 2000 sample Monte Carlo PDFs differed by 0.03 or less in 99 % of tested locations. The Individual PDF shapes showed only occasional small variations at the extremities. These differences tended to be due to statistically unlikely, outlying sample cases which cannot be avoided when taking a large number of random samples.

The computational effort associated with area statistics was also compared to that associated with the Monte Carlo calculations using MATLABs tic and toc functions. As might be expected, given its simple formulation, area statistics is significantly more efficient than Monte Carlo calculations. With the baseline TL calculation as a starting point for both approaches, area statistics does not require another TL field calculation whereas the Monte Carlo approach as implemented here involves 1999 more. Thus, the difference in computational burden is substantial. For a single location, the Monte Carlo calculations (using 10 Pad terms and a computational range $\times$ depth resolution of $\lambda_s/1.25 \times \lambda_s/12$ in RAM's PE solver) required between 11 thousand and 5.8 million times more computational effort than area statistics, depending on the environment and frequency. The mean and median ratio of computational effort required for the Monte Carlo-generated PDFs to that required for the area statistics-generated PDFs were both on the order of one million. In general, it was noted that the more expensive a single field calculation was, the greater the speedup achieved by area statistics. Additionally, once the baseline TL calculation is complete, area statistics can provide PDFs of TL in milliseconds of real time, making it practical for real-time applications of TL uncertainty.

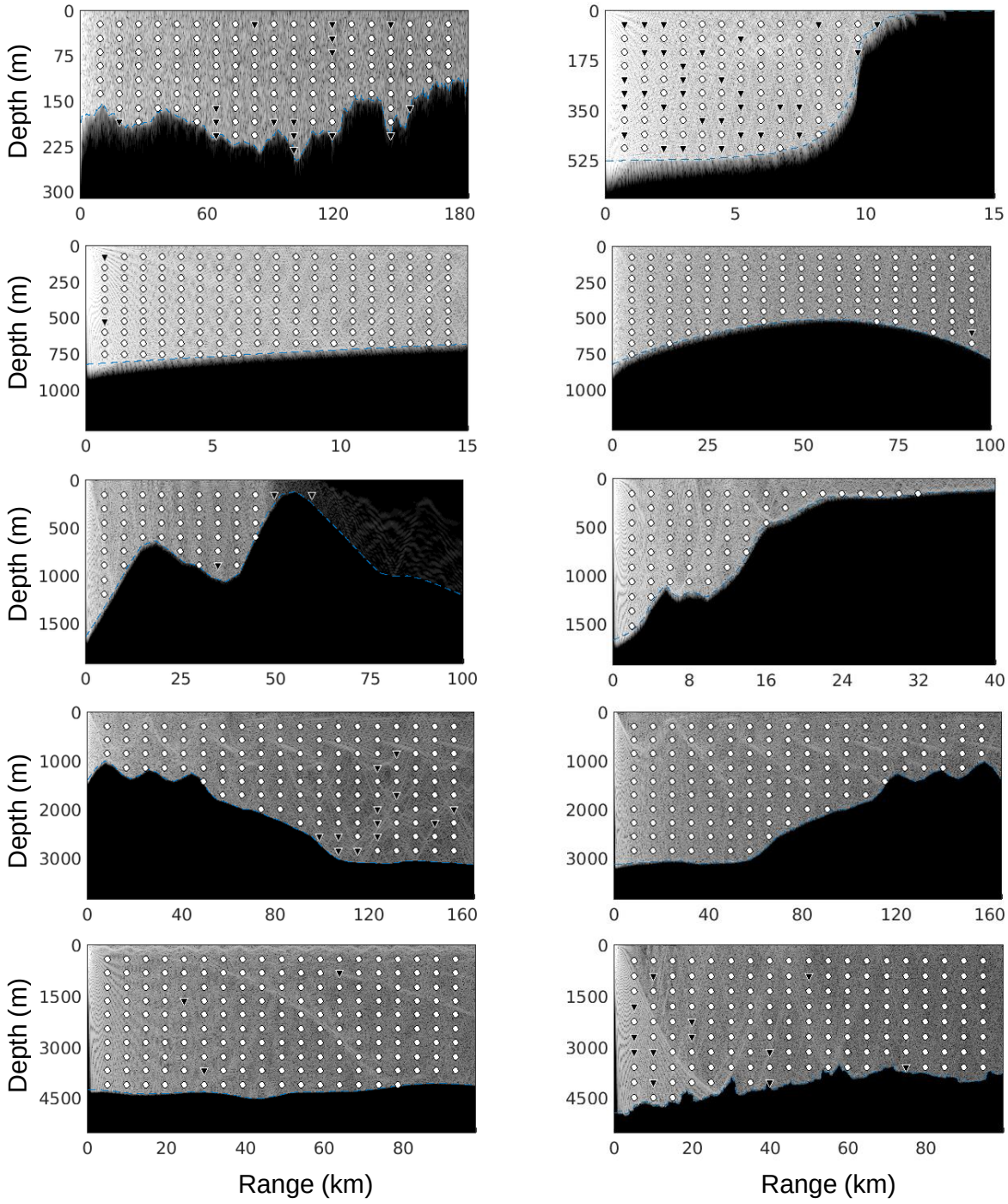

Figure 6.5: TL fields with area statistics test locations and indication of success vs failure at each. For the ten environments shown in Figure 6.1 with a 200 Hz source, Markers indicate locations where area statistics and Monte Carlo-generated PDFs of TL were compared. White circles indicate locations where area statistics results compare favorably with those from Monte Carlo calculations ($L_1 < 0.5$). Black triangles indicate locations where such comparisons are unfavorable ($L_1 \geq 0.5$).

6.4 Summary and Conclusions

This paper describes the area statistics technique for efficiently estimating transmission loss (TL) uncertainty in underwater acoustics. The technique is based on the idea that the TL variation found near the point of interest in real space is similar to that found at the location of interest when environmental parameters are varied as described here. The technique is simple and can be used to produce approximate PDFs of TL in uncertain ocean sound channels from a single (baseline) TL field calculation completed using the most probable value for each uncertain parameter. To implement the technique, TL values near a location of interest in the baseline TL field are collected and sorted into a histogram that is smoothed and normalized to obtain an approximate PDF of TL at the location of interest. To determine the technique's accuracy, PDFs of TL created using area statistics were compared to PDFs generated using 2000 sample Monte Carlo calculations in ten different ocean environments at three source frequencies f_s = 100, 200, and 300 Hz at three different source depths z_s = 91, 137m, 183m (300, 450, 600 ft). The area statistics-generated PDFs of TL achieved engineering-level accuracy ($L_1 < 0.5$) in 91% of test locations overall.

The effort reported here supports the following three conclusions. (1) The area statistics technique is a viable alternative, or worthy complement, to Monte Carlo calculations or other more computationally intensive techniques for estimating the uncertainty of TL field calculations in uncertain ocean environments with sufficient range and/or sound speed uncertainty. In this investigation, the technique produced engineering-level accuracy at 94% of sample locations in the 9 environments considered with greatest sound speed variability. The technique was far less successful in the single outlying environment that was short range and had little sound speed variability, achieving engineering-level accuracy in only 56% of test locations. (2) The area statistics technique is so simple and computationally inexpensive that it should be implemented even when a more reliable but more computationally demanding approach is the primary means for TL uncertainty estimation. As part of this investigation, the area statistics approach was found to require less than one-millionth of the computational cost of the Monte Carlo calculations for the cases

considered here. Thus, the computational penalty for implementing both, if the latter is preferred, is vanishingly small. Moreover, the technique is computationally inexpensive enough for use in real time applications. (3) The sample rectangle size, TL sample weighting, and other implementation details of the area statistics algorithm described here are likely to need adjustment if the ocean sound channel uncertainties of interest differ from those given in Table 6.1. The area statistics technique is ad-hoc and the implementation parameters in its current formulation were tuned to achieve a high percentage of engineering-accurate predictions for ocean sound channels with the uncertainties specified in Table 6.1 and in the ocean data bases used here. However, the uncertainties specified in Table 6.1 are generic and may serve as a useful starting point for many uncertain ocean sound channels. Thus, the area statistics formulation provided here may be broadly applicable.

Environment Number	Source Depth (m)	Average L_1			% of test locations with $L_1 \leq 0.5$		
		Source Frequency f_s (Hz)			Source Frequency f_s (Hz)		
		100	200	300	100	200	300
1*	91	0.32	0.29	0.32	87	93	95
	137	0.31	0.34	0.33	90	89	92
2	91	0.68	0.44	0.37	34	69	78
	137	0.63	0.48	0.4	33	61	69
	183	0.7	0.49	0.38	29	59	76
3	91	0.21	0.18	0.19	91	98	98
	137	0.2	0.17	0.16	94	98	100
	183	0.19	0.16	0.15	95	98	100
4	91	0.24	0.25	0.23	98	98	99
	137	0.23	0.21	0.24	99	99	100
	183	0.22	0.22	0.24	100	100	98
5	91	0.33	0.34	0.35	90	88	80
	137	0.28	0.27	0.3	92	94	92
6	183	0.23	0.25	0.26	98	93	96
	91	0.29	0.28	0.26	92	90	98
	137	0.29	0.21	0.24	87	100	100
	183	0.27	0.22	0.21	94	97	100
7	91	0.32	0.28	0.27	91	96	93
	137	0.3	0.28	0.24	91	91	98
	183	0.28	0.26	0.26	92	93	98
8	91	0.26	0.23	0.22	96	98	96
	137	0.26	0.2	0.2	93	100	99
	183	0.24	0.21	0.21	96	96	99
9	91	0.25	0.26	0.28	95	94	97
	137	0.24	0.24	0.26	95	98	97
	183	0.25	0.23	0.26	94	98	97
10	91	0.34	0.31	0.33	79	89	85
	137	0.36	0.3	0.3	81	92	91
	183	0.32	0.29	0.31	85	91	89
Average	91, 137, 183	0.30	0.27	0.26	86	92	94

Table 6.2: Summary of L_1 error of area statistics-generated TL PDFs, compared to Monte Carlo-generated PDFs. Results for source frequencies f_s = 100, 200, and 300 Hz and source depths z_s = 91, 137, and 183 (300, 450, and 600 ft) in each of the ten environments. *A 183m source depth could not be tested in Environment 1 as this would put the source beneath the ocean floor.

Appendices

Appendix A

Appendices for Chapter 3

A.1 Order of magnitude analysis of vorticity-generation mechanisms

To quantifiably compare the various mechanisms by which vorticity changes in the flow we perform an order of magnitude analysis on each term of the vorticity transport equation (3.8). Initially, there is no vorticity. Given the present problem set-up, the only mechanism that can lead to the production of vorticity is the baroclinic torque, which is clearly non-zero during the interaction of the ultrasound wave with the interface since the pressure (wave) and the density (interface) gradients are misaligned. For this reason, we focus on the relative magnitude of each term during the interaction time, $\Delta t_a \approx 5\ell/c_{water}$. Since the average perturbation amplitude during the interaction is sufficiently small ($\sim 0.96a_0$), we assume the interface remains static and undeformed throughout the interaction, such that the density gradient is approximately constant. We treat the divergence and magnitude of curls/gradients of quantity f as $\sim \Delta f/\Delta L$, where ΔL is the problem's characteristic length scale. Since flow is driven by the acoustic wave $\Delta p = \Delta p_a$, $\Delta u = \Delta u_a$, and $\Delta\rho = \Delta\rho_a$, where the subscript $_a$ denotes acoustic quantities. The quantities are related according to (Anderson, 1990),

$$\Delta p_a = \pm\Delta u_a \rho c = c^2 \Delta\rho_a. \tag{A.1}$$

Since $a_0/\ell \ll 1$ (indicating small misalignment between $\nabla\rho$ and ∇p), we can approximate $\sin\theta \approx \theta$. It thus follows that the magnitude of the baroclinic term is

$$\left\| \frac{\nabla\rho \times \nabla p}{\rho^2} \right\| = |\nabla\rho||\nabla p| \sin\theta| = O\left(\frac{|\Delta\rho_I|}{|\Delta L_I|} \frac{|\Delta p_a|}{|\Delta L_a|} \frac{1}{|\rho|^2} |\theta| \right). \tag{A.2}$$

where $\Delta\rho_I$ is the density jump across the interface, Δp_a is the pressure amplitude of the wave, ΔL_I is the characteristic length of the interface (thickness) and ΔL_a that of the wave (wavelength). Approximating the vorticity as of equal magnitude to the baroclinic term, the dilational term can be estimated as

$$||-\boldsymbol{\omega}\,(\nabla \cdot \boldsymbol{u})|| = O\left(\frac{|\Delta u_a|}{|\Delta L_a|} \frac{|\Delta\rho_I|}{|\Delta L_I|} \frac{|\Delta p_a|}{|\Delta L_a|} \frac{1}{|\rho|^2} |\theta| \right). \tag{A.3}$$

Making use of Equation (A.1), the relative magnitude of the baroclinic to dilational terms is:

$$\frac{\left\| \frac{\nabla\rho \times \nabla p}{\rho^2} \right\|}{||-\boldsymbol{\omega}\,(\nabla \cdot \boldsymbol{u})||} \sim O\left(\frac{|c|}{|\Delta u_a|} \right) = O\left(\frac{|\rho|}{|\Delta\rho_a|} \right) \tag{A.4}$$

To evaluate the above expressions for comparison with our computational results, we consider our base trapezoidal wave case where $p_a = \Delta p_a = 10$ MPa. The length scale associated with the acoustic wave is the initial length of the pressure compression $\Delta l_a = 5\ell$. The initial interface length scale ΔL_i, defined as the thickness of the mixed layer from $\alpha = 0.05$ to 0.95 volume fraction of water is estimated as $\Delta L_i \approx 0.05\ell$. We approximate the order of θ based on its average value along a half-wavelength of the interface for $a_0 = 0.03\ell$ such that the average value of $|\theta| \approx 0.12$. evaluating expression (A.4) we to find that $|c|\,/\,|\Delta u_a| = O\left(10^2\right)$ and thus expect that the relative contribution of baroclinic to compressible/advective vorticity generation is approximately of order $O\left(10^2\right)$ at $t = \Delta t_a \approx 5$.

To compare our computational results to the analysis we consider the integral of the vorticity

and vorticity generation terms over the right-half domain,

$$\Gamma = \int_{A_{rh}} \omega \, dA_{rh}, \tag{A.5}$$

where $\int_{A_{rh}} dA_{rh} = \int_{-\infty}^{+\infty} \int_{\ell/2}^{\ell} dy\, dx$. Only the right-half domain is considered because the total circulation over the whole domain is 0 due to symmetry. Circulation is chosen as the quantity of comparison as it is a global quantity, which better captures the overall vorticity dynamics than the vorticity at any single point. As a single quantity rather than a field, it is also simpler to compare the computational and analytical results. The relative order of magnitude relationships obtained in (A.4) are spatially independent and expected to hold when integrated over the right-half domain. Accordingly we evaluate the vorticity generation terms from our computational results integrated over the right-half domain. At $t \approx 5.0$ we find that

$$\frac{\int_{A_{rh}} \left[\frac{\nabla\rho \times \nabla p}{\rho^2}\right] dA_{rh}}{\int_{A_{rh}} \left[-\boldsymbol{\omega}\left(\nabla \cdot \boldsymbol{u}\right)\right] dA_{rh}} = \mathcal{O}\left(10^2\right). \tag{A.6}$$

Hence the computational results and analysis are in agreement and suggest that the vorticity is nearly entirely baroclinic.

A.2 Convergence: interface length per unit circulation, $s(t)/\Gamma(t)$

We investigate the convergence of the results in Figure A.1 for Γ/s, which is the relevant quantity of interest. The presented results are based on simulations run at a resolution of 100 points/ℓ in both the horizontal and vertical directions. At this resolution, neither the circulation or the interface amplitude are fully converged, though the qualitative behavior of each does not appear to very greatly with increasing resolution. Figure A.1 shows plots of interface length per unit circulation, $s(t)/\Gamma(t)$ for variable resolutions of 50, 75, 100, and 125 points/ℓ. Overall the results are converging to the solution on the finest grid. While the early-time behavior shows discrepancy, the late-time behavior appears to have largely converged to asymptotic growth. Although the numerical value

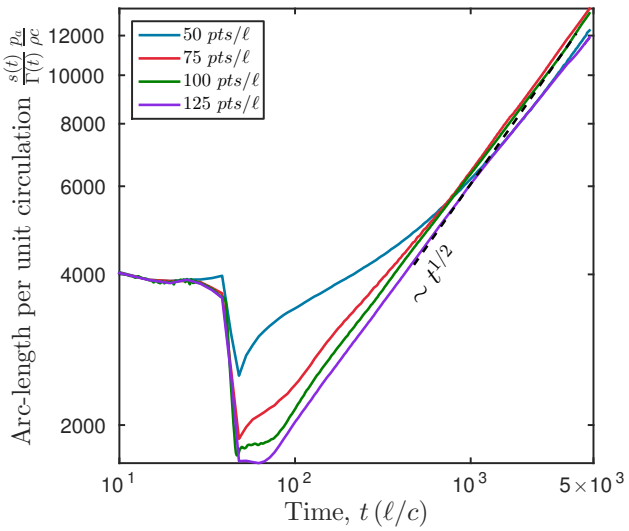

Figure A.1: Convergence of the interface length at long times. Interface length histories $s(t)$ scaled by the inverse circulation density per unit input pressure, $[(\Gamma(t)/s(t))/p_a]^{-1}$. Curves are shown for the baseline 10 MPa trapezoidal wave cases or variable x and y resolution: 50 pts/ℓ (blue) 75 pts/ℓ (red), 100 pts/ℓ (green), 100 pts/ℓ (purple). For comparison sake, time has been shifted by t_p such that the instant the phase inverts occurs simultaneously in each case. The black dashed line above the curves at late times corresponds to power law growth with $t^{1/2}$.

of the time exponent of the growth may be sensitive to the grid resolution, the qualitative behavior does not appear to change. To obtain accurate quantitative measurements of the time exponent, finer simulations would have to be conducted, which would be computationally prohibitive given the exceedingly long run time.

Plots of circulation and amplitude for 50, 75, and 100 cells per ℓ are also presented in Figure . It can be seen that while neither the interface amplitude or circulation are completely converged, there values appear to change little with increasing resolution.

A.3 Vorticity distribution

To better understand the distribution of vorticity generation within the gas-liquid mixture region of the interface we perform an order of magnitude analysis to compare the baroclinic vorticity from equation (A.2) in pure water vs air. As this can already be evaluated in water from what we have provided up to this point, we will focus on evaluation of the order of baroclinic vorticity generation

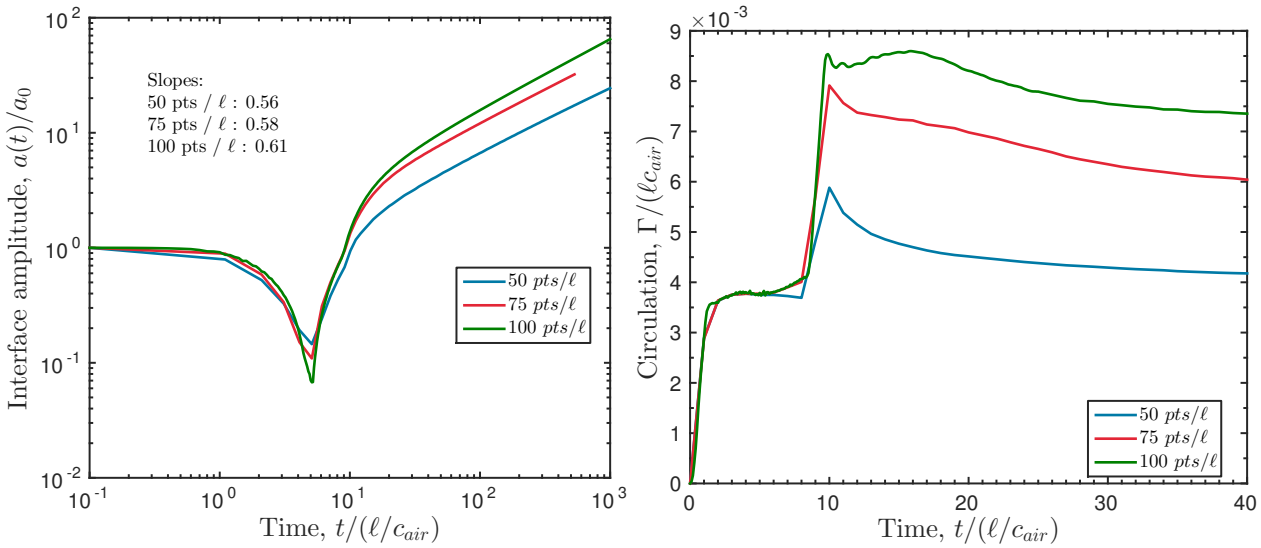

(a) Interface amplitude $a(t)$

(b) Circulation $\Gamma(t)$

Figure A.2: Convergence of the interface amplitude and circulation. Interface amplitude and circulation histories are presented for increasing resolution 50, 75, and 100 cells per domain width/dimensionless length scale ℓ

in air.

Throughout this analysis we will denote the properties of the incoming wave and water with a subscript $-$, and the transmitted wave and air with a subscript $+$. For water, we will use the values for $\Delta\rho_I, \Delta L_I, \Delta\rho_a, \Delta L_a$ and θ previously defined in Appendix A.1, based on our initial condition. Our treatment of the density gradient across the interface will remain unchanged for evaluation in air such that $\Delta\rho_I^- = \Delta\rho_I^+$ and $\Delta L_I^- = \Delta L_I^+$. To evaluate the remaining terms in air we will borrow techniques from linear acoustics. To find the pressure rise in the transmitted wave Δp_a^+, we recognize that $a_0/\ell << 1$ and treat the incoming wave as a plane wave impinging normally on a flat material interface such that $\Delta p_a^+ = \boldsymbol{T}\Delta p_a^-$, where $\boldsymbol{T}$ is the acoustic transmission coefficient, $\boldsymbol{T} = 2\rho^+c^+/(\rho^+c^+ + \rho^-c^-)$ (Kinsler *et al.*, 1982). For our water-air interface $\boldsymbol{T} \approx 4.97 \times 10^{-4}$. Because of the strong impedance mismatch between fluids, the acoustic wave is almost entirely reflected, decreasing the pressure gradient in the air. Because of the drop in sound speed across the interface, the transmitted wave is compressed into a smaller physical area (i.e., the wavelength decreases) relative to the incoming wave, such that $\Delta L_a^+ = \Delta L_a^-(c^+/c^-)$. This effect increases the pressure gradient in the air. To evaluate θ^+, we utilize Snell's law which states that $c^- \sin\theta^- = c^+ \sin\theta^+$.

Because $a_0/\ell << 1$ it is also true that $\theta^- << 1$, thus we use the small angle approximation of sin to find that $\theta^+ \approx \theta^-(c^+/c^-)$. This refraction effect decreases the misalignment between the pressure and density gradients for the transmitted wave relative to the incoming wave. Quantitatively it also approximately cancels the increase in vorticity deposition that arises as a result of the increased pressure gradient created by the decrease in the length of the transmitted wave.

To get an idea of where within the mixed gas-liquid region at the interface the vorticity will be generated, we consider equation (A.2) in air and water and write the ratio to find

$$\begin{aligned}\frac{\left\|\frac{\nabla\rho\times\nabla p}{\rho^2}\right\|_{air}}{\left\|\frac{\nabla\rho\times\nabla p}{\rho^2}\right\|_{water}} =& O\left(\frac{\left[\frac{|\Delta\rho_I^+|}{|\Delta L_I^+|}\frac{|\Delta p_a^+|}{|\Delta L_a^+|}\frac{1}{|\rho^+|^2}|\theta^+|\right]}{\left[\frac{|\Delta\rho_I^+|}{|\Delta L_I^+|}\frac{(|\Delta p_a^+|/|\boldsymbol{T}|)}{|\Delta L_a^+|(|c^+|/|c^-|)}\frac{1}{|\rho^-|^2}(|c^+|\,/\,|c^-|)|\theta^+|\right]}\right), \\ =& O\left(|\boldsymbol{T}|\left(\frac{|\rho^-|}{|\rho^+|}\right)^2\right). \end{aligned} \tag{A.7}$$

For our water-air interface, we evaluate equation (A.7) to find that the ratio of baroclinic vorticity generation in air to that in water would be of order $O\left(10^2\right)$. While this analysis considers vorticity generation in pure air and water, as opposed to the mixed fluid region that is exactly relevant to this work, we make two observations based on this result. First, this result analysis is for an extreme case in which all of the vortical energy relevant to this problem, is able to be concentrated in pure air and water, and thus this result acts as an upper bound on the change in vorticity deposition we expect as the wave move from water across the interface into air. Additionally, this result suggests that for the mixed water-air region, where the strongest density gradient exists, vorticity generation is likely to occur in gas dominated fluid regions with a higher volume fraction of air than water.

From the vorticity contours at $t = 1.0$ shown in 3.6, the vorticity is clearly concentrated in the region with volume fraction of water $\alpha < 0.5$. To quantify this, numerically integrating the vorticity over the right-half domain we find that 97% of the circulation occurs in this region. To further illustrate the dependence of the vorticity deposition on the relative gas-liquid composition of the fluid within the interface region, Figure A.3 shows a scatter plot of the vorticity values in each cell vs the mean volume fraction of water in the cell $< \alpha >$ (Left). The average circulation per-cell

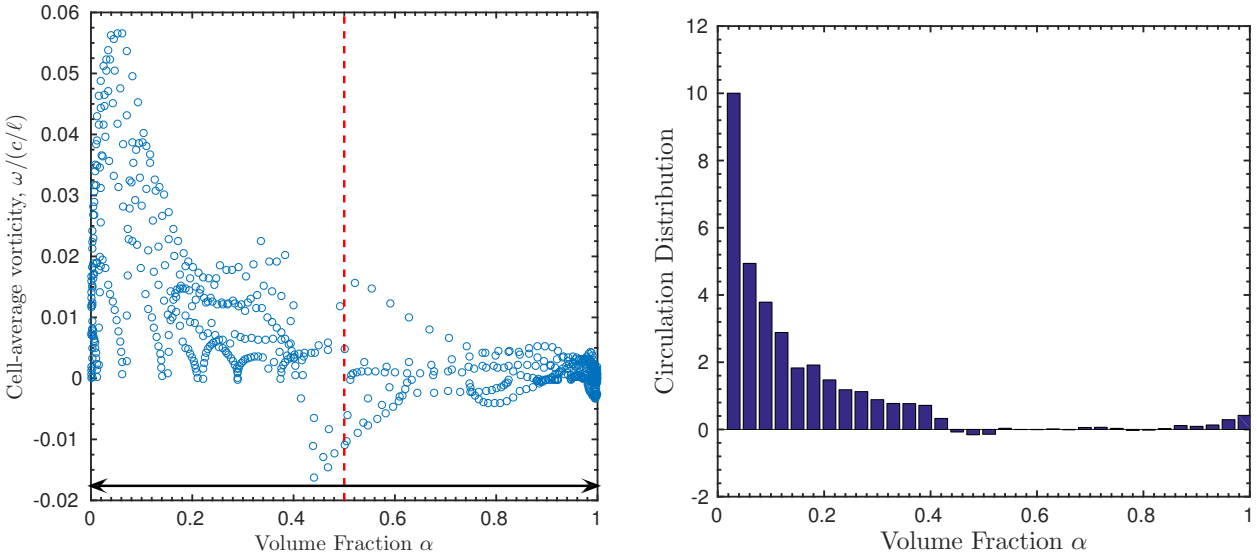

Figure A.3: Dependence of vorticity on volume fraction across the interface. For cells with non-negligible vorticity, a scatter plot of the mean vorticity in each cell is plotted as a function of volume fraction water (Left).

is seperated into bins based on the relevant volume fraction to obtain a histogram and normalized to obtain the circulation distribution circulation as a function of α (Right). The observed circulation deposition in air-dominated fluid, $\alpha < 0.5$, and is within the predicted upper bound. This is qualitatively consistent with our analysis.

A.4 Numerical treatment of the initial interface

The prescribed interface thickness parameter (typically $\delta = 0.08\ell$) was used to determine the initial volume fraction and density condition where the a distance parameter from the interface is defined as

$$d = \frac{\delta + y(x)_{interface} - y}{2\delta}.$$

and the initial Volume fraction is written as

$$\alpha = \begin{cases} 1, \\ exp\left(log\left(10^{-16}\right)|d|^8\right), \\ 0, \end{cases}$$

such that d is normalized within the mixed air-water region.

Theoretical vs simulated reflection coefficients

To ensure that the numerical implementation of the interface is sufficiently captures the dynamics of a discontinuous interface, the simulated acoustic reflection coefficient $\boldsymbol{R}_S$ was calculated for the case of the 10 MPa trapezoidal wave for the prescribed thickness parameter δ and compared to the theoretical acoustic reflection coefficient $\boldsymbol{R}$, where,

$$\boldsymbol{R}_{\boldsymbol{theoretical}} = \frac{(\rho c)_{air} - (\rho c)_{water}}{(\rho c)_{air} + (\rho c)_{water}} = 0.999$$

$$\boldsymbol{R}_{simulated} = \frac{p_R}{p_I} = \frac{-p_{reflected} - p_{atm}}{p_a - p_{atm}} = 0.991.$$

Thus for default value $\delta_0 = 0.08\ell$, the calculated reflection coefficient for the simulation was approximately within 1% of the theoretical reflection coefficient. This reflection is illustrated in Figure A.4, which shows snapshots of the pressure field at several times throughout and after the passage of the wave. To determine the sensitivity of the simulations to changes in δ, the simulated reflection coefficient is calculated for $delta = 0.02\ell, 0.04\ell, 0.08\ell$, and 0.16ℓ in Figure A.5. It is found that $\boldsymbol{R}_{simulated}$ is approximately constant for $\delta_0/4 \leq \delta \leq 2\delta_0$.

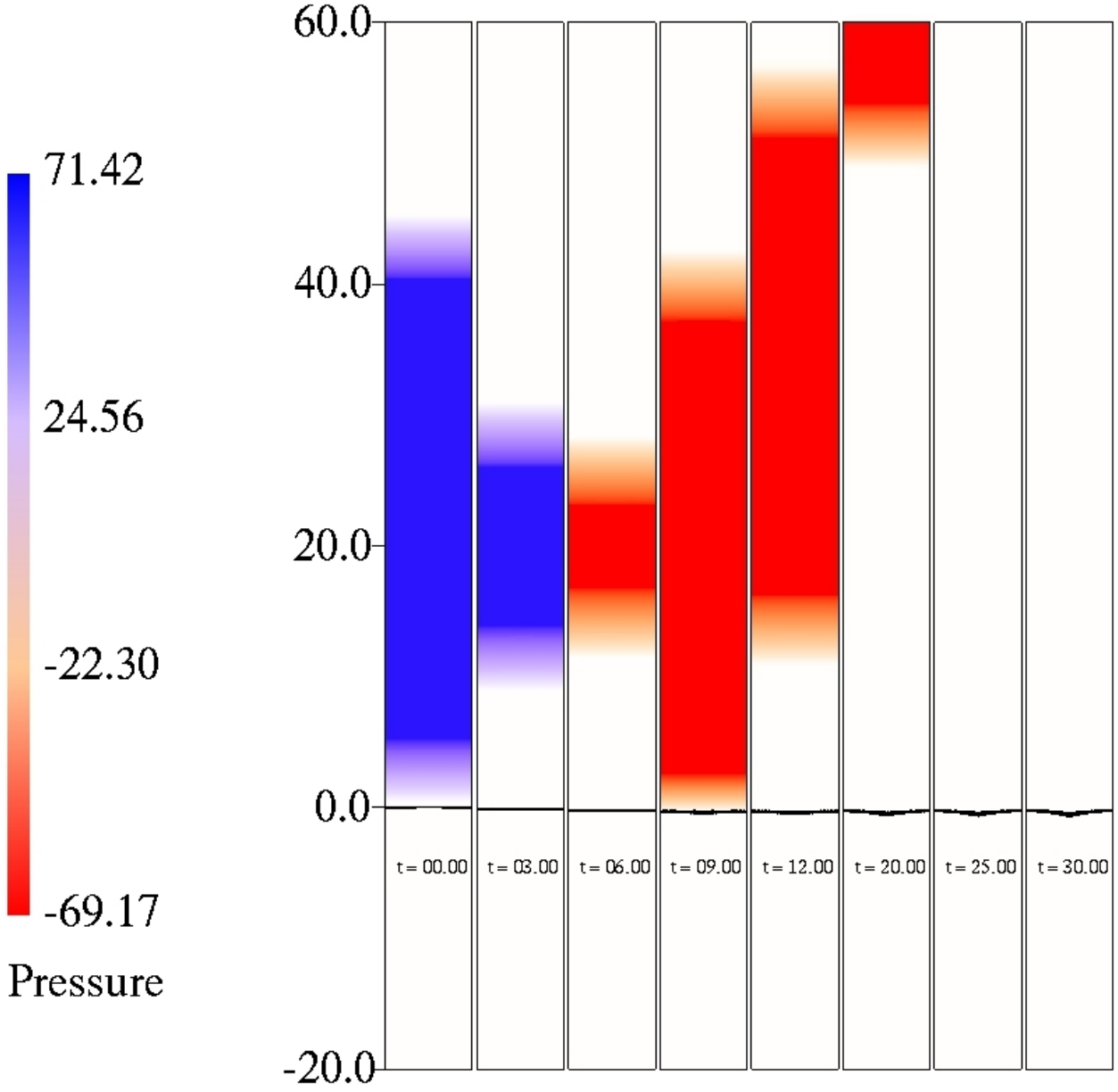

Figure A.4: Evolution of the pressure field for the $p_a = 10$ MPa trapezoidal wave. Snapshots of pressure throughout the waves time in the domain and shortly thereafter at $t/(\ell/c_{air}) = 0, 3, 6, 9, 12, 25$, and 30. We observe that once the wave leaves the domain at approximately $t/(\ell/c_{air}) = 21$, after which noticeable reflections do not occur.

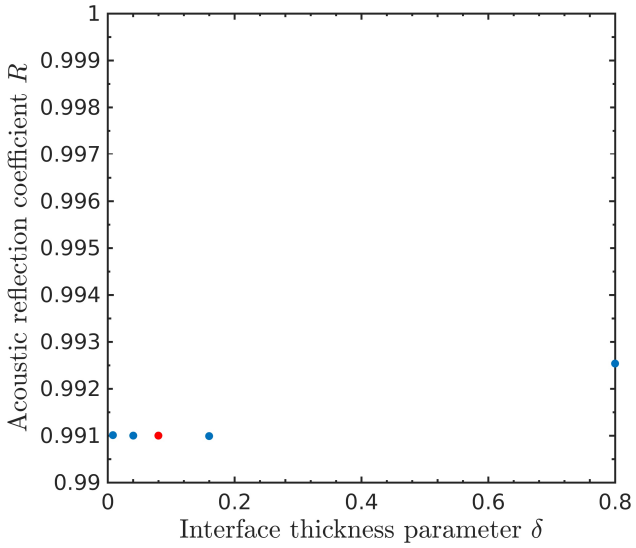

Figure A.5: Numerical reflection coefficient at the interface vs interface thickness parameter δ. The reflection coefficient $\boldsymbol{R}$ based on calculated wave amplitudes is shown for various values of the interface thickness parameter $\delta = 0.01, 0.04, 0.08$, and 0.16. The default value for results in chapters 3 and 4 is $\delta = 0.08$ and indicated in red. The computed reflection coefficient appears to be approximately constant at $\boldsymbol{R}_{computed} = 0.991$ for the range of interface thicknesses considered here.

A.5 Perturbation growth for the -10 MPa trapezoidal wave

To demonstrate that the long term growth of the interface does not require a positive definite wave, a trapezoidal wave with -10 MPa amplitude used to drive the perturbed water-air interface of Chapter 3. The amplitude growth and The amplitude growth (left) and circulation (right) are shown in Figure A.6. The late time growth goes as $t^{0.61}$ and as consistent with that driven by the positive trapezoidal wave. The total circulation deposited after the passage of the wave is similar order of magnitude to that left by the positive trapezoidal wave.

The nature of the circulation deposition for the negative wave is somewhat different from that of the positive wave. The initial rarefaction of the negative wave causes the immediate growth of the interface perturbation while simultaneously creating baroclinic vorticity. By the time the compression arrives near the end of the wave, the interface amplitude has grown appreciably, such that there is greater misalignment between the pressure gradient of the compression wave and the interface density gradient. Consequently the compression creates vorticity of opposite

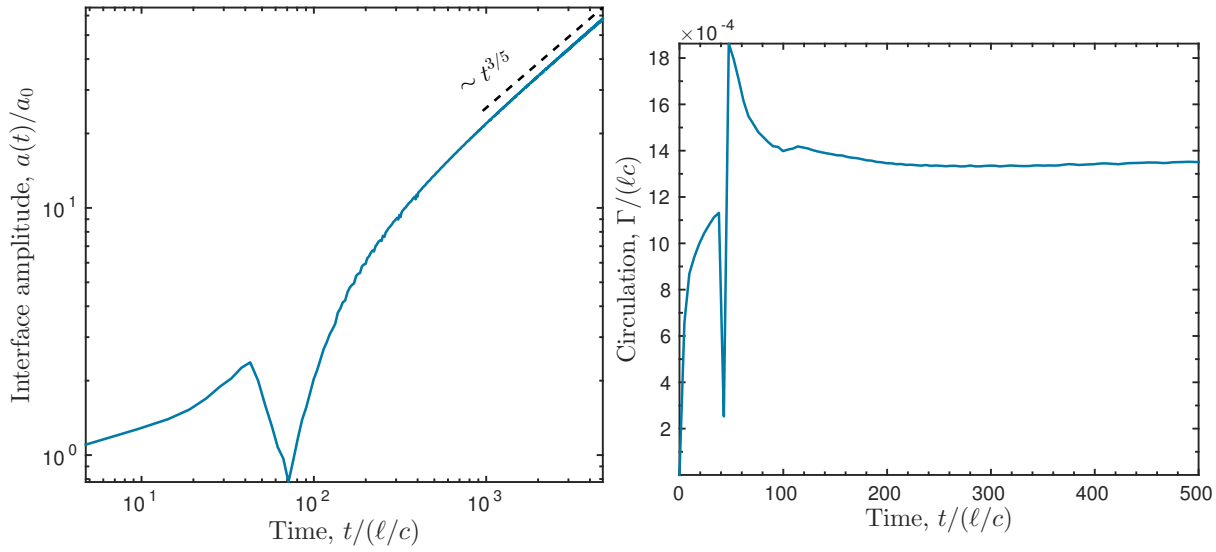

Figure A.6: Perturbation amplitude (left) and circulation (right) histories for the -10 MPa trapezoidal wave. The growth follows a power law in time with exponent ≈ 0.61, and is thus consistent with the results for the positive wave shown in Chapter 3.

sine, but greater magnitude than that of the earlier rarefaction. This is in contrast to what was previously observed for the positive wave, for which the compression deposited baroclinic vorticity and also drove the perturbation of the interface to phase invert before the rarefaction occurred. Thus changing the direction of the interface density gradient such that the baroclinic vorticity created by the rarefaction was of the same sine as that created by the compression.

A.6 Perturbation growth for the 10 MPa sinusoidal wave

To demonstrate the growth of the interface driven by a simple wave with both positive and negative parts, a sinusoidal wave (positive pressure followed by negative) with 10 MPa amplitude is used to drive the perturbed water air interface of Chapter 3. The amplitude growth and The amplitude growth (left) and circulation (right) are shown in Figure A.7. The late time growth goes as $t^{0.66}$ which is faster than that observed for the positive and negative trapezoidal wave. However we note that this simulation was only able to run for half as long as those of Chapter 3, and at the end of the simulation the exponential growth rate appears to be decreasing in time. The total circulation deposited after the passage of the wave is similar order of magnitude to that left by the positive

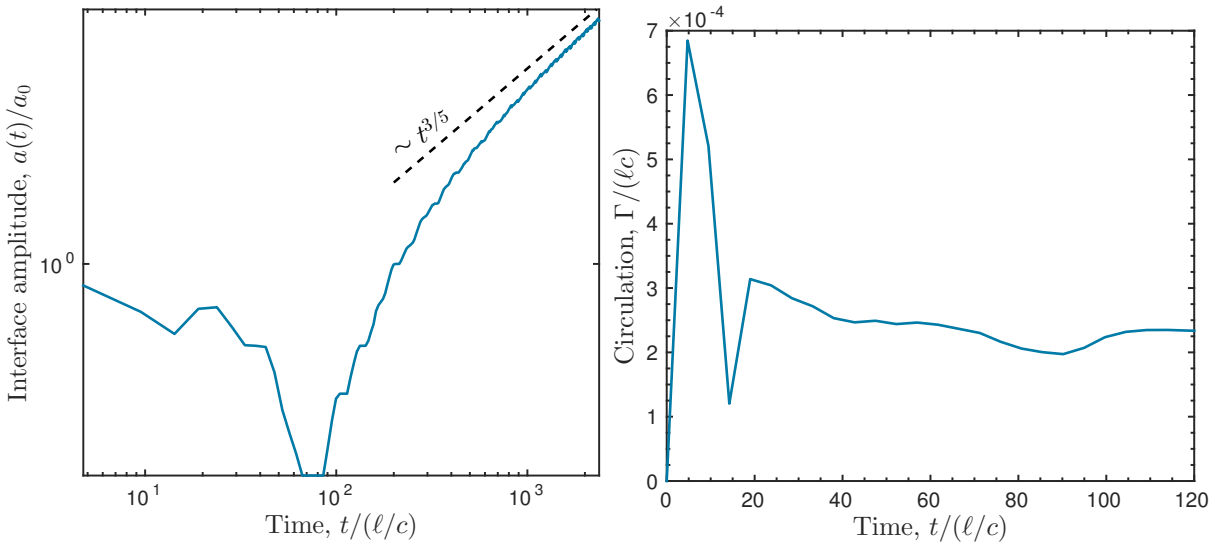

Figure A.7: Perturbation amplitude (left) and circulation (right) histories for the 10 MPa sinusoidal wave. The growth follows a power law in time with exponent ≈ 0.66, which is faster than the $t^{3/5}$ growth observed 3, seemingly because the simulation was not able to reach late time behavior with the computational resources provided.

trapezoidal wave.

A.7 Comparison of elastic and inertial forces for the 10 MPa trapezoidal wave

In my pursuit of a better understanding of Diagnostic Ultrasound (DUS)-induced lung hemorrhage, one of the most common hesitancies of my work that I have encountered is my choice to model the alveolar septum as an interface between two fluids. The alveolar septa is, after all, composed of elastic tissue, which would intuitively resist the vorticity-driven deformation that I observe. Dimensional arguments have been previously presented in which the ratio of elastic and inertial forces relevant to diagnostic ultrasound of an alveolus is considered via Cauchy number and I do not wish to recapitulate those argument here. Rather, to address this issue in a perhaps more concrete, intuitive fashion I have developed a model to approximate the approximate elastic and inertial forces at the interface. Using these models each will be calculated as a function of time and compared for the 10 MPa trapezoidal wave of Chapter 3.

The inertial force of the moving fluid at the interface, in the vertical direction, per unit depth into the page, is approximated as

$$F(t)_{I,y} = s(t)\delta\rho_{\alpha_{50}}\overline{\ddot{y}(t)_{interface}}, \tag{A.8}$$

where $s(t)$ is the interface length; δ is the interface thickness parameter, $\rho_{\alpha_{50}}$ the density of a fluid mixture of equal parts air-water by volume (as this isocontour was previously used to define the interface location); and $\overline{\ddot{y}(t)_{interface}}$ is the mean y-velocity of the interface. We note that this is little more than $F_y = ma_y$, where the mass per unit depth m is the interface area $s(t)\delta$ and the vertical acceleration a_y is that of the mean interface location.

The elastic, restorative force of the interface, in the vertical direction, per unit depth into the page, is approximated as

$$F(t)_{E,y} = \frac{s(t) - s(0)}{s(0)} E_a s(t) \left|\overline{\boldsymbol{e}_s(x,t) \cdot \boldsymbol{e}_y}\right| \tag{A.9}$$

where E_a is the elastic modulus of the alveolar wall, which depends on the transmural pressure, and ranges from 12 to 140 kPa (Perlman & Wu, 2014). Note, the lower value $E_a = 5$ kPa Cavalcante (2005), used for in the non-dimensional arguments of Chapters 1 and 3, is perhaps more realistic, though here we aim to consider the worst case scenarios, so here we have used the largest value for the elastic modulus of the alveolar wall available in the literature. $\boldsymbol{e_s(x,t)}$ and $\boldsymbol{e_y}$ are unit vectors in the direction tangential to the interface, which varies in space and time. $\left|\overline{\boldsymbol{e}_s(x,t) \cdot \boldsymbol{e}_y}\right|$ is the average alignment between the interface tangent and vertical direction and corresponds to the portion of the restorative force which acts to resist the vertical inertia of the fluid. Note that in practice, is initially small (≈ 0.2), but approaches 1 as the interface deforms, and as such it played little role in the results.

Based on these models the inertial and elastic forces were calculated for the 10 MPa wave of Chapter 3, and the results were dimensionalized to increase intuitive physicality as was done in Chapter 4. In Figure A.8, the results are plotted as a force per unit depth (on a logarithmic scale) vs

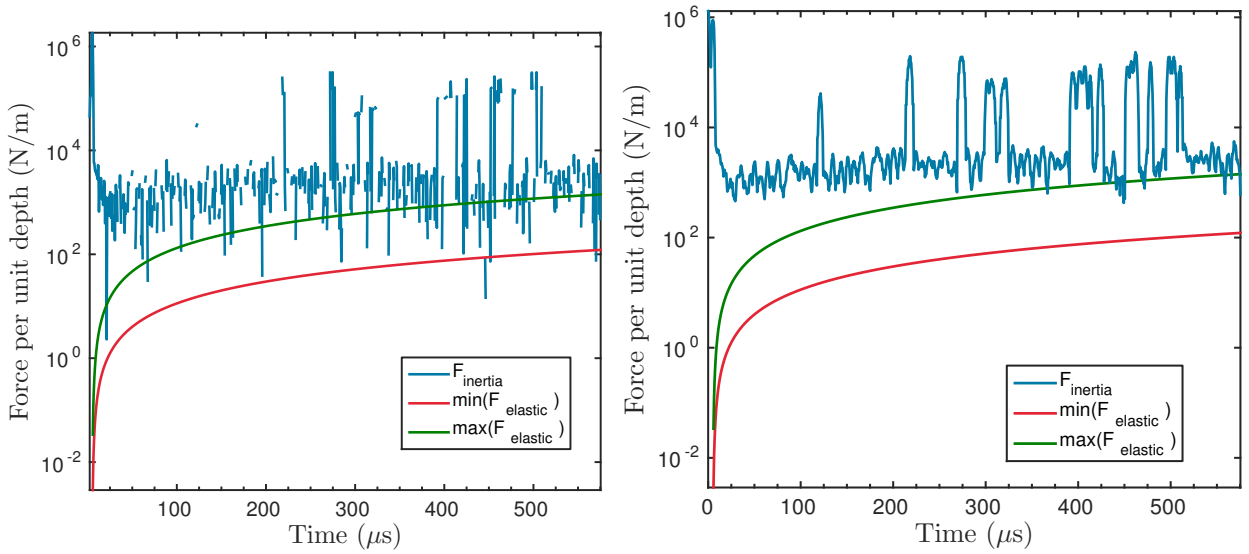

Figure A.8: Comparison of elastic and inertial forces for the $p_a = 10$ MPa trapezoidal wave. To help visualize the noisy data, the plot on the right contains the absolute value of the inertial force, with a moving average filter applied.

time in μs. The inertial force data is rather noisy as a result of the interface acceleration being taken as numerical second derivative of the interface position. In spite of this, it appears that the inertial force of the fluid upon the interface, per unit depth is on the order of hundreds to thousands of Pa/m. Minimum and maximum elastic force values are given for $E_a = 12$ and 140 kPa, and range from less than 100 *Pa* to approximately 10 kPa. While a crude estimate of each, this demonstrates within reason that the fluid inertia at the alveolar wall is expected to dominate its elastic restorative force for several hundreds of microseconds, over which considerable deformation and strain of the interface occurs.

Appendix B

Appendices for Chapter 4

B.1 Circulation due to $1, 2.5,$ and 5 MPa Ultrasound Pules with dependence on p_a and a_0

To illustrate that the circulation remains after the passage of the wave for Ultrasound (US) pulses within the diagnostic regime, and to explore the dependence of the ultrasound-generated circulation on p_a, Figure B.1b shows the circulation history $\Gamma(t)$ for the $a_0 = 0.3\ell$ case for $a_0 = 0.03\ell$ (blue), 0.1ℓ (red), and 0.3ℓ (green). During the wave-interface interaction $t \leq 10$, the circulation again fluctuates rapidly, however it can be seen that the chronologically local mean circulation increases with increasing p_a as would be expected since the amplitude of the pressure gradient also rises. After the passage of the wave the amount of circulation remaining increases with increasing p_a, though not necessarily according to a purely linear relationship.

B.2 Ultrasound-induced interface growth, strain, and circulation

The interface amplitude growth $a(t)/a_0$, strain $\varepsilon(t)$, and circulation Γ are plotted for all $p_a = 1, 2.5,$ and 5 MPa cases.

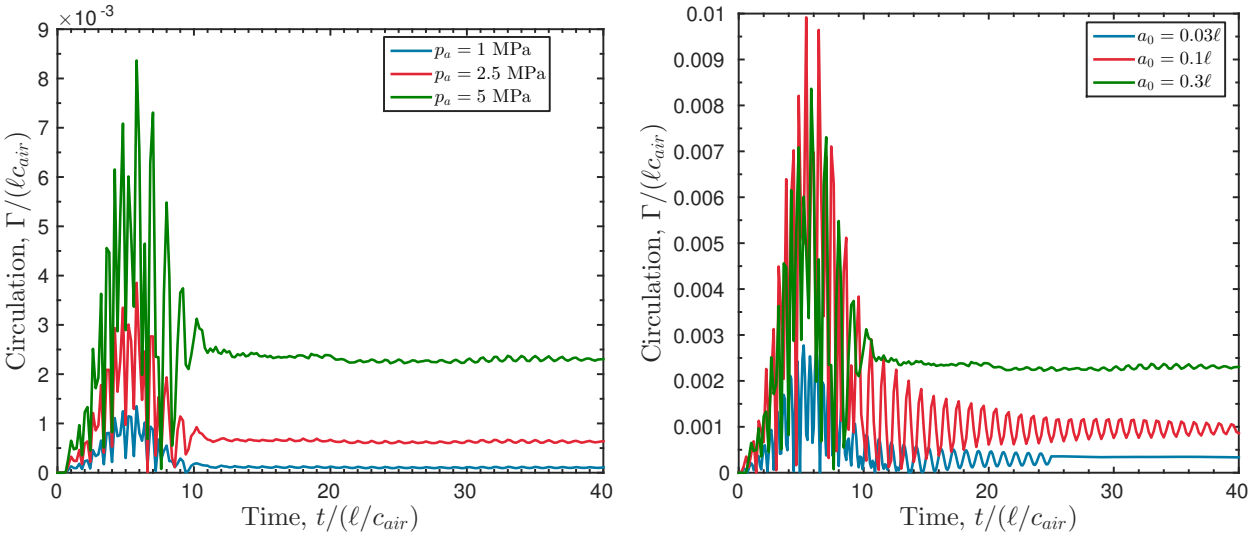

(a) $p_a = 1, 2.5, 5$ MPa, $a_0 = 0.3\ell$ (b) $p_a = 5$ MPa, $a_0 = 0.03\ell, 0.1\ell, 0.3\ell$

Figure B.1: Dependence of circulation deposition on pressure amplitude (left) and initial perturbation amplitude (right).

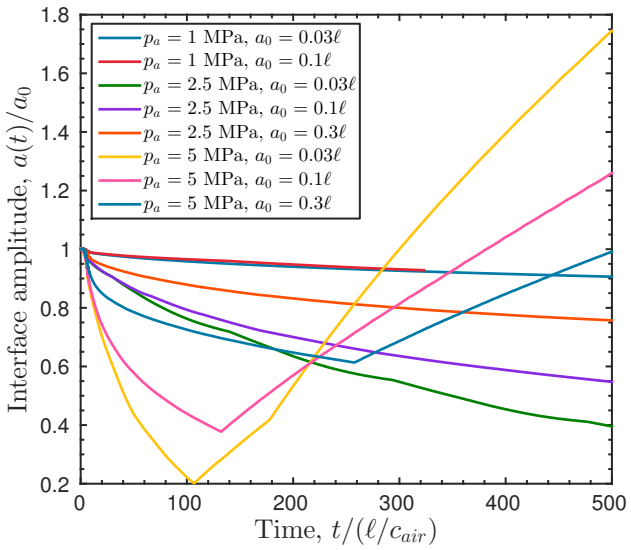

(a) Interface amplitude $a(t)$

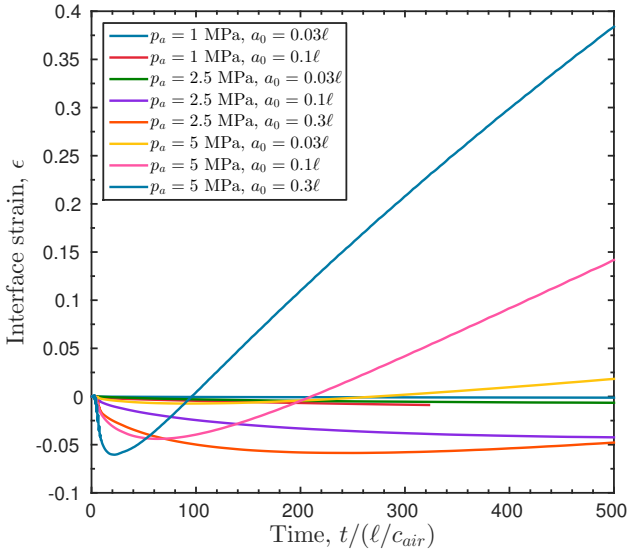

(b) Strain $\varepsilon(t)$

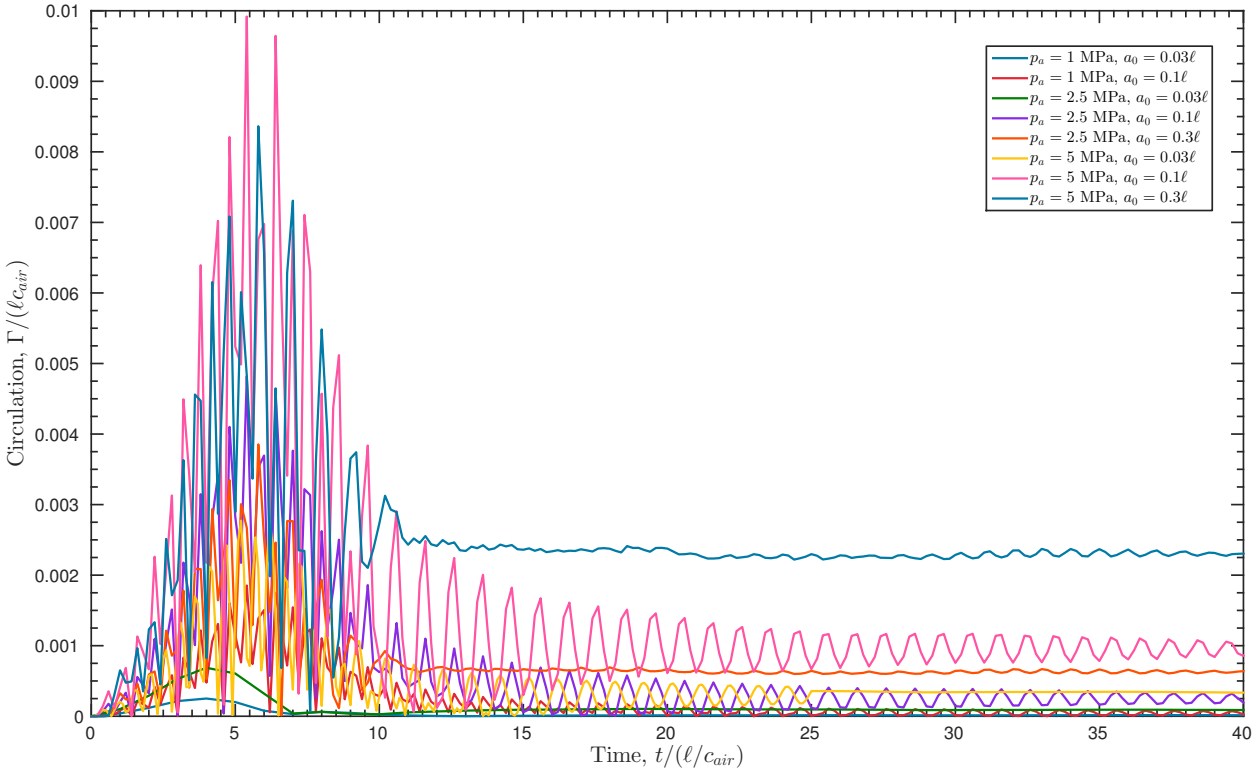

(c) Circulation $\Gamma(t)$

Figure B.2: Interface amplitude, circulation, and strain histories are presented for all ultrasound pulse cases considered in Chapter 4.

Appendix C

Underwater uncertainty Monte Carlo Randomization Techniques

C.1 Area statistics randomizations

This appendix is meant largely to serve for personal reference and serves to explain some of the finer points of the Monte Carlo randomization techniques used in Chapter 6. Specifically, some of the details useful in replicating or programming the bathymetry and sound speed randomization are detailed herein.

C.1.1 Bathymetry

For each of N Monte Carlo sample runs, the bathymetry profile is a function of range r, depth z, and is determined through a stochastic process represented by ξ.

$$D_n(r;\xi) = D_\mu(r) + D_\sigma(r, \xi_n(r)).$$

Where $n = 0, 1, 2, ..., N$. D_μ is the best estimate bathymetry profile based on available databases. $D_\sigma(r, z; \xi)$ is the stochastic portion of the sound speed profile and ξ_n is a random event. The random portion of the sound speed profile D_σ is defined based on the work of Lermusiaux *et al.* (2010), and is dependent upon local depth, normalized slope, and a global parameter ϵ representing relative

deviation from the best guess (e.g. 1%, 2%, 3%),

$$D_\sigma(r,z) = D_m u(r) \epsilon \hat{S}(x,y) \xi,$$

where $\hat{S}$ is local slope normalized by the maximum slope for the best guess bathymetry profile.

$$\hat{S}(r) = \frac{\left|\nabla D_\mu(r)\right|}{max(|\nabla D(r|)},$$

such that $\hat{S}(x,y) \subseteq [0,1]$.

$$D_n(r;\xi) = D_\mu(r) + D_\sigma(r,\xi_n).$$

C.1.2 Sound speed profile

For each of N Monte Carlo sample runs, the sound speed profile $c = c(r,z;\xi)$ is a function of range r, depth z, and is determined through a stochastic process represented by ξ.

$$c_n(r,z;\xi) = c_\mu(r,z) + c_\sigma(r,z;\xi_n)$$

Where $n = 0,1,2,...,N$. c_μ is the best estimate sound speed profile, which is calculated as the month-averaged velocity profile at a given location (r,z). $c_\sigma(r,z;\xi)$ is the stochastic portion of the sound speed profile and ξ_n is a random event. At each range of interest, c_μ is obtained by finding the average averaging 1 sound speed profile per month over an M month timespan. Monthly profiles are obtained from private databases.

To calculate $c_\sigma(r,z;\xi_n)$ empirical orthogonal functions are used to randomize the sound speed profile for each Monte Carlo sample calculation. At a given range, the sound speed variation at each fixed depth can be thought of an independent variable, such that the value of that sound speed calculated for each month represents a new observation of that variable. Hence, at each range, a

matrix $\boldsymbol{C}$ is constructed such that each column of $\boldsymbol{C}$ constitutes a single sound speed profile taken at D constant depths from a each of the M months considered. Such that we have D random variables, each with M observations and $\boldsymbol{C}$ is of dimensions $D \times M$ (rows $\times$ columns). The covariance matrix of $\boldsymbol{C}^{\intercal}$ is constructed

$$\boldsymbol{\chi} = \frac{\left(\boldsymbol{C} - \boldsymbol{\mathcal{M}}_{\mu}\right)\left(\boldsymbol{C} - \boldsymbol{\mathcal{M}}_{\mu}\right)^{\intercal}}{M - 1}.$$

Here $\boldsymbol{\mathcal{M}}_{\mu}$ is a matrix with the dimensions equal to that of $\boldsymbol{C}$, for which each column is c_{μ}, a $D \times 1$ vector containing the row average of $\boldsymbol{C}$. We solve

$$\boldsymbol{\chi}\mathbf{v}_i = \lambda_i \mathbf{v}_i$$

to find the eigenvalues λ_i and corresponding right eigenvectors $\mathbf{v}_i$ of $\boldsymbol{\chi}$. Each of the random sound speed profiles will be constructed from the mean sound speed profile c_{μ}, and a sum over S randomly weighted orthogonal eigenfunctions. We define S as the number of eigenfunctions necessary to capture 95% of the variance in the sample sound speed profiles, such that S is the minimum integer which satisfies

$$0.95 \leq \frac{\sum_{j=1}^{S} \lambda_j}{\sum_{j=1}^{\infty} \lambda_j}.$$

Hence the random component of each of the n^{th} sound speed profiles is defined as

$$c_{\sigma,n}(r, z; \xi) = \sum_{j=1}^{S} \xi_{j,n} \sqrt{\lambda_j(r)} \mathbf{v}_j(r, z),$$

where random event $\xi_{j,n}$ is sampled from a Gaussian distribution centered at 0 with unit variance. Thus for the n^{th} sample calculation, the randomized sound speed profile at a range-depth location

(r, z) is described by

$$c_n(r, z; \xi) = c_\mu(r, z) + \sum_{j=1}^{S} \xi_{j,n} \sqrt{\lambda_j(r)} \mathbf{v}_j(r, z).$$

BIBLIOGRAPHY

Abbot, P., & Dyer, I. 2002. Sonar Performance Predictions Incorporating Environmental Variability. *Pages 611–618 of:* Pace, N. G., & Jensen, F. B. (eds), *Impact Littoral Environ. Var. Acoust. Predict. Sonar Perform.* Dordrecht: Springer Netherlands.

Abbot, P., Dyer, I., & Emerson, C. 2006. Acoustic Propagation Uncertainty in the Shallow East China Sea. *IEEE J. Ocean. Eng.*, **31**, 368–383.

Allen, J. S., & Roy, R. A. 2000a. Dynamics of gas bubbles in viscoelastic fluids. I. Linear viscoelasticity. *J. Acoust. Soc. Am.*, **107**, 3167.

Allen, J. S., & Roy, R. A. 2000b. Dynamics of gas bubbles in viscoelastic fluids. II. Nonlinear viscoelasticity. *J. Acoust. Soc. Am.*, **108**, 1640–1650.

American Institute of Ultrasound in Medicine. 2000. Section 7–discussion of the mechanical index and other exposure parameters. *J. Ultrasound Med.*, **19**, 143–8, 154–68.

Anderson, J. D. 1990. *Modern compressible flow: with historical perspective vol. 2*. series in aeronautical and aerospace engineering, vol. 2. New York: McGraw–Hill.

Apfel, R. E. 1982. Acoustic cavitation: a possible consequence of biomedical uses of ultrasound. *Br. J. Cancer. Suppl.*, **5**, 140–6.

Apfel, R. E., & Holland, C. K. 1991. Gauging the likelihood of cavitation from short-pulse, low-duty cycle diagnostic ultrasound. *Ultrasound Med. Biol.*, **17**, 179–85.

Arda, K., Ciledag, N., Aktas, E., Aribas, B. K., & Köse, K. 2011. Quantitative assessment of normal soft-tissue elasticity using shear-wave ultrasound elastography. *AJR. Am. J. Roentgenol.*, **197**, 532–6.

Averkiou, M., Powers, J., Skyba, D., Bruce, M., & Jensen, S. 2003. Ultrasound Contrast Imaging Research. *Ultrasound Q.*, **19**, 27–37.

Baggs, R., Penney, D. P., Cox, C., Child, S. Z., Raeman, C. H., Dalecki, D., & Carstensen, E. L. 1996. Thresholds for ultrasonically induced lung hemorrhage in neonatal swine. *Ultrasound Med. Biol.*, **22**, 119–128.

Barajas, C., & Johnsen, E. 2017. The effects of heat and mass diffusion on freely oscillating bubbles in a viscoelastic, tissue-like medium. *J. Acoust. Soc. Am.*, **141**, 908–918.

Barnett, S. B., Ter Haar, G. R., Ziskin, M. C., Nyborg, W. L., Maeda, K., & Bang, J. 1994. Current status of research on biophysical effects of ultrasound. *Ultrasound Med. Biol.*, **20**, 205–218.

Bayliss, L. E., & Robertson, G. W. 1939. THE VISCO-ELASTIC PROPERTIES OF THE LUNGS. *Q. J. Exp. Physiol. Cogn. Med. Sci.*, **29**, 27–47.

Belete, H. A., Godin, L. M., Stroetz, R. W., & Hubmayr, R. D. 2010. Experimental models to study cell wounding and repair. *Cell. Physiol. Biochem.*, **25**, 71–80.

Brouillette, M. 2002. The Richtmyer-Meshkov Instability. *Annu. Rev. Fluid Mech.*, **34**, 445–468.

Brujan, E. A. 2011. *Cavitation in non-newtonian fluids: With biomedical and bioengineering applications*. Berlin, Heidelberg: Springer Berlin Heidelberg.

Calder, B. 2006. On the uncertainty of archive hydrographic data sets. *IEEE J. Ocean. Eng.*, **31**, 249–265.

Carstensen, E. L., Gracewski, S., & Dalecki, D. 2000. The search for cavitation in vivo. *Ultrasound Med. Biol.*, **26**, 1377–1385.

Cavalcante, F. S. A. 2005. Mechanical interactions between collagen and proteoglycans: implications for the stability of lung tissue. *J. Appl. Physiol.*, **98**, 672–679.

Chen, C.T., & Millero, F. J. 1977. Speed of sound in seawater at high pressures. *J. Acoust. Soc. Am.*, **62**, 1129–1135.

Child, S. Z., Hartman, C. L., Schery, L. A., & Carstensen, E. L. 1990. Lung damage from exposure to pulsed ultrasound. *Ultrasound Med. Biol.*, **16**, 817–825.

Church, C. C. 2002. Spontaneous homogeneous nucleation, inertial cavitation and the safety of diagnostic ultrasound. *Ultrasound Med. Biol.*, **28**, 1349–1364.

Claudon, M., Dietrich, C., Choi, B., Cosgrove, D., Kudo, M., Nolsøe, C., Piscaglia, F., Wilson, S., Barr, R., Chammas, M., Chaubal, N., Chen, M.-H., Clevert, D., Correas, J., Ding, H., Forsberg, F., Fowlkes, J., Gibson, R., Goldberg, B., Lassau, N., Leen, E., Mattrey, R., Moriyasu, F., Solbiati, L., Weskott, H.-P., & Xu, H.-X. 2012. Guidelines and Good Clinical Practice Recommendations for Contrast Enhanced Ultrasound (CEUS) in the Liver Update 2012. *Ultraschall der Medizin - Eur. J. Ultrasound*, **34**, 11–29.

Cocchi, J. P., Saurel, R., & Loraud, J. C. 1996. Treatment of interface problems with Godunov-type schemes. *Shock Waves*, **5**, 347–357.

Collins, M. D. 1994. Generalization of the split-step Pade solution. *J. Acoust. Soc. Am.*, **96**, 382.

Dalecki, D. 2004. Mechanical bioeffects of ultrasound. *Annu. Rev. Biomed. Eng.*, **6**, 229–248.

Dalecki, D., Keller, B. B., Raeman, C. H., & Carstensen, E. L. 1993. Effects of pulsed ultrasound on the frog heart: I. Thresholds for changes in cardiac rhythm and aortic pressure. *Ultrasound Med. Biol.*, **19**, 385–90.

Dalecki, D., Child, S. Z., Raeman, C. H., Cox, C., & Carstensen, E. L. 1997. Ultrasonically induced lung hemorrhage in young swine. *Ultrasound Med. Biol.*, **23**, 777–781.

Denny, E., & Schroter, R. C. 2000. Viscoelastic behavior of a lung alveolar duct model. *J. Biomech. Eng.*, **122**, 143–51.

Drake, P. 2006. *High-Energy-Density Physics*. Shock Wave and High Pressure Phenomena. Springer Berlin Heidelberg.

Dussik, K. T. 1942. On the possibility of using ultrasound waves as a diagnostic aid. *Z Neurol Psychiatr*, **174**, 153–168.

Emerson, C., Lynch, J. F., Abbot, P., Lin, Y.-T., Duda, T. F., Gawarkiewicz, G. G., & Chen, C.-F. 2014. Acoustic Propagation Uncertainty and Probabilistic Prediction of Sonar System Performance in the Southern East China Sea Continental Shelf and Shelfbreak Environments. *IEEE J. Ocean. Eng.*, 1–15.

Escoffre, J.-M., & Bouakaz, A. 2016. *Therapeutic Ultrasound*. Advances in Experimental Medicine and Biology, vol. 880. Cham: Springer International Publishing.

Faffe, D. S., Rocco, Patricia, R. M., Negri, E. M., & Zin, W. A. 2002. Comparison of rat and mouse pulmonary tissue mechanical properties and histology. *J. Appl. Physiol.*, **92**, 230–234.

FDA. 1997. Information for manufacturers seeking marketing clearance of diagnostic ultrasound systems and transducers. *Rockville, MD Cent. Devices Radiol. Heal. US Food Drug Adm.*

Filonenko, E. A., & Khokhlova, V. A. 2001. Effect of acoustic nonlinearity on heating of biological tissue by high-intensity focused ultrasound. *Acoust. Phys.*, **47**, 468–475.

Finette, S. 2005. Embedding uncertainty into ocean acoustic propagation models (L). *J. Acoust. Soc. Am.*, **117**, 997.

Finette, S. 2006. A stochastic representation of environmental uncertainty and its coupling to acoustic wave propagation in ocean waveguides. *J. Acoust. Soc. Am.*, **120**, 2567.

Finette, S. 2009. A stochastic response surface formulation of acoustic propagation through an uncertain ocean waveguide environment. *J. Acoust. Soc. Am.*, **126**, 2242–7.

Flynn, H. G. 1975a. Cavitation dynamics. I. A mathematical formulation. *J. Acoust. Soc. Am.*, **57**, 1379.

Flynn, H. G. 1975b. Cavitation dynamics: II. Free pulsations and models for cavitation bubbles. *J. Acoust. Soc. Am.*, **58**, 1160–1170.

Flynn, H. G. 1982. Generation of transient cavities in liquids by microsecond pulses of ultrasound. *J. Acoust. Soc. Am.*, **72**, 1926.

Frizzell, L. A. 1976. Shear properties of mammalian tissues at low megahertz frequencies. *J. Acoust. Soc. Am.*, **60**, 1409.

Frizzell, L. A., Chen, E., & Lee, C. 1994. Effects of pulsed ultrasound on the mouse neonate: Hind limb paralysis and lung hemorrhage. *Ultrasound Med. Biol.*, **20**, 53–63.

Frizzell, L. A., Zachary, J. F., & O'Brien, W. D. Jr. 2003. Effect of pulse polarity and energy on ultrasound-induced lung hemorrhage in adult rats. *J. Acoust. Soc. Am.*, **113**, 2912.

Gaudron, R., Warnez, M. T., & Johnsen, E. 2015. Bubble dynamics in a viscoelastic medium with nonlinear elasticity. *J. Fluid Mech.*, **766**, 54–75.

Gerstoft, P., Huang, C.-F., & Hodgkiss, W. S. 2006. Estimation of Transmission Loss in the Presence of Geoacoustic Inversion Uncertainty. *IEEE J. Ocean. Eng.*, **31**, 299–307.

Gil, J., Bachofen, H., Gehr, P., & Weibel, E. R. 1979. Alveolar volume-surface area relation in air- and saline-filled lungs fixed by vascular perfusion. *J Appl Physiol*, **47**, 990–1001.

Haas, J.-F., & Sturtevant, B. 1987. Interaction of weak shock waves with cylindrical and spherical gas inhomogeneities. *J. Fluid Mech.*, **181**, 41.

Harrison, G. H., Eddy, H. A., Wang, J.-P., & Liberman, F. Z. 1995. Microscopic lung alterations and reduction of respiration rate in insonated anesthetized swine. *Ultrasound Med. Biol.*, **21**, 981–983.

Heaney, K. D., & Cox, H. 2006. A Tactical Approach to Environmental Uncertainty and Sensitivity. *IEEE J. Ocean. Eng.*, **31**, 356–367.

Hecht, J., Alon, U., & Shvarts, D. 1994. Potential flow models of RayleighTaylor and Richtmyer-Meshkov bubble fronts. *Phys. Fluids*, **6**, 4019–4030.

Heifetz, E., & Mak, J. 2015. Stratified shear flow instabilities in the non-Boussinesq regime. *Phys. Fluids*, **27**, 086601.

Henry de Frahan, M. T., Varadan, S., & Johnsen, E. 2015a. A new limiting procedure for discontinuous Galerkin methods applied to compressible multiphase flows with shocks and interfaces. *J. Comput. Phys.*, **280**, 489–509.

Henry de Frahan, M. T., Movahed, P., & Johnsen, E. 2015b. Numerical simulations of a shock interacting with successive interfaces using the Discontinuous Galerkin method: the multilayered RichtmyerMeshkov and RayleighTaylor instabilities. *Shock Waves*, **25**, 329–345.

Holian, K. S. 1984. *T-4 handbook of material properties data bases*. Los Alamos National Laboratory.

Holland, C. K., & Apfel, R. E. 1989. An improved theory for the prediction of microcavitation thresholds. *IEEE Trans. Ultrason. Ferroelectr. Freq. Control*, **36**, 204–208.

Holland, C. K., Deng, C. X., Apfel, R. E., Alderman, J. L., Fernandez, L. A., & Taylor, K. J. W. 1996. Direct evidence of cavitation in vivo from diagnostic ultrasound. *Ultrasound Med. Biol.*, **22**, 917–925.

Jabaraj, D. J., & Jaafar, M. S. 2012. Theoretical Modelling of Alveolar Resonance Mechanism of Ultrasound-Induced Lung Haemorrhage. *Polish J. Med. Phys. Eng.*, **18**, 59–71.

Jabaraj, D. J., & Jaafar, M. S. 2013. Theoretical Calculation of Resonant Frequencies of the Human Alveolar Wall and Its Implications in Ultrasound Induced Lung Hemorrhage. *Int. J. Biosci. Biochem. Bioinforma.*, **3**, 5–9.

Jabaraj, D. J., & S., Jaafar M. 2013. Theoretical Calculation of Bending Stiffness of Alveolar Wall. *J. Membr. Biol.*, **246**, 981–984.

James, K. R., & Dowling, D. R. 2008. A method for approximating acoustic-field-amplitude uncertainty caused by environmental uncertainties. *J. Acoust. Soc. Am.*, **124**, 1465–1476.

James, K. R., & Dowling, D. R. 2011. Pekeris waveguide comparisons of methods for predicting acoustic field amplitude uncertainty caused by a spatially uniform environmental uncertainty (L). *J. Acoust. Soc. Am.*, **129**, 589–592.

Jensen, Finn B., Kuperman, William A., Porter, Michael B., & Schmidt, Henrik. 2011. *Computational Ocean Acoustics*. Springer Science & Business Media.

Johnsen, E., & Colonius, T. 2009. Numerical simulations of non-spherical bubble collapse. *J. Fluid Mech.*, **629**, 231.

Johnsen, E., & Hua, C. 2012. Bubble Dynamics in a Standard Linear Solid (Viscoelastic) Medium. *Pages 103–107 of: Proc. 8th Int. Symp. Cavitation*. Singapore: Research Publishing Services.

Keller, J. B. 1980. Bubble oscillations of large amplitude. *J. Acoust. Soc. Am.*, **68**, 628.

Khokhlova, V. A., Bailey, M. R., Reed, J. A., Cunitz, B. W., Kaczkowski, P. J., & Crum, L. A. 2006. Effects of nonlinear propagation, cavitation, and boiling in lesion formation by high intensity focused ultrasound in a gel phantom. *J. Acoust. Soc. Am.*, **119**, 1834–1848.

Kinsler, L. E., Frey, A. R., Coppens, A. B., & Sanders, J. V. 1982. Fundamentals of Acoustics by Lawrence. *J. Acoust. Soc. Am.*, **72**, 1090.

Knust, J., Ochs, M., Gundersen, H. J. G., & Nyengaard, J. R. 2008. Stereological Estimates of Alveolar Number and Size and Capillary Length and Surface Area in Mice Lungs. *Anat. Rec. Adv. Integr. Anat. Evol. Biol.*, **292**, 113–122.

Kowe, R., Schroter, R. C., Matthews, F. L., & Hitchings, D. 1986. Analysis of elastic and surface tension effects in the lung alveolus using finite element methods. *J. Biomech.*, **19**, 541–549.

Kramer, J. M., Waldrop, T. G., Frizzell, L. A., Zachary, J. F., & O'Brien, W. D. 2001. Cardiopulmonary function in rats with lung hemorrhage induced by pulsed ultrasound exposure. *J. Ultrasound Med.*, **20**, 1197–1206.

Krouskop, T. A., Wheeler, T. M., Kallel, F., Garra, B. S., & Hall, T. 1998. Elastic Moduli of Breast and Prostate Tissues under Compression. *Ultrason. Imaging*, **20**, 260–274.

Kundu, P. K., Allen, J. S., & Smith, R. L. 1975. Modal Decomposition of the Velocity Field near the Oregon Coast. *J. Phys. Oceanogr.*, **5**, 683–704.

Lanir, Y. 1983. Constitutive equations for the lung tissue. *J. Biomech. Eng.*, **105**, 374–80.

Latini, M., Schilling, O., & Don, W. S. 2007. Effects of WENO flux reconstruction order and spatial resolution on reshocked two-dimensional RichtmyerMeshkov instability. *J. Comput. Phys.*, **221**, 805–836.

LeBlanc, L. R., & M., Foster H. 1980. An underwater acoustic sound velocity data model. *J. Acoust. Soc. Am.*, **67**, 2055–2062.

Lehmann, J. F., & Herrick, J. F. 1953. Biologic reactions to cavitation, a consideration for ultrasonic therapy. *Arch. Phys. Med. Rehabil.*, **34**, 86–98.

Leighton, T. G. 1997. *The Acoustic Bubble, Volume 10*. Academic Press.

Lermusiaux, P. F. J., Xu, J., Chen, C.-F., Jan, S., Chiu, L. Y., & Yang, Y.-J. 2010. Coupled Ocean-Acoustic Prediction of Transmission Loss in a Continental Shelfbreak Region: Predictive Skill, Uncertainty Quantification, and Dynamical Sensitivities. *IEEE J. Ocean. Eng.*, **35**, 895–916.

Lichtenstein, D. A. 2009. Ultrasound examination of the lungs in the intensive care unit. *Pediatr. Crit. Care Med.*, **10**, 693–698.

Linder, C. A., Gawarkiewicz, G. G., & Taylor, M. 2006. Climatological Estimation of Environmental Uncertainty Over the Middle Atlantic Bight Shelf and Slope. *IEEE J. Ocean. Eng.*, **31**, 308–324.

Litzlbauer, H. D. 2006. Three-dimensional imaging and morphometric analysis of alveolar tissue from microfocal X-ray-computed tomography. *AJP Lung Cell. Mol. Physiol.*, **291**, L535–L545.

Livingston, E. S., Goff, J. A., Finette, S., Abbot, P., Lynch, J. F., & Hodgkiss, W. S. S. 2006. Guest editorial: Capturing uncertainty in the tactical ocean environment. *IEEE J. Ocean. Eng.*, **31**, 245–248.

MacRobbie, A. G., Raeman, C. H., Child, Sally Z., & Dalecki, Diane. 1997. Thresholds for premature contractions in murine hearts exposed to pulsed ultrasound. *Ultrasound Med. Biol.*, **23**, 761–765.

Madsen, E. L., Sathoff, H. J., & Zagzebski, J. A. 1983. Ultrasonic shear wave properties of soft tissues and tissuelike materials. *J. Acoust. Soc. Am.*, **74**, 1346–1355.

Marmottant, P., van der Meer, S., Emmer, M., Versluis, M., de Jong, N., Hilgenfeldt, S., & Lohse, D. 2005. A model for large amplitude oscillations of coated bubbles accounting for buckling and rupture. *J. Acoust. Soc. Am.*, **118**, 3499.

Marsh, S. P., & Los Alamos Data Center for Dynamic Material Properties (U.S.). 1980. *LASL shock hugoniot data*. University of California Press.

McLean, A. R., Richards, M. E., Crandall, C. S., & Marinaro, J. L. 2011. Ultrasound determination of chest wall thickness: implications for needle thoracostomy. *Am. J. Emerg. Med.*, **29**, 1173–1177.

Meltzer, R. S., Adsumelli, R., Risher, W. H., Hicks, G. L., Stern, D. H., Shah, P. M., Wojtczak, J. A., Lustik, S. J., Gayeski, T. E., Shapiro, J. R., & Carstensen, E. L. 1998. Lack of Lung Hemorrhage in Humans After Intraoperative Transesophageal Echocardiography with Ultrasound Exposure Conditions Similar to Those Causing Lung Hemorrhage in Laboratory Animals. *J. Am. Soc. Echocardiogr.*, **11**, 57–60.

Mercer, R. R., Russell, M. L., & Crapo, J. D. 1994. Alveolar septal structure in different species. *J. Appl. Physiol.*, **77**, 1060–6.

Meshkov, E. E. 1969. Instability of the interface of two gases accelerated by a shock wave. *Fluid Dyn.*, **4**, 101–104.

Mikaelian, K. O. 1996. Numerical simulations of RichtmyerMeshkov instabilities in finite-thickness fluid layers. *Phys. Fluids*, **8**, 1269.

Mikaelian, K. O. 2009. Nonlinear hydrodynamic interface instabilities driven by time-dependent accelerations. *Phys. Rev. E*, **79**, 065303.

Miller, D. L. 2012. Induction of Pulmonary Hemorrhage in Rats During Diagnostic Ultrasound. *Ultrasound Med. Biol.*, **38**, 1476–1482.

Miller, D. L. 2016a. Mechanisms for Induction of Pulmonary Capillary Hemorrhage by Diagnostic Ultrasound: Review and Consideration of Acoustical Radiation Surface Pressure. *Ultrasound Med. Biol.*, **42**, 2743–2757.

Miller, D. L. 2016b. The interaction of pulsed ultrasound with mammalian lung. *J. Acoust. Soc. Am.*, **140**, 3246–3246.

Miller, D. L., & Thomas, R. M. 1990. Lung damage from exposure to pulsed ultrasound. *Ultrasound Med. Biol.*, **16**, 817–825.

Miller, D. L., Averkiou, M. A., Brayman, A. A., Everbach, E. C., Holland, C. K., Wible, J. H., & Wu, J. 2008a. Bioeffects considerations for diagnostic ultrasound contrast agents. *J. Ultrasound Med.*, **27**, 611–632; quiz 633–636.

Miller, D. L., Dou, C., & Wiggins, R. C. 2008b. Frequency Dependence of Kidney Injury Induced by Contrast-Aided Diagnostic Ultrasound in Rats. *Ultrasound Med. Biol.*, **34**, 1678–1687.

Miller, D. L., Dou, C., & Raghavendran, K. 2015. Dependence of Thresholds for Pulmonary Capillary Hemorrhage on Diagnostic Ultrasound Frequency. *Ultrasound Med. Biol.*, **41**, 1640–1650.

Millero, F. J., & Li, X.u. 1994. Comments on "On equations for the speed of sound in seawater" [J. Acoust. Soc. Am. 93, 255-275 (1993)]. *J. Acoust. Soc. Am.*, **95**, 2757–2759.

Movahed, P., & Johnsen, E. 2013. A solution-adaptive method for efficient compressible multifluid simulations, with application to the RichtmyerMeshkov instability. *J. Comput. Phys.*, **239**, 166–186.

Munk, W. H. 1994. The Heard Island Feasibility Test. *J. Acoust. Soc. Am.*, **96**, 2330.

National Council on Radiation Protection and Measurements. Scientific Committee 66 on Biological Effects of Ultrasound., & National Council on Radiation Protection and Measurements. 2002. *Exposure criteria for medical diagnostic ultrasound. II, Criteria based on all known mechanisms : recommendations*. National Council on Radiation Protection and Measurements.

Nyborg, W. L. 2001. Biological effects of ultrasound: Development of safety guidelines. Part II: General review. *Ultrasound Med. Biol.*, **27**, 301–333.

O'Brien, W. D., Jr., Frizzell, L. A., Schaeffer, D. J., & Zachary, J. F. 2000a. Role of pulse repetition frequency and exposure duration on the superthreshold behavior of ultrasound-induced lung haemorrhage in adult mice and rats. *2000 IEEE Ultrason. Symp. Proceedings. An Int. Symp. (Cat. No.00CH37121)*, **2**, 267–277.

O'Brien, W. D., Jr., Simpson, D. G., Frizzell, L. A., & Zachary, J. F. 2001a. Age-dependent threshold and superthreshold behavior of ultrasound-induced lung hemorrhage in pigs. *2001 IEEE Ultrason. Symp. Proceedings. An Int. Symp. (Cat. No.01CH37263)*, **2**.

O'Brien, W. D. 2007. Ultrasoundbiophysics mechanisms. *Prog. Biophys. Mol. Biol.*, **93**, 212–255.

O'Brien, W. D., & Zachary, J. F. 1997. Lung damage assessment from exposure to pulsed-wave ultrasound in the rabbit, mouse, and pig. *IEEE Trans. Ultrason. Ferroelectr. Freq. Control*, **44**, 473–485.

O'Brien, W. D., Frizzell, L. A., Weigel, Ronald M., & Zachary, J. F. 2000b. Ultrasound-induced lung hemorrhage is not caused by inertial cavitation. *J. Acoust. Soc. Am.*, **108**, 1290–1297.

O'Brien, W. D., Simpson, D. G., Frizzell, L. A., & Zachary, J. F. 2001b. Superthreshold behavior and threshold estimates of ultrasound-induced lung hemorrhage in adult rats: role of beamwidth. *IEEE Trans. Ultrason. Ferroelectr. Freq. Control*, **48**, 1695–1705.

O'Brien, W. D., Frizzell, L. A., Schaeffer, D. J., & Zachary, J. F. 2001c. Superthreshold behavior of ultrasound-induced lung hemorrhage in adult mice and rats: role of pulse repetition frequency and exposure duration. *Ultrasound Med. Biol.*, **27**, 267–277.

O'Brien, W. D., Kramer, J. M., Waldrop, T. G., Frizzell, L. A., Miller, R. J., Blue, J. P., & Zachary, J. F. 2002. Ultrasound-induced lung hemorrhage: Role of acoustic boundary conditions at the pleural surface. *J. Acoust. Soc. Am.*, **111**, 1102.

O'Brien, W. D., Simpson, D. G., H., Moon-Ho, Miller, R. J., Frizzell, L. A., & Zachary, J. F. 2003a. Superthreshold behavior and threshold estimation of ultrasound-induced lung hemorrhage in pigs: Role of age dependency. *IEEE Trans. Ultrason. Ferroelectr. Freq. Control*, **50**, 153–169.

O'Brien, W. D., Simpson, Douglas G., Frizzell, L. A., & Zachary, J. F. 2003b. Threshold estimates and superthreshold behavior of ultrasound-induced lung hemorrhage in adult rats: Role of pulse duration. *Ultrasound Med. Biol.*, **29**, 1625–1634.

O'Brien, W. D., Simpson, D. G., Frizzell, L. A., & Zachary, J. F. 2004. Effect of Contrast Agent on the Incidence and Magnitude of Ultrasound-Induced Lung Hemorrhage in Rats. *Echocardiography*, **21**, 417–422.

O'Brien, W. D., Simpson, D. G., Frizzell, L. A., & Zachary, J. F. 2005. Superthreshold behavior of ultrasound-induced lung hemorrhage in adult rats: Role of pulse repetition frequency and exposure duration revisited. *J. Ultrasound Med.*, **24**, 339–348.

O'Brien, W. D., Yang, Y., Simpson, D. G., Frizzell, L. A., Miller, R. J., Blue, J. P., & Zachary, J. F. 2006a. Threshold estimation of ultrasound-induced lung hemorrhage in adult rabbits and comparison of thresholds in mice, rats, rabbits and pigs. *Ultrasound Med. Biol.*, **32**, 1793–1804.

O'Brien, W. D. Jr., Simpson, D. G., Frizzell, L. A., & Zachary, J. F. 2006b. Superthreshold Behavior of Ultrasound-Induced Lung Hemorrhage in Adult Rats: Role of Pulse Repetition Frequency and Pulse Duration. *J. Ultrasound Med.*, **25**, 873–882.

Ochs, M., Nyengaard, J. R., Jung, A., Knudsen, L., Voigt, M., Wahlers, T., Richter, J., & Gundersen, H. J. G. 2004. The Number of Alveoli in the Human Lung. *Am. J. Respir. Crit. Care Med.*, **169**, 120–124.

Pace, N. G., & Jensen, F. 2002. *Impact of Littoral Environmental Variability on Acoustic Predictions and Sonar Performance*. Springer Science & Business Media.

Parameswaran, H., Bartolak-Suki, E., Hamakawa, H., Majumdar, A., Allen, P. G., & Suki, B. 2009. Three-dimensional measurement of alveolar airspace volumes in normal and emphysematous lungs using micro-CT. *J. Appl. Physiol.*, **107**, 583–592.

Patterson, B., & Dowling, D. (In preparation). Efficient estimation of the probability density function of acoustic transmission loss in uncertain ocean environments using area statistics.

Patterson, B., & Johnsen, E. 2017. Dynamics of pulsed-ultrasound driven gas-liquid interfaces. *J. Acoust. Soc. Am.*, **141**(5), 4014–4014.

Patterson, B., & Johnsen, E. (In preparation). Growth of liquid-gas interfacial perturbations driven by acoustic waves.

Patterson, B., Miller, D. L., & Johnsen, E. 2012a. Theoretical microbubble dynamics in a homogeneous viscoelastic medium at capillary breaching thresholds. *J. Acoust. Soc. Am.*, **131**, 3385–3385.

Patterson, B., Miller, D. L., & Johnsen, E. 2012b. Theoretical microbubble dynamics in a viscoelastic medium at capillary breaching thresholds. *J. Acoust. Soc. Am.*, **132**, 3770.

Peng, G., Zabusky, N. J., & Zhang, S. 2003. Vortex-accelerated secondary baroclinic vorticity deposition and late-intermediate time dynamics of a two-dimensional RichtmyerMeshkov interface. *Phys. Fluids*, **15**, 3730–3744.

Penney, D. P., Schenk, E. A., Maltby, K., Hartman-Raeman, C., Child, S. Z., & Carstensen, E. L. 1993. Morphological effects of pulsed ultrasound in the lung. *Ultrasound Med. Biol.*, **19**, 127–135.

Perlman, C. E., & Wu, Y. 2014. In situ determination of alveolar septal strain, stress and effective Young's modulus: an experimental/computational approach. *Am. J. Physiol. Lung Cell. Mol. Physiol.*, **307**, L302–10.

Picone, J. M., & Boris, J. P. 1988. Vorticity generation by shock propagation through bubbles in a gas. *J. Fluid Mech.*, **189**, 23—-51.

Porter, T. M., Smith, D. A. B., & Holland, C. K. 2006. Acoustic Techniques for Assessing the Optison Destruction Threshold. *J. Ultrasound Med.*, **25**, 1519–1529.

Pozrikidis, C. 2000. Theoretical and computational aspects of the self-induced motion of three-dimensional vortex sheets. *J. Fluid Mech.*, **425**, 335–366.

Quirk, J. J., & Karni, S. 1996. On the dynamics of a shockbubble interaction. *J. Fluid Mech.*, **318**, 129.

Raeman, C. H., Child, S. Z., & Carstensen, E. L. 1993. Timing of exposures in ultrasonic hemorrhage of murine lung. *Ultrasound Med. Biol.*, **19**, 507–512.

Raeman, C. H., Child, S. Z., Dalecki, D., Cox, C., & Carstensen, E. L. 1996. Exposure-time dependence of the threshold for ultrasonically induced murine lung hemorrhage. *Ultrasound Med. Biol.*, **22**, 139–141.

Raeman, C. H., Dalecki, D., Child, S. Z., Meltzer, R. S., & Carstensen, E. L. 1997. Albunex Does Not Increase the Sensitivity of the Lung to Pulsed Ultrasound. *Echocardiography*, **14**, 553–557.

Raisinghani, A., Rafter, P., Phillips, P., Vannan, M. A., & DeMaria, A. N. 2004. Microbubble contrast agents for echocardiography: rationale, composition, ultrasodund interactions, and safety. *Cardiol. Clin.*, **22**, 171–180.

Reifenrath, R. 1975. The significance of alveolar geometry and surface tension in the respiratory mechanics of the lung. *Respir. Physiol.*, **24**, 115–37.

Richtmyer, R. D. 1960. Taylor Instability in Shock Acceleration of Compressible Fluids. *Commun. Pure Appl. Math.*, **XIII**, 297–319.

Roan, E., & Waters, C. M. 2011. What do we know about mechanical strain in lung alveoli? *Am. J. Physiol. - Lung Cell. Mol. Physiol.*, **301**.

Rognin, N. G., Frinking, P., Costa, M., & Arditi, M. 2008. In-vivo perfusion quantification by contrast ultrasound: Validation of the use of linearized video data vs. raw RF data. *Pages 1690–1693 of: 2008 IEEE Ultrason. Symp.* IEEE.

Samtaney, R., & Pullin, D. I. 1996. On initialvalue and selfsimilar solutions of the compressible Euler equations. *Phys. Fluids*, **8**, 2650–2655.

Samtaney, R., & Zabusky, N. J. 1994. Circulation deposition on shock-accelerated planar and curved density-stratified interfaces: models and scaling laws. *J. Fluid Mech.*, **269**, 45.

Sboros, V., MacDonald, C. A., Pye, S. D., Moran, C. M., Gomatam, J., & McDicken, W. N. 2002. The dependence of ultrasound contrast agents backscatter on acoustic pressure: theory versus experiment. *Ultrasonics*, **40**, 579–583.

Schürch, S., Goerke, J., & Clements, J. A. 1976. Direct determination of surface tension in the lung. *Proc. Natl. Acad. Sci. U. S. A.*, **73**, 4698–702.

Sha, L., & Nolte, L. W. 2005. Effects of environmental uncertainties on sonar detection performance prediction. *J. Acoust. Soc. Am.*, **117**, 1942.

Shyue, K.-M. 1998. An Efficient Shock-Capturing Algorithm for Compressible Multicomponent Problems. *J. Comput. Phys.*, **142**, 208–242.

Simon, J. C., Sapozhnikov, O. A., Khokhlova, V. A., Wang, Y.-N., Crum, L. A., & Bailey, M. R. 2012. Ultrasonic atomization of tissue and its role in tissue fractionation by high intensity focused ultrasound. *Phys. Med. Biol.*, **57**, 8061–78.

Singh, S., & Goyal, A. 2007. The origin of echocardiography: a tribute to Inge Edler. *Texas Hear. Inst. J.*, **34**, 431–8.

Skyba, D. M., Price, R. J., Linka, A. Z., Skalak, T. C., & Kaul, S. 1998. Direct in vivo visualization of intravascular destruction of microbubbles by ultrasound and its local effects on tissue. *Circulation*, **98**, 290–3.

Srebro, Y., Elbaz, Y., Sadot, O., Arazi, L., & Shvarts, D. 2003. A general buoyancydrag model for the evolution of the RayleighTaylor and RichtmyerMeshkov instabilities. *Laser Part. Beams*, **21**.

Stone, L. D., & Osborn, B. R. 2004. <title>Effect of environmental prediction uncertainty on target detection and tracking</title>. *Pages 58–69 of:* Drummond, Oliver E. (ed), *Def. Secur.* International Society for Optics and Photonics.

Suki, B., Barabási, A. L., & Lutchen, K. R. 1994. Lung tissue viscoelasticity: a mathematical framework and its molecular basis. *J. Appl. Physiol.*, **76**, 2749–2759.

Tarantal, A. F., & Canfield, D. R. 1994. Ultrasound-induced lung hemorrhage in the monkey. *Ultrasound Med. Biol.*, **20**, 65–72.

Taylor, G. 1950. The Instability of Liquid Surfaces when Accelerated in a Direction Perpendicular to their Planes. I. *Proc. R. Soc. A Math. Phys. Eng. Sci.*, **201**, 192–196.

Thompson, K. W. 1987. Time dependent boundary conditions for hyperbolic systems. *J. Comput. Phys.*, **68**, 1–24.

Thompson, K. W. 1990. Time-dependent boundary conditions for hyperbolic systems, II. *J. Comput. Phys.*, **89**, 439–461.

Tjan, K. K., & Phillips, W. R. C. 2007. On impulsively generated inviscid axisymmetric surface jets, waves and drops. *J. Fluid Mech.*, **576**, 377.

Tjan, K. K, & Phillips, W. R. C. 2008. On the impulsive generation of drops at the interface of two inviscid fluids. *Proc. R. Soc. A Math. Phys. Eng. Sci.*, **464**, 1125–1140.

Toulopoulos, Ioannis, & Ekaterinaris, John A. 2011. Artificial boundary conditions for the numerical solution of the Euler equations by the discontinuous galerkin method. *J. Comput. Phys.*, **230**, 5974–5995.

Towns, J., Cockerill, T., Maytal, D., Foster, I., Gaither, K., Grimshaw, A., Hazlewood, V., Lathrop, S., Lifka, D., Peterson, G. D., Roskies, R., Scott, J. R., & Wilkens-Diehr, N. 2014. XSEDE: Accelerating Scientific Discovery. *Comput. Sci. Eng.*, **16**, 62–74.

Tryggvason, G. 1988. Numerical simulations of the Rayleigh-Taylor instability. *J. Comput. Phys.*, **75**, 253–282.

Urick, R. J. 1962. Generalized Form of the Sonar Equations. *J. Acoust. Soc. Am.*, **34**, 547.

Warnez, M. T., & Johnsen, E. 2015. Numerical modeling of bubble dynamics in viscoelastic media with relaxation. *Phys. Fluids*, **27**, 063103.

West, J. B. 2000. Pulmonary capillary stress failure. *J. Appl. Physiol.*, **89**, 2483 LP – 2489.

West, J. B., Tsukimoto, K., Mathieu-Costello, O., & Prediletto, R. 1991. Stress failure in pulmonary capillaries. *J. Appl. Physiol.*, **70**, 1731–1742.

Yang, T. C., & Y., Kwang. 1999. Internal wave spectrum in shallow water: measurement and comparison with the Garrett-Munk model. *IEEE J. Ocean. Eng.*, **24**, 333–345.

Yang, X., & Church, C. C. 2005. A model for the dynamics of gas bubbles in soft tissue. *J. Acoust. Soc. Am.*, **118**, 3595–3606.

Zachary, J. F., & O'Brien, W. D. 1995. Lung Lesions Induced by Continuous- and Pulsed-Wave (Diagnostic) Ultrasound in Mice, Rabbits, and Pigs. *Vet. Pathol.*, **32**, 43–54.

Zachary, J. F., Sempsrott, J. M., Frizzell, L. A., Simpson, D. G., & O'Brien, W. D. 2001a. Superthreshold behavior and threshold estimation of ultrasound-induced lung hemorrhage in adult mice and rats. *IEEE Trans. Ultrason. Ferroelectr. Freq. Control*, **48**, 581–592.

Zachary, J. F., Frizzell, L. A., Norrell, K. S., Blue, J. P., Miller, R. J., & O'Brien, W. D. 2001b. Temporal and spatial evaluation of lesion reparative responses following superthreshold exposure of rat lung to pulsed ultrasound. *Ultrasound Med. Biol.*, **27**, 829–839.

Zachary, J. F., Blue, James P., Miller, R. J., Ricconi, B. J., Eden, J. G., & O'Brien, W. D. 2006. Lesions of ultrasound-induced lung hemorrhage are not consistent with thermal injury. *Ultrasound Med. Biol.*, **32**, 1763–1770.

Zeqiri, B. 2003. Exposure criteria for medical diagnostic ultrasound: II. Criteria based on all known mechanisms. *Ultrasound Med. Biol.*, **29**, 1809.

Zingarelli, R. A. 2008. A mode-based technique for estimating uncertainty in range-averaged transmission loss results from underwater acoustic calculations. *J. Acoust. Soc. Am.*, **124**, EL218–L222.